Effects of Processing Conditions and Ambient Environment on the Microstructure and Fracture Strength of Copper/Niobium/Copper Interlayer Joints for Alumina

ROBERT ALAN MARKS
B.S. (University of California, at Berkeley) 1996

A thesis submitted in partial satisfaction
of the requirements for the degree of

Master of Science
in
Engineering, Materials Science and Mineral Engineering

in the

GRADUATE DIVISION

of the

UNIVERSITY OF CALIFORNIA, at BERKELEY

Committee in charge:

Professor Andreas M. Glaeser, Chair
Professor Robert O. Ritchie
Professor Timothy D. Sands

Spring 2000

The master's thesis of Robert Alan Marks is approved:

Andreas M. Glaeser Dec. 13th 1999
Professor Andreas M. Glaeser, Chair Date

Dec. 15, 1999
Professor Robert O. Ritchie Date

12/14/99
Professor Timothy D. Sands Date

Effects of Processing Conditions and Ambient Environment on the Microstructure and Fracture Strength of Copper/Niobium/Copper Interlayer Joints for Alumina

by

Robert Alan Marks

Abstract

Effects of Processing Conditions and
Ambient Environment on the Microstructure and
Fracture Strength of Copper/Niobium/Copper
Interlayer Joints for Alumina

by

Robert Alan Marks
Master of Science in Engineering, Materials Science and Mineral Engineering

UNIVERSITY OF CALIFORNIA, at BERKELEY

Professor Andreas M. Glaeser, Chair

Partial transient liquid phase (PTLP) bonding is a technique which can be used to join ceramics with metals and is used to form niobium-based joints for alumina. The principal advantage to PTLP bonding is that it enables refractory joints to be fabricated at temperatures below those typically required by solid state diffusion bonding. A thorough review of the important parameters (chemical compatibility, thermal expansion match, sufficient wettability of the liquid phase on the solid phases) in choosing a joining material for ceramics by the PTLP method is provided. As in conventional PTLP joining, the current study uses thin (≈3 μm) copper layers sandwiched between the alumina (bulk) and niobium (127 μm). However, unlike the case of copper/nickel/copper and copper/platinum/copper interlayer joints, the solubility of copper in niobium is limited. Consequently, the copper is not entirely dissolved in the process, resulting in a two phase (copper-rich and niobium-rich phases) microstructure. Different processing conditions (temperature and applied load) result in different morphologies of the copper-rich and niobium-rich phases at the interface. These different microstructures exhibit distinct strength characteristics. Extended annealing of as-processed joints can influence the strengths differently depending on the ambient partial oxygen pressure at the annealing temperature. The focus of this work is to correlate processing conditions, microstructure,

and resulting joint strength. Under optimum processing conditions (1400°C, 2.2 MPa), joints with strengths in excess of 200 MPa at 1200°C are fabricated.

Andreas M. Glaeser

Table of Contents

Table of Tables

Table of Figures

Acknowledgments

First, I would like to thank my advisor, Professor Andreas M. Glaeser, for giving me this wonderful opportunity as a graduate student. I am truly honored to do graduate work at one of the best universities in the world, as well as a leading institution in materials science. This work would have been impossible and less enjoyable without his ideas, helpful insight for interpretation, and various other discussions.

I would also like to thank Professor Robert O. Ritchie and Professor Timothy D. Sands as members of my thesis committee for taking the time to review this document, especially upon rather short notice. Their thorough review, constructive criticism, and general interest in this work is greatly appreciated. Additionally, I appreciate the helpfulness and encouragement of my academic advisor Professor Ronald Gronsky throughout the duration of this master's degree program.

Several people have contributed both directly and indirectly to the success of this project. I would like to thank Dr. (not quite yet) Mark Locatelli for his assistance during the initial experiments of this project and several useful discussions througout its life. I would also like to acknowledge Daniel Chapman, David Danielson, and Joshua Sugar for preparing some of the joining specimens and assisting with optical microscopy. I would also like to thank Dr. Kuni Nakashima and Nikkato Corporation of Japan for providing the high strength alumina used in some experiments. Professor Mikito Kitayama and Dr. James Powers have been excellent teachers of various laboratory equipment used in this work (New Hot Press, SEM, and various furnaces). Similarly, I would like to thank Dr. Eduardo Saiz for his assistance with the SEM, controlled atmosphere furnaces (particularly after the move to Davis Hall), and several ideas and useful discussions on these and other relevant issues. Additionally, I would like to thank Mark Sixta and Dr. Jim McNaney for their assistance with the high temperature bend tester.

Certainly this experience would not have been as enjoyable without the friendship of other people working in the ceramics group for part of or the entirety of this project. In addition to those already mentioned, I thank Dr. Rowland Cannon, Laura Esposito, Silvia Foppiano, Jose Gomez-Vega, Dr. Lawrence Kulinsky, Ennio Mammana, Professor Takayuki Narushima, Dr. Antony Tomsia, and Loucas Szebeszczyk.

I am continually grateful for the love, support, and companionship of many other friends and members of my family throughout this rewarding yet stressful time. In particular, I'd like to acknowledge my mother (Paulette), my best friend (Earendil Burd-believe it or not, I was actually able to get this thesis to have more pages than my golf game has strokes), my sister (Jeanne) and my father (Donald). Finally, I would like to thank the Lord for giving me the ability to complete this project.

Chapter 1
Introduction

1.1 Purpose

Many advancements have been made in improving the mechanical integrity of structural ceramics. Such materials are an attractive alternative to metal alloys (*e.g.*, nickel-based superalloys) due to their low density and the high strength they maintain at high temperatures. The application of ceramic components in engines would enable engines to be run at even higher temperatures than possible today. Increasing the operating temperature of an engine will increase its energy efficiency, and one study reports that increasing the operating temperature of engines to 1200-1400°C would save 18 billion dollars annually [1]. Additionally, the lighter weight of ceramics would require less energy to initiate and maintain the motion of parts provided that lubricants can be developed to reduce friction to the same levels as in traditional metal-based engines. Ceramics can also be extremely stable in chemically aggressive environments, and therefore, could replace parts currently used in such environments and have a longer lifetime.

Industrially, ceramic parts with complicated geometry can be very difficult, time-consuming, and costly to fabricate. Often such parts require extensive machining in order to obtain the final part. Diamond tooling is required to machine the hardest of ceramics such as aluminum oxide[†] (Al_2O_3) or silicon carbide (SiC). Forming green compacts into complex shapes runs the risk of producing ceramic preforms with inhomogeneous packing density. Upon sintering, such compacts may develop into parts with an inhomogeneous

---

[†] In this work, the term aluminum oxide will generally refer to both polycrystalline and single crystalline aluminum oxide. More frequently, the term alumina will be used for information pertaining to polycrystalline aluminum oxide, but need not necessarily exclude applicability to single crystalline aluminum oxide. When such a distinction is relevant or necessary, the terms polycrystalline alumina or sapphire will be used, unless otherwise obvious.

microstructure which would adversely affect the parts' mechanical properties. Other inhomogeneities such as regions of open porosity would be unsuitable for a part that must be leakproof. Additionally, during sintering, green bodies with non-uniform packing may undergo non-uniform shrinkage (warpage), thus generating flaws and/or inducing residual stresses in the final products.

To combat these difficulties, ceramics parts have typically been pre-formed into compacts which somewhat resemble the final part, yet require some minimal amount of machining subsequent to sintering. A process (rapid prototyping) has also been developed which prints multiple layers of ceramic tapes (3-D printing). Each tape (layer) can be "printed" in a shape such that the final layered assembly exhibits the geometry of the desired part. This has been particularly useful for small-scale features in smaller ceramic parts [2]. The technique can also produce relatively large parts (≈35 cm); however, it is quite costly [3]. Another solution to these problems would be to join ceramic parts with relatively simple geometry to produce a more complicated part.

Manufacturing large ceramic parts is difficult regardless of the complexity of their geometry. Large parts require heavy machinery to form green bodies, and uniform packing is difficult to achieve. Isothermal processing of large parts is another obstacle, especially since many ceramics are thermal insulators. These issues increase the probability of obtaining critical flaws in large ceramic parts, while smaller parts can more easily be tested for such flaws. Batches of smaller parts which do not meet screening requirements would not be as costly to discard and replace [4]. As commonly done with metal parts, fastening smaller ceramic parts together with bolts, rivets, or clamps (shrink fitting) is not always practical for several reasons. Bolts and rivets may concentrate stresses and cause failure upon tightening. These devices would also require additional machining (*i.e.*, drilling holes), which may result in additional stress concentration sites. Clamping simply may not securely hold structures together to the extent necessary, especially for parts undergoing cyclic loading (*e.g.*, start and stop cycles of a rotating engine).

Consequently, a type of joining equivalent to welding in metal alloys is required, *i.e.*, one in which there is intimate contact (chemical bonding) between the surfaces being joined.

Joining ceramic components with metal interlayers is an advantageous approach for achieving these goals. Such joints often exhibit increased fracture toughness in comparison to the bulk ceramic, since the metal layer will exhibit some plasticity [5-8]. Structures which undergo some plastic deformation instead of catastrophic failure would be preferred, and joining smaller ceramic parts is beneficial in comparison to fabricating larger parts for this reason also. Metal-based joining would enable the manufacturing of large lightweight structures, requiring only a small fraction of the total volume to consist of denser metals. Additionally, ceramic-based assemblies joined in this way would only require that portions or single parts be replaced upon failure instead of an entire structure [4]. Joining ceramics with metals may be beneficial for other reasons such as producing structures in which each part may be made of a different material which is chosen such that its properties are optimum for the conditions it is subjected to, or the task it must fulfill. For example, aluminum nitride (AlN) joined with copper joints would enable a thermally conducting but electronically insulating ceramic to be intimately connected with an electric conductor [3], thus aluminum nitride could serve as an excellent heat sink in electronic applications.

Future application of structural ceramics in engines and electronic devices will certainly require that ceramics be joined to either other components made of the same material, or dissimilar materials (usually a metal or semiconductor). The joint in such structures will often need to withstand high temperatures and chemical attack, in addition to the applied loads the bulk material is subjected to. This work focuses on the joining of aluminum oxide to aluminum oxide with thin copper/niobium/copper interlayers and the effects different processing conditions and atmospheric environments have on the mechanical reliability of such joints. Additionally, the mechanical reliability and durability of these joints at high temperatures is explored. Although the work is dedicated to this specific system, some general implications regarding joining of other ceramics and dissimilar materials will also be apparent.

1.2 Traditional Ceramic Joining Techniques (Diffusion Bonding versus Brazing)

Ceramics have been successfully joined with metals *via* liquid-phase brazing or solid-state diffusion bonding (also referred to as solid-state welding); however, these techniques possess many limitations in both processing and application. Brazing is essentially a higher temperature version of soldering, and many of the same issues involved with choosing a good solder arise in brazing. In particular, the wettability of a liquid braze on the material(s) to be joined will determine whether or not the liquid spreads over the surfaces to be joined and how well it fills in flaws and defects on these surfaces. In general, liquid metals do not wet ceramic surfaces (oxides in particular [9-11]) very well, and unfilled flaws may act as stress concentration sites in a joined assembly. Consequently, surface cleaning is also important as it will increase the surface tension of the free surfaces to be joined, thus increasing the thermodynamic driving force for the braze to spread over the joining surfaces. Brazed joints are also limited in that the maximum possible temperature parts joined by such techniques can be used at is the joining temperature.

Solid-state diffusion bonding is usually carried out for joints which must survive at high temperatures and is typically used for joining ceramics to refractory metals such as niobium, molybdenum, platinum, tantalum, or tungsten. This joining process operates in a fashion very similar to sintering by eliminating pores or voids at the mated surfaces [12-14]. As a result, surface cleaning is very important for similar reasons as in brazing, *i.e.*, to increase the thermodynamic driving force to form an interface between the two materials. Surface flattening and polishing are also required to minimize the size of these voids, thus minimizing the required bonding time. Although diffusion bonding avoids wetting issues in the sense that no liquid has to be spread, wetting characteristics should not be completely ignored. The contact angle the solid metal makes with the ceramic will affect the geometry of flaws at the interface [15], which will determine the extent of stress concentrations. The work of adhesion also contributes to the fracture energy of the resulting metal/ceramic interface. Additionally, the quality of solid-state diffusion bonds depends on the applied pressure during bonding. Applied pressure serves to initially deform the metal (and sometimes the ceramic, if high enough temperatures are used) to increase the area of initial contact. Consequently, diffusion bonding is limited to fabricating assemblies of simple geometry, as required bonding pressures can be greater than that which parts of more complicated geometry are able to withstand.

Clearly, forming refractory joints by brazing requires extremely high temperatures or may not even be possible (*e.g.*, a case in which the metal has a greater melting point than the ceramic such as alumina joined with niobium, molybdenum, tantalum, or tungsten; or the liquid metal does not wet the ceramic well enough like brazing alumina with platinum [16]). Although diffusion bonding can be accomplished at 50% of the absolute melting point, T_f, of the joining material, temperatures in the range $0.8\text{-}0.9T_f$ are typically required for successful joints [17]. Processing at high temperatures can increase the likelihood of chemical reactions that would otherwise be thermodynamically or kinetically unfavorable at lower temperatures. Additionally, the magnitude of thermal stresses that develop upon cooling due to thermal mismatch between ceramics and joining materials are likely to be more crucial the greater the processing temperature, even for refractory metals with low thermal expansion coefficients. Residual thermal stresses are the primary reason aluminum nitride cannot simply be brazed with copper [3], and it would obviously not be productive to melt the constituents (copper) of an electronic device. In light of these concerns, methods of joining ceramics with refractory materials at lower temperatures is of great interest; ideally the development of techniques which join ceramic parts below their intended use temperature would be very beneficial.

1.3 Niobium-Based Joints for Aluminum Oxide

A niobium-based joint is promising because its thermal expansion coefficient nearly matches that of alumina. This match prohibits the development of extensive thermal stresses during the cooling cycle of processing, and implies that such a joint would be advantageous for applications in which parts undergo thermal cycling [18]. In fact, diffusion-bonded joints have remained intact for cooling rates as high as 215°C/min [19,20]. As mentioned in Section 1.2, niobium is quite refractory, having a melting point (2469°C) in excess of that of aluminum oxide (≈2050°C), and in principle, joints would be useful up to 1500°C [21].

One major drawback to niobium-based joints for alumina is that niobium is readily oxidized. Simple equilibrium partial oxygen pressure, p_{O_2}, calculations (as outlined in Appendix I) predict niobium oxide (NbO) will begin to form at a $p_{O_2} \approx 4\times10^{-15}$ atm at 1500°C. Higher values of p_{O_2} (1×10^{-13} and 5×10^{-11} atm) would result in the formation of other niobium oxides (NbO_2 and Nb_2O_5) at 1500°C. NbO and NbO_2 are quite volatile [22] and Nb_2O_5 decomposes at 1510°C [23], causing joints to disintegrate in air. In fact, a joint fabricated with a process used in the current study disintegrated before the sample could be heated to 1000°C in air [24]. These properties limit the high-temperature use of niobium-based joints in air, even if significant strength is maintained at low temperatures. Additionally, this work will show that exposing joints to extremely low p_{O_2} for extended periods of time degrades their mechanical reliability. Thus there is a limited range of p_{O_2} for which a niobium-based joint is useful. Although the reliability of niobium-based joints for alumina can be sensitive ambient oxygen activities, the thermal expansion match suggests they would be ideal for high-temperature applications in non-oxidizing environments (*e.g.*, high-temperature vacuum systems). In fact, all Lucalox tubes have niobium-alumina joints [3].

The primary goal of this work is to investigate the effects of various low-temperature processing conditions on alumina joined with copper/niobium/copper interlayers and to assess the high-temperature strength of such joints in environments which are known to not significantly alter the joint properties. It is hoped that this research will provide insight for many relevant issues affecting the development of joints more compatible with oxidizing environments, and provide a potential solution for at least some applications of structural ceramics.

Chapter 2
Background

2.1 Low-Temperature Joining Techniques (A Brief History)

Joining metals to oxides has been of interest ever since the invention of the electric light, which required connection of glass to tungsten or molybdenum filaments [10]. In fact, the metallization of ceramics has been accomplished for over one-thousand years by sintering metal powder coatings (usually silver, gold, platinum, and copper) on ceramic works [10]. Some metallization techniques used in the past involved firing metal oxide powders to a ceramic surface followed by the reduction of this oxide layer [10]. Additionally, several techniques were devoted to establishing sufficient wetting conditions on oxide ceramics. Van Houten [10] provides an excellent summary of joining techniques developed prior to 1959; however, it was not until after this that low-temperature techniques for joining materials began to be developed.

One of the first efforts in producing mechanical joints at low temperatures was the solid-liquid interdiffusion (SLID) technique discussed by Bernstein and Bartholomew [25]. The process relies on forming a low-temperature liquid (indium or tin) which reacts to form higher melting point intermetallic compounds with, or is completely dissolved by, higher melting point metals (copper, gold, nickel, or silver). SLID has been used to join several materials including metallized ceramics. The process is very similar to partial transient liquid phase (PTLP) bonding used in this research as well as other works [17,26-29], which will be discussed in detail in the following section.

During the early 1970's a method termed transient liquid phase (TLP™) bonding was developed to join high melting point alloys [30]. The TLP™ process is executed by melting a thin layer of a low melting point metal between the two metal parts to be joined and allowing this liquid layer to interdiffuse with the metal parts. The melted layer will isothermally solidify and the composition of the joined parts will homogenize.

This results in an assembly only slightly different in composition from the initial parts since the amount of TLP™ used is relatively small. Unlike conventional welding, the TLP™ method does not alter the microstructure adjacent to the joint interface [30]. Thus, a joined assembly with material properties approaching those of the original unjoined parts is produced. This process is also very beneficial because the bonding pressures (<70 kPa) and temperatures (1093-1204°C) are both well below those (3.5-35 MPa) required for diffusion bonding such alloys [30]. Additionally surface preparation is minimal in comparison to diffusion-bonding techniques.

Thus far, low-temperature joining techniques have been developed for the joining of metals. Direct application of the TLP™ technique to ceramics is quite limited because the solubility of metals in ceramics is typically extremely small. This implies that very small amounts (thin layers) of the TLP™ liquid would be necessary in order for the joined assembly to homogenize; however, such small amounts of liquid would generally be insufficient to fill gaps between the joining surfaces, thus prohibiting complete contact between parts being joined. Although TLP™ bonding will generally not be useful for joining ceramics with metals, it has been successfully used to join some ceramics in a few cases worth mentioning.

Silicon carbide containing excess silicon has been joined with germanium at 1180°C [31,32]. Although germanium melts at 937°C, a higher temperature was used for bonding to insure favorable wetting conditions [32]. Strengths in excess of 400 MPa were obtained at 1000°C for such joints, which increased from an average strength of approximately 150 MPa at room temperature. This increase is likely due to the relaxation of residual stresses at higher temperatures [32]. Loehman [33] has successfully joined silicon nitride (Si_3N_4) with an interlayer of the same composition as the glassy phase at the grain boundaries in the bulk material. In principle, such joints are potentially as strong as the bulk since the only effect they have on the material is the addition of a grain boundary; however, further investigation [34] revealed that optimum joint strength

(460 MPa) was obtained for joint thicknesses in the range 20-30 μm, much thicker than any grain boundary phase. Chemical analysis on the joining layer revealed that silicon oxynitride and beta-silicon nitride were present in joining layers [35], thus indicating an evolution of the joining layer and/or interaction between silicon nitride and the joining material. Recently, Glass *et al.* [36] have used this technique to produce joints having a strength of 555 MPa at 1000°C.

Gopal *et al.* [37,38] have used a similar approach by extending the idea of using rare-earth oxides (*e.g.*, Yb_2O_3, Y_2O_3, Dy_2O_3, and Er_2O_3) and silica (SiO_2) as sintering additives for silicon nitride to a joining process. Although such oxides and silica react to form high melting rare-earth disilicates (*e.g.*, $Yb_2O_3•2SiO_2$ melts at 1850°C) lower temperature eutectics close in composition to the rare-earth disilicate exist in such systems (1650°C for the yttria-silica system). The liquid-forming temperature can be reduced further by taking advantage of eutectics which form between various rare-earth disilicates. For example, Gopal *et al.* [38] used yttria (Y_2O_3), ytterbia (Yb_2O_3), and silica powder mixtures to produce silicon nitride joints at 1600-1700°C. The joining layer frequently had to be identified by measuring from the edge of the silicon nitride substrates since its microstructure was remarkably similar to the bulk; implying minimal (if any) reduction in strength of the joined assembly compared to the bulk silicon nitride should be observed.

Walls and Ueki [39,40] were able to join beta-sialon with various mixtures of silicon nitride, alumina, yttria, and silica powders at 1600°C (10-20 min, 2 MPa applied load). During the intermediate stages of heating (≈1350°C), the alumina, yttria, and silica form a liquid phase, while the silicon nitride remains stable. Upon further heating (1500-1550°C), the silicon nitride is dissolved and beta-sialon grains are precipitated. The resulting joining-layer microstructure is similar to the bulk; however the grain size is smaller due to the relatively lower processing temperature and shorter processing time compared to the sintering of beta-sialon (1750°C, 5 h). Joint strengths of ≈750 MPa could be obtained with this process, and post-bonding hot isostatic pressing improved the strength of the bulk substrate and joined assemblies to ≈1.0 GPa [40].

Iino and Taguchi [41] have used nickel/niobium/nickel and niobium/nickel/niobium layered assemblies to join silicon nitride at 950°C and 20 MPa. When joining was attempted with either nickel or niobium layers alone, the assembly did not bond, and sufficiently thin layers of niobium in the niobium/nickel/niobium assembly were required to achieve bonding. Liquid cannot form in the nickel-niobium system below 1175°C [23], and solid-state interdiffusion of niobium and nickel apparently makes the metal more reactive with the ceramic, thus requiring lower temperatures to form a bond in comparison to those required for diffusion bonding either niobium or nickel alone. The process may be thought of as a reaction-assisted diffusion bonding process and is essentially a solid-state version of the PTLP method developed shortly thereafter.

By taking advantage of a low-temperature eutectic (942°C) in the nickel-titanium system, Iino [26] used titanium/nickel/titanium layer assemblies to join silicon nitride parts at 1050°C. The thin liquid layer formed insures intimate contact between parts of the assembly, while the solubility of titanium in nickel is sufficient (≈10 at% at 800°C [23]) to allow isothermal solidification. Although intermetallic compounds form in the nickel-titanium system, these compounds melt below the melting point of nickel [23] and diffusion rates should still be sufficiently high in these compounds to insure complete interdiffusion. Iino [26] reported bend strengths of 234 MPa for multilayer interlayer assemblies (ceramic failure) compared to 56 MPa for joints formed using only a nickel layer (interfacial failure). Such multilayer interlayer assemblies could also be used to join silicon nitride to other materials such as Kovar or stainless steel, producing a strength of 313 MPa for the Kovar joint (ceramic failure). This process was termed partial transient liquid-phase (PTLP) bonding since the entire joining layer does not melt, and has also been applied to the joining of alumina with copper/platinum/copper [27], copper/nickel/copper [28], and copper/niobium/copper [17] interlayers by Glaeser and coworkers as well as in joining silicon nitride with copper-titanium/palladium/copper-titanium and titanium/copper/titanium interlayers by Paulasto *et al.* [29].

2.2 Theory of PTLP Bonding

As illustrated in the work by Iino [26], PTLP bonding of ceramics is based on the ability to form a low-temperature liquid phase that will isothermally solidify by interdiffusion, and ideally form a homogeneous joint that melts at temperatures exceeding the processing temperature. In principle, processing only requires that the joint be heated to just above the liquid-forming temperature; however, enough liquid must form such that gaps between the ceramic and remaining unmelted portion of the joining layer are filled by the liquid. In addition, as in brazing or TLP™ joining, the wetting behavior of the liquid layer must promote the filling of voids and flaws on both the ceramic and solid metal layer surfaces.

PTLP bonding systems may be assembled by inserting a thin metal layer (typically a few microns) between the surfaces to be joined. This layer is referred to as the cladding layer. A relatively thicker metal layer (tens or hundreds of microns, *e.g.*, rolled metal foils) can be placed adjacent to the cladding layer, and is referred to as the core layer. Figure 2.1 illustrates several joint assemblies which may be used to join similar or dissimilar materials. Core layers should generally be chosen to have properties desired in the final joint, *e.g.*, high melting point, thermal expansion match with the ceramic, and chemical stability. The core layer will nominally have sufficient solubility of the cladding material(s) so that the assembly produces a diffusion couple which upon equilibration is capable of forming a homogeneous metal joint. Diffusion of the thin cladding layers into the core will only slightly alter the core layer composition, thus producing a joint with properties similar to those of the unbonded core.

Formation of a liquid phase at a low temperature is achieved in the choice of the cladding layer. This may be done by simply using a low melting point material, or one which forms a low-temperature liquid phase with the core layer (*e.g.*, the titanium cladding/nickel core combination used by Iino [26]). Figures 2.2 and 2.3 illustrate the phase and composition evolution of the joining layer for both a simple lens and eutectic binary system used in PTLP bonding. For simplicity, dissolution of the ceramic into the joining layer, and any diffusion of the joining materials into the ceramic are currently ignored. For many systems at these relatively low temperatures, this is a reasonable assumption.

There are a few key similarities and differences in the evolution of the joining layers depicted in Figures 2.2 and 2.3. In the simple-lens case, the liquid forms initially at the ceramic/cladding interface, while for the eutectic-based joint, liquid is initially formed at the cladding/core interface and widens into the core layer and toward the ceramic. In both systems, the amount liquid will increase from that initially formed since dissolution of the solid metal is more rapid than diffusion of the cladding component into the core. However, greater amounts of liquid will generally form in eutectic-based joints since eutectic compositions are often nearly equally composed of each component, while for the low processing temperature used in the simple-lens joint an almost negligible increase in liquid thickness will occur. Generally, the amount of liquid formed depends on the liquidus composition dictated by the phase diagram; for example, higher processing temperatures for the simple-lens case would result in a thicker liquid layer during bonding. Eutectic compositions can be very close to that of a pure cladding end member (particularly in systems for which the melting points of the pure end members are very different), and result in minimal extent of liquid formation. Additionally, the eutectic joint will generally require less time to homogenize since the last liquid to solidify is closer in composition to the core layer than in the simple lens case. However, small deviations from the average composition can markedly reduce the maximum use temperature due to the relatively high slope of the solidus.

PTLP bonding of ceramics is not limited to the simple systems illustrated in Figures 2.2 and 2.3, but peritectics as well as melting point maximum and minimum systems serve as potential candidates. In principle, any system capable of forming a liquid at low temperature can be used for PTLP bonding; however, systems containing intermediate compounds (*e.g.*, aluminum-niobium) are not preferred. The formation of such compounds can act as diffusion barriers between the liquid and core layer; thus inhibiting the formation of a homogeneous bond. Intermetallic phases are often very brittle and may limit the mechanical properties of the joint. Attempts at joining alumina with tin/niobium/tin interlayers at very low temperatures have been unsuccessful for these reasons [42]. The current research will examine the importance in choosing a system in which there is extensive solubility of the cladding material(s) in the core layer. Additionally, the components chosen should not react excessively with the ceramic, *e.g.*, the reduction of alumina by titanium.

An additional requirement of exemplary PTLP systems is that the liquid layer sufficiently wet both the ceramic and core layer. The wettability of the liquid layer on the ceramic and metal will determine how effective it is in eliminating voids and flaws from the joined assembly. Figure 2.4 illustrates a PTLP joint in the early stages of processing and labels the surface free energies of interest. From this diagram, one would conclude that in order to prevent the liquid layer from dewetting the ceramic and core layer surfaces, the following inequality must be satisfied.

$$\gamma_{lm} + \gamma_{lc} < \gamma_{mv} + \gamma_{cv} \tag{2.1}$$

Note that this inequality ignores the increase/decrease in area of the liquid/vapor surface associated with dewetting/spreading of the liquid. This will result in a conservative condition for liquid spreading, and a more rigorous version of this condition is provided in Appendix II. Rearranging the terms of Equation 2.1 re-expresses the condition for liquid spreading as:

$$\gamma_{lm} - \gamma_{mv} < \gamma_{cv} - \gamma_{lc} \tag{2.2}$$

Applying the well-known Young equation to each side of Equation 2.2 yields:

$$-\gamma_{lv} \cos\theta_{lm} < \gamma_{lv} \cos\theta_{lc} \tag{2.3}$$

$$\cos\theta_{lm} + \cos\theta_{lc} > 0 \tag{2.4}$$

From Equation 2.4, it can be concluded through a simple geometric argument that an equivalent expression for the condition of liquid spreading is:

$$\theta_{lm} + \theta_{lc} < \pi \tag{2.5}$$

In general, it is not difficult to find systems which satisfy Equation 2.5; however, this alone does not guarantee a strong joint will result from processing. Wetting data for pure liquid metals (*e.g.*, copper, cobalt, gallium, gold, indium, iron, lead, manganese, mercury, nickel, palladium, and silver) on alumina reveal that θ_{lc} is typically in the range 100-150° [9,15,43-46]. Contact angles, θ_{lm}, for liquid metals on more refractory metals can be relatively low, often below 30° (*e.g.*, copper on tungsten [9], copper on nickel [47], and gold on nickel [15]). It is worth stating that many liquid metal-solid metals systems do not exhibit such low contact angles; however, the contact angle is generally less than 90°. In general, liquid metal-solid metal systems containing extensive mutual solubility or intermetallic compounds tend to exhibit better wetting properties [9]. Metal-metal systems tend to exhibit substantial reductions in contact angle with increased temperature as well [9,48,49]. As mentioned, systems in which there is sufficient solubility of the cladding metal in the core metal are often chosen for PTLP joining, thus the value of θ_{lm} is frequently not of concern.

Ideally, a PTLP system in which both contact angles (θ_{lc} and θ_{lm}) are less than 90° is preferred. Liquids having a contact angle below 90° (termed wetting liquids) will enable flaws on solid surfaces to be filled by liquid, whereas non-wetting liquids (contact angles >90°) will tend to bridge flaws thus creating regions of stress concentration. Figure 2.5 illustrates some of the types of flaws that are likely to develop in a bond in which the liquid wets the metal core layer, but does not wet the ceramic. Such flaws may result from a lack of liquid availability, resulting in an inability to completely fill regions where the core and ceramic are not in contact (f). Other flaws (a,b,c,g) result from the inability of the liquid to wet the ceramic, and the liquid front can be pinned at the edge of flaws in the ceramic surface (see Appendix II). Trapped pockets of gas which are unable to diffuse out of the assembly may result in any of the types of flaws shown (d,e, and f in particular). Due to their sharp curvatures or crack-like nature, flaws at the ceramic surface in Figure 2.5 are more stress concentrating than those in the metal layer(s). Should the liquid not wet the metal, similar crack-like flaws would develop in the metal layer, and although undesirable, they would not be as detrimental to the joint since such flaws would be more capable of blunting upon subjection to applied loads. However, the crack growth resistance (fracture energy) of the metal layer will also decrease as its thickness decreases to values smaller than the plastic zone size at the tip of a crack [50]. Many of the chemical aspects which influence wetting on oxides are discussed in the next section.

The other primary concern in PTLP joining is the mechanics of the metal/ceramic composite system. The development of residual stresses during cooling can result from the metal and ceramic having different thermal expansion coefficients (termed thermal mismatch or misfit). Additionally, metals and ceramics will generally have different elastic moduli (modulus misfit) causing a complex stress state to develop when a joined assembly is loaded [6,50]. Stresses resulting from thermal misfit and modulus misfit are concentrated in regions near the interface and are further concentrated near beam edges, a frequent initiation site for failure [6,51]. These stress distributions can potentially cause joined structures to fail in the ceramic at applied loads lower than required to fracture the bulk ceramic. The mechanical constraint on a thin metal joining layer reduces the extent of plastic deformation the metal/ceramic bimaterial structure can undergo [8,50]. Other factors such as surface roughness can shield cracks, thus contributing to a high fracture energy [7]. A liquid-phase joining technique such as PTLP bonding is beneficial in this regard as surfaces will not necessarily require extensive polishing, thus there is an effective increase in the length and area an interfacial crack must propagate.

Studies on metal/ceramic joints indicate that the fracture path depends on the particular metal/ceramic combination (misfit characteristics) as well as the failure initiation site, *i.e.*, within the metal layer, at the metal/ceramic interface, in the ceramic close the metal/ceramic interface, or in the ceramic sufficiently far from the metal/ceramic interface [50,52]. Crack propagation is governed by two competing factors; namely, the path of least microstructural resistance and the path of largest mechanical driving force. Generally, the extent of modulus misfit in a metal/ceramic system can be defined in terms of the two Dundurs parameters (non-dimensional parameters dependent on the elastic moduli and Poisson ratios of the two materials) [50,53]. The Dundurs parameters can be used to determine the expected crack propagation path; however, this analysis ignores thermally induced stresses (the T-stress), and actual crack paths may deviate from those predicted [50]. Additionally, crack propagation depends upon whether a crack is quasistatic, or results from dynamic loading [52]. Cyclic versus monotonic loading can also affect crack propagation [50]. Consequently, many factors play a role in determining failure modes in ceramic/metal joints; some results specifically relevant to the current study will be discussed in later sections and chapters.

The primary advantages to PTLP joining are that joints may be potentially used at temperatures exceeding their processing temperature, and in principle, no applied load is required during bonding. Nakashima [54] has fabricated copper/nickel-chromium/copper joints for alumina using only a small weight on top of the joined assembly (≈20 kPa) which exhibit the same strength characteristics as those formed with the smallest applied load (≈5 MPa) possible with the equipment used by Locatelli [15]. Upon consideration of all the issues affecting the reliability of PTLP joints, a limited number of systems are left to serve as likely formers of good PTLP bonds. Ternary systems (and potentially higher order systems) may serve as good PTLP candidates as well. Ternary eutectics may enable further reduction in joining temperature or incorporate the use of refractory components that do not form binary eutectics at sufficiently low temperature (*e.g.*, the work of Gopal *et al.* [37,38]). Ternary systems may also be useful in joining two different ceramics (Figure 2.1d) where different cladding layers may be beneficial from a wetting perspective. Such systems are worth investigating since they may enable discovery of systems suitable for joining ceramics that could not otherwise be joined *via* the binary approach. Additional components may also improve the wetting characteristics of the liquid layer, reduce thermal misfits (*e.g.*, refractory metal-refractory metal alloy cores), or improve the chemical stability of joints.

2.3 Wetting and Work of Adhesion between Oxide Ceramics and Molten Metals

In general, the wettability of a metal on an oxide depends on the particular oxide/metal combination. Li [44] reports that the wettability of a metal is strongly determined by its ability to bond with an oxide. Due to the vastly different type of bonding in oxides (ionic/covalent) compared to metals, the exact nature of interfacial bonding is difficult to predict. However, Li [44] proposes that free electrons in metals can fill valence band holes in the nearby ceramic. Thus, smaller band gap oxides and metals with higher electron densities represent better wetting pairs. Since the thermodynamic stability of an oxide largely determines its band gap, more stable oxides (alumina in particular) are more difficult to wet [44]. The fact that liquid metal/oxide contact angles tend to decrease with increasing temperature [43] is also related to these correlations [44]. Metals also tend to wet their own oxides particularly well [9], and more reactive (higher oxygen affinity) metals tend to exhibit lower contact angles on alumina [45]. Alumina is wet by reactive metals such as chromium, titanium, and zirconium [9,44,45]; however, these are not good candidates for liquid formers in PTLP bonding since their melting points range from 1670°C for titanium to 1857°C for chromium. Fortunately, it has been shown that small additions of such reactive metals to non-wetting metals can decrease their contact angle to less than 90° [45.47,55-58].

Reductions in the contact angle of metals on oxides are typically due to formation of a liquid/solid interfacial reaction layer [56,58,59], segregation of an active species (*e.g.*, metal oxide clusters) to the liquid/solid interface [55,57], and variations in the ambient atmosphere (p_{O_2}) [59-63]. Naidich and Zhuravlev [58] studied the effects of titanium additions on the wettability of copper, gold, molybdenum-nickel, nickel, and tin on various oxides, *i.e.*, alumina, magnesia (MgO), and silica. With the exception of nickel on alumina, contact angles were reduced to less than 90° with only ≈2 at% titanium additions. Depending on the system, either TiO or Ti_2O_3 reaction layers were observed between the metal and oxide substrates, and those forming a TiO reaction layer exhibited better wetting. This is likely due to the more metallic nature of bonding in TiO compared with Ti_2O_3, thus the liquid metals form a more favorable interface with titanium in lower oxidation states. This was verified by comparing the contact angle of pure copper on $TiO_{0.86}$ (72°), $TiO_{1.14}$ (82°), and Ti_2O_3 (113°).

Experiments by Kritsalis *et al.* [56] have focused on the wettability of alumina by copper with titanium additions. The results were indeed consistent with Naidich and Zhuravlev [58] in that a TiO reaction layer was observed between the copper and alumina; however, an additional reaction layer (Cu_2Ti_2O) was also observed. The additional phase is believed to have formed during cooling since its thickness was roughly independent of hold time at the wetting temperature. Cu_2Ti_2O thus has no influence on the wetting characteristics of the alloys, but may have pronounced effects on the mechanical properties of the interface. Naidich and Zhuravlev [58] analyzed reaction layer materials by dipping a rod of the substrate material into the liquid and allowing the reaction layers to form on the rod; presumably no liquid was transferred upon removal of the rod, and the possibility of additional phase formation during cooling was eliminated.

Chatain and coworkers [59] systematically observed the contact angle of copper on alumina at 1092°C at various p_{O_2}. The contact angle (130±2°) remained constant for p_{O_2} in the range $\approx 10^{-20}$-10^{-12} atm, and remained constant (119±3°) for p_{O_2} in the range $\approx 10^{-12}$-10^{-8} atm, indicating a critical p_{O_2} ($\approx 10^{-12}$ atm) at which the contact angle is reduced. This critical p_{O_2} is associated with the formation of a "2-D" copper aluminate ($AlCuO_2$) phase at the interface, which serves to replace the relatively high-energy copper/alumina interface with lower-energy copper/copper aluminate and alumina/copper aluminate interfaces. The copper aluminate layer thickness increases as the p_{O_2} at which bulk copper aluminate becomes stable is approached [59]. As the p_{O_2} is increased beyond values required to form bulk copper aluminate ($\approx 10^{-6}$ atm), the contact angle begins to decrease monotonically.

The contact angle reduction "step" ($\approx 10^{-12}$ atm) observed by Chatain and coworkers [59] is contrary to many other copper-on-alumina wetting studies which report a gradual decrease in contact angle with p_{O_2} [62,63]. Chatain and coworkers argue that data is relatively scattered due to difficulties in controlling p_{O_2}, and fitting to a monotonic decrease has been influenced by adsorption models predicting plateau and decent regions in the contact angle [60,63]. Furthermore, some contact angles in previous wetting studies have been measured at partial oxygen pressures in the range where bulk copper aluminate is stable. Regardless of these details, wetting data for copper on alumina collectively suggests that the contact angle is at best slightly below 90° for relatively high (10^{-6} atm)

p_{O_2} at temperatures up to 1200°C [59,62,63]. Oxygen concentrations well beyond the solubility limit in solid copper (0.03 at%) [23] are required for excellent wetting of copper on alumina [9,64].

Wetting studies generally focus on the chemistry of the ceramic/liquid interface in determining mechanisms associated with contact angle reductions; however, the contact angle can also be reduced by decreasing the liquid/vapor surface energy or by increasing the ceramic/vapor surface energy (*e.g.*, cleaning the surface). Reductions in contact angle are often associated with an increase in the work of adhesion, defined as the reversible work (per unit area) required to form a ceramic/vapor and liquid/vapor interface from a ceramic/liquid interface.

$$W = \gamma_{cv} + \gamma_{lv} - \gamma_{lc} \tag{2.6}$$

The work of adhesion can be related to the contact angle *via* application of the Young equation.

$$W = \gamma_{lv}\left(1 + \cos\theta_{lc}\right) \tag{2.7}$$

If reductions in γ_{lv} are solely responsible for contact angle reductions, W would decrease (Equation 2.6). Chatain and coworkers [59] and O'Brien and Chaklader [62] have reported such variations at higher oxygen activities; however, wetting data often exhibit an almost mirror image correlation between work of adhesion and contact angle [9], thus indicating that variations in γ_{lc} are primarily responsible for contact angle reductions. Naidich and Zhuravlev [58] observed that titanium additions as high as 10 at% to several melts did not affect their surface tensions with the exception of "unreduced" nickel. (Unreduced nickel was pre-annealed in an alumina crucible, while other samples were reduced in a graphite crucible.) Chromium additions to liquid copper have little or no effect on its surface tension [47,55], and if anything are responsible for a slight increase [55]. Generally, it appears as though decreases in γ_{lv} are generally associated with oxygen, and these reductions are typically less than that in γ_{lc}, so that W may still increase when γ_{lv} decreases.

Kritsalis and coworkers have examined the effects of chromium on the wettability of copper [55], nickel-palladium [57], and nickel-iron [57] alloys on alumina. By using a relatively oxygen-free (8 ppm) copper source, and chromium sources containing substantial oxygen (700 ppm and 3700 ppm) the authors [55] were able to investigate the contact angle over various chromium and oxygen concentration ranges. Additions of small amounts (<2 at%) of the more heavily oxygenated chromium resulted in larger reductions in the contact angle than additions of the same amount of 700 ppm oxygen chromium. The authors [55] were also able to determine that their contact angle data fit well to a curve that depended on oxygen concentration only. Thus far, it would appear that the decrease in contact angle was solely due to oxygen and that the chromium had little influence; however, ≈10 times as much adsorbate was observed at the copper/alumina interface in comparison to that present for oxygen in copper not containing chromium. Additionally, the authors [55] report an increase in the work of adhesion four times that observed for oxygen in copper without chromium. Finally, for sufficiently large additions (≈4 at%) of low and high oxygen chromium, the same contact angle is observed (110°). These observations imply that there is some form of coupling or interaction between chromium and oxygen in liquid copper. Thermodynamic considerations single out the metal oxide cluster (CrO) as the active species responsible for γ_{lc} reduction [55].

The effect chromium additions on the wettability of nickel alloys on alumina [57] is substantially different than in the copper case. The contact angle of nickel-palladium alloys was not significantly altered by additions of chromium regardless of the oxygen concentration (chromium containing 700 ppm or 3700 ppm oxygen). Any such reductions (<5°) are obscured by the experimental uncertainty. Chromium additions to nickel and nickel-iron alloys decrease the contact angle (112±3° to 95±4° for nickel, and 112±2° to 90±2° for nickel-19 at% iron), but the effects were again independent of the chromium source. These results are indeed consistent with the fact that the wettability of pure nickel on alumina exhibits only a subtle dependence with oxygen content. The degree of ionicity in metal oxide clusters determines how influential they are in reducing contact angles, thus only small amounts of oxygen (tens of ppm) are required to improve the wettability of chromium on alumina, while hundreds of ppm are required for similar effects with nickel and iron. Kritsalis *et al.* [57] have proposed generally, that the wettability of oxides by metals containing dissolved oxygen can be improved by additions of a metal which interacts strongly with oxygen. Although chromium additions to liquid metals reduce the contact angle less than titanium additions, these studies [55,57] represent an important wetting phenomena that may be relevant in other systems.

In wetting studies, changes in the alumina/vapor surface energy are rarely addressed or the energy is assumed to be independent of ambient environment (*e.g.*, p_{O_2}) [63]. Due to kinetic factors, metals on ceramics and any additives (*e.g.*, titanium) may not achieve thermodynamic equilibrium with the ceramic surface during relatively short (≈30 min) wetting experiments at relatively low temperatures. (However, the surface only need be equilibrated near the three-phase boundary.) It is worth noting that at thermodynamic equilibrium, the wetting characteristics could potentially be different. Titanium and other additions (calcium and magnesium) to alumina are known change its surface energies, and such changes depend on the valence state of impurities like titanium, *i.e.*, p_{O_2} affects the valence [65]. Therefore, alumina with different impurities exposed to different atmospheres may be wet differently. Additionally, surface energies may change due to surface reconstructions at elevated temperatures; Brennan and Pask [66] have focused on these as well as other ceramic surface effects on the wettability of alumina by aluminum. Some attention has also been given to the effects of surface energy anisotropy in the ceramic on contact angle; and even though the energy of different low-index surfaces varies as much as

≈25% [65], substantial effects on contact angle are not observed (variation of ≈2°, usually within the extent of experimental uncertainty) [55,56]. In spite of these issues, the net effects are generally small, and results from study to study appear reasonably consistent, even though different types of aluminum oxide substrates have been used.

The work of adhesion contributes (non-linearly) to the fracture energy of metal/ceramic interfaces, thus better wetting liquids may not only produce stronger joints due to reduction of stress concentrating flaws, but by producing an interface that is intrinsically stronger as well. However, it is worth noting that after a PTLP process is complete, the metal/ceramic interface formed is often quite different in composition from the liquid used in bonding. Thus, the work of adhesion of the liquid has little relevance with regard to intrinsic interfacial strength, but is very important in determining flaw geometry at the metal/ceramic interface. Locatelli and coworkers demonstrated that the strength of copper-nickel based joints could be significantly increased by using nickel core layers containing chromium [15,46] or titanium [67]. The wetting phenomena presented here represent only a small fraction of the vast amount of work done in the area; however, they address some of the potentially relevant issues affecting wetting in the copper-niobium-alumina system, since wetting studies in this system have been quite limited.

2.4 Copper-Niobium as a PTLP System for Joining Alumina

The copper-niobium binary system is in some respects a rather unconventional choice for a PTLP joining system. Figure 2.6 illustrates the copper-niobium phase diagram; copper ($T_f = 1085°\mathrm{C}$) is the obvious choice for the cladding layer, and niobium ($T_f = 2469°\mathrm{C}$) the core. The solubility of copper in niobium is quite limited (≈1.2 at% maximum at the eutectic temperature) [23], and substantial amounts of residual copper in the joint can potentially limit the high-temperature application of such joints. The solubility of niobium in liquid copper is only a few atomic percent up to temperatures of ≈1500°C, thus the amount of liquid formed during PTLP bonding is essentially determined by the amount of cladding material present. The copper-niobium phase diagram (Figure 2.6) implies that either very thin copper layers or relatively thick niobium layers would be necessary to produce a single-phase niobium-rich joint. Thin copper layers may result in weak joints as there may not be enough liquid phase present to eliminate or fill defects and flaws in the joining surfaces. Thicker joining layers enable more extensive plastic deformation in the joined assembly; however, niobium/sapphire joints with thicker metal layers produced by diffusion bonding have failed at lower stresses in compression tests [8]. Additionally, impractical processing times may be required for complete dissolution and diffusion of the copper to occur. The diffusivity of copper in niobium has not been measured; however, the self diffusion coefficient of niobium [68] allows an estimate of a diffusion distance, $\sqrt{Dt}$, of ≈1 μm after 6 h at 1400°C for substitutional metals. Admittingly, the diffusion distance of copper in niobium may be substantially greater; copper is a smaller atom (atomic radius ≈1.28 Å) than niobium (≈1.43 Å), and may have a lower activation energy of migration in niobium. Nevertheless, this estimation implies that even if complete grain boundary diffusion of copper in niobium occurs, the bulk core of large niobium grains will not dissolve any copper.

An older version of the copper-niobium phase diagram exhibits greater solubility of copper in niobium and niobium in liquid copper (Figure 2.7). This phase diagram appears to be a pseudo-binary (subset of a ternary or higher order system) since the “invariant” temperature (1550°C) violates thermodynamic construction rules for binary systems. The phase diagram was published in the 1960’s [69] and metals used in phase diagram determination during this era typically contained substantial amounts of impurities, in particular dissolved oxygen. Massalski [23] reports that the solubility of copper in niobium may be higher for niobium containing oxygen or other impurities. Thus using niobium core layers containing dissolved oxygen for copper/niobium/copper PTLP joints may enable formation of a homogeneous single-phase joint and enable the formation of more liquid. However, diffusion kinetics of copper in niobium may still be too slow for reasonably quick homogenization. In light of the aforementioned concerns, it appears that the best approach to producing strong copper-niobium joints for alumina *via* PTLP processing may be to select processing conditions that produce an optimum copper-rich/niobium-rich† two-phase microstructure as the joining layer.

Shalz *et al.* [17] have in fact shown that reasonably strong (average fracture strength of 181 MPa) two-phase copper/niobium joints for alumina can be made *via* PTLP processing at 1150°C. All failures occurred along the metal/ceramic interface; however, cracks often deviated into the alumina at the interfacial copper phase, termed ceramic pullout. These results suggests that excess copper at the interface is actually quite favorable in terms of interface strength and/or that the ceramic is locally stressed due to the thermal misfit between copper and alumina. Due to the similarity between this work [17] and the current study, the work of Shalz *et al.* will be discussed further in Chapter 4.

In addition to the high melting point of niobium and relatively low melting point of copper, perhaps the most attractive feature of a copper-niobium based joint for alumina is the close thermal expansion match between alumina and niobium. Figure 2.8 illustrates the temperature dependence of the thermal expansion coefficients of alumina, niobium, and a few other metals for comparison. Clearly, niobium is the closest to alumina of the refractory metals, particularly in the range 200-1200°C. Thus essentially no stresses will develop during cooling for the great majority of temperature ranges cycled during processing and service.

Since thermal stresses in niobium/alumina joints are minimized, the stress state is predominantly due to modulus misfit effects; in fact, the elastic modulus of niobium (105 GPa) is about one-fourth that of alumina (400 GPa) [52]. This system thus serves as an

---

† From now on, the copper-rich and niobium-rich phases will simply be referred to as copper and niobium respectively. The limited mutual solubility between the two elements implies that their thermodynamic activities are close to unity in both phases.

excellent system to isolate and investigate the effects of modulus misfit and its effects on crack propagation, which will be discussed in the next section. The effects of mechanical misfits on the mechanical properties of joints will determine whether it is feasible to join ceramics with fundamentally dissimilar materials, *i.e.*, whether or not it is possible to construct a joint as strong and tough as the material being joined.

Better joints are expected if joints are processed under conditions that exhibit good wettability of copper on niobium and copper on alumina. The wetting characteristics of the copper-niobium-alumina system are sensitive to the experimental conditions (temperature, time, and ambient environment), and conditions associated with good wetting of copper on alumina do not necessarily imply good wetting behavior of copper on niobium. The remainder of this section focuses on these issues.

In addition to the effects of oxygen on the wettability of copper on alumina discussed in the previous section, 2 wt% niobium additions to copper also reduce its contact angle on alumina [46,61]. Initially, copper containing niobium exhibits a contact angle (≈105°) less than that of pure copper on alumina (≈125°) at 1150°C [46]. The contact angle is reduced further to less than 60° after 3 h and below 20° after 5 h at 1150°C in vacuum [46,61] ($p_{O_2} \approx 10^{-22}$ atm [3]). Generally speaking, wetting experiments achieve equilibrium after much shorter times (2-30 min) [48,55-57,63] than required for Nakashima and coworkers [46]; the slow decrease in the contact angle may be due to slow dissolution of the niobium in copper† [61]. Tomsia *et al.* [61] report high contact angles (>100°) for copper-1.4 at% niobium on alumina in argon ($p_{O_2} \approx 10^{-7}$ atm [70]) at 1150°C. It is possible that the high p_{O_2} in the argon enabled precipitation or vaporization of niobium oxide(s), thus making the composition of the wetting liquid close to pure copper (see Figure 2.9). The observed contact angle (>100°) is consistent with other results for copper on alumina at this p_{O_2}.

---

† Assuming a diffusivity of $10^{-9}\ \mathrm{m^2/s}$ for niobium in liquid copper, predicts a diffusion distance of ≈3 mm after 3 h.

The mechanism by which niobium reduces the contact angle of copper on alumina is not known, but a reaction layer was ruled out for observations in vacuum [46,61]. Niobium oxide clusters are not expected to be the active species since essentially no dissolved oxygen will exist in pure copper for the estimated oxygen activity (see Figure 2.9). However, niobium in copper may still increase the equilibrium oxygen concentration in the liquid and such clusters may form. The reduction in contact angle may simply be due to the reactive nature of niobium, *i.e.*, a tendency for niobium to segregate to the interface and bond with an oxide. Although is is difficult to predict whether or not oxygen is operative in the contact angle reduction of copper-niobium on alumina, Figure 2.9 implies that oxygen activities should be well below those necessary to reduce the contact angle of "pure" copper on alumina are required to insure oxidation of niobium is unfavorable.

The contact angle of copper with dissolved niobium is likely to be reduced further at higher temperatures, following the trends of pure copper on alumina [71,72]. Even though niobium segregation to the copper/alumina interface will be reduced at higher temperatures, the solubility of niobium in copper increases from ≈1 at% to ≈2 at% between 1150°C and 1400°C [23], thus the contact angle may also be reduced even further at higher temperatures due to a factor of ≈2 increase in the amount of niobium in solution.

Unlike many liquid metal-solid metal systems, the wetting angle of copper on niobium is relatively high (≈67° at 1090°C), thus making the liquid spreading condition (Equation 2.4) more difficult to meet. Furthermore, niobium containing 6.5 at% oxygen is nearly not wet by copper at 1090°C, having a contact angle of 85°. Although liquid copper completely wets niobium under reducing environments (hydrogen) at higher temperatures (1300°C), the contact angle remains sufficiently high (59°) for oxygen-doped (6.5 at%) niobium [48]. De Lima *et al.* [48] also studied the contact angle of copper on niobium of different grades (oxygen-free or 1.5 at% oxygen), different surfaces (rough and polished polycrystalline, and (100) and (110) single crystalline), and under different ambient environments (vacuum, hydrogen, and argon). Their results are summarized in Table 2.1. Hodkin *et al.* [49] report a contact angle of copper on niobium <2° at 1500°C. Thus higher processing temperatures and oxygen-free niobium will provide a favorable wetting condition for the cladding (copper) on the core (niobium) in copper-niobium PTLP bonding.

De Lima *et al.* [48] indicate that niobium containing oxygen hinders the wetting of copper on niobium; however, Saiz [70] has shown that electronic copper (contains oxygen) has a contact angle below 20° on niobium at 1150°C, while 99.999% copper exhibits a much higher contact angle (≈80°) under similar conditions. Saiz [70] has also observed that annealing electronic copper in a reducing environment (hydrogen) prior to the sessile drop experiment causes the contact angle to rise to near 80°. Should the niobium used by Saiz contain oxygen, the observed contact angles for reduced and 99.999% copper are more or less consistent with the observations made by De Lima *et al.* [48] for oxygen doped niobium. (De Lima *et al.* [48] also used 99.999% copper.) However, since De Lima *et al.* report an increased contact angle for niobium containing oxygen (1.5 at% and 6.5 at%), while Saiz reports a decreased contact angle for copper containing oxygen, these results suggests either one or both systems have not reached global chemical equilibrium with respect to oxygen. A plausible explanation for the differences may be related to the effects of oxygen on the surface energies of copper and niobium. It is well known that as the oxygen content of copper is increased, its surface energy decreases [59,62,63], which would serve to reduce its contact angle on a solid. If dissolved oxygen (1.5 at%) in niobium similarly reduces its surface energy, a higher contact angle would be favored. Additionally, 6.5 at% oxygen is beyond the solubility limit for niobium in the temperature range studied by De Lima *et al.*; in accordance with this, a niobium oxide (NbO) layer was observed on the niobium surface [48]. The higher contact angle observed is associated with the general trend for high contact angles of liquid metals on oxides.

Higher temperatures will assist in improving the wettability of both niobium and alumina by copper; however, the net effects of oxygen are uncertain, or may even be competing. Figure 2.9 illustrates the p_{O_2} in equilibrium with copper and niobium as a function of dissolved oxygen content at 1100°C and 1200°C. The figure implies that for any reasonable oxygen concentration in copper, the oxygen can reduce its activity (chemical potential) by diffusing into niobium[†]. Diffusion of oxygen in niobium is fast (a diffusion distance of ≈60 μm, roughly half the niobium joint thickness in the current study, is expected after 36 s at 1150°C, see Figure 2.10), and bulk niobium can effectively getter oxygen from thin (≈3 μm) copper layers. The ambient environment may also serve as an oxygen source to copper; however, substantially high p_{O_2} is required to establish a significant oxygen concentration in copper. Furthermore, such oxygen activities would promote oxidation of the niobium. In other words, fluxes of oxygen through copper to or from niobium are likely to be very low in typical vacuum-processing conditions. Figure 2.11 illustrates the anticipated oxygen distribution during copper-niobium PTLP bonding for relatively high and low p_{O_2}. The figure assumes that residual oxygen in the copper is immediately gettered by niobium and ignores any effects from alumina dissolution or mutual solubility between copper and niobium; thus the resulting profile is dictated by the ambient p_{O_2}. It will certainly be difficult to maintain a high oxygen activity in copper at the joint interior during processing.

These predictions along with the fact that dissolution of niobium in the thin copper layers (≈3 μm) should occur well within one second of processing at 1150°C, imply that little change in wetting conditions will occur with processing time. However, spatial variance in the wetting conditions may exist since the edges of the joining assembly will equilibrate more rapidly with the ambient p_{O_2} (Figure 2.11). It would generally appear

---

[†] Assuming niobium is saturated with oxygen, and 10^{-5} ppm oxygen in copper, the driving force ($\mu_{\text{O in Nb}} - \mu_{\text{O in Cu}} = RT \ln \frac{a_{\text{O in Nb}}}{a_{\text{O in Cu}}}$) is still large (≈-200 kJ/mol at 1150°C) for oxygen to diffuse into niobium.

that processing joints in a low p_{O_2} environment would be beneficial in order to minimize the niobium oxygen content and optimize liquid wettability on the core. However, due to the uncertainties in the effects of oxygen on the wetting of alumina, oxygen activities equivalent to a $p_{O_2} \approx 10^{-22}$ atm at 1150°C may be necessary. This work focuses on the effects of temperature and ambient p_{O_2} on joint strength, and acknowledges the effects of various other parameters (applied load). The remainder of this chapter focuses on studies done on niobium/alumina and copper/alumina joints and interfaces individually, as few studies have been done on the copper-niobium two-phase matrix/alumina interface.

2.5 Mechanical Properties of Diffusion Bonded Niobium/Alumina Joints

Previous studies on alumina joined to niobium relied on diffusion bonding as the joining technique. Generally, this required relatively high temperatures (920-1950°C) and pressures (2-16 MPa) [8,14,19,20,73-85] in comparison to those used in the current study. Additionally extensive surface preparation and cleaning techniques were often required, and some joints were fabricated in ultra high vacuum (UHV) conditions [8,75,79,81,86,86]. However, the primary purpose of these studies was not necessarily to develop a mass production joining method, but rather to study the intrinsic properties of niobium/aluminum oxide interfaces. Figure 2.12 illustrates the bonding conditions for those studies dedicated to mechanical measurements of the joints. In general, it can be seen that higher pressures and UHV conditions were used for joints formed at lower temperatures.

The first studies investigating alumina joined by niobium were performed by Elssner and coworkers [76]. Joints were formed between 1400°C and 1600°C in high vacuum, using various grades of alumina. After processing, 0.1 mm notches were cut into beams at the niobium/alumina interface in order to evaluate the fracture resistance of the joints. In general, three types of fracture paths were observed: purely ceramic failure, fracture entirely within the niobium layer, and fracture along the metal/ceramic interface.

The fracture path and resistance depended on the microstructure and composition of the alumina. Joints fabricated with alumina containing excess silica failed within the niobium layer as a result of dissolution of silicon and oxygen in niobium which harden the metal. The formation of niobium silicide (Nb_4Si) is even suggested near the niobium/alumina interface. Fracture paths in the ceramic occurred for relatively porous aluminas (≈35%), and the measured fracture resistance was greater than for such unbonded aluminas, likely due to additional sintering which occurred during bonding. Finally, interfacial failures were observed for aluminas which were compactly sintered and have poor flow properties [76].

Evans *et al.* [52] studied crack growth behavior in diffusion-bonded niobium/alumina joints by initiating small cracks with indentations at various locations within the alumina. The joints were loaded in tension to 80 MPa in order to observe which cracks preferentially grew. Cracks far from the beam edge and interface exhibited very little growth in comparison to those near the edge or near the interface. Cracks initiated near the interface, but inclined to it, underwent redirection and became more parallel to the interface. Additionally, cracks at the interface or cracks which extended to the interface stopped extending, and crack blunting is observed. After preloading specimens at 80 MPa and observing crack growth behavior, the samples were reloaded to failure. Cracks at the interface were never the cause of failure, and samples which failed due to cracks near the interface did so at lower applied loads, thus in accordance with the anticipated stress concentrations. The observed crack propagation agreed with predictions from the Dundurs parameters for niobium/alumina joints [50] since cracks were drawn toward and along interface, and cracks near edges grew the most in accordance with expected stress state from modulus misfit considerations [6]. The results also imply that reasonably tough niobium/alumina interfaces can be fabricated. However, the fracture resistance of the interface may be substantially lower under dynamic loading conditions since dislocation mobility may not be sufficient to enable plasticity at interfacial crack tips.

Morozumi *et al.* [77] performed tensile tests on niobium/sapphire/niobium joint structures. The joints were fabricated between 1500°C and 1800°C with applied loads of 3-15.2 MPa. Both basal plane (0001) and $(10\bar{1}0)$ sapphire were diffusion bonded between two threaded niobium polycrystals. The room-temperature strength of the joints was approximately 120 MPa; presumably, all failures occurred at a niobium/sapphire interface. It was estimated that strengths near 260 MPa could be obtained since only slightly less than half the area of the niobium/sapphire interface was actually bonded. However, this is likely an underestimate since it does not account for the fact that higher percentages of bonded areas will generally result in smaller interfacial flaws, thus reducing stress concentrations at the interface. Bend strengths measured by Elssner and Krohn [87] as reported by Klomp [88] were 259 MPa, 198 MPa, and 365 MPa for niobium/polycrystalline alumina joints processed at 1300°C, 1400°C, and 1600°C respectively.

Morozumi *et al.* [77] also measured the temperature dependence of joint strength. Strengths near 100 MPa were maintained up to temperatures of ≈900°C, and fell to ≈35 MPa at 1000°C and ≈15 MPa at 1600°C for joints processed at 1600°C for 1 h at 8.8 MPa. The authors also noted that bond strength increased with applied pressure during processing, and pressures above 8 MPa were required to achieve fracture strengths over 100 MPa. Additionally, bonding times as short as 15 min could attain reasonable strength (≈80 MPa), and extended bonding time did not necessarily improve bond strength. These results seem contrary to the studies of Reimanis [14] who observed the evolution of pores at diffusion-bonded niobium/sapphire interfaces and concluded that applied pressure had little effect on their closure. However, Reimanis [14] applied a relatively small load (2 MPa) during the initial stages (first 12 h) of bonding and used a lower temperature

(1447°C). Deformation mechanisms associated with diffusion bonding may not have been substantially activated in Reimanis' study.

Several studies have been devoted to determining the fracture energy of specific types of niobium/aluminum oxide interfaces [8,75,79,81,82,85,86]. Many of these works focused on single-crystal niobium/sapphire joints of various relative orientations [8,79,81,82,85,86], while others joined polycrystalline niobium to either sapphire [82] or polycrystalline alumina [75,81,86]. Gibbesch and coworkers [75,81,86] reported higher fracture energies (62.4-80.6 J/m^2) when joining surfaces were bombarded with argon ions and bonded in UHV at 1400°C, compared to high vacuum bonding at 1600-1700°C (43.6-55.0 J/m^2) [75]. However, joints produced with these procedures at 920°C had fracture energies below 20 J/m^2, while bonding temperatures between 1000°C and 1200°C yielded fracture energies comparable to the joints processed in high vacuum [81,86]. Bonding temperature thus still plays an important role in determining bond quality, as many of the diffusion bonding mechanisms discussed in the next section require higher temperatures to occur to a reasonable extent in a reasonable time frame.

For sapphire joined to single-crystal niobium, the results depended on the orientation of the sapphire, as well as the orientation of the niobium relative to the sapphire. One would expect such a result, as differently oriented niobium/sapphire interfaces will have different interfacial energies, implying different values of the work of adhesion and fracture energy. As the niobium orientation is changed, resolved shear stresses will activate different slip systems (bcc), thus orientations with many easily activated slip systems are likely to exhibit increased fracture energies. Additionally, the anisotropy of mechanical properties (*e.g.*, elastic moduli which in turn affect Dundurs parameters) will affect the way stresses are distributed due to modulus misfit effects. For the orientation relationships studied [8,79,81,82,85,86], reported fracture energies vary from ≈60 J/m^2 to ≈2400 J/m^2. The values are summarized in Table 2.2 along with a letter (A-J) to be used as an abbreviation to refer to specific orientation relationships.

From study to study, the results are reasonably consistent except for those at orientation relationships B and C. For orientation relationship C, it is possible that the greater processing temperature and time are responsible for the observed increase in fracture energy; however, higher temperature, applied load, and longer processing time clearly did not have this effect for orientation B. Korn *et al.* [79] report that the crack deviated into the sapphire during fracture, thus the measured fracture energy represents a lower bound for that of the interface. These studies [79,81,85] do not report along which crystallographic direction notches were made, and cracks may have been propagated along orthogonal directions from test to test, thus a different sets of slip systems may have been activated between the studies. Elssner *et al.* [85] acknowledge the importance of crack propagation direction in measuring fracture energy. Anisotropy in the elastic moduli can also introduce different stress states depending on the pre-notch orientation. Additionally, there is thermal expansion anisotropy in the $(11\bar{2}0)$ plane of sapphire (see Figure 2.8), which may also contribute to the stress state. Many of the preferred orientation relationships studied here depend on the degree of lattice matching, chemical bonding, and the resulting interfacial structure between niobium and sapphire; these issues will be explored in the next section.

Low-index orientation relationships will generally represent the lowest interfacial energies, and bonding with a polycrystal (a randomly oriented set of single crystals) would induce the formation of higher energy interfaces for several of the niobium grains. From a work of adhesion point of view, regions of high interfacial energy provide a path of least resistance for a propagating crack or enable preferential nucleation of cracks, thus increasing crack size and further concentrating stresses on other regions of relatively low interfacial energy. This has been verified by joining polycrystalline niobium to (0001) sapphire which resulted in a relatively low fracture energy (26 J/m^2), while similarly joined $(1\bar{1}00)$ sapphire resulted in a fracture energy of 55 J/m^2 [82]. It is interesting that the basal plane sapphire joints were weaker even though joining basal plane sapphire to single crystal niobium (joined in orientation relationship A) consistently revealed the highest fracture energy studied. No analogous fracture strength dependencies were noted by Morozumi *et al.* [77] who used these same two sapphire orientations. The fracture energies for $(1\bar{1}00)$ (orientation relationships D,F,G, and I) and other basal plane sapphire (C,H, and J) joined to single crystal niobium are comparable. Using (110) textured Nb could potentially yield a different result. In light of this, it is difficult to use single crystal studies to predict properties of polycrystalline assemblies. The single crystal niobium/sapphire studies do provide fundamental information about these interfaces, and only small changes in the interfacial energy (work of adhesion) are required to significantly alter "strength" [85,88,89].

Additionally, the fracture energy of the polycrystalline niobium/sapphire joints depended on the niobium grain size as well as the amount of grain growth which occurred during bonding. The fracture energy of these samples decreased with increasing niobium grain size, but increased with increasing change in grain size during the bonding process [82]. This peculiar result may be explained in several ways. First, samples with smaller initial grain size will undergo the greatest increase in grain size due to grain growth during processing, while samples with relatively large initial grain sizes will experience very little grain growth. Furthermore, although samples with relatively small initial grain sizes will increase their grain size the most, the final grain size will still be less than in samples with a larger initial grain size. Although this explains the relationship between these two trends, it does not explain the dependency of fracture energy on grain size. Smaller grain samples may allow grains forming a low energy interface with the sapphire to preferentially grow, while the large grains in other samples will not be able to adjust their orientation to form a more favorable interface [82].

Finally, Korn and coworkers [79,85] investigated the effects of interfacial impurities (titanium, silver, and sulfur) on the fracture energy of niobium/sapphire interfaces. Titanium and silver were electron beam evaporated onto one of the bonding surfaces.

Sulfur impurities were obtained on the niobium surface by annealing the crystals prior to diffusion bonding; sulfur impurities segregated to the crystal surface during these anneals. The fracture energy of the samples was measured and compared to values for surfaces not containing the impurities. Titanium additions were responsible for an increase in the fracture energy from 160 J/m^2 to 740 J/m^2 for orientation relationship E, while silver impurities decreased the fracture energy from 2107 J/m^2 to <100 J/m^2 for orientation relationship A. Sulfur appeared to have a rather mild effect on the fracture energy (reduced from 62 J/m^2 to 52 J/m^2), which is likely due to the fact that sulfur does not segregate to the niobium/sapphire interface nearly as much as it does to the niobium surface. The increase in fracture energy due to titanium additions is attributed to the strong interaction titanium has with oxygen and the associated increase in the work of adhesion. Silver does not interact strongly with oxygen, and the decrement in fracture energy is explained in terms of a model by Seah [90] which states that segregants of large atomic radii and/or small heats of sublimation in comparison to the bulk material reduce the boundary (interface) cohesion.

The decrement in fracture energy due to silver was much more pronounced for interfaces of higher fracture energy. The observation is consistent with a model by McMahon [89] in which the fracture energy is proportional to the work of adhesion raised to some power (>1). Thus, in the upper realm of fracture energies (high work of adhesion), small changes in the work of adhesion (due to interface segregants) can produce large changes in fracture energy, while weaker interfaces are not weakened much, even for relatively large decreases in interfacial energy. This may also explain why sulfur had relatively small effect on fracture energy; a similar study on orientation relationships A,B, or C may yield a more conclusive result for sulfur. Admittingly, such models [89,90] are based on behavior in steels and have several simplifying assumptions [89], thus their application to a heterophase interface is not necessarily direct; however, the experimental evidence suggests they can be more widely applied.

Clearly the microstructure (whether single crystal or porous polycrystal), orientation relationship, and chemical composition of the alumina and niobium being joined has effects on the resulting mechanical properties of niobium/aluminum oxide joints. Indeed this system is capable of forming strong bonds and maintaining strength to elevated temperatures (≈900°C) [77,87]. This research examines a more practical approach to fabricating such bonds.

2.6 Diffusion Bonding Mechanisms and Structure of the Niobium/Alumina Interface

Many experimental studies have been dedicated to determining the interactions between alumina and niobium responsible for strong bonding. The first of these [77] proposed that a reaction layer of niobium oxide (NbO_x) is formed between aluminum oxide and niobium. Such a reaction layer may be influential upon the observed strengths since an oxide may form stronger bonds with another oxide than a metal, and metals can form very strong bonds with their own oxides. Evidence for a NbO_x reaction layer was found in the increased hardness of the joint as the niobium/sapphire interface was approached. A region of dark contrast was observed in optical micrographs near the niobium/sapphire interface, and the thickness of this reaction layer appeared to increase with processing time and temperature. Additionally, the reaction layer developed a unique orientation relationship with the adjacent sapphire suggesting that niobium grains of various orientation did not completely extend to the interface [77].

Although Morozumi *et al.* [77] report some convincing evidence supporting the formation of a NbO_x reaction layer at the niobium/sapphire interface, no other studies [19,20,73,74,78,80,83,84,91-96] on these interfaces have observed such a layer. The hardness values reported by Morozumi *et al.* [77] are comparable to those measured by Elssner *et al.* [97] for niobium containing a few atomic percent oxygen. The increased hardness nearer the interface may alternatively be due to dissolved oxygen in niobium, resulting from dissolution of alumina during processing. Rühle and coworkers [74,83] argue that the contrast region in optical micrographs may be due to a shadow effect from preferential thinning near the interface during TEM sample preparation as such an effect did occur in their own samples. No additional diffraction spots for such a NbO_x phase were present in these studies [74,83] which were presumably bonded under similar processing conditions as used by Morozumi *et al.* [77]. Additionally, no reaction layer has been observed at niobium/alumina interfaces produced by internal oxidation of niobium-aluminum alloys [92,96], which were processed at higher partial oxygen pressures ($\approx 10^{-7}$ atm) and lower temperatures (1450-1500°C) compared with those (total vacuum pressure $\approx 10^{-8}$ atm, 1600-1800°C) used by Morozumi *et al.* [77].

Although the results of Morozumi *et al.* [77] may be wrong, there are some plausible kinetic and thermodynamic based explanations for oxide layer formation. Impurities in the niobium or sapphire used may extend the composition of the niobium phase beyond its phase boundary, particularly as small amounts of sapphire are dissolved. For example, niobium containing additional oxygen may dissolve even more oxygen and some aluminum during processing. Upon cooling, a niobium oxide phase may precipitate. Although alumina is the preferred precipitate phase (more stable oxide), due to the small amounts of aluminum in solution, it may be difficult for aluminum to recombine with oxygen and a NbO_x phase may persist for kinetic reasons. However, Rühle and coworkers argue that niobium oxides will not be stable above 1100°C, and that such oxides cannot form during cooling [78]. Morozumi *et al.* may have observed a statistical distribution of dissolved oxygen in niobium [74,83]. Limited purity information is provided by Morozumi *et al.* [77]; however, hardness measurements on the niobium prior to bonding are consistent with ≈1 at% dissolved oxygen [97].

Studies by Rühle and coworkers [19,20,74,83,84] have indicated that significant dissolution of alumina (≈0.7 wt% aluminum) by niobium occurs when diffusion bonding is carried out at sufficiently high temperatures (≈1950°C). A consequence of this dissolution is that small precipitates (≈2 μm) of a metastable transition alumina, theta-alumina (monoclinic) [20,74,84], are formed ≈15 μm from the interface during cooling. Some niobium grains did not contain these precipitates, and precipitates were observed further into the niobium along grain boundaries [74]. Sufficiently slow cooling rates are required for such precipitation, *i.e.*, precipitates were not observed for samples cooled at 215°C/min, while samples cooled at 20°C/min did exhibit this phenomenon [20]. The dissolution of alumina in niobium is correlated with a migration rate of the interface into the alumina (≈900 nm after 2 h of bonding at 1950°C [20]), and is potentially important in forming a continuous niobium/alumina interface.

The formation of alumina precipitates in the niobium matrix is associated with the relative diffusivities of aluminum and oxygen in niobium. Oxygen diffuses interstitially in niobium, compared with the substitutional diffusion of aluminum, thus the diffusivity of oxygen in niobium is expected to be substantially greater than that of aluminum, and the difference between the two diffusivities should be greater at lower temperatures due to the activation energies associated with these two types of diffusion. Figure 2.10 plots the temperature dependence of the diffusivities for aluminum and oxygen in niobium. Upon cooling a niobium/alumina sample both aluminum and oxygen will be relatively mobile in the first stages of cooling, and thus alumina may precipitate onto the bulk sapphire. This is the thermodynamically preferred site for condensation, as no nucleation is required, and results in a depletion of aluminum near the niobium/sapphire interface. During the latter stages of cooling, the aluminum is essentially immobile, and precipitates are formed in the region away from the interface where substantial amounts of aluminum remain [80]. Faster cooling will prevent nucleation of alumina precipitates away from the interface, or will severely limit their ability to coarsen. These mechanisms explain the aluminum concentration profiles observed by Rühle and coworkers [19,20].

To investigate the diffusion bonding process further, Burger and coworkers [19,20,74,83] monitored the evolution of controlled-geometry flaws at the interface. Photolithographically introduced channels (5-200 μm wide, ≈2 μm deep) were fabricated across the surface of polycrystalline niobium substrates which were diffusion-bonded to sapphire. This geometry prevented complete closure of the channels during bonding (1700°C for 2 h) and the surfaces could easily be separated for analysis. An imprint of the niobium grain boundaries could be clearly seen on sapphire side of fracture surfaces. Although the introduced channels were too large for closure, reprecipitation of alumina in the flaws was apparent; this is a result of back diffusion of aluminum and oxygen during cooling of the specimen, and precipitation was more extensive for slow-cooled samples.

Additionally, square hardness indentations of various sizes were made in the niobium surface prior to bonding and processed at 1850°C for 4 h [20]. During processing, the indentations developed a circular (cylindrical in 3-D) shape; the diameter of the cylinders was independent of the initial indent size, however, the depth was such that volume of the indent was conserved. Many of the cylindrical voids were completely filled by alumina precipitation. Fast-cooled samples filled voids with initial diagonal dimensions <10 μm while slow-cooled samples filled voids up to 20 μm in diagonal dimension, suggesting that reprecipitation is indeed more extensive in the slow-cooled specimens.

The reprecipitation of alumina at interfacial flaws aids in the elimination of voids at the bonding interface; however, this is unlikely the primary process responsible for complete diffusion-bonding in niobium/alumina joints. Good niobium/sapphire adhesion has been obtained for niobium with height fluctuations as large as ≈1 μm and a fluctuation periodicity of ≈200 μm by bonding at 1700°C for 2 h at 10 MPa [78]. The roughness of such a niobium surface is large compared to the extent of interface migration (<50 nm at 1700°C) due to alumina dissolution, and reprecipitation would only provide a <3 nm thick alumina layer [78]. Clearly, it seems unreasonable to believe that the quality of diffusion bonds in this system is strongly governed by interface migration (alumina dissolution) or by the cooling cycle(s) in processing (reprecipitation). More likely, diffusion bonding is assisted by plastic deformation. Creep of both aluminum oxide [98] and niobium occur at ≈1700°C during diffusion bonding [74,91]. Interface migration and reprecipitation may be beneficial for eliminating very small voids; however, the extent of this effect will decrease as lower bonding temperatures are used.

Reimanis [14] found that during diffusion bonding (0001) sapphire to a highly (111) textured niobium, initial contact between niobium and sapphire occurs near niobium grain boundaries due to the formation of thermal grooves. These points of contact expand to form facetted bonding fronts. The facets are triangular (roughly equilateral) and their orientation (rotation) varies from grain to grain suggesting they are a result of the near three-fold symmetry within grains of the textured niobium foil. The height of grain boundary grooves was in the range 0.2-0.4 μm, such that the voids are too large to be filled by interface migration (alumina dissolution) or recondensation of alumina for the bonding temperature used (1447°C). Furthermore, evolution of the pores seemed to occur whether or not an applied load was present during annealing. This suggests that the elimination of pores can be assisted by some other mechanism than deformation, involving diffusion of either alumina and/or niobium. All three of the mechanisms discussed will aid in diffusion bonding. Deformation processes will be dominant in the early stages of processing; however, as the contact area between the niobium and alumina is increased, deformation will be limited and voids will close by diffusional processes. Finally, interface migration and reprecipitation will only be useful for eliminating the smallest of voids; unless processing is done at extremely high temperatures (1950°C ≈ $0.96T_f^{\mathrm{Al_2O_3}}$).

Further studies on diffusion bonds of single-crystal niobium with sapphire enabled detailed analysis of niobium/alumina interfacial structures by high-resolution electron microscopy (HREM). Such studies [74,78,80,83,84,91,93] were performed on samples of specific orientations relationships since HREM analysis requires that the electron beam be near parallel to low-index zone axes of both the sapphire and niobium [78,93]. Many of the studies [74,78,83,91,84] focused on orientation relationship C (see Table 2.2) . Other studies [80] examined an orientation relationship (A in Table 2.2) that was more fundamental to the system as it was observed for alumina particles in a niobium matrix formed by the internal oxidation of a niobium-aluminum alloy [92,96]. Orientation relationship A may be obtained by a 90° rotation of the niobium crystal about its [110] axis from orientation C and implies that the close-packed planes of the sapphire and niobium are still parallel†. Additional studies [93,94] deposited niobium onto sapphire substrates and found a unique orientation relation between niobium and sapphire regardless of the substrate surface to which the niobium was deposited.

Niobium/sapphire interfaces with orientation relationship C exhibit some general features relevant to niobium/alumina interfaces. Due to the high processing temperatures (≈1700°C) used for fabricating diffusion-bonded samples, both the sapphire and niobium undergo plastic deformation by creep, resulting in 3-5 distorted atomic layers of niobium nearest the interface. Consequently, a relatively high dislocation density is observed in the niobium near the interface. Such dislocations may be responsible for the resistance of the interface to the growth of quasi-static cracks. Small-angle grain boundaries are also present in both the niobium and sapphire near the interface. The interface is facetted in accordance with the misorientation of the crystals, and the dissolution and reprecipitation of alumina discussed may enable small orientation adjustments to yield an interface of lower energy. After such orientation adjustments, the close-packed planes of niobium and alumina are not exactly parallel indicating that an ≈3° tilt of the niobium close-packed planes with respect to the oxygen close-packed planes in alumina is energetically more favorable than perfect alignment. [74,78,83,91,84]

Samples diffusion-bonded with orientation relationship A [80] revealed an interface with some similarities as well as notable differences to those observed in the internal oxidation studies [92,96]. Niobium (3,3.5 at% aluminum alloy) was internally oxidized

---

† Although one study [92] on the internal oxidation of niobium-aluminum alloy states an orientation relationship equivalent to C as the lowest energy relationship, other studies refer to the results of this internal oxidation study as orientation relationship A [80,93].

by exposure to a partial oxygen pressure of $(5\times10^{-8}, 1\times10^{-7}$ atm) at (1450,1500°C) for (40,30 min) [92,96], and the diffusion-bonded interfaces were processed under similar conditions (1500±50°C for 1 h) in high vacuum [80]. The alumina precipitates observed in internal oxidation did not exactly duplicate the corundum structure of sapphire used in diffusion bonding, but were a closely related four-layer stacking sequence variant of alpha-alumina [92]. Orientation relationship A possesses a niobium/alumina lattice misfit of ≈3%, which is accommodated by misfit dislocations in niobium. The internally oxidized interface is atomically flat, and the resulting misfit dislocations are equally spaced (8.5-9.8 nm) and located at a "stand-off" distance of 4 niobium layers from the interface [92,96]. The artificially produced interfaces [80] were not atomically flat, and misfit dislocations tended to be situated near interfacial steps (their spacing varied between 5 nm and 15 nm). The "stand-off" distance of misfit dislocations was 2-4 niobium lattice spacings. The difference in these dislocation structures may be related to the fact that dislocation loops are formed around internally oxidized precipitates [80,96], which cannot occur in the diffusion-bonded geometry. Dislocations at a "stand-off" distance may have crack shielding or antishielding effects depending on variations in "stand-off" distance and crack tip position [92]. No "stand-off" was observed for bicrystals of orientation relationship C [78].

Efforts have been made to determine the terminating layer of sapphire at niobium/sapphire interfaces. By comparing various TEM image simulations with actual images, Knauss and Mader [80] were able to determine that the sapphire was terminated with an aluminum layer at the interface. Although such a determination could not be explicitly made for internally oxidized samples [92,96], oxygen termination was anticipated due to excess dissolved oxygen and aluminum's greater affinity for oxygen in comparison to that of niobium [92]. By comparing the free energies of formation of alumina, niobium oxide (NbO), and niobium aluminides (Nb_3Al and Nb_2Al) it can be concluded that aluminum and niobium would both prefer to bond to oxygen rather than each other [96]; this is most simply achieved by oxygen termination. Samples bonded in orientation relationship C suggest aluminum termination since the aluminum-to-oxygen interface concentration ratio (measured during bonding at high temperature) was ≈10; however, the cooling cycle may have altered the surface termination [78]. Aluminum termination in studies by Knauss and Mader [80] is believed to be the result of a kinetic phenomena. Since oxygen diffusion in niobium is much faster than aluminum diffusion, the oxygen concentration profile will be deep and shallow compared that of aluminum. Upon cooling, reprecipitation of alumina at the interface will deplete niobium of oxygen relatively far from the interface. As back diffusion of oxygen continues during cooling, the alumina precipitation zone (≈15 μm from the interface) may act as a trap for oxygen as it diffuses back toward the interface [80].

A general correlation for metal/oxide systems is that the lowest energy interfaces are formed when the closest-packed oxygen and metal planes are parallel. This arrangement provides a high density of metal-oxygen bonds across the interface, resulting in strong adhesion. Orientation relation A possesses these characteristics and is believed to be the lowest energy of the niobium/alumina interfaces. This is exemplified by the large area of this interface in the platelike precipitates formed in internally oxidized samples [92,96]. Surface termination can play an important role in determining the work of adhesion at the interface and will ultimately influence the resulting mechanical properties.

Finally, niobium/alumina interfaces were also investigated by depositing niobium on (0001), $(11\bar{2}0)$, and $(1\bar{1}00)$ sapphire substrates *via* molecular beam epitaxy (MBE) [93,94]. Interestingly, the orientation of the niobium film relative to the sapphire (orientation J in Table 2.2) was the same regardless of the substrate orientation. This relationship has also been observed for epitaxial films on $(1\bar{1}02)$ sapphire, and a 2.87° misorientation between (001) niobium and $(1\bar{1}02)$ sapphire was observed to accommodate the relationship (J) [99]. Misfit dislocations were formed; however, no "stand-off" distance was observed [93,94]. This may be due to kinetic reasons, since the deposition was performed at much lower temperatures (850°C) than diffusion bonding or internal oxidation experiments [93,94]. Ohuchi [100,101] was able to determine that chemical bonding between niobium and oxygen does indeed occur at the interface by evaporating ≈6 monolayers of niobium onto (0001) sapphire. By monitoring energy shifts in x-ray photoelectron spectroscopy (XPS) peaks for niobium and oxygen after various stages in the deposition (roughly every monolayer), Ohuchi was able to conclude that niobium-oxygen bonds were present for the first niobium monolayer, thus this is the extent of reaction between alumina and niobium [101]. Additionally the appearance of a surface-sensitive (top monolayer) metallic aluminum peak indicates that alumina dissolution occurs.

The niobium/alumina bicrystal studies discussed in this section indicate that the niobium/alumina interfaces are morphologically stable. It is well known that the $(1\bar{1}00)$ surface of sapphire is unstable [65,102-104]; and such facetting can occur after only a few hours of annealing at 1400°C [102-104]. However, when this surface is bonded to niobium, the facetting no longer occurs. If facetting were to occur at niobium/$(1\bar{1}00)$ sapphire interfaces, the imposed facets on the niobium side of the interface would most likely not be parallel with low-energy niobium planes and/or have extensive lattice mismatch. None of the studies which were diffusion bonded with a temperature/time profile capable of inducing facets reported such an observation [8,79,82,85].

Clearly, all aspects (extent of pore closure, chemical reaction, dislocation network, and morphology) of niobium/alumina interfaces can influence the work of adhesion and/or mechanical properties of joints. Development of a polycrystalline niobium/alumina interface may be substantially different. For example, small angle grain boundaries are unlikely to develop, particularly if the alumina or niobium grain sizes are smaller than the observed sub-grains. Processing at lower temperatures and pressures may reduce deformation in the niobium as well as the number of dislocations formed at the interface, thus limiting interfacial fracture resistance. Joining with aluminas containing glassy phases may not require misfit dislocations to form in regions of metal/glass interface [80]. The bicrystal studies provide fundamental information about niobium/sapphire interfaces and may enable predictions about the vast number of randomly oriented interfaces present in a polycrystalline niobium/alumina joint.

2.7 Copper/Alumina Joints (Mechanical Properties and Interfacial Microstructure)

The primary role of copper in the present research is to serve as a liquid phase. The properties of this phase have been discussed in Sections 2.3 and 2.4. However, since the resulting microstructure in copper-niobium PTLP bonding will have a copper-rich phase, most likely in contact with the alumina, the copper/alumina interface may also be relevant in determining joint properties.

Klomp [105] diffusion bonded copper to alumina at 1000-1050°C, which resulted in strengths ranging from 20 MPa to 150 MPa. Generally, higher loads (up to 20 MPa) and longer bonding times (15-20 min) were required for stronger joints. Crispin and Nicholas [106] obtained an optimum joint strength of 54 MPa by diffusion bonding copper to alumina at 875°C (50 MPa applied load). Many samples failed in the ceramic near the interface; likely due to thermally induced stresses. Additionally, joint strength could be improved to 86 MPa by annealing joints at 250°C to relieve residual stresses [106]. Contrary to Klomp [105], Crispin and Nicholas observed that applying the 50 MPa load for only 1 min of the 30 min bonding cycle resulted in a slight strength increase. This is likely due to the fact that small cracks in the alumina (resulting from surface grinding) were not propagated as far during bonding.

Esposito *et al.* [107] have obtained strengths of 177±13 MPa for copper diffusion bonded to alumina at 1025°C and 50 MPa (15 min). Failure occurred exclusively at the interface (three-point bend tests were performed); however, some alumina grains remained adhered to the copper after failure. Although processing conditions were similar to those used by Crispin and Nicholas [106], the improvement in strength may be due to several factors; the most notable are that thicker copper layers (0.5 mm versus 50 μm) were used by Crispin and Nicholas, and additional surface preparation (polishing versus ground flat) was done by Esposito *et al.*. Thicker metal layers will not be as constrained and can impose larger stresses on the ceramic due to thermal misfit [108]. In addition to the effects of surface preparation on the diffusion-bonding process previously discussed (Sections 1.2 and 2.6), a well-polished surface will minimize flaw size on the ceramic surface, thus limiting stress concentrations and crack growth which may occur during processing at high loads (50 MPa).

Elssner and coworkers [81,86] have measured the fracture energy of polycrystalline copper/alumina interfaces fabricated by diffusion bonding (830-1010°C, 16 MPa, 1 h) in UHV. The interfaces had higher fracture energies than similarly produced (920-1450°C, 16 MPa, 1 h) niobium/alumina interfaces [81,86]; however, bonding was achieved at higher homologous temperatures. Collectively, these studies indicate that copper/alumina interfaces are potentially as strong [77,105-107] and more fracture resistant [81,86] than niobium/alumina interfaces. Crack path observations [107] and fracture energy measurements [81,86] are consistent with observations made by Shalz *et al.* [17] for copper-niobium PTLP joints, *i.e.*, interfacial cracks deviated into the alumina where copper was present at the metal/ceramic interface, thus implying a crack path of less resistance in the ceramic.

Mulder and Klomp, Rühle *et al.*, and Ernst *et al.* have studied copper/sapphire interfaces formed by diffusion bonding [109,110], MBE [110], and internal oxidation of copper-aluminum alloys [111]. Mulder and Klomp [109] diffusion-bonded 8 μm copper foils to (0001) sapphire at 1067°C for 1 h under 20 MPa. The copper foil orientation was initially (100); however, after bonding, XRD revealed that (111), (241), and (263) planes of copper were parallel to (0001) sapphire. The results suggest that an orientation adjustment occurred during bonding in order to form a more favorable interface. TEM revealed the majority of the interface was oriented such that (111) copper was parallel with

(0001) sapphire, and $\langle\bar{2}46\rangle$ copper was aligned with $\langle 1\bar{1}00\rangle$. This orientation relationship exhibited good lattice matching between the two materials.

Rühle *et al.* [110] deposited copper films on (0001) sapphire at 200°C *via* MBE. The films grew such that (111) copper was parallel to (0001) sapphire, and $\langle 110\rangle$ copper was parallel to $\langle 10\bar{1}0\rangle$ sapphire. The difference in orientation relationship compared to that observed by Mulder and Klomp [109] may be due to the fact that epitaxial films tend to grow on substrates preserving the symmetry of the substrate plane [93,94]. (This may explain the difference in orientation relationship between epitaxial grown and internally oxidized niobium/alumina interfaces as well.) Additionally, films deposited at 600°C only exhibited a {111} texture, and thus there was no preferred twist orientation relationship between the copper and sapphire. Rühle *et al.* additionally fabricated diffusion-bonded specimens according to this orientation relationship so that interfaces fabricated by the two methods could be compared. By internally oxidizing copper-aluminum alloys, Ernst *et al.* [111] observed both alpha-alumina and cubic alumina (η'-Al_2O_3) precipitates. The alpha-alumina precipitates were observed at grain boundaries in the metal matrix, while the cubic alumina was found as platelets in the grain interiors. Although a different structure, the cubic alumina was oriented such that the close-packed oxygen planes were parallel to the (111) copper planes, as in the studies by Mulder and Klomp [109] and Rühle *et al.* [110]. TEM investigations of all three interfaces types (MBE, diffusion-bonded, and internally oxidized) revealed that the boundary is incoherent, *i.e.*, the copper lattice was rigid (no relaxations) up to the interface and no misfit dislocations were observed. Image simulations run by Ernst *et al.* [111] indicate that the alumina is most likely terminated by oxygen at the interface. The incoherence of the interface is consistent with the weak ionic and van der Waals bonding interactions between copper and oxygen in alumina observed by Ohuchi [112]. However, the interaction is favorable enough that surfaces other than (0001) alumina undergo distortions in order for copper to bond with oxygen; *i.e.*, oxygen is drawn toward the surface and aluminum is displaced toward the bulk [112].

Lack of misfit dislocations implies the mechanisms responsible for the fracture resistance of copper/alumina interfaces may be quite different than for the niobium case. The relatively low yield strength of copper (40 MPa [108]) compared to niobium (≈100 MPa [113]) would enable copper/alumina interfaces to exhibit more plasticity, and thus be more fracture resistant. The thermal expansion mismatch between copper and alumina (or niobium) may be quite detrimental to joint properties; however, the thin and/or small regions of copper phase likely to be present at the interface in the current study will be highly constrained, and impose little stress on the surrounding alumina and niobium bulk.

In addition to the previously described joints, Rühle *et al.* [110] have also diffusion-bonded (111) copper containing 60 ppm oxygen to (0001) sapphire. Oxygen additions resulted in a marked increase (factor of 3-6) in the interfacial fracture energy. TEM investigations revealed a thin (<50 nm) interfacial copper aluminate ($CuAlO_2$) layer. Additionally, cuprous oxide (Cu_2O) particles are believed to have formed at the interface during cooling. Esposito *et al.* [107] have acknowledged that a thin interfacial copper aluminate ($CuAlO_2$ or $CuAl_2O_4$) layer is likely present, although it could not be explicitly detected *via* XRD. These effects of oxygen are consistent with what would be expected from wetting and work of adhesion characteristics of copper containing oxygen.

The effects of oxygen on copper/alumina interfaces have been exploited in the development of copper-copper oxide eutectic bonding [64,114,115]. Eutectic bonding operates in a fashion very similar to PTLP bonding. By oxidizing the joining surfaces of copper, an effective cladding/core/cladding couple can be made to insert between two pieces of alumina. The copper-oxygen system possesses a eutectic at 1066°C between the copper-rich and cuprous oxide phases [23]. By processing the joint in the temperature range 1066-1083°C, phase evolution will occur in a similar fashion as illustrated in Figure 2.3 without melting the entire copper layer. Generally, the process results in formation of a copper aluminate ($CuAlO_2$) layer between the alumina and copper, and the copper phase contains cuprous oxide precipitates [64,114,115]. By using this process, Beraud *et al.* [64] were able to improve the strength of copper/alumina joints (≈140 MPa) compared to those obtained by diffusion bonding (≈50 MPa). S.T. Kim and C.H. Kim [115] obtained an optimum strength (≈250 MPa) by processing for 20 h. Additional processing time resulted in a slight decrement in bond strength due to increasing thickness of the copper aluminate layer (>10 μm) and resulting thermal stresses. Based on crack paths and fracture strengths, these results [64,110,114,115] collectively imply that the copper aluminate/alumina, copper aluminate/cuprous oxide, and copper aluminate/copper interfaces are stronger than copper/alumina, cuprous oxide/alumina, and copper/cuprous oxide interfaces.

In the current research, copper aluminate and cuprous oxide will be difficult to form due to the gettering effects of the neighboring niobium. Should the solubility limit of oxygen in niobium be reached, additional oxygen in the copper would rather form niobium oxides than aid in the formation of a copper aluminate layer (see Figure 2.9). Shalz *et al.* [17] have observed that alumina adheres to regions of copper at the metal/ceramic interface and suggested that copper aluminate may have formed at the interface. It is possible that upon cooling, ambient oxygen continues to diffuse into copper faster than the niobium can accommodate it (see Figures 2.10 and 2.11). Other mechanisms such as interfacial diffusion may also be relatively active. Additionally, dissolution of alumina may play a role in such phase formation.

In the interest of fabricating joints for high temperature use, the area fraction of copper at the copper-niobium/alumina interface is ideally minimized. Above copper's melting point, pockets of copper will effectively act as interfacial flaws or unbonded regions. If the copper regions are of sufficiently small stress intensity compared to the flaws in the alumina, then in principle, they should not limit the strength of the joint. In other words, relatively large regions of copper at the interface (in comparison to the alumina flaw size) may be tolerated provided that their fracture resistance is sufficiently large. Similarly, if the copper regions are sufficiently small, the nature of the interface (whether or not copper aluminate or cuprous oxide reaction products form) will not be very influential on resulting joint strength at lower temperatures. The results presented here indicate that the copper/alumina interface is in fact quite fracture resistant. The other interface of concern is the boundary between the copper and niobium phases. In all likelihood this interface is very tough in comparison to the metal/ceramic interfaces; however, impurity segregants can make it potentially weak. Ideally copper/alumina and copper/niobium interfacial areas will be minimized, thus maximizing niobium/alumina contact so that a strong refractory joint may be fabricated.

Table 2.1: **Contact Angle of Copper on Niobium at Various Conditions and Temperatures**

Niobium Characteristics and Treatment	**Contact Angle [deg]** 1090°C	1100°C	1200°C	1300°C
Polycrystal (after 5 min) 0.87 atm H_2 atmosphere	68	65	14	-
Polycrystal 1.5×10^{-9} atm vacuum	65	60	35	15
Polycrystal 0.87 atm Ar atomosphere	69	66	42	17
Polycrystal (6.5 at% oxygen) vacuum	85	85	79	59
(100) Single crystal vacuum	64	64	43	34
Polycrystal (1.5 at% oxygen) vacuum	65	64	56	19
Polycrystal (rough surface) vacuum	76	76	51	12
(110) Single crystal vacuum	74	74	44	9
Polycrystal (after 25 min) 0.87 atm H_2 atmosphere	38	-	8	0

Data taken from De Lima, Krehl, and Schulze [48].

Table 2.2: **Fracture Energies for Various Orientations of Single Crystal Niobium/Sapphire Diffusion-Bonded Joints**

	Orientation Relationship	**Fracture Engery** [J/m^2]	**Processing Conditions**	temp. [°C]	time [h]	load [MPa]	**Reference**
A	$(110)_{Nb} \parallel (0001)_{Al_2O_3}$ $[001]_{Nb} \parallel [1\bar{1}00]_{Al_2O_3}$	2390±430	UHV	1300	1	6.5	[81]†
		2107	UHV	1400	3	10	[85]
		1899±213	UHV	1400	3	7	[8]
		>150	HV	1700	2	10	[82]
B	$(110)_{Nb} \parallel (11\bar{2}0)_{Al_2O_3}$ $[001]_{Nb} \parallel [0001]_{Al_2O_3}$	2330±750	UHV	1300	1	6.5	[81]
		370	UHV	1400	3	10	[85]
		≈340	UHV	1400	3	10	[79]‡
C	$(110)_{Nb} \parallel (0001)_{Al_2O_3}$ $[001]_{Nb} \parallel [11\bar{2}0]_{Al_2O_3}$	1876±610	UHV	1400	3	7	[8]
		182±45	UHV	1300	1	6.5	[81]
D	$(110)_{Nb} \parallel (1\bar{1}00)_{Al_2O_3}$ $[001]_{Nb} \parallel [11\bar{2}0]_{Al_2O_3}$	175±38	UHV	1300	1	6.5	[81]
		110	HV	1700	2	10	[82]
E	$(100)_{Nb} \parallel (11\bar{2}0)_{Al_2O_3}$ $[001]_{Nb} \parallel [0001]_{Al_2O_3}$	150	UHV	1300	1	-	[85]*
		115	UHV	1400	3	10	[85]
		101±22	UHV	1300	1	6.5	[81]
		≈100	UHV	1400	3	10	[79]
F	$(100)_{Nb} \parallel (1\bar{1}00)_{Al_2O_3}$ $[011]_{Nb} \parallel [11\bar{2}0]_{Al_2O_3}$	100±26	UHV	1300	1	6.5	[81]
G	$(110)_{Nb} \parallel (1\bar{1}00)_{Al_2O_3}$ $[001]_{Nb} \parallel [0001]_{Al_2O_3}$	114±25	UHV	1400	3	7	[8]
		74	HV	1700	2	10	[82]
H	$(100)_{Nb} \parallel (0001)_{Al_2O_3}$ $[001]_{Nb} \parallel [11\bar{2}0]_{Al_2O_3}$	68±13	UHV	1300	1	6.5	[81]
I	$(100)_{Nb} \parallel (1\bar{1}00)_{Al_2O_3}$ $[001]_{Nb} \parallel [11\bar{2}0]_{Al_2O_3}$	77	UHV	1400	3	10	[85]
		≈60	UHV	1400	3	10	[79]
J	$(111)_{Nb} \parallel (0001)_{Al_2O_3}$ $[1\bar{2}1]_{Nb} \parallel [10\bar{1}0]_{Al_2O_3}$	112±51	UHV	1400	3	7	[8]

Joints fabricated in UHV are also cleaned with argon sputtering prior to bonding.

†Specimen fractured at the unnotched polycrystalline niobium/alumina interface, indicating the given value is a lower bound to the actual fracture energy of the interface.

‡Fracture deviated from the interface into the sapphire, thus, a lower bound was measured.

*Bonding load not reported

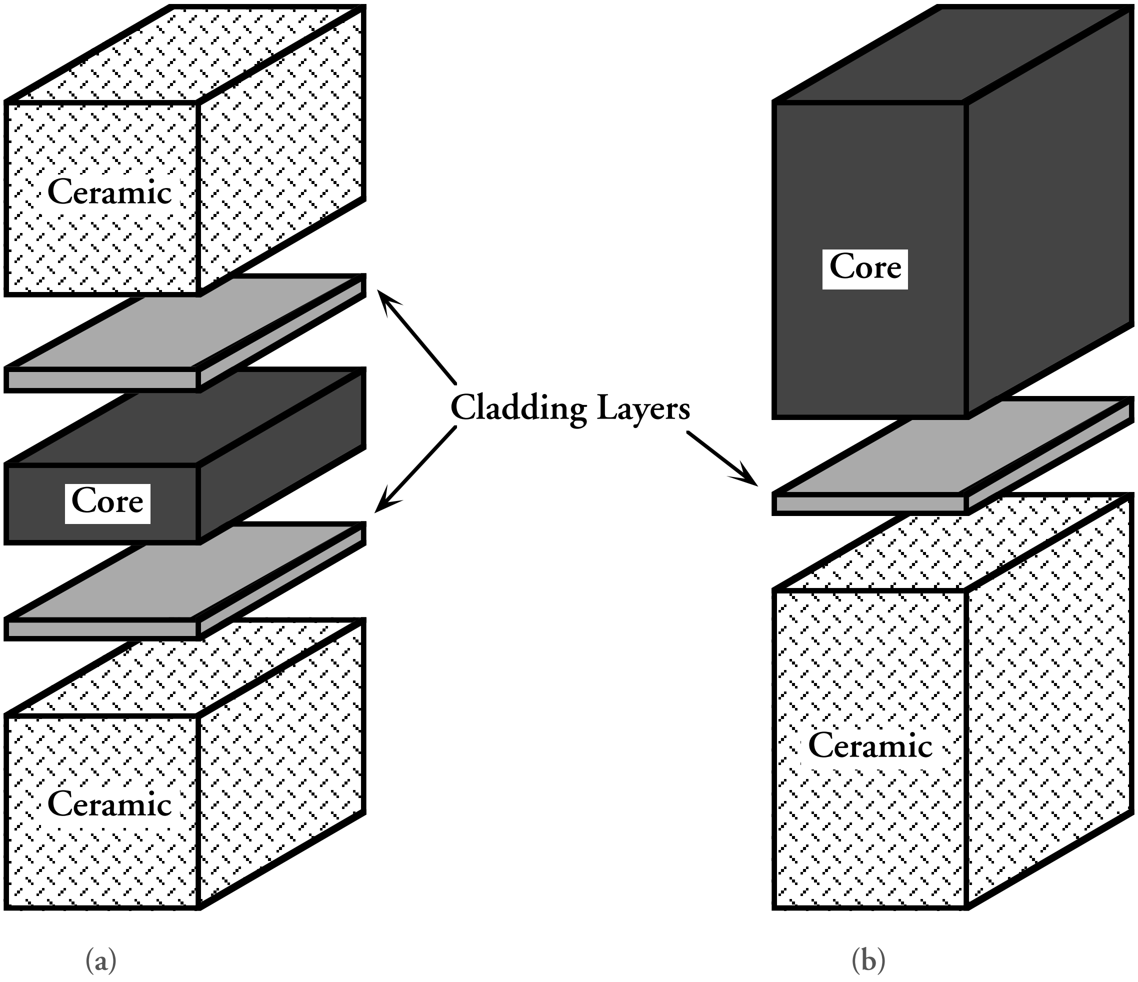

Figure 2.1: Illustration of a basic PTLP joining assembly (a). The technique may be applied to join bulk metal parts to a ceramic as well (b).

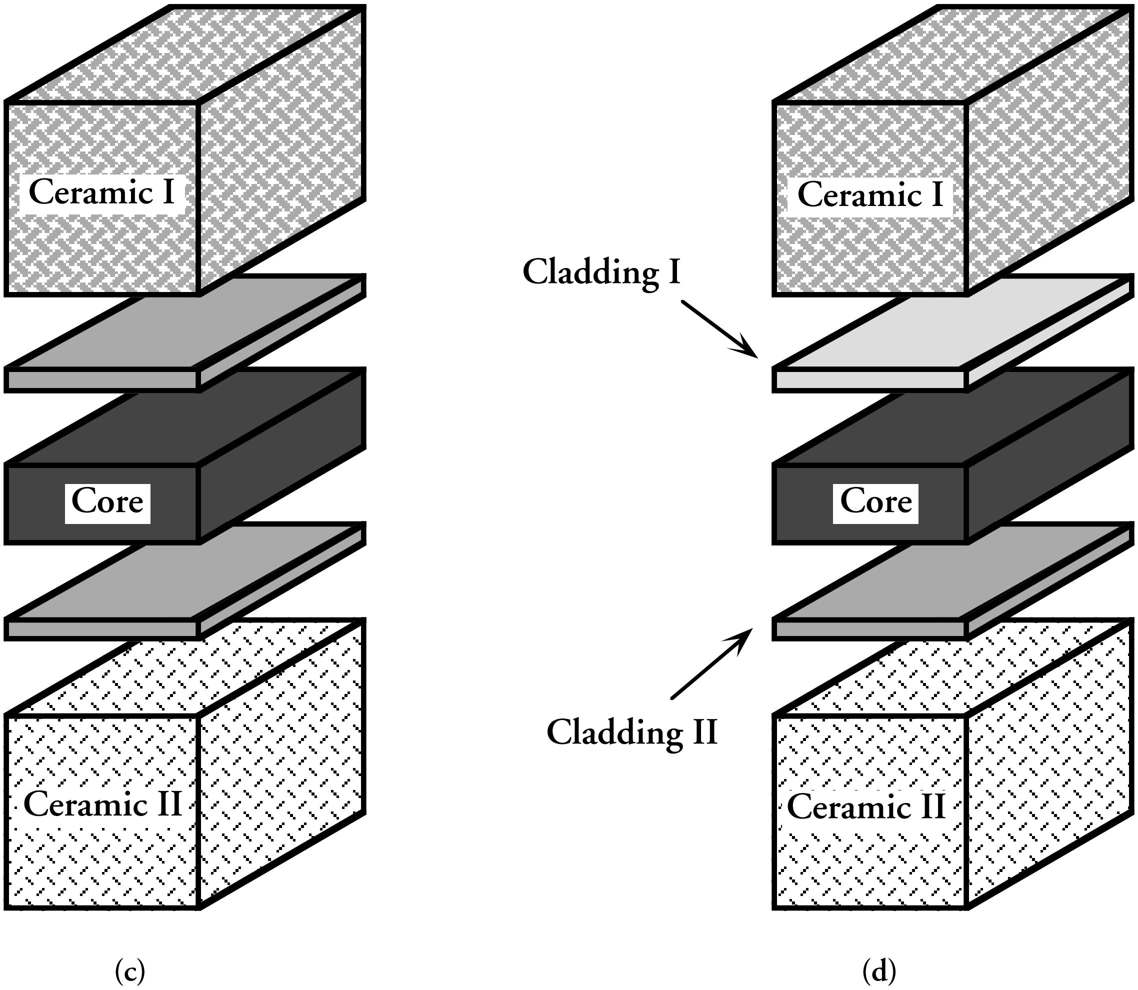

Figure 2.1: Illustration of a PTLP joining assembly for joining different ceramics (c). Different cladding layers may be used to optimize the properties between the liquid and each ceramic (d).

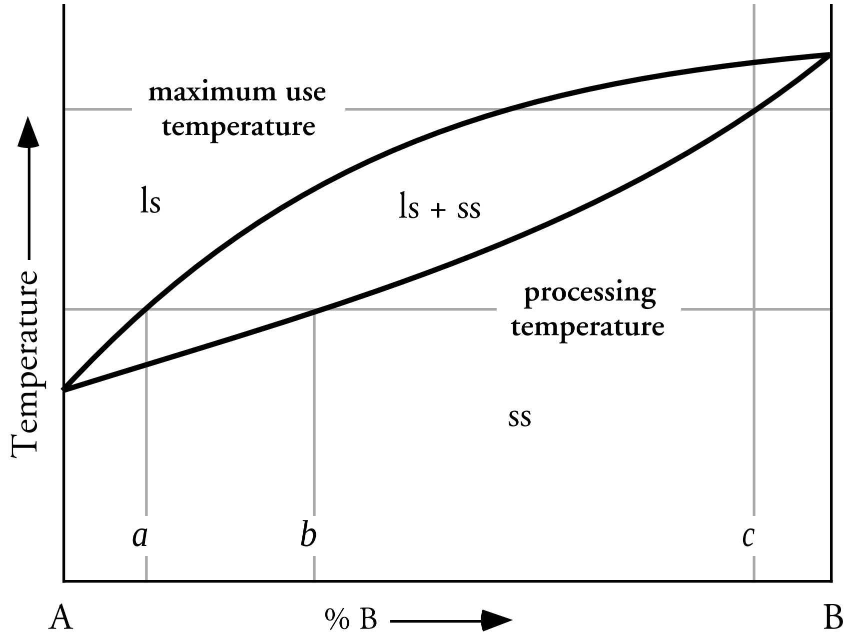

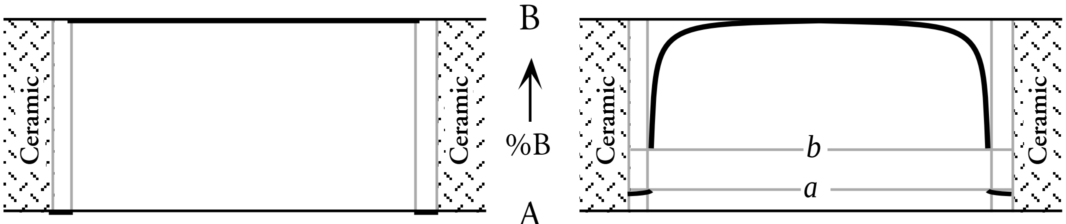

(1) Initial assembly, pure A *and pure* B*.*

(4) Liquid will widen slightly until it is saturated with B*, composition b.*

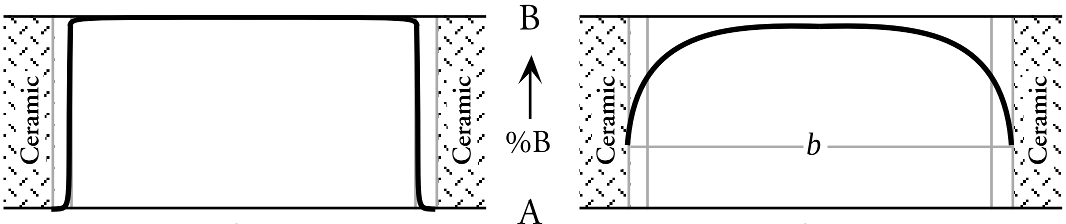

(2) A slight amount of solid state interdiffusion occurs during heating.

(5) Isothermal solidification proceeds until entire liquid layer is consumed.

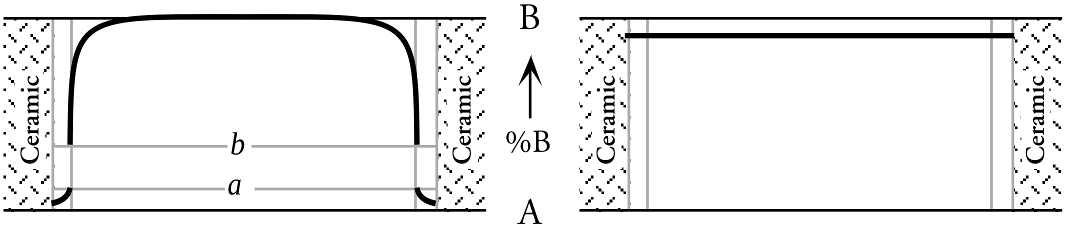

(3) Liquid begins to form once the melting point of A *is reached. It spreads toward the core layer until the composition a is reached.*

*(6) Solid state diffusion forms homogeneous joint with composition c, determined by initial amouts of cladding (*A*) and core (*B*) used.*

Figure 2.2: Phase and composition evolution of a PTLP joining layer whose components have a simple lens phase diagram. The vertical gray lines in the composition profiles represent the initial cladding and core boundaries.

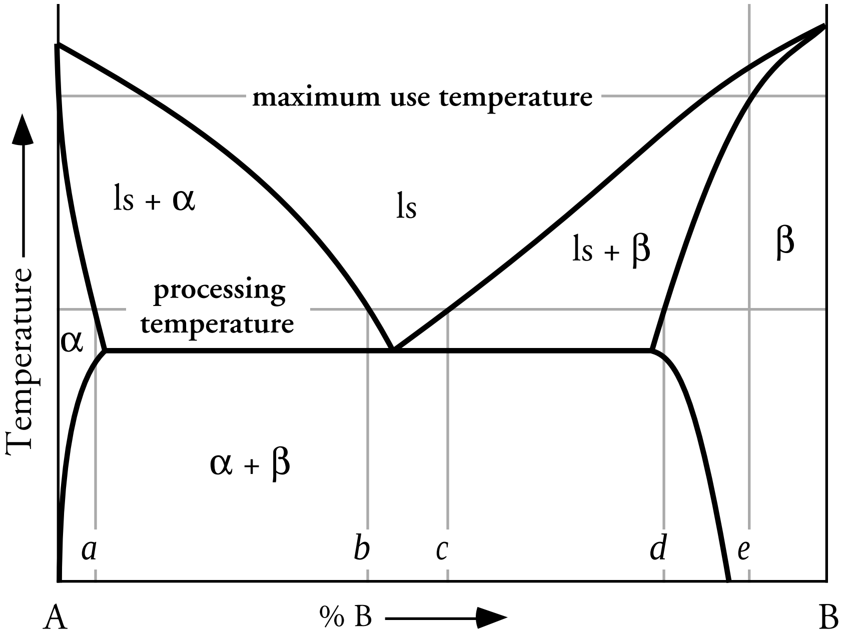

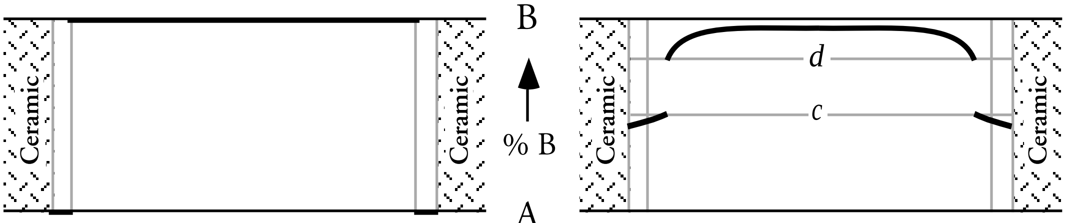

(1) Initial assembly, pure A *and pure* B.

(4) Liquid contiues to widen until entire cladding layer is dissolved, and liquid is saturated with B, *composition c.*

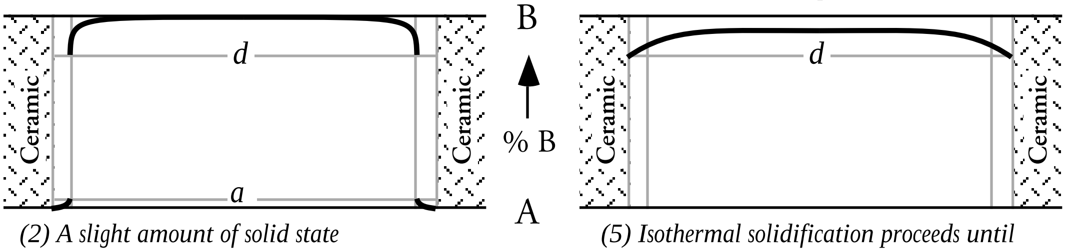

(2) A slight amount of solid state interdiffusion occurs during heating.

(5) Isothermal solidification proceeds until entire liquid layer is consumed.

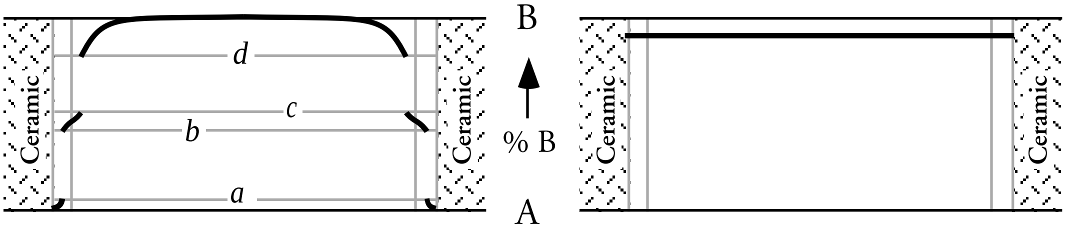

(3) Liquid begins to form once eutectic temperature is reached and spreads having composition from b to c.

*(6) Solid state diffusion forms homogeneous joint with composition e, determined by initial amouts of cladding (*A*) and core (*B*) used.*

Figure 2.3: Phase and composition evolution of a PTLP joining layer whose components have a eutectic phase diagram. The vertical gray lines in the composition profiles represent the initial cladding and core boundaries.

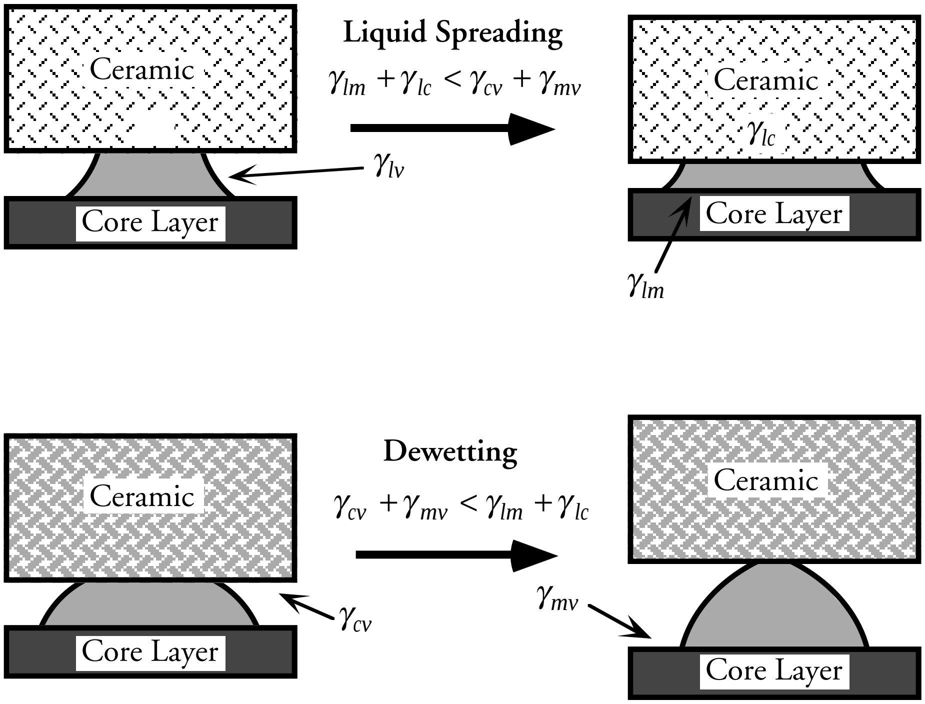

Figure 2.4: PTLP joining system in the early stages of processing. The surface free energies which dictate liquid phase evolution (spreading or dewetting) are labeled.

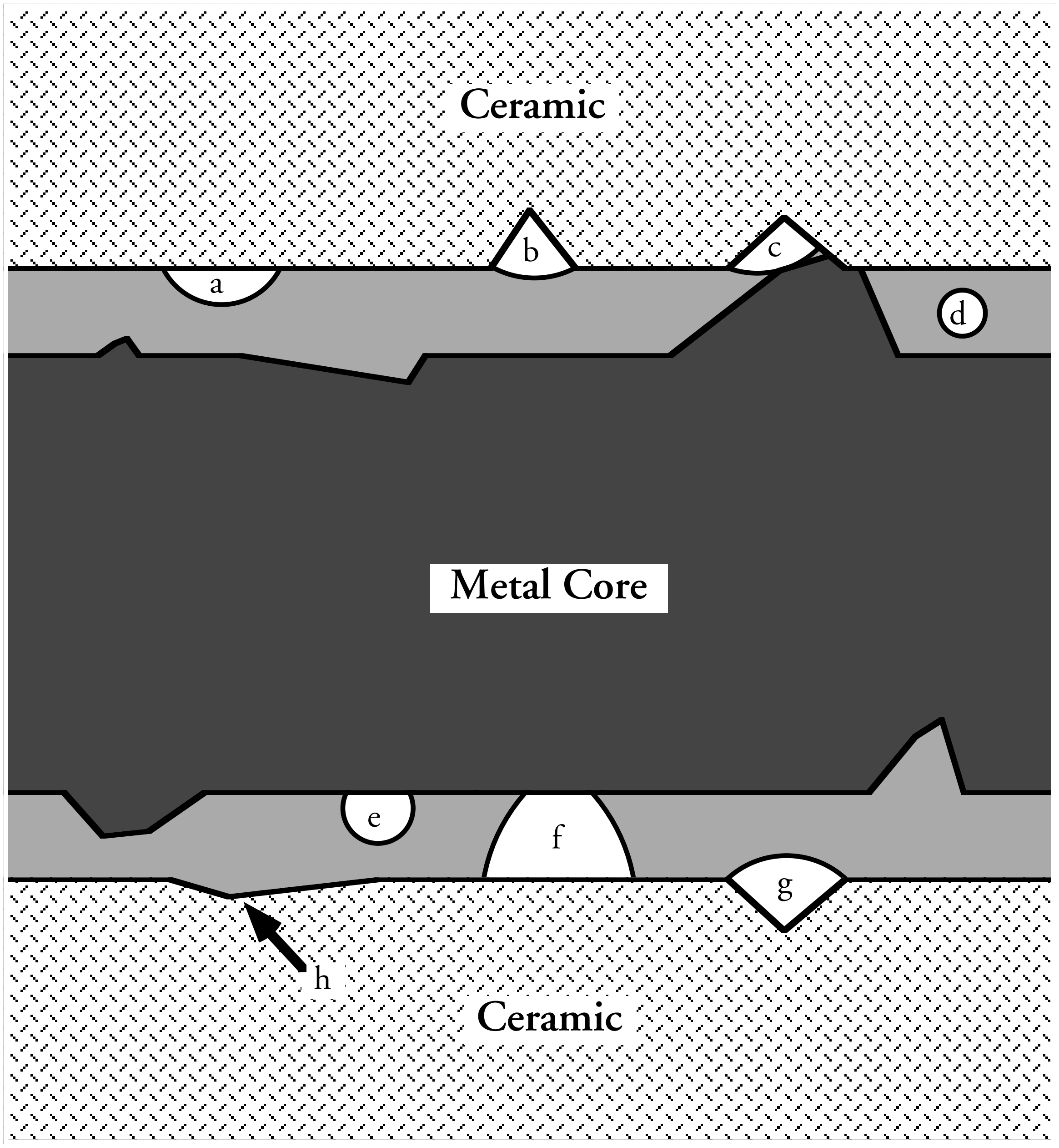

Figure 2.5: Flaws that are likely to develop in a PTLP joint in which the liquid phase wets the core layer, but does not wet the ceramic.

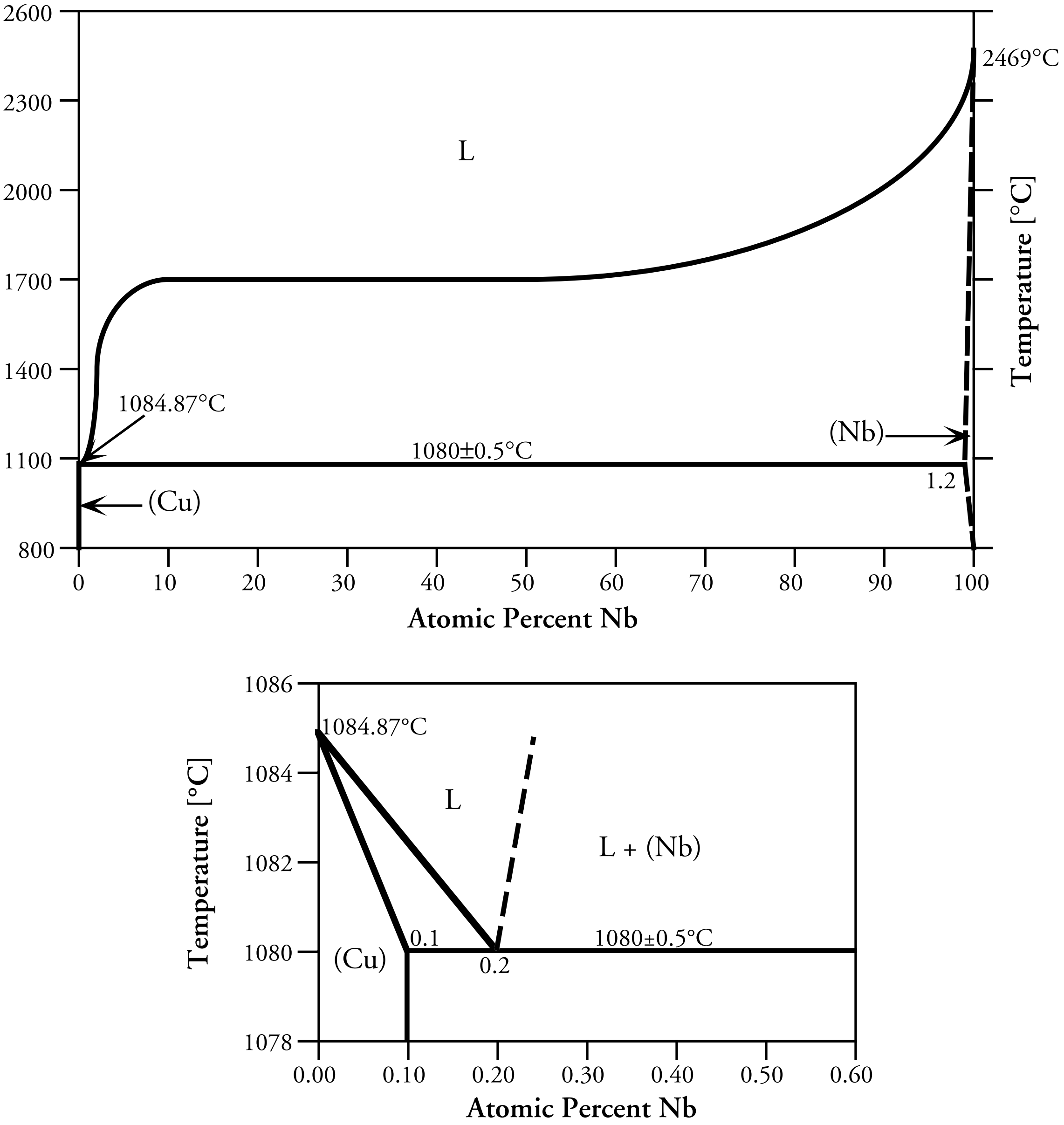

Figure 2.6: Schematic representation of the copper-niobium phase diagram presented in Massalski [23].

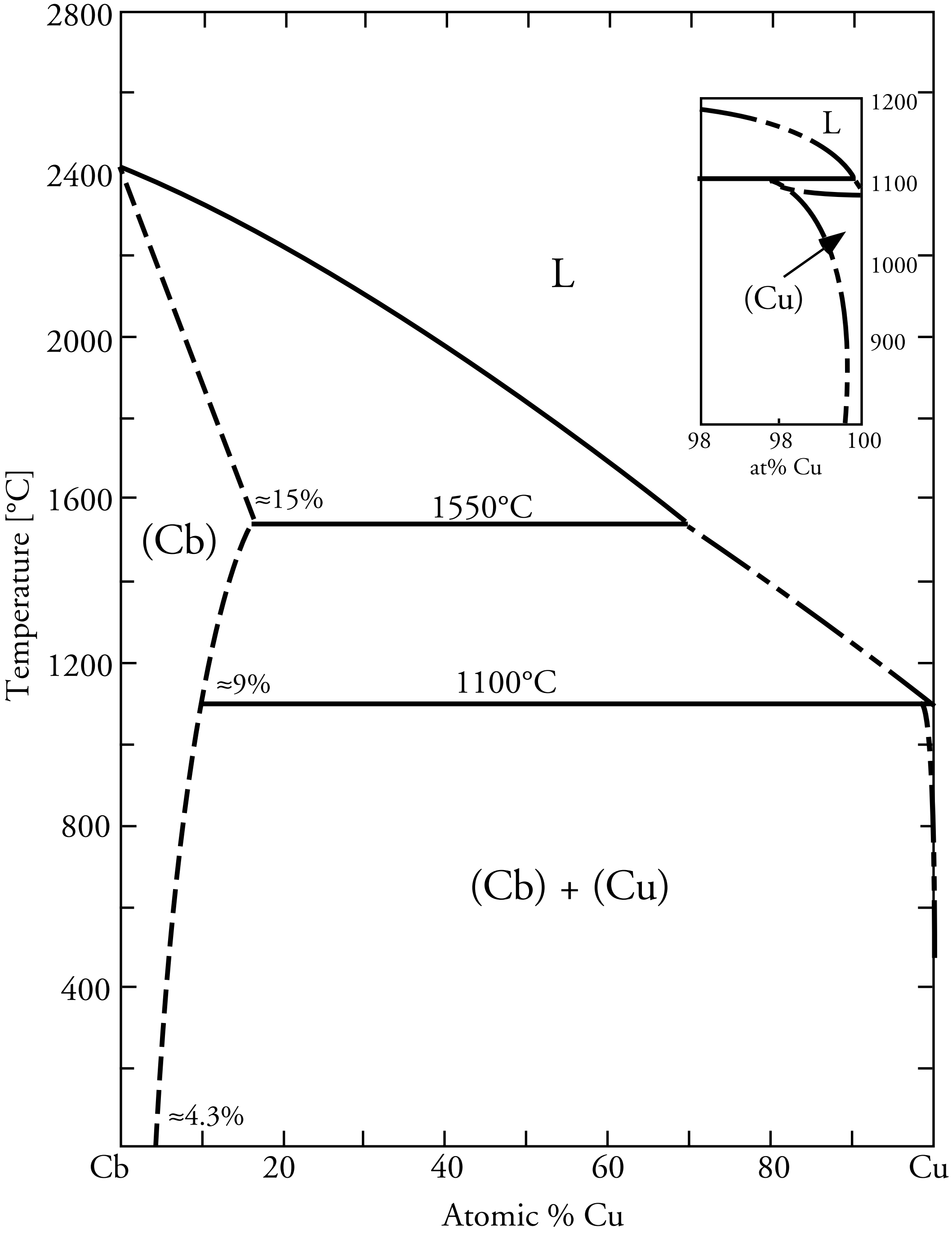

Figure 2.7: Copper-niobium phase diagram as presented in Elliot [69]. Columbium (Cb) is another name for element 41 (niobium), often used in older literature.

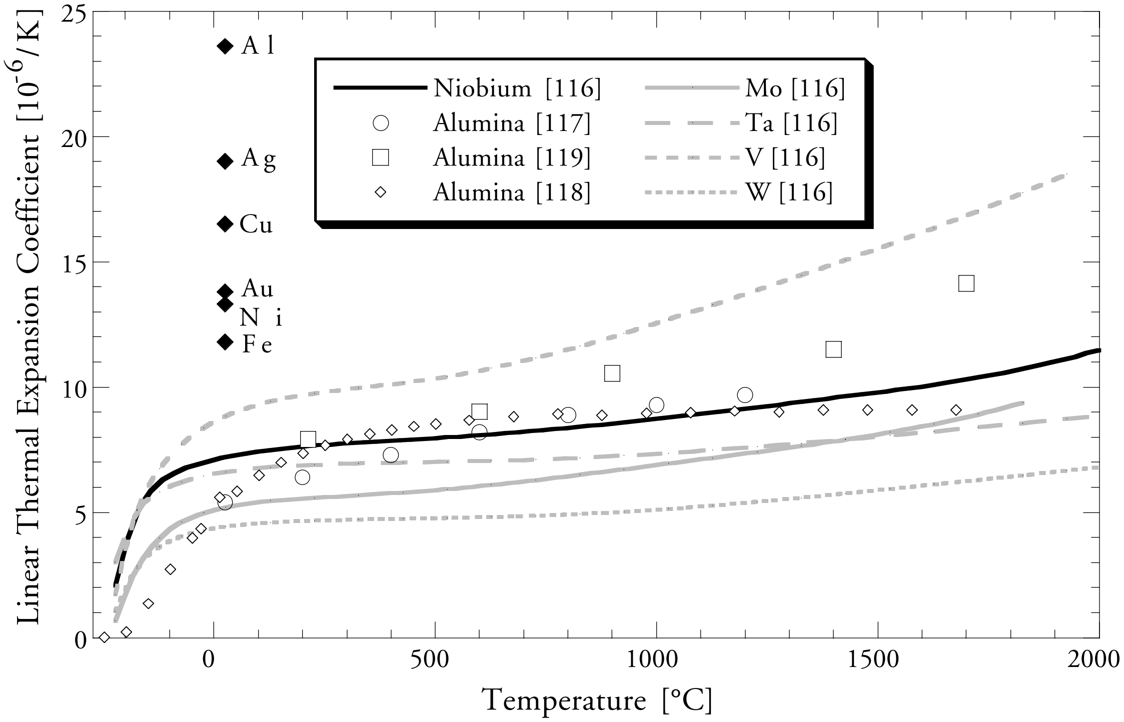

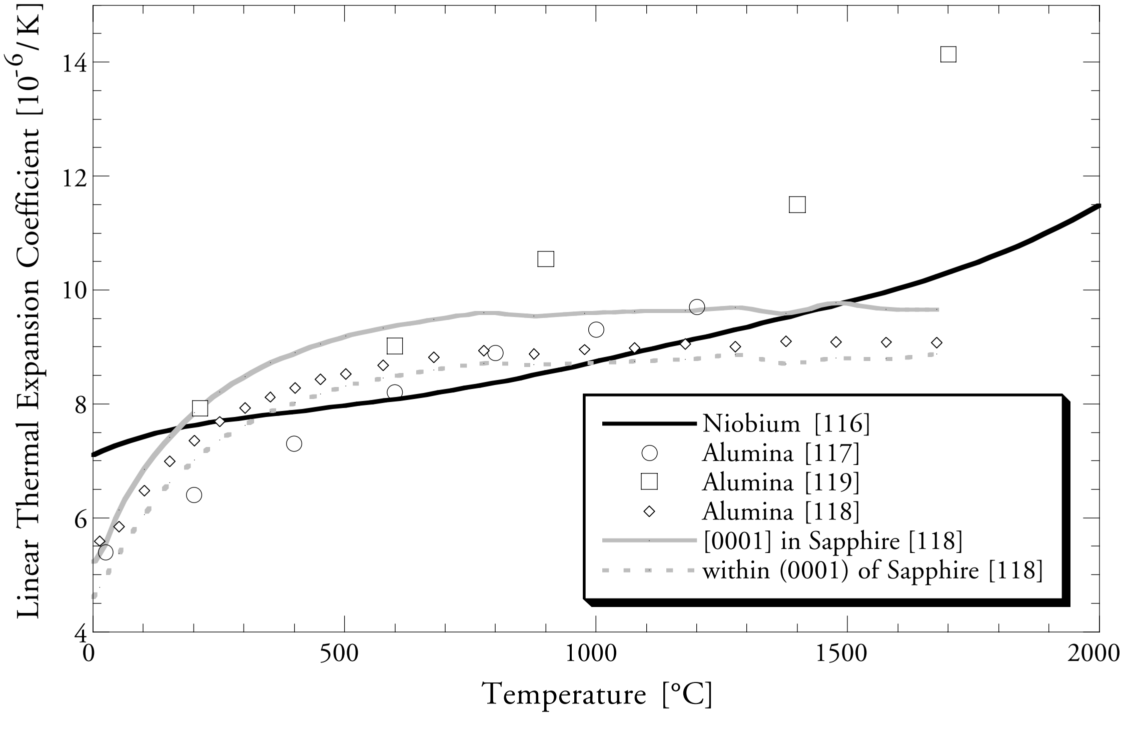

Figure 2.8: Linear thermal expansion coefficient of niobium [116], alumina [117-119], and various metals [116-120] (top). Thermal expansion anisotropy in sapphire compared with isotropic thermal expansion in niobium and polycrystalline alumina (bottom).

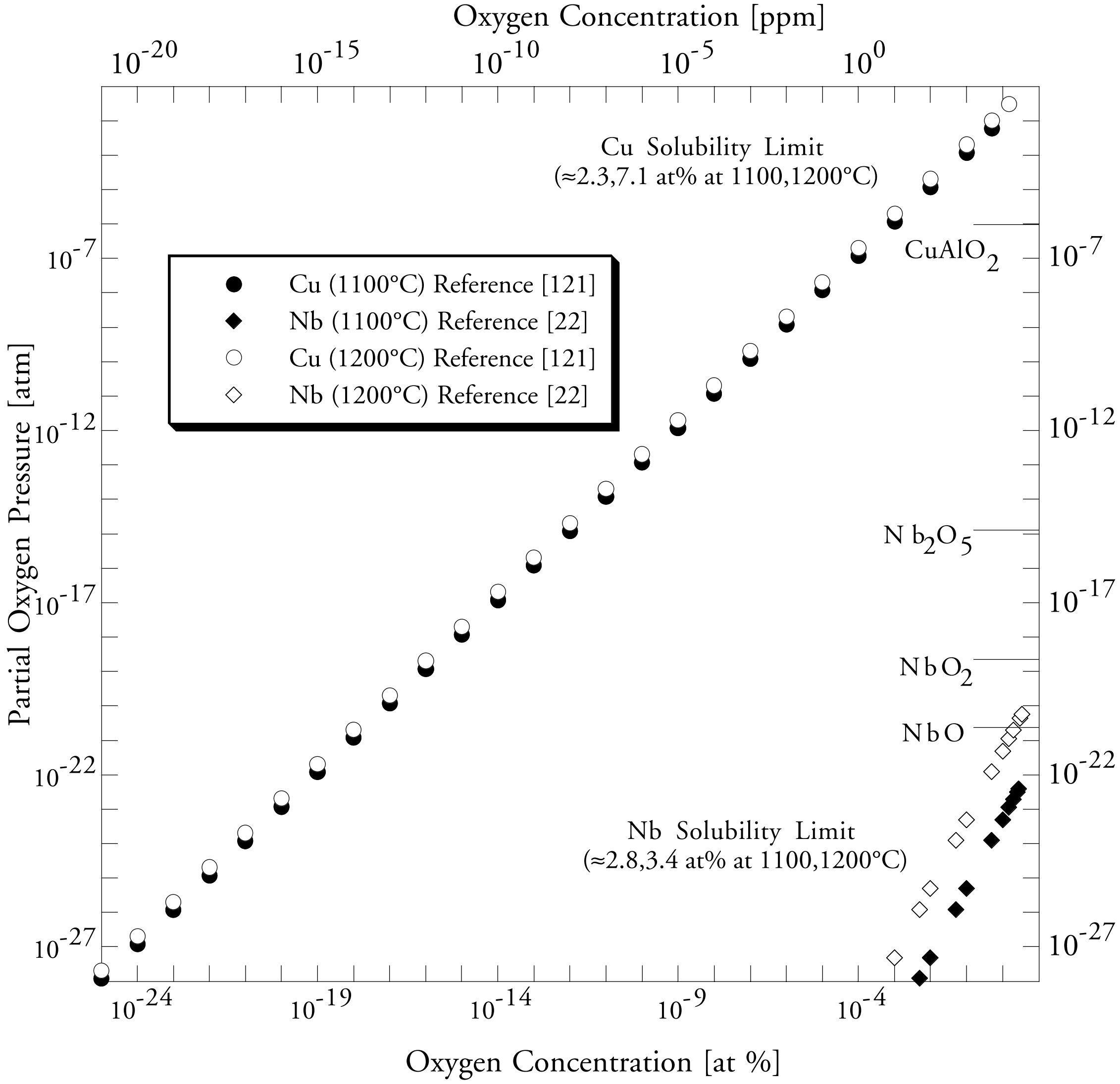

Figure 2.9: Equilibrium oxygen pressure for copper-oxygen [121] and niobium-oxygen [22] solutions. The horizontal lines along the right vertical axis represent the partial oxygen pressures at which the labeled phases become stable at 1150°C.

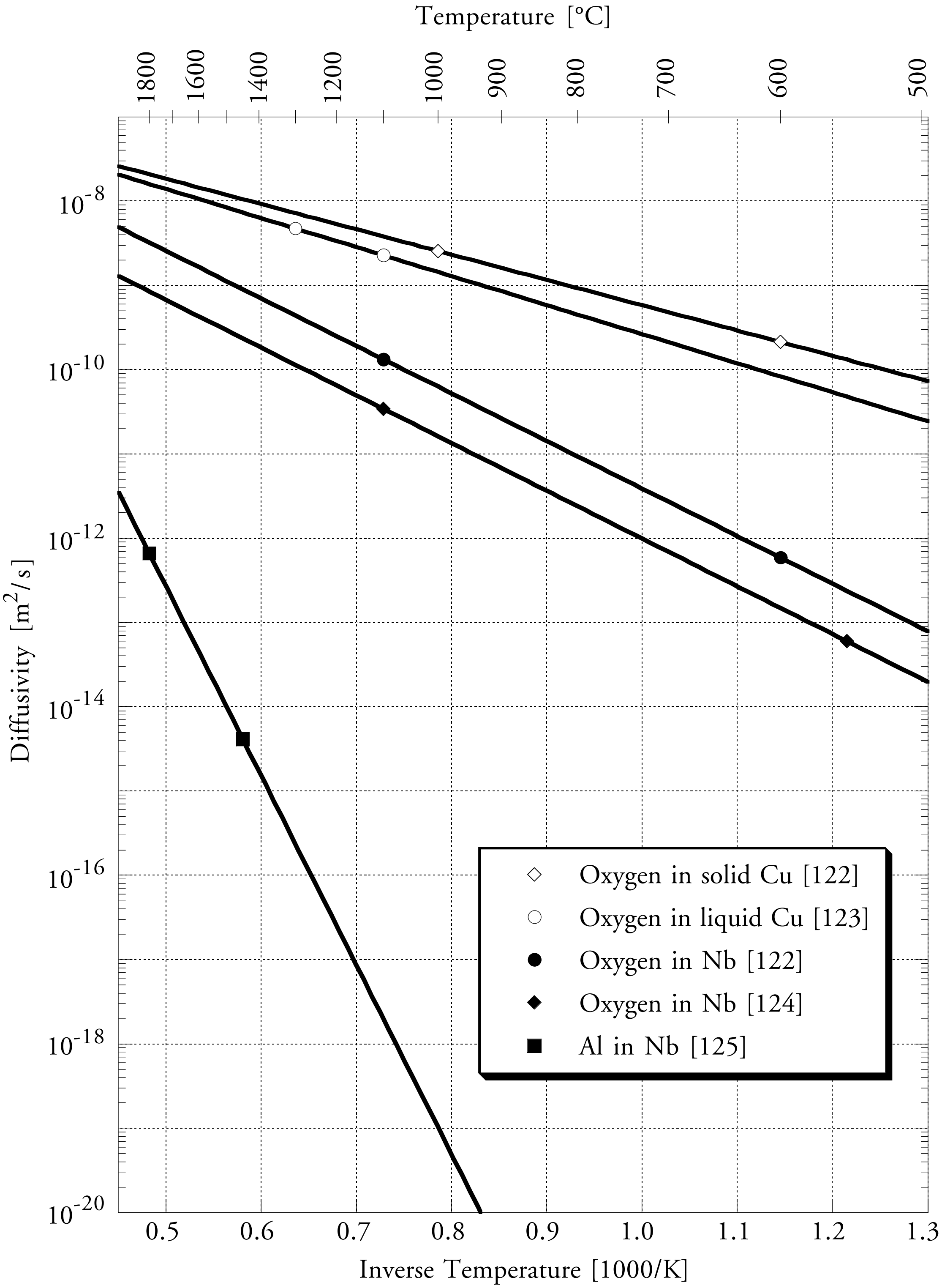

Figure 2.10: Temperature dependence of various diffusivities in copper and niobium. Points on the lines represent the temperature range over which experimental data was recorded.

High Oxygen Pressure (≈10^{-12} atm)

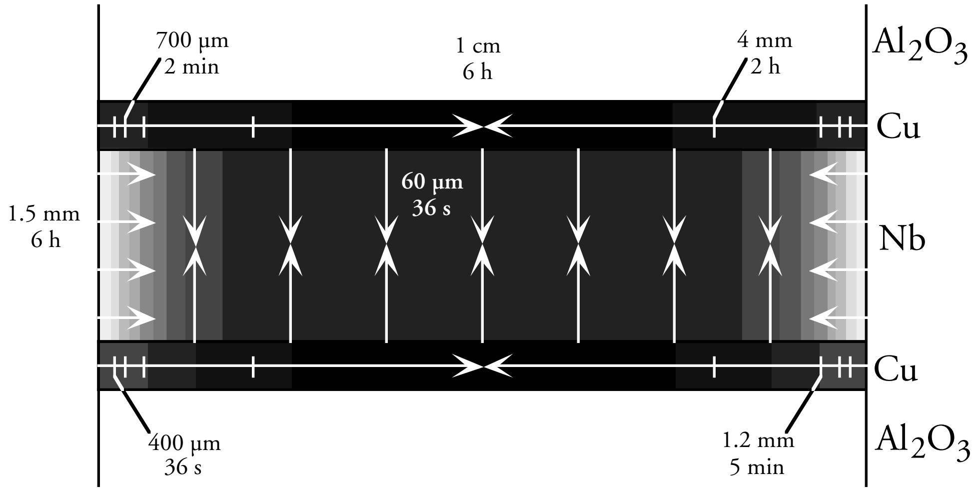

Low Oxygen Pressure (≈10^{-30} atm)

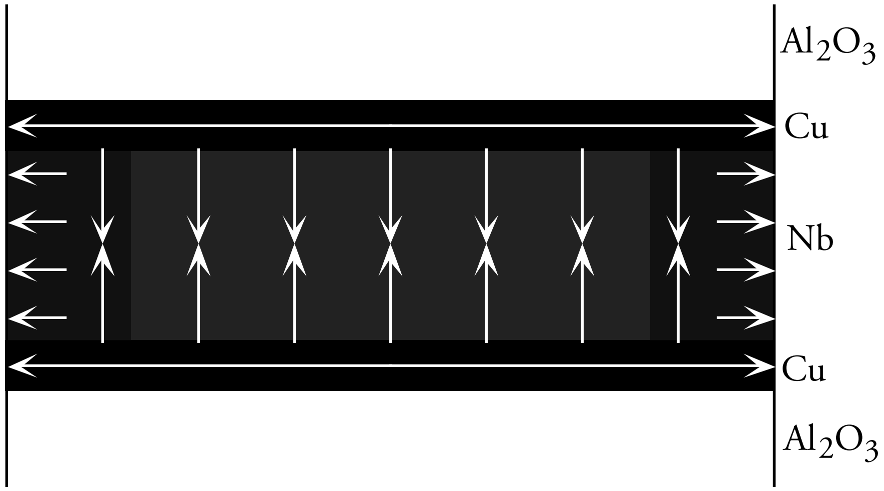

Figure 2.11: Example of oxygen concentration profiles in bonding assemblies during processing (1150°C). Darker regions indicate lower oxygen content.

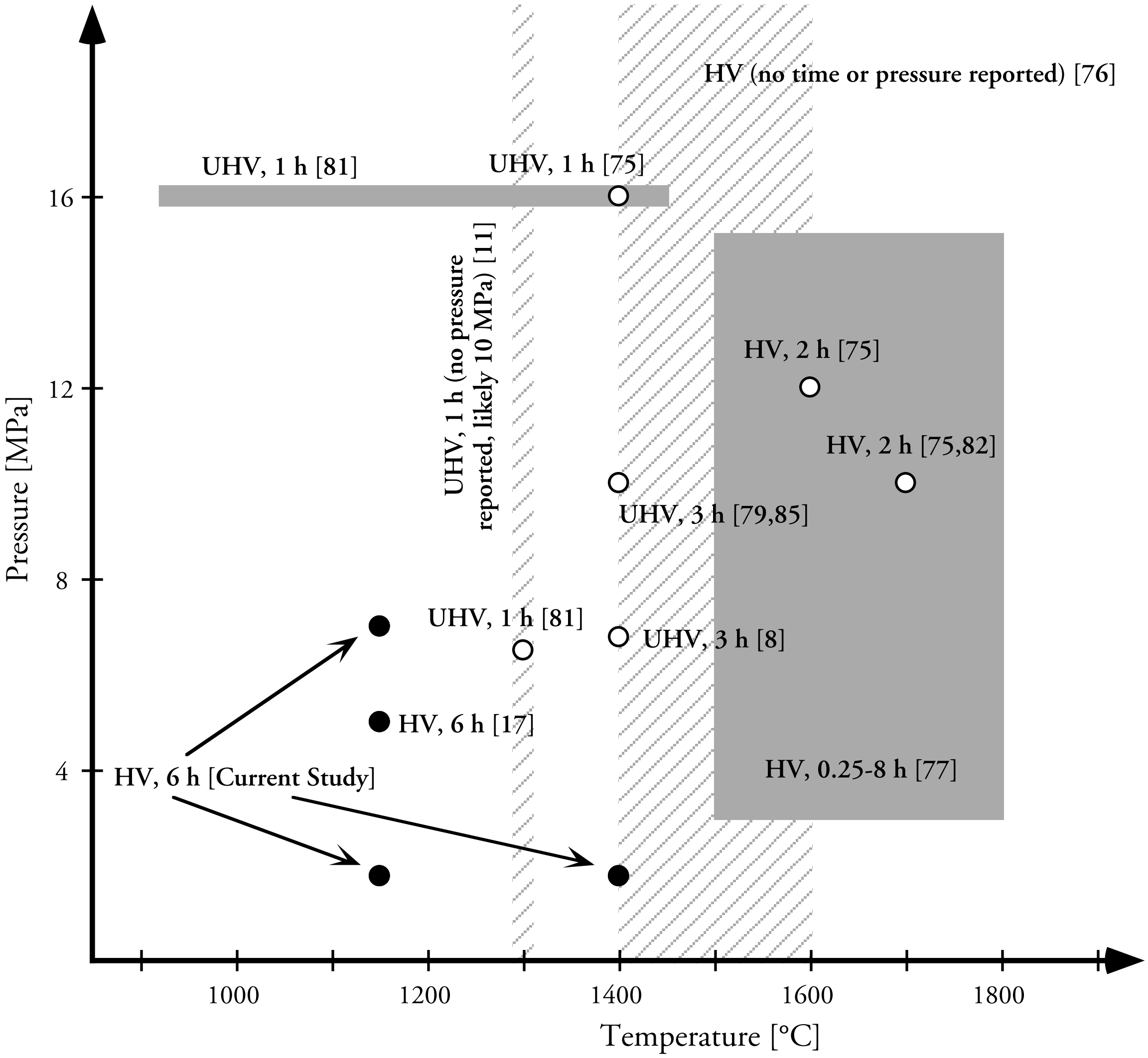

Figure 2.12: Diffusion bonding conditions for several studies focusing on mechanical properties of niobium/aluminum oxide joints. The current study and [17] represent processing conditions for PTLP joining of alumina *via* copper-niobium interlayers.

Chapter 3
Experimental Procedures

3.1 Overview

The partial transient liquid phase (PTLP) joining of ceramics is achieved by coating the ceramic with a relatively thin cladding layer which serves to form a liquid at a relatively low temperature. In principle, thin foils may be used as the cladding layer; however, coatings proved to be the most viable technique for this research. A more refractory and thicker core layer is placed between the coated ceramic surfaces, and the resulting sandwich assembly is processed in a hot press. In the present study, copper was chosen as the cladding layer, and niobium as the core layer to join aluminum oxide. Several joints were processed at ≈1150°C and ≈1400°C with an applied load of approximately 2 MPa. Each joint was then machined into beams for fracture strength measurements. Further characterization of the joints was performed to relate microstructure and processing conditions to the observed strengths.

3.2 Preparation of Aluminum Oxide Substrates

The majority of joints formed used a 99.5% pure, ≥98% dense alumina with a bimodal grain size distribution (the large mode ≈25 μm). This alumina was machined into $19.5\ \mathrm{mm} \times 19.5\ \mathrm{mm} \times 22.5\ \mathrm{mm}$ blocks (Coors Technical Ceramics Co., Oak Ridge, TN). Some joints were also fabricated using ≈0.5 mm thick sapphire windows (Meller Optics Inc., Providence, RI) or 1 inch diameter by 1 inch tall cylindrical sapphire plugs (Insaco Inc., Quakertown, PA). Additionally, one joint was made with high strength alumina blocks $2\ \mathrm{cm} \times 2\ \mathrm{cm} \times 2\ \mathrm{cm}$ in dimension (Nikkato Corp., Osaka, Japan).

The surface of largest area was polished on the polycrystalline alumina substrates with a lapping machine (Logitech, Scotland). These surfaces were first ground flat with a diamond wheel on a surface grinder (K.O. Lee Co., Aberdeen, SD). A more finely ground surface was then prepared by lapping the alumina blocks with 9 μm, 6 μm and/or 3 μm diamond suspension (South Bay Technologies, San Clemente, CA) on a cast-iron plate. Subsequent polishing was achieved by lapping the blocks with 3 μm and/or 1 μm diamond suspension on solder plates. A final polish was achieved by lapping with a colloidal-silica suspension on a polyurethane plate. The polished surface of these substrates is referred to as the joining surface, *i.e.*, the surface to which the copper cladding layer would be applied. The sapphire substrates were joined with the as-received factory polish (optical grade). The polished (0001) surface of sapphire substrates served as the joining surface. A set of two substrates would be used in a joining experiment, and each set of two is referred to with a particular block number (abbreviated BK23 for example). Table 3.1 summarizes the polishing done on each of the blocks.

Prior to loading the substrates into the copper deposition system, they were thoroughly cleaned. Each substrate was cleaned ultrasonically in the following solutions for at least 15 min: liquid detergent and tap water, tap water, distilled water, acetone, and isopropyl alcohol. Following the final ultrasonic cleaning in isopropyl alcohol, the substrates were blown dry with warm air and annealed in air at ≈1000°C for at least 1 h. The sapphire plugs were annealed in air at 1600°C for 20 h in an attempt to heal any microscopic cracks in the material.

3.3 Application of Copper Cladding Layer to Substrates

Copper was deposited on the alumina substrates by evaporation in a high vacuum chamber (Mikros Inc., Portland OR). A commercial copper wire (Consolidated Companies Wire and Associated, Chicago, IL) was cut into pieces ≈0.5 cm and ≈1.5 cm in length. The longer pieces were bent into a tight U-shape configuration. (These geometries served most effective in the loading of the deposition system.) The copper pieces were then cleaned ultrasonically in isopropyl alcohol for at least 15 min. Following ultrasonication, the copper pieces were rinsed in distilled water and bright dipped in a 5:1

nitric acid:distilled water solution for 5-10 s to remove the surface oxide. After bright dipping, each piece of copper was immediately rinsed in distilled water and left to soak in isopropyl alcohol. Just prior to loading the deposition system, the copper pieces were rinsed in nanopure water (minimum resistivity of 18 MΩ•cm) and blown dry with air.

Concurrently, a glass slide and 25 mm diameter glass cover slip were cleaned in isopropyl alcohol and blown dry with warm air. These glass parts would aid in the determination of the copper coating thickness. The cover slip was placed on top of the glass slide in the deposition chamber. The mass gain of the cover slip could be measured as well as the step height of the copper on the glass slide *via* an alpha step profilometer. Of course this technique assumes that the deposition rate of copper on the glass is the same as that on alumina; however, once a thin copper layer is deposited on both substrate types, the deposition rates should match thereafter.

For each joining experiment, the cleaned alumina substrates, glass slide, and glass cover slip were placed on a rotating plate inside the deposition system. The cleaned copper pieces are placed into tungsten wire baskets 3-7 cm above the rotating substrate surfaces. The chamber was evacuated to below 2.5×10^{-9} atm before heating of the tungsten baskets began. During the heating, melting, and evaporation of the copper, the pressure in the deposition chamber typically rose to values in the range from 3×10^{-8} atm to 3×10^{-7} atm. After coating, the chamber pressure quickly fell back below 2.5×10^{-9} atm. The copper coated substrates were left in the vacuum deposition chamber until the niobium core layer was cleaned and ready for sample assembly.

The thicknesses determined by mass gain and profilometry techniques are summarized in Table 3.2. Thickness variations are indeed observed from the profilometry measurements, and coatings tend to be thicker on the portion of the substrate surface closest to the center of the deposition chamber. Hence, the mass gain measurements indicate an effective average coating thickness. Additionally, the results from the mass gain do not necessarily coincide with the midpoint of the range observed by profilometry.

This is partially due to the fact that the thickness variations observed in the profilometry measurements are not necessarily linear with distance over the coated surface and are mostly likely weighted toward the thicker measurements.

The other contributing factor to greater thicknesses determined by the mass gain method is the spattering of small copper droplets onto the substrate surfaces. This typically occurred when the copper initially melted. If a single 1-mm diameter spherical drop of copper were present on the surface of the coated substrates, this would increase the effective coating thickness by ≈1 μm, and 8 such 0.5 mm droplets would be required for the same increase in average coating thickness. No 1 mm droplets were observed on coated substrates; however some substrates may have had one or two droplets as large as 0.5 mm along with several significantly smaller ones. If the copper spatter-droplet density and size distribution is the same on the glass cover slip as for the coated substrates, the mass gain technique is believed to provide the more reliable coating thickness. Clearly the profilometry measurements indicate that thickness inhomogeneities exist for other reasons than copper droplets on the cladding layer.

3.4 Processing of Joints (PTLP Bonding)

A 127 μm thick niobium foil (99.99% pure) foil (Goodfellow Corp., Malvern, PA) was cut to the size of the bonding surface of the aluminum oxide substrates. The cut piece of foil was pressed between two pieces of steel gauge plate to remove any wrinkles in the foil, particularly near the cut edges. Afterwards, the foil was washed with tap water and liquid detergent followed by an ultrasonic cleaning in isopropyl alcohol for at least 15 min. The niobium foil was next rinsed in ethanol followed by a rinse in nanopure water (minimum resistivity of 18 MΩ•cm). Finally, the foil was dried with warm air. After this, the coated substrates were ready to be removed from the deposition chamber and loaded into a hot press with the niobium foil sandwiched between them. The sapphire plugs were oriented such that the top and bottom substrate had approximately the same orientation (±5°).

Joints were processed at ≈1150°C or ≈1400°C for 6 h under high vacuum (total pressure maintained below 1.3×10^{-7} atm). The temperature was increased at 4°C/min, and cooling was done at 2°C/min. Occasionally the heating cycle had to be interrupted in order to maintain the vacuum below 1.3×10^{-7} atm. Table 3.3 summarizes the processing conditions of each joined assembly and notes the temperature and length of time for which any holds in the program occurred above the melting point of copper.

Most joints were processed in a hot press which uses graphite heating elements, graphite shields, and graphite furniture (referred to as the graphite hot press or new hot press). Other joints (BK29, BK35, and BK37) were processed in a hot press with molybdenum heating elements and shields (referred to as the molybdenum hot press or old hot press). The molybdenum hot press uses alumina furniture; however, thin and soft graphite foils (Graphoil®, UCAR Carbon Company Inc., Cleveland, OH) are stacked between alumina blocks to insure uniform contact throughout the stacked column of this hot press. The main differences between the two hot presses are that the molybdenum hot press is only capable of reaching 1200°C, while the graphite hot press can easily reach >1600°C. The old hot press relies on the manual operation of a hydraulic jack to obtain the load during its runs, while the new hot press has an automated hydraulic system which does a much better job of controlling load and/or holding the load fixed during a given run. Additionally, the environment samples are exposed to during processes in the two hot presses are different due to the different heating element, shielding, and furniture materials; in particular, the partial oxygen pressure, p_{O_2}, is of concern.

Although no equipment is available for *in situ* measurements of the gas composition, or even the p_{O_2}, it is expected that for a given temperature, the p_{O_2} in the graphite hot press is considerably less than that in the molybdenum hot press. If it is assumed that the large amount of material in the heating elements and shields is responsible for determining the p_{O_2}, then the p_{O_2} in each furnace can be estimated by considering the oxidation reactions of graphite and molybdenum. In other words, since the elements do not appear substantially oxidized or deteriorated after these furnace runs, the p_{O_2} is likely at a low enough value that oxidation is not favorable, or at least at a value where the kinetics of oxidation are sufficiently slow. The estimated values of p_{O_2} in each hot press at temperatures of interest are listed in Table 3.4, and a detailed discussion of how these estimations are obtained is provided in Appendix I. Table 3.4 also provides values of the p_{O_2} for aluminum/alumina equilibrium, and in some cases (*e.g.*, graphite hot press) this will serve as a more reasonable lower bound to the furnace p_{O_2}. Due to the lack of any actual measurements, the temperature used in these calculations is assumed to be the processing temperature of the joint. Admittingly, it is possible that a cooler part of the furnace elements, shields, or furniture may dominate in controlling the p_{O_2}, thus making it lower than expected.

At room temperature, a $p_{O_2} \approx 10^{-30}$ atm implies that within a sphere of diameter 42 m, only a single oxygen molecule would be found. This volume is at least 75,000 times the volume of the furnace chambers, thus making it highly improbable for a single oxygen molecule to be present in the graphite hot press; or alternatively, an oxygen molecule would only be present for about 0.3 s of the 6 h processing time. In comparison, at 1400°C a $p_{O_2} \approx 10^{-15}$ atm implies that approximately 300,000 oxygen molecules would be present within a sphere of diameter 5 cm. Clearly it is unreasonable to expect that samples processed in the graphite-element hot press are not exposed to a single oxygen molecule since oxygen may penetrate small leaks in the system or permeate through the walls of the furnace. However, it is expected that the great majority of oxygen reacts with the graphite in the furnace; whereas, a significant amount of oxygen can be left unreacted in a furnace with molybdenum elements and shields. Consequently, the numbers reported in Table 3.4 are considered rough estimates and serve to support the qualitative assertion that the p_{O_2} in the graphite hot press is significantly lower than that in the molybdenum hot press. Additionally, the calculated p_{O_2} for molybdenum furnaces implies that niobium should be oxidized. In all likelihood, the amount of oxygen the niobium sees will not be sufficient for extensive oxidation. If a thin niobium oxide (NbO) surface layer were to form, it would likely vaporize or be dissolved in the bulk niobium due to the high diffusivity of oxygen in niobium.

3.5 Machining of Beams and Strength Testing

The as-processed blocks were machined into rectangular beams ≈3 mm by ≈3mm in cross section and 4-5 cm in length. This was accomplished by first slicing the joined block assembly into $40\ \text{mm} \times 20\ \text{mm} \times 3\ \text{mm}$ plates with a diamond saw blade. The plates were numbered in the order in which they were cut from the joint assembly; *i.e.*, plates numbered 1 or 5 typically refer to plates that were near the edges of the joint assembly. One of the ≈2 cm by ≈4 cm surfaces of each plate was ground flat and polished; this surface would become the tension face of the beams in four-point bend testing.

The polishing of the tension face was accomplished by a combination of several different techniques which are summarized in Table 3.5 for each individual joint. Some plates were polished with diamond suspension on a nylon cloth with an automatic polisher (Pedemax, Struers Inc., Westlake, OH). This automatic polisher rotated samples on a spinning plate (300 rpm) to which the nylon cloth was attached. The samples could be applied to the cloth at various pressures numbered 1 through 9, 9 being the largest pressure. Vibratory polishing (Syntron FMC Corporation, Homer City, PA) was accomplished by applying diamond paste and lapping oil to a nylon cloth. The plates were mounted on weighted polishing jigs which rested on the nylon cloth, and the vibratory action of the Syntron caused them to slowly circle the perimeter of the cloth. After surface grinding, there were often striation marks left on plates from the grinding wheel. These marks were difficult to remove by either the Pedemax or Syntrons; however, grinding these plates with diamond paste and lapping oil on a glass plate was effective. Finally some samples were polished by the method used to prepare the bonding surfaces discussed in Section 3.2.

The position of each beam within a plate was recorded and an indexing system developed so that it was possible to identify the location of a particular beam in the bonded assembly. For example, a beam denoted as BK23BM15 would represent the fifth beam cut from the first plate of the joint assembly referred to as BK23 (This would typically be a beam near the corner of the bonded assembly.) Such a system was used so that any potential trends in strength or interfacial microstructure resulting from non-uniform pressure in the hot press, crowning of the bonding surface during lapping, or preferential interaction of edge beams with furnace environments could be observed.

In the interest of measuring the strength of the fabricated joint, it is useful to have a reasonably strong ceramic that does not fail preferentially to the joint (or metal/ceramic interface). On the other hand, bonded assemblies which fail in the ceramic indicate that the joint is sufficiently strong for joining that particular material. In light of this, a few precautions are taken to avoid ceramic failures at relatively low stresses and to reduce scatter in the data. First the tension surface of the plates was polished in order to reduce the flaw size on this surface (see Table 3.5). Additionally, after cutting each plate into beams, the two long edges of the tension face were bevelled on a 6 μm grinding plate to reduce stresses at beam edges. Subsequently, beams were cleaned with acetone, soap and water, and isopropyl alcohol. Just prior to mechanical testing, the beams were cleaned ultrasonically in a denatured HPLC grade ethanol (Aldrich Chemical Company Inc., Milwaukee, WI) and blown dry with warm air. This process primarily serves to remove water trapped in the pores of the ceramic.

After blow drying the ethanol-treated beams with air, the cross-sectional dimensions of the beam are measured with a micrometer (±0.01 mm). Fracture strengths were measured at room temperature and elevated temperatures. For the room-temperature tests, a beam is loaded into a four-point bend testing jig for which the inner span of the load application points is 9 mm, and the outer span is 25 mm. A flat cross-head is then lowered until it nearly contacts a steel sphere which rests on top of the jig. The cross-head is then lowered at 50 μm/min until it contacts the steel sphere, displaces, and fractures the joint specimen. The load is measured with a 100 kg load cell and is sent to a chart recorder which plots the load versus time (displacement).

The high-temperature bend tests are conducted in a similar manner. Beams are loaded into a graphite testing jig (9 mm inner span, 25 mm outer span) which fits between a graphite ram assembly in a tungsten heating element furnace. The furnace chamber is evacuated and backfilled with argon which flows during heating, mechanical testing, and cooling of the sample. Typically, the specimen is heated to and cooled from the testing temperature at 10°C/min and 30°C/min respectively. The system is held at the desired test temperature for 15-30 min so that thermal equilibrium is achieved throughout the sample. The system is then displaced at ≈1 μm/s and the load versus displacement data is exported to a computer data acquisition system.

In measuring the fracture strength of beams, standard static loading techniques are used to calculate the fracture stress, *i.e.*, no attempts are made to account for residual stresses due to thermal or modulus misfits. These measured values are those that would primarily be of interest for practical applications. A derivation of the formula used is provided in Appendix III. Additionally, the failure mode of each beam is characterized by visual inspection according to the abbreviations presented in Table 3.6.

3.6 Additional Processing (Post-Bonding Anneals)

In order to investigate how beam strength and microstructure are affected by prolonged exposure to elevated temperatures and different p_{O_2}, two different furnaces were used. Beams which had been bevelled and cleaned were placed inside an alumina crucible. Anneals were conducted at 1000°C, 1200°C, and 1400°C for various lengths of time in gettered argon and high vacuum. The temperature was ramped at 30°C/min for both heating and cooling in these anneals (some exceptions are noted in the following chapter).

The argon furnace has molybdenum mesh heating elements and molybdenum shields, and the samples were placed in the hot zone of the furnace on top of a stack of alumina. The argon was gettered by letting it flow through two tube furnaces (≈10 mL/min). The first tube furnace is held at ≈40°C and contains anhydrous calcium sulfate (Drierite, W.A. Hammond Drierite Co., Xenia, OH). The Drierite removes excess water vapor from the argon. Just prior to entering the furnace, the argon passes through a second tube furnace with titanium and zirconium chips which are held at ≈800°C. The titanium and zirconium chips react with excess oxygen (and nitrogen [126]) in the argon, and the methods discussed in Appendix I predict a $p_{O_2} \approx 10^{-44}$ atm at 800°C. Additionally, as the argon passes to cooler parts of the tube furnace, the p_{O_2} should be reduced further; however, for reasons stated in Section 3.4, a $p_{O_2} \approx 10^{-44}$ atm implies not even a single oxygen molecule would be present in the furnace. Thus, the actual p_{O_2} may even be greater than that in the graphite hot press since no gettering materials are local to the sample. Additionally, a $p_{O_2} \approx 10^{-44}$ atm would favor the reduction of alumina; however, the extent of any such reaction would be undetectable. The values of the p_{O_2} for aluminum/alumina equilibrium given in Table 3.4 thus serve as a more reasonable lower bound for the furnace p_{O_2}. At 1000°C, a single gaseous molecule occupying a sphere of 5 cm diameter exerts a partial pressure of $\approx 3\times10^{-21}$ atm, implying that this may be a more reasonable estimate of the p_{O_2} in the furnace. Again the p_{O_2} calculation is made to qualitatively certify that the ambient environment contains minimal oxygen in comparison to other furnaces.

The vacuum furnace has tungsten mesh elements and molybdenum shields. During the high vacuum anneals, the pressure was typically lower than 7×10^{-8} atm during heating and fell below 1×10^{-8} atm after a short time at the annealing temperature. For longer anneals, the total pressure was in the 10^{-10} atm range for a significant portion of the anneal.

Table 3.4 gives estimated values of the p_{O_2} for anneals in high vacuum at 1000°C, 1200°C, and 1400°C using the procedure discussed in Appendix I.

Table 3.1: **Summary of Polishing Done on the Joining Surface of Aluminum Oxide Substrates**

Block	Substrate	Polishing of Joining Surface
BK23	Coors alumina	• 3 μm diamond (cast iron plate) • 1 μm diamond (solder plate) • colloidal silica (poly-urethane plate)
BK24	Coors alumina	• 3 μm diamond (solder plate, 12 h) • 1 μm diamond (solder plate, 8.5 h) • colloidal silica (poly-urethane plate, 5.5 h)
BK26	Coors alumina	• 3 μm diamond (solder plate, 23 h) • 1 μm diaomnd (solder plate, 11.5 h) • colloidal silica (poly-urethane plate, 9 h)
BK27	Coors alumina	Polished simultaneously with BK26
BK27s	(0001) sapphire window	As received factory polish
BK28	(0001) sapphire window	As received factory polish
BK29†	Coors alumina	• 6 μm diamond (cast iron plate, 1-2 h) • 3 μm diamond (solder plate, 1-2 h) • 1 μm diamond (solder plate, 1-2 h) • colloidal silica (poly-urethane plate, 1-2 h)
BK30†	Coors alumina	Polished simultaneously with BK29
BK31	(0001) sapphire plug	As received factory polish
BK33†	high strength alumina	• 6 μm diamond (cast iron plate, 1-2 h) • 3 μm diamond (solder plate, 1-2 h) • 1 μm diamond (solder plate, 1-2 h) • colloidal silica (poly-urethane plate, 1-2 h)
BK34	(0001) sapphire window	As received factory polish
BK35	(0001) sapphire window	As received factory polish
BK36	(0001) sapphire window	As received factory polish
BK37	(0001) sapphire window	As received factory polish

†For these blocks, the Logitech polishing plates were recently machined flat. As a result, the times required to complete each polishing step are shorter. Although the roughness (smoothness or finish quality) of each final polish is believed to be the same as blocks 23 through 27, the crowning is expected to be more severe in blocks 23 through 27. This has been verified by comparison with an optical inferomograph from recently polished blocks to those polished in the past [42].

Table 3.2: **Summary of Copper Coating Thickness for Individual Blocks**

Joint	Substrate	Cu Coating Thickness (Mass Gain) [±0.1 μm]	Cu Coating Thickness (Alphastep) [μm]
BK23†	Coors alumina	3.9	2.84-5.07
BK24†	Coors alumina	3.8	3.11-4.29
BK26	Coors alumina	2.9	≈2‡
BK27	Coors alumina	≈3	≈4‡
BK27s	(0001) sapphire window		1.73-2.44
BK28	(0001) sapphire window	3.1	2.41-3.78
BK29	Coors alumina	3.0	2.09-3.13
BK30	Coors alumina	3.0	2.09-3.13
BK31*	(0001) sapphire plug	3.9	2.56-4.48
BK33	high strength alumina	2.9	2.27-3.35
BK34	(0001) sapphire window		
BK35	(0001) sapphire window		
BK36	(0001) sapphire window		
BK37	(0001) sapphire window		

†A significantly greater amount (mass) of copper wire was loaded in the tungsten baskets for these experiements.

‡Large portions of the coating on the glass slide had peeled off making systematic measurements impossible.

*This greater copper thickness on this joint may be due to the fact that the sapphire plugs are ≈5 mm taller than the alumina blocks, and therefore were closer to the copper source during coating.

Table 3.3: Summary of Processing Conditions for Each Joint

Joint	Substrate	Hot Press	Joining Temperature [°C]	Applied Load [MPa]	Holds [°C-min]
BK23	Coors alumina	graphite	1394	2.2	none
BK24	Coors alumina	graphite	1150	2.2	none
BK26	Coors alumina	graphite	1394	2.2	1199-30
BK27	Coors alumina	graphite	1394	2.2	1169-56
BK27s	(0001) sapphire window	graphite	1394	2.9	1108-96 1218-139 1329-111
BK28	(0001) sapphire window	graphite	1382	2.2	none
BK29	Coors alumina	molybdenum	1150	6.8-8.2	none
BK30	Coors alumina	graphite	1144	2.2	none
BK31	(0001) sapphire plug	graphite	1382	1.9	1153-30 1288-60 1369-15
BK33	high strength alumina	graphite	1382	2.3	none
BK34	(0001) sapphire window	graphite	1150	5.0	none
BK35	(0001) sapphire window	molybdenum	1150	5.0	none
BK36	(0001) sapphire window	graphite	1150	1.6	none
BK37	(0001) sapphire window	molybdenum	1150	5.0-13	none

Table 3.4 Estimates of Partial Oxygen Pressure in Graphite, Molybdenum, and Tungsten Furnaces

Material Controlling Furnace Oxygen Potential	Temperature [°C]	Partial Oxygen Pressure [atm]
graphite	1150	$\approx 10^{-32}$
	1400	$\approx 10^{-30}$
molybdenum	1000	8×10^{-16}
	1150	2×10^{-13}
	1200	9×10^{-13}
	1400	2×10^{-10}
tungsten	1000	3×10^{-15}
	1200	4×10^{-12}
	1400	8×10^{-10}
aluminum/alumina	1000	2×10^{-35}
	1150	1×10^{-30}
	1200	4×10^{-29}
	1400	2×10^{-24}

Table 3.5: **Summary of Polishing Steps for the Tension Face of Plates**

Joint	Substrate	Description
BK23†	Coors alumina	• 15 μm diamond, Pedemax, 15 min at each of six successively lighter pressures (9,7,5,3,2,1) • 3 μm diamond, Pedemax, 15 min at each of six successively lighter pressures (6,5,4,3,2,1)
BK24‡	Coors alumina	• 15 μm diamond, Pedemax, 10 h total at various pressures. • 3 μm diamond, Pedemax, 15 min at each of six successively lighter pressures (6,5,4,3,2,1) • 15 μm diamond, Pedemax, 15 min at each of six successively lighter pressures (9,7,5,3,2,1) • 3 μm diamond, Pedemax, 15 min at each of six successively lighter pressures (6,5,4,3,2,1) • 15 μm diamond, Pedemax, 24 h total at six successively lighter pressures (6,5,4,3,2,1) • 3 μm diamond, Pedemax, 20 min at each of six successively lighter pressures (6,5,4,3,2,1)
BK26	Coors alumina	6 μm and 1 μm diamond paste, Sintrons
BK27	Coors alumina	• ground with 15 μm diamond paste on glass plate • 15 μm, 6 μm, and 1 μm diamond paste on Sintrons
BK29	Coors alumina	• 15 μm diamond paste on Sintrons (43.5 h) • ground with 15 μm diamond paste on glass plate • 6 μm (190 h), 15 μm (48 h), 6 μm (192 h), and 1 μm (115 h) diamond paste on Sintrons
BK30	Coors alumina	Polished simultaneously with BK29 plates
BK31*	(0001) sapphire plug	• 9 μm diamond suspension (cast iron plate, 1-2 h) • 3 μm diamond suspension (cast iron plate, 1-2 h) • 3 μm diamond suspension (solder plate, 1-2 h) • 1 μm diamond suspension (solder plate, 1-2 h) • colloidal silica (poly-urethane plate, 1-2 h)
BK33	high strength alumina	as BK31 except only the tension face was polished

†Additional vibratory polishing was done on plates 4 and 6 from BK23. This consisted of 79 h with 15 μm diamond paste, 63 h with 6 μm diamond paste, and 52.5 h with 1 μm diamond paste.

‡Significantly longer times were required to polish BK24 in comparison to BK23 in order to remove striation marks from the surface grinder. Only plates 2, 3, and 6 from BK24 were polished with this procedure. Plates 1 and 5 broke during surface grinding, and plate 4 was polished on the Sintrons for 50 h with 15 μm diamond paste and for 65 h with 6 μm diamond paste.

*Three sides of the beams from this block were polished; the compression faces were left unpolished.

Table 3.6: Abbreviations for Fracture Path Characterization

Abbreviation	**Description**
CFF	Beam failed entirely in the ceramic far from the joining layer
CFC	Beam failed entirely in the ceramic near the joining layer (<1 mm)
CF to C/I	Failure initiated in the ceramic (near the joining layer); however, part of the interlayer was exposed
CF to IF	Failure initiated in the ceramic (near the joining layer), but deviated to the interface
I/C to IF	The tension face of the beam exhibited both interfacial and ceramic failure; however, failure ultimately proceeded along the interface. It is difficult to know whether such a failure actually initiates at the interface or in the ceramic. From modulus misfit mechanics, one would expect that the failure would have had to initiate in the ceramic; however, in the interest of providing a conservative estimate on the frequency of ceramic failure, these beams are treated generally as interfacial failures.
IF	Beam failed entirely along the metal/ceramic interface
ID	Some peeling of the joining layer from the ceramic was observed.
ILF	Interlayer failure. A portion of the interlayer could be observed on both pieces of the fractured specimen

Chapter 4
Results and Discussion

4.1 Block 24 - A Joint Processed at 1150°C (2.2 MPa) in the Graphite Hot Press

A joint (BK24) was processed at 1150°C with an applied load of 2.2 MPa in the new hot press to investigate whether the strength characteristics reported by Shalz *et al.* [17] could be improved upon. It was initially thought that better surface preparation equipment (*i.e.*, the Logitech) could potentially reduce the flaw size at the metal/ceramic interface, promoting failure by another mode (*i.e.*, in the ceramic) or by the same mode at higher stresses. Additionally, the ability of the new hot press to apply a lower minimum load (Shalz *et al.* used a load of 5.1 MPa in the old hot press) would enable conditions closer to those of ideal PTLP processing to be used.

Instead of improving the strength, a dramatic decrease in strength was observed (average strength, $\bar{\sigma}_F = 78 \pm 22$ MPa compared to $\bar{\sigma}_F = 181 \pm 45$ MPa obtained by Shalz *et al.* [17]). Table 4.1 contains the strengths of the beams tested from BK24 and notes their failure mode according to the abbreviations described in Table 3.6. Each box in Table 4.1 corresponds to a beam labeled according to the indexing system discussed in Section 3.5; for example, the box in the lower right corner represents data for BK24BM65. The mechanical reliability of BK24 was so poor that three of the plates broke as a result of handling and machining. When such failures occur, it is difficult to estimate the failure strength; however, since other plates and beams survived the same handling and machining, these plates (1, 2, and 5) are likely to be substantially weaker than the weakest beams (perhaps <10 MPa). Furthermore, as in the case of plate 5 of BK24, two plates from other blocks have been dropped, but remained intact, and no substantial deviation from data obtained for more carefully handled specimens is observed.

Figure 4.1 is a plot of the failure probability against fracture strength for the beams tested from BK24 compared with data from Shalz *et al.* [17] and strength data on the similarly prepared beams of bulk Coors alumina measured by Sugar [127] and Dalgleish [128]. Each data set can generally be fit to a power law ($P_F = a\sigma_F^b$, where P_F is the failure probability and a and b are constant fitting parameters) dependence. This type of curve fit appears as a straight line in a plot for which both axes have a logarithmic scale. Steeply sloped lines represent more tightly bounded data, while lines with lower slopes imply more scattered data. A horizontal line at 50% will intersect each data set near its average strength value. Clearly the results from BK24 represent the lowest strengths with a relatively larger degree of scatter. If quantitative data could be obtained for the plates (plates 1,2 and 5) which failed, the average strength would likely be reduced, and the scatter would increase further.

Figure 4.2 illustrates the ceramic and metal side of a fracture surface representative of BK24 (BK24BM65, $\sigma_F = 65$ MPa). The micrograph is taken in a region of the beam under tension, thus illustrating a microstructure characteristic of failure. The imprint of the alumina grains on the metal side indicates intimate metal/ceramic contact is achieved over the majority of the interface. A continuously connected copper film also covers the majority of the interface. Some of the stronger beams (83-100 MPa) exhibited marginally less copper coverage at the interface; however, the area coverage is still above ≈50%. Clearly such a microstructure is unsuitable for high-temperature application.

Based on the results of Shalz *et al.* [17], one would not expect a high area fraction of copper at the interface to necessarily be detrimental to room-temperature strength. Shalz *et al.* frequently observed (by adjusting the focus on an optical microscope) an interfacial copper phase below alumina grains which were "pulled-out" from the ceramic upon fracture. The association of the interfacial copper with ceramic pullout suggests that the copper/alumina interface is one of the stronger parts of the joint, or at least more fracture resistant. Based on the discussion in Section 2.4 (see also Figure 2.9) one would expect the copper phase to contain very little oxygen regardless of which hot press was used to process the joints. Thus, the oxygen concentration in copper for each experiment should be similar, likely below levels (≈60 ppm) required to improve the copper/alumina interfacial fracture energy as reported by Rühle *et al.* [110]; and certainly well below levels characteristic of the strong interfaces produced by eutectic bonding [64,115] or diffusion bonding under high ambient oxygen pressure [107,129].

Despite the anticipated chemical similarities in the copper phase, the interfacial morphologies observed in the two experiments are vastly different. Shalz *et al.* [17] report that the copper phase was broken-up into isolated particles, rather than appearing as a continuous film. These different morphologies may influence the mechanics and fracture resistance of the interface. A thin "pancaked" layer of copper at the interface may be highly constrained due to the thermal misfits between alumina and copper and niobium and copper. Such constraint may promote interfacial failure. Smaller isolated copper particles may more easily deform during slow (2°C/min) cooling, thus providing a locally tougher interface and promoting a crack into the ceramic.

Additional processing (see Table 4.1) on Plate 4 of BK24†, using the graphite hot press as a simple annealing furnace (≈1400°C, no applied load), resulted in a marked increase in strength ($\overline{\sigma}_F = 221 \pm 62$ MPa) relative to the rest of the joint. Figure 4.3 illustrates the microstructure of BK24BM42 near the tension face. The copper film appears to be much more broken-up, and an imprint of the alumina grains is still present. Unlike the other joints (plates 1-3, 5, and 6), substantial portions of the copper phase have remained attached to the ceramic side of the fracture surface. The narrow strips of copper reflect copper lying in niobium grain boundary grooves. The blurry region in the lower left corner of the metal side image (Figure 4.3) indicates ceramic pullout has occurred. The smoothly textured shape at the center of the metal side image represents a small unbonded region of niobium. A faint line tracing the perimeter of such unbonded regions

---

† The results from this particular plate will be referred to several times throughout this chapter. It is worthwhile for the reader to make a mental note of the sample identification numbers and post-bonding treatment done.

can be seen on the ceramic-side image. Weaker beams from this plate, *e.g.*, BK24BM43 ($\sigma_F = 143$ MPa) and BK24BM45 ($\sigma_F = 163$ MPa) exhibited a much larger population of unbonded flaws, which were larger in size as well. This post-bonding anneal suggests that applied pressure is not necessary to obtain reasonably strong joints; however, a small applied load may have eliminated the large unbonded regions characteristic of the two weaker beams. Processing temperature appears to have a pronounced effect on the resulting interfacial microstructure. A microstructure characteristic of that observed in this re-annealed plate may retain substantial strength at high temperature.

4.2 Blocks 29 and 30 - Joints Processed Simultaneously at 1150°C

In order to further investigate the cause for the differences between the behavior of BK24 and the joint fabricated by Shalz *et al.* [17], two joints (BK29 and BK30) were identically prepared until hot pressing. Ideally, the only difference between the two joints is the hot press environment and the applied load during bonding (see Table 3.3). Tables 4.2 and 4.3 contain the data and failure mode for each of the beams in these joints. Although the difference in average strength (205±49 MPa for BK29 versus 173±73 MPa for BK30) is relatively small compared to that between BK24 and the results of Shalz *et al.*, the large degree of scatter obtained from the joint made in the new hot press (BK30), and the relative rankings of the two strengths are consistent. Figure 4.4 is a failure probability plot comparing the data for Blocks 24, 29, and 30, as well as the data from Shalz *et al.* and the appropriate reference alumina strength statistics.

Figure 4.5 illustrates a series of optical micrographs of the metal side of fracture surfaces for progressively stronger beams from the joint processed in the molybdenum hot press at 1150°C and ≈7.5 MPa (BK29). The images are taken near the tension edge of the beam, in regions most extensively covered with copper. A similar series is produced in Figure 4.6 for the joint processed in the graphite hot press at 1150°C and 2.2 MPa (BK30). Although there is a reasonable amount of variability in the extent of copper film break-up in each joint; it appears that this break-up is considerably more complete and homogeneous in BK29 (molybdenum hot press); consistent with more tightly bounded strength statistics. The more extensive variability in the interfacial microstructure of BK30 (graphite hot press) is consistent with the relatively large scatter in strength (*i.e.*, a few lingering beams with low strength). Within each joint individually, there also appears to be a correlation between joint strength and the degree of copper film continuity at the interface. In comparing interfaces of similar strength (see for example Figures 4.5b and 4.6b), it appears that joints fabricated in the graphite hot press are more extensively covered with copper at the interface; however, the weakest of beams (BK30) are essentially completely covered with copper at the interface (Figure 4.6a). Similarly, comparing joints with similar extent of copper film break-up from each hot press (see for example Figures 4.5a and 4.6c), implies that those processed in the graphite hot press are stronger. Based on these observations, one would conclude that either the applied load and/or ambient p_{O_2} is instrumental in determining the interfacial microstructure and resulting joint strength.

Unfortunately it would be extremely difficult to examine the interfaces of the generally stronger beams which failed in the ceramic. Sugar and Marks [130] have produced c-axis sapphire window joints under various conditions (molybdenum and graphite hot presses at different applied loads) at 1150°C in an attempt to replicate the interfacial microstructures observed in similarly processed alumina joints. Two joints processed simultaneously (BK34 and BK35, see Table 3.3) at 5.0 MPa generally exhibited substantial variability in copper film continuity or extent of break-up; however, the two samples generally appeared similar, suggesting p_{O_2} has little to do with the morphology of the copper film. However, p_{O_2} could have pronounced effects on interfacial adhesion. Figure 4.7 illustrates some of the typical morphologies observed within the sample produced in the graphite hot press (1150°C, 5.0 MPa).

By reducing the bonding pressure to 1.6 MPa in the graphite hot press (BK36), the variability in microstructure (copper coverage) was somewhat larger, and on average, a higher area fraction of copper was visible (see Figure 4.8). Very few regions similar to Figure 4.8a were observed in samples produced at higher pressure, except near the perimeter of the joint, where the copper is preferentially displaced due to the applied load. Finally, a sapphire joint (BK37) processed in the old hot press with an applied load reaching 13 MPa, appeared to exhibit the most extensive copper film break-up of any of this set of samples (Blocks 34-37). Contrary to conventional PTLP bonding theory, these studies along with the strength results from Blocks 29 and 30 seem to indicate that applied load plays an important role in determining interfacial microstructure and joint quality. The interfacial microstructural evolution of joints will be discussed further in the last section of this chapter.

At this stage, it is difficult to determine whether or not ambient p_{O_2} influences joint strength. As already discussed, one would expect the composition of the copper/alumina interfaces to be similar regardless of the hot press used. Portions of copper remain adhered to the ceramic side of failures in both joints, and do so in a similar fashion (see Figures 4.9 and 4.10), *i.e.*, in regions where the phase is broken-up. This additionally supports the expectation that the chemistry of each copper phase is similar (at least from a mechanics perspective). Although the ambient p_{O_2} will not influence the composition of the copper phase, it can influence the niobium oxygen content. Ideally, the ambient will only affect the niobium oxygen content near the joint perimeter (within ≈1.5 mm). However, the interior oxygen content can be changed during the heating cycle, prior to the melting of the copper. Small copper droplets which formed on the alumina during the copper coating procedure, or small gaps that are not closed due to non-uniform foil thickness and/or flatness will prevent the niobium foil from being sealed from the ambient. Consequently, a joint processed in the old hot press may contain more dissolved oxygen.

Additional oxygen in the niobium may decrease the fracture resistance of these niobium/alumina interfaces. Thus relatively lower strengths are observed for beams processed in the old hot press which exhibit comparable niobium/alumina interfacial area to those processed in the new hot press. Such effects of oxygen would be small compared to the overall ability of the copper film to break-up, and would be contrary to the findings of Elssner *et al.* [97] who determined that the fracture toughness of niobium/alumina joints was essentially independent of niobium oxygen (and other dissolved gases) content. Certainly producing a joint under higher applied load in the graphite hot press would be necessary to conclusively evaluate whether or not ambient furnace environment influences joint strength.

It is worth noting that the interfacial microstructure observed by Shalz *et al.* [17] is more like that observed in a sample (plate 4 of BK24) re-annealed at 1400°C in the graphite hot press (Figure 4.3) than any of the joints processed at 1150°C (BK29 or BK30 in particular) [3,17]. The similarity of these two microstructures suggests that joints processed at 1150°C may be weaker than those annealed at 1400°C due to the greater ambient p_{O_2} in the old hot press, or possibly more extensive interfacial segregation of impurities at lower temperatures. However, extended anneals of joints (processed at 1400°C) in vacuum at 1000°C produce no obvious strength reduction (this will be discussed further in Section 4.4). The slight increase in strength of BK29 relative to the results of Shalz *et al.* (see Figure 4.4) is probably due to better surface preparation techniques employed and/or the slightly higher applied load during bonding. The reasons for these differences have not been determined. The strength difference between Blocks 24 and 30 (Figure 4.4) may be attributed to the difference in copper coating thickness (see Table 3.2). Inhomogeneities in copper and niobium foil thickness may be responsible for the ability of the copper film to preferentially break-up in certain regions during processing; perhaps those exhibiting ceramic failure. The post-bonding anneal executed for plate 4 of BK24 indicates that in order to consistently obtain a favorable copper/niobium microstructure, higher processing temperatures are required.

4.3 Blocks 23, 26, and 27 - Joints Processed at ≈1400°C in the Graphite Hot Press

The strength increase due to a 1400°C post-bonding anneal (plate 4 of BK24) suggests that processing at higher temperatures will form a favorable copper/niobium two-phase microstructure and stronger joints. Blocks 23, 26, and 27 were processed under such conditions, and high beam strengths with a relatively small degree of scatter were obtained ($\overline{\sigma}_F = 241 \pm 18$ MPa for 42 beams tested). Figure 4.11 compares the strength results of these joints to those processed at 1150°C. With many failures in the ceramic, the strength statistics nearly match those of the bulk alumina, suggesting the joint can be used for joining this alumina without significantly reducing the ideal assembly strength (*i.e.*, that of the bulk Coors alumina).

Shalz *et al.* [17] observed that extensive polishing on plates may have caused a strength reduction; however, it was not certain whether these lower strengths were a result of additional polishing, or were characteristic of interior beams in the joining assembly. No significant failure variations (strength or mode) in joints processed at 1400°C were apparent due to additional polishing on plates 4 and 6 of BK23 (see Table 4.4). Additionally, the plates from blocks 29 and 30 were polished for nearly 600 h (see Table 3.5), and if anything, the strength statistics for BK29 imply the joint is slightly stronger than that fabricated by Shalz *et al.* [17].

Generally, it can be seen that failures initiating in the ceramic near (<1 mm) the interface (designated CF to IF, CFC in Figure 4.11) are slightly biased toward lower stresses (ranging from 190 MPa to 258 MPa, $\overline{\sigma}_F = 237 \pm 24$ MPa) than other ceramic failures (designated CFF, ranging from 220 MPa to 274 MPa, $\overline{\sigma}_F = 245 \pm 15$ MPa) in Figure 4.9. Such a result may be anticipated from modulus misfit effects. If the critical flaw from which failure initiates is in close proximity to the metal/ceramic interface, modulus misfit effects will reduce the globablly applied load required to induce failure. Clearly such an effect is very subtle and verifying this effect by testing specimens with controlled (pre-machined) size flaws in both locations (far from and near the interlayer) would be more instructive.

Ceramic failures far from the interlayer (CFF) occur at stresses below the average fracture stress of the bulk alumina ($\overline{\sigma}_F = 279 \pm 22$ MPa [127,128]). Just as ceramic failure indicates a minimum strength for the joining layer (interface), interfacial failures imply a minimum ceramic strength for those particular beams. It is possible that the ceramic failures observed are biased toward a lower value. Additionally, Sugar [127] has demonstrated that a slight decrease ($\overline{\sigma}_F = 277 \pm 19$ MPa to $\overline{\sigma}_F = 267 \pm 27$ MPa) in the fracture strength of the bulk alumina may occur if beams are annealed at 1400°C for 6 h; and ceramic failures far from the interface (CFF) in the joints processed at 1150°C seem to exhibit a slightly higher average fracture strength ($\overline{\sigma}_F = 250 \pm 22$ MPa). However, it is difficult to draw any definitive conclusions from these statistics as strength may vary from batch to batch of alumina, and the differences fall well within the standard deviations. Clearly the strength characteristics of joints processed at 1400°C are close to those of the reference alumina, unlike any of the blocks processed at 1150°C. For simplification purposes, any failure initiating in the ceramic (CF to IF), failures close to the interlayer but in the ceramic (CFC), or in the ceramic far from the interlayer (CFF) will simply be referred to as ceramic failures.

Interfacial failures also tend to be concentrated at lower stresses (ranging from 206 MPa to 264 MPa, $\overline{\sigma}_F = 235 \pm 19$ MPa for 11 beams) in the plot (Figure 4.9). Figures 4.12 and 4.13 illustrate the interfaces of two beams (near the tension edge) from BK23. It is worth noting that the interfacial microstructures observed in BK23 appear somewhat different than those from BK26 and BK27 (which will be illustrated in several subsequent images). Interfacial failures in BK23 tended to contain more copper (although very broken-up) and a much larger area fraction of ceramic pullout (larger pieces as well). Additionally, large unbonded regions of the order of the niobium grain size are frequently observed at interfaces in BK23 (see Figure 4.12). The differences between these microstructures may be attributed to a thicker copper coating and the possibility that the foil flattening technique was not as well developed in this initial experiment (BK23). Generally however, the interfacial microstructure of these joints (Blocks 23, 26, and 27) processed at 1400°C appears similar to that observed for plate 4 of BK24 (Figure 4.3).

In the weakest of these interfacial failures, extensive unbonded areas or unbonded networks (continuously connected regions similar to the copper network in Figure 4.2) are observed. Such flaws highly concentrate stresses on the small bonded areas, thus failure occurs at lower applied stresses. The fact that beams with large interfacial defects exhibit failure strengths >200 MPa suggests that the joint strengths can be greatly improved by reducing unbonded area. No failure strengths as low (143 MPa and 163 MPa) as those from two beams annealed at 1400°C for 6 h (plate 4 of BK24, no applied load) were measured from blocks 23, 26, and 27, suggesting that the small applied load during bonding may be somewhat beneficial. The high frequency (≈75%) of ceramic failure in joints processed at 1400°C suggests that the actual average strength of the joint (metal/ceramic interface) is potentially greater than that of the bulk Coors alumina.

4.4 Post-Bonding Anneals on Coors Alumina Joints Processed at 1400°C

In order to gain some insight on how the strong joints produced at 1400°C would behave during extended service at elevated temperature, prolonged anneals were conducted in both gettered-argon and high-vacuum at 1000°C and 1200°C. Furthermore, comparison of the results obtained from the two environments could potentially reveal information about the effects of the ambient p_{O_2} on joint characteristics. Details on each anneal conducted are provided with the data tables (Tables 4.5 and 4.6).

In a prior study by Shalz *et al.* [17], anneals in gettered-argon were conducted for 10 h at 1000°C. The results suggested there may have been a slight increase in strength as a result of the annealing; however, a definite conclusion could not be drawn since these beams were from the edge of the bonding specimen, and other (unannealed) beams near the edge appeared to be preferentially stronger. In the current study, there are no obvious spatial variations in strength (see Table 4.4) for joints processed at 1400°C. Thus, after a few beams were tested from blocks 26 and 27, one could expect with reasonable certainty that other beams in these joints would not alter the already obtained statistics. Consequently, post-bonding anneals could be conducted on untested beams, and deviations from the base statistics (unannealed beams) are considered to be a result of annealing.

The first set of anneals were conducted for 5 h, 50 h, and ≈200 h at 1000°C in gettered argon. Figure 4.14 plots the failure strength of the joints against annealing time and indicates the failure mode. Generally, a gradual decline in strength with argon-annealing time can be observed; however, perhaps of greater interest is the change from predominantly ceramic failures (shorter annealing times) to purely interfacial failures (5 at ≈200 h at 1000°C). Two microstructurally distinct "reaction layers" developed along the perimeter of annealed beams (≈200 h), as depicted in Figures 4.15 and 4.16. The interior microstructure is similar to that of as-processed beams. Incidents of ceramic pullout after extended argon annealing (200 h) imply the (interior) interface still retains reasonable strength, and that the reaction layers invoke the change in mechanical behavior. By adjusting the focus on an optical microscope, it can be determined that the "reaction product" (Figure 4.15) lies on the niobium side of the niobium/alumina interface, and that failure proceeds through such a layer (see Figure 4.17). A particularly brittle reaction layer may enable crack initiation near the interface at lower stresses, thus allowing the crack to subsequently propagate along the metal/ceramic interface. The exact nature of any of these "reaction layers" has not yet been determined; however, energy dispersive spectroscopy (EDS) results (see figures 4.18 and 4.19) suggest they contain niobium and aluminum.

In a low p_{O_2} environment, one may expect that as niobium dissolves alumina (stoichiometrically), oxygen continually diffuses out of the niobium[†], thus higher aluminum concentrations in the niobium may be obtained. Although an aluminum-niobium-oxygen ternary phase diagram is not available, the increased aluminum content in niobium may induce precipitation (either by supersaturation at temperature or upon cooling) of one or more niobium aluminides (*e.g.*, Nb_3Al, see Figure 4.20). The small aluminum peak obtained from EDS may be due to the low atomic mass of aluminum. Although the expected diffusion distance of oxygen in niobium for these anneals (200 h at 1000°C) is of the order of the beam dimensions (≈3 mm by 3 mm), such a reaction product may only be observed near the edge of the beam since niobium will be continually saturated with oxygen (*via* alumina dissolution) at the interior of the beam (see Figure 4.21). Consequently, a penetration depth (along the interface) of the order of the joining layer thickness (≈100 µm) should be expected for a niobium aluminide reaction layer.

The possibility of niobium silicide (or a ternary or higher order compound) formation also exists since Coors alumina is known to contain an intergranular glassy phase. A small silicon EDS peak would be obscured by the left shoulder of the niobium peak (see Figures 4.18 and 4.19). Sapphire couples (Blocks 27s and 28) were annealed simultaneously with the beams in some of the argon anneals, and no obvious reaction layer could be observed except in the case of Anneal 5 (see Figure 4.22). This suggests that some other impurity in the alumina may be instrumental in reaction layer formation. Furthermore, the reaction layer need not necessarily imply a phase change has occurred at

---

[†] Note that such a mechanism implies that oxygen increases its chemical potential by diffusing into niobium; otherwise, the surrounding bulk alumina would exert an oxygen pressure larger than that which allows diffusion of oxygen out of the niobium. This is related to the complex problem of ternary diffusion where two of the three chemical potentials are independent by the Gibbs-Duhem relation. In binary diffusion, a diffusing species always reduces its chemical potential. In higher order systems, this need not be true of every diffusing species as long as there is a net reduction in free energy; *i.e.*, the aluminum reduces its chemical potential enough to compensate for an increase in that of oxygen [3,131].

the interface, instead dissolution of embrittling additives in niobium may alter the fracture path; thus giving the appearance of a reacted layer.

The more extensive reaction layer depicted in Figure 4.15 was only observed on beams from Anneal 5 (see Table 4.6); a less extensive reaction layer (Figure 4.16) was reproduced in all subsequent gettered-argon anneals. It appears as though the reaction layer depicted in Figure 4.16 is also present at the very inner perimeter of that in Figure 4.15. Initially, it was believed that the more extensive reaction layer (Figure 4.15) may have been due to the fact that the titanium and zirconium gettering chips in the furnace had minimal prior use, while in subsequent anneals, they may not have been as efficient in gettering the argon. Anneals were conducted in which the gettering chips were intentionally replaced; however, an extensive reaction layer (Figure 4.15) could not be reproduced. Furthermore, it was thought that a quenching of the samples (furnace lost power) may be related; however, similar occurrences in anneals conducted at 1200°C failed to produce such a layer. It is also possible that during such modifications to the furnace, small leaks were introduced, thus it was operating under optimum conditions for Anneal 5. The cause for the difference between the two different reaction layers remains to be understood.

In order to investigate potential reasons for the reaction layer, whether or not the strength reduction was due to ambient environment, or simply due to exposure time at temperature, vacuum anneals at 1000°C for 200 h were conducted. Of the four beams annealed, three failed in the ceramic (232 MPa, 222 MPa, and 225 MPa), seeming to mimic the behavior of as-processed joints. The strengths of these beams are also plotted in Figure 4.14. No reaction layer was observed in the single joint that failed at the interface (233 MPa). Figures 4.23 and 4.24 compare the ceramic and metal sides of the fracture surface for beams annealed in argon and vacuum at the tension edge. The vacuum-annealed surface is indistinguishable from those observed in unannealed beams.

The results from argon anneals conducted at 1200°C are similar to those obtained at 1000°C, as plotted in Figure 4.25. Figure 4.26 illustrates the fracture surfaces of a beam annealed at 1200°C in gettered argon. It was anticipated that a more extensive reaction layer could be obtained after shorter anneals, due to faster aluminum diffusion. Additionally, if the argon was not optimally gettered, such an ideally low p_{O_2} would not be required to drive diffusion of oxygen out of niobium at higher temperatures. There is evidence for accelerated reaction layer formation at 1200°C; the ultimate extent does not appear to be much greater. The layer does seem to be thicker since the reaction layer is more out of focus than those produced at 1000°C. Figure 4.27 illustrates a portion of the layer that remained attached to the ceramic side of the failure. A small aluminum peak could not be detected by EDS in these reaction layers formed at 1200°C.

One might expect that if the ambient p_{O_2} is indeed responsible for reaction layer formation, the low p_{O_2} in the graphite hot press should cause such a reaction layer to form in the as-processed joints. However, for all joints formed, the edges (1-2 mm) are trimmed off in order to produce a flat joint since it is difficult to perfectly align the alumina blocks and niobium foil. These edge trimmings are much thicker than any of the observed reaction layers; consequently, none of the (unannealed) beams tested exhibited such a layer. It was difficult to determine whether some of these edge trimmings had such a reaction layer; certainly nothing as obvious as in the argon-annealed beams was present. Furthermore, beams from plate 4 of BK24 (re-annealed at 1400°C) did not contain such a layer. It is possible that 6 h of processing is simply not long enough to induce the formation of such a layer, particularly if a liquid copper film is present for a substantial fraction of the processing time.

In order to investigate whether or not the effects of argon-annealing is reversible, anneals in gettered argon followed by vacuum (1000°C and 1200°C) were performed. Figures 4.14 and 4.25 indicate that the strength may be improved relative to that obtained if the beams were tested after argon-annealing. An improvement relative to vacuum-annealing alone[†] is also indicated at 1200°C (Figure 4.25). Figure 4.32 illustrates the fracture surface of a beam annealed in argon and then in vacuum at 1000°C. It is apparent that a "reaction zone" is still present. If the reaction layer obtained from argon-annealing is indeed niobium aluminide (Nb_3Al), aluminum should be preferentially oxidized after sufficient exposure at sufficient p_{O_2}. Such an oxidation reaction may be kinetically inhibited in vacuum, and even if it did occur, the reacted region may still exhibit a similar appearance in an optical microscope.

The post-bonding anneals (particularly those at 1000°C) suggest an influence of p_{O_2} on joint strength whether it be due to a reaction layer and/or interfacial adhesion effects. The possibility of impurities segregating to the interface should not be ignored and any segregation would be dependent on oxygen activity as indicated by the results obtained at 1000°C (where segregation should be most severe). Certainly more data points and further characterization of reaction layers and interfaces would be necessary to provide indisputable evidence supporting the effects discussed here. Experiments using equipment capable of monitoring furnace oxygen activities would be very beneficial to more convincingly support such conclusions.

4.5 High-Temperature Strength of Coors Alumina Joints Processed at 1400°C

Since a reasonably large and consistent set of room temperature strength data was obtained for joints processed at 1400°C, and the interfacial microstructure appeared suitable for high-temperature use (high niobium/alumina interfacial area), a few bend tests were conducted at high temperature. Based on the results from the previous section, it is

---

[†] Anneals conducted in vacuum at 1200°C were complicated by deposition of tungsten (from the furnace elements) onto the annealed beams; thus making it difficult to isolate any effects of ambient p_{O_2} in the 1200°C anneals. Figures 4.28-4.31 illustrate some of these findings. The reader is referred to Appendix IV for further information pertaining to vacuum and argon anneals at 1200°C.

believed that these high-temperature tests are of short enough duration that the ambient environment has no significant influence on joint properties.

Figure 4.33 plots the temperature dependence of fracture strength. Five beams from block 27 which were tested at room temperature were used for data at 25°C. These beams had an average strength (245±22 MPa) consistent with other beams from blocks 23 and 26 tested at room temperature. Indeed, a substantial degree of ceramic failure is observed at elevated temperature, even at a temperature (≈1100±25°C) in excess of 99% of the melting point of copper. The two low-strength interfacial failures which occurred at 800°C and 1000°C appear to be associated with a large unbonded network at the interface (see Figure 4.34). The primary difference between interfacial fracture surfaces at room temperature and high-temperature tests appears to be in the deformation the copper undergoes. This is illustrated by comparing the ceramic side of room temperature failures (Figures 4.3, 4.12, 4.13, 4.15, 4.16, 4.23, 4.24, 4.26, and 4.32) to that in Figure 4.35. The frequent occurrence of ceramic failure suggests that in order to more accurately probe the strength limits of the copper-niobium based joint, a higher-strength aluminum oxide must be joined.

4.6 Block 31 - Sapphire Plug Joint (≈1400°C, ≈2 MPa, Graphite Hot Press)

The first attempt at using a stronger aluminum oxide involved joining two cylindrical sapphire plugs (BK31). The resulting joint was not even as strong as those processed using Coors alumina (Blocks 23, 26, and 27). Upon machining the joint into plates, portions of the sapphire were shattered, and only a fraction of each plate was suitable for cutting into beams. Ten beams were salvaged from the wreckage. The strengths of these ten beams are summarized in Table 4.7, and all failed at the interface. Certainly this sapphire experiment was unsuccessful in that the anticipated strength improvement was not attained. However, the joint does enable a limited amount of comparison and relation of interfacial microstructures to joint strength, and is useful since the majority of interfaces could not be observed from polycrystalline specimens.

Since one beam failed during ultrasonic cleaning and four others failed at low strength ($\overline{\sigma}_F = 142 \pm 29$ MPa), the remaining five beams were annealed in vacuum for 10 h at 1400°C in an attempt to heal small cracks that may have been introduced during the machining. These beams seemed to exhibit some strength increase ($\overline{\sigma}_F = 185 \pm 60$ MPa), but the result should be accepted with caution due to the large degree of scatter in the strengths and few data points taken. A layer (see Figure 4.36) resembling the tungsten layer observed on beams from a vacuum anneal at 1200°C is present (see Figure 4.28d and Appendix IV). Additionally, some instances of niobium pullout (Figure 4.37 and 4.38) were observed, consistent with vacuum annealing of Coors alumina joints at 1200°C.

Figures 4.37 through 4.43 illustrate various interfaces from this joint. Niobium grain boundaries can be observed on the sapphire side, indicating good ceramic/metal contact is achieved (see Figures 4.37-4.41). Additionally, regions in which there are no copper particles (on both the ceramic and metal sides) correspond with unbonded regions which can be seen on metal-side images (see Figures 4.37-4.39). In all beams, the copper phase is well broken-up; however, some beams contained some small patches or strips as illustrated in Figures 4.41-4.43, which tend to be in weaker beams. However, some of the weaker interfaces exhibit some unbonded area (see Figure 4.39), while the copper film appears to be completely broken-up. The amount of unbonded area is comparable to that in Coors alumina joints which failed (interfacial) at much higher stresses. Such a sapphire joint may be much more sensitive to flaw size distributions, and the low strengths may be due to a lower sapphire/niobium interfacial fracture resistance. Thermal grooves in the Coors alumina joints will redirect interfacial cracks parallel to alumina grain boundaries such that they are near parallel to the applied tensile stress. Such redirection of an interfacial crack will require higher loads for extension, thus the polycrystalline alumina joints are stronger. It is also possible that a glassy phase in the Coors alumina is responsible for the high strength of these joints. The faint trace of unbonded geometries on the ceramic side of the interfacial failures (see Figure 4.3) has previously been attributed to the flow of glass to the contact area [3,17]. However, such tracings can also be observed in this sapphire plug joint (see Figures 4.37-4.41) and may just be due to a ridging in the ceramic at the bonding front.

4.7 Block 33 - High-Strength Alumina Joint (≈1400°C, ≈2 MPa, Graphite Hot Press)

Another joint was made using a high-strength alumina (Nikkato alumina) with a reported fracture strength of ≈700 MPa. Since a fair amount of interfacial failures occurred in Coors alumina joints in the low-to-mid 200 MPa range, and the stronger of these interfaces appeared relatively well-bonded, it was anticipated that the strength of the Nikkato alumina would be far greater than that of the interfaces, thus enabling the theoretical maximum strength of these copper-niobium based joints to be measured. However, five beams were tested at room temperature and surprisingly, they all failed in the ceramic ($\bar{\sigma}_F = 359 \pm 26$ MPa).

During processing (6 h, 1400°C) a substantial amount of grain growth occurred in the alumina. Figure 4.44 illustrates the microstructure of the alumina before and after processing, and a noticeable increase in grain size (a factor of ≈2-3) is present. An increase in grain size should increase the flaw size at the tension surface of the ceramic as grains may be pulled out from the ceramic during machining and/or the polishing of beams. An increase in flaw size of this magnitude (roughly a factor of 2-3) would decrease the strength by approximately a factor of $\sqrt{2} - \sqrt{3}$ (to ≈400-500 MPa). Elastic mismatch may also contribute to the strength reduction. Coors alumina joints failed in the ceramic at strengths ≈15% below the bulk alumina strength. Assuming this is primarily due to modulus misfit effects, one would expect the effective strength of the Nikkato alumina to be ≈85% of ≈400-500 MPa (≈340-425 MPa).

The remainder of the beams from BK33 were tested at elevated temperature. Figure 4.45 plots the test results. Ceramic failures continued to be observed up to 1100°C. At 1200°C all four beams tested failed at the interface, but stresses above 200 MPa are consistently measured. This 1200°C data appears to be a good measure of the joint strength since there is little scatter amongst the four data points ($\bar{\sigma}_F = 215 \pm 6$ MPa). Two beams were tested at 1300°C. The two beams exhibited a substantial amount of creep as indicated by the insert in Figure 4.45 and stress versus displacement curves in Figure 4.46. One of these two beams never failed, even after ≈1500 μm displacement (the displacement limit the machine was set to). The other beam tested at 1300°C failed at the interface after some deformation of the alumina occurred (see insert in Figure 4.45). Both beams tested at 1300°C reached a peak stress of ≈140 MPa during the bend tests. These results seem to imply that the joint once again has mechanical behavior nearly matching and potentially exceeding that of the ceramic.

The strength of this Nikkato alumina joint may exceed that of Coors alumina joints for several reasons. Grain growth during processing may enable grains with a particularly low niobium/alumina interfacial energy to preferentially grow. The heterophase interfacial energies will generally be greater than alumina grain boundary energies, thus the niobium/alumina interfaces would be most influential in dictating which grains grow from an interfacial energy/interfacial area (γA) product point of view. In the Coors alumina, the grains are substantially larger (≈25 μm) and thus the driving force for coarsening is much lower. Furthermore, there may be more impurities in Coors alumina segregating to the interface which reduce strength. The smaller grain size of the Nikkato alumina may also reduce the interfacial flaw size, particularly the size of unbonded areas.

Figure 4.47 illustrates the ceramic and metal side of a fracture surface representative of the interfacial failures in beams from BK33. The speckled appearance of the interface is due to the fact that the alumina grain size is near the resolution limit at the magnification used. A faint reflection of the niobium grain boundaries is observed on the ceramic-side of the fracture surfaces. The unbonded areas are much less populated and smaller than typically observed at the Coors alumina interfaces. The alumina grains are revealed more clearly in Figure 4.48; they are obviously facetted. The impressions made by the alumina grains in the niobium suggests an interfacial roughness wavelength much shorter than would be obtained from coarser alumina (*i.e.*, Coors alumina). This interfacial structure will certainly require interfacial cracks to propagate along more area, provides a relatively more tortuous crack path, and makes a significant contribution to the improved strength.

Finally, perhaps the most notable feature of this interface is the lack of a sizable copper phase. Contrary to Coors alumina joints, only a limited amount of interfacial copper can be found in an optical microscope as illustrated in Figures 4.49 and 4.50. The left portion of Figure 4.49 (blurry) is where failure occurred in the ceramic. Some copper can be seen below the somewhat transparent ceramic, and it is possible that many of the other beams (ceramic failures) exhibited a similar interfacial structure, and isolated copper particles are correlated with stronger interfaces. Figure 4.50 illustrates the ceramic side of an interfacial failure. A pink shading on the surface in some regions indicates copper may have been present at this portion of the interface. Corresponding features cannot be found on the metal side. Focusing below the ceramic surface, reveals what appears to be small particles of bulk copper. It is possible that copper has diffused into the alumina and precipitated upon cooling; Esposito *et al.* [107] report copper concentrations 15 μm into alumina as high as 1 wt% after diffusion bonding copper to alumina. Furthermore, small copper particles on fracture surfaces may quickly evaporate after fracture, while the beam is at high temperature; however the presence of copper at the interface of a Coors alumina beam tested at 1000°C implies this Nikkato alumina joint must have substantially less interfacial copper. Closer examination *via* SEM (see Figure 4.48) revealed small (≈0.1 μm) copper particles at alumina grain boundaries. The interfacial microstructure of this high-strength alumina joint is substantially different from both the Coors alumina and sapphire plug joints; these differences are discussed in the next section.

4.8 Microstructural Evolution of Copper/Niobium/Copper Interlayers

Focusing on the Coors alumina joints, there appears to be a dramatic strength increase as the copper film dewets the interface, the weakest joints being processed at 1150°C with small applied load (Blocks 24 and 30), while strengths near that of the ceramic are obtained *via* higher processing temperature. Since the majority of beams processed at 1400°C failed in the ceramic, sapphire window joints (Blocks 27s and 28) were processed in the graphite hot press at 1400°C using conditions duplicating those used to fabricate polycrystalline alumina joints. Ideally, these sapphire couples will simulate the microstructure of the interface.

The metal/sapphire interfacial microstructure of these couples exhibited some variability, as illustrated in Figure 4.51. Furthermore, these images seem to suggest a sequence by which the copper develops its final structure. Initially, a continuous copper film is divided into patches lying interior to niobium grain boundaries as thermal grooving of the niobium grain boundaries occurs (Figure 4.51a). These isolated patches of copper then begin to break-up into copper ligaments (Figure 4.51b), which finally break up into discrete particles (Figures 4.51c and 4.51d) *via* Rayleigh instabilities. The process is very similar to observations by Lange and Clarke [132] for a grain-boundary phase in magnesium aluminate spinel ($MgAl_2O_4$) sintered with lithium fluoride additions. Regions that appear to be in the early stages of this evolution sequence tend to be concentrated toward the outer edge(s) of the samples, where copper is preferentially displaced and thicker. Copper film break-up may be influenced by other energetics such as differences in the interfacial energies associated with each niobium grain and/or differences in niobium grain boundary energies which will affect grooving kinetics.

During the break-up process, liquid copper will dissolve and re-precipitate niobium as required to conserve volume (*i.e.*, the volume interior to the niobium grain boundaries and sapphire, see Figure 4.52), thus increasing the niobium/sapphire interfacial area. The process is somewhat similar to liquid phase sintering, *i.e.*, liquid-phase-assisted diffusion bonding. Variations in the niobium foil thickness and differences in grain boundary groove heights imply variations in the copper film thickness, which will affect the kinetics of break-up and final copper particle size (see Figures 4.51c and 4.51d). Higher bonding pressures will aid in deforming the niobium foil so that more of the niobium thermal grooves will contact the sapphire, thus accelerating the initial stage of bonding and copper break-up. Increased applied load will also increase the contact area at thermal grooves by plastic deformation. Higher processing temperatures will accelerate the kinetics of thermal grooving as well as the break-up kinetics of the copper-patch instabilities. Additionally, at higher temperatures niobium will more easily deform, and smaller loads will be necessary to insure thermal grooves contact the joining surface.

These observations imply that it is thermodynamically favorable for the copper film to break-up and form a niobium/alumina interface, thus replacing copper/alumina and copper/niobium interfaces. This suggests a set of constraints that must be satisfied. To obtain a high degree of metal/ceramic contact throughout the joint, good wetting of copper on alumina and niobium is preferred, and low copper/alumina and copper/niobium interfacial energies promote wetting. However, a situation in which these interfacial energies are so low that the copper film does not break-up is not ideal for producing refractory joints. One might expect that due to the effects of niobium on the wetting of copper on alumina that the niobium/alumina interface will be favored. Additionally, the formation of a niobium/alumina interface as copper break-up proceeds eliminates two interfaces, thus this constraint may not be difficult to satisfy. However, these issues may be of concern in applying the technique to other systems.

It is interesting to note that the joints processed at 1150°C had substantially less unbonded area than those processed at 1400°C. Such a result seems counterintuitive since at higher temperature, the niobium should deform more easily, and the wettability of copper is improved. BK29 (molybdenum hot press 1150°C, ≈7.5 MPa) exhibited essentially no unbonded area, while BK30 (graphite hot press, 1150°C, 2.2 MPa) contained only a few relatively small and isolated patches of unbonded area, as one may expect due to the relative applied loads. Interestingly, the unbonded areas in joints processed at 1400°C have a rounded shape and are frequently networked, appearing as if they at one point contained the liquid copper phase in the intermediate stages of break-up. If such regions did in fact contain copper (or were at least partially filled with copper), it is possible that the copper diffused into the niobium or was driven by capillary forces into other regions of the joint. Additionally, such a phase may have evaporated provided there is a viable transport route (continuous film, interfacial diffusion) to the ambient environment. (Note that at 1400°C, the total vacuum pressure is far below the vapor pressure of copper.) Based on the observed strength results, one might conclude that it is better to have an unbonded region in the joint, rather than a highly constrained (thin) copper layer. A region of the interface that is weakly bonded (copper/alumina interface) may serve as a crack initiation site; thus allowing a dynamic crack to propagate along the interface; whereas an unbonded region is less stress concentrating (*i.e.*, not as sharp as an interfacial crack) and has no crack velocity.

The interlayer microstructure of the sapphire window joints was also compared before and after gettered-argon and vacuum annealing for 200 h at 1000°C. Microstructurally, there appeared to be minimal change as illustrated in Figures 4.53 and 4.54. These anneals on sapphire imply the morphological evolution of the copper film is extremely sluggish with solid copper. It is anticipated that upon conducting an anneal above the melting point of copper for a relatively short time (a few hours), evolution in the copper phase will be noticeable. The break-up sequence discussed should occur more rapidly due to faster niobium diffusion in liquid copper (of the order of a factor of 1000 increase in diffusivity) and an increase in niobium flux through the liquid due to higher solubility (of the order of a factor of 10-30, see Figures 2.6 and 2.7). In fact, after annealing (1400°C, 10 h, vacuum) beams from BK31 (sapphire plug joint), the copper film was completely broken-up into isolated round particles (see Figures 4.37-4.39), while some small copper patches or string like portions in unannealed beams could be observed (Figures 4.41-4.43). The microstructural change plate 4 of BK24 underwent due to re-annealing (1400°C, 6 h) also supports this evolution sequence.

Joints using three different aluminum oxide substrates (Coors alumina, Nikkato alumina, and sapphire) exhibit distinct ceramic/interlayer interfacial microstructures. In the sapphire couples, there is some variability in the nature of the copper film; while in the Coors alumina samples the film is homogeneously broken up. Furthermore, the Nikkato alumina joint revealed very little (sizable) copper at the interface as shown in Figures 4.47 through 4.50. One might expect to observe more variability in the copper film from joints formed with polycrystalline alumina since alumina grains imply a greater amount of differently oriented copper/alumina, copper/niobium, and niobium/alumina interfacial energy combinations, thus locally changing the driving force for the break-up process. However, alumina grains may reduce the spatial scale of fluctuations in the copper film to periodicities below the niobium grain size. Regions of copper at the metal/ceramic interface that are smaller than the alumina grain size (<25 μm) are likely to be sufficiently small that they are not of critical size to cause failure, thus resulting in strong interfaces and enabling preferential failure in the ceramic, as observed in such joints processed at 1400°C. Furthermore, grain boundary grooving of the ceramic may induce perturbations in the copper film, thus assisting break-up *via* Rayleigh instabilities.

The ability to produce joints with very homogeneous copper film break-up using polycrystalline alumina partially explains why these joints exhibit substantially higher strengths than the joint made with sapphire plugs. Although both aluminas likely contain some glassy phase, the Nikkato alumina (99.9% pure) likely contains less than the Coors alumina (99.5% pure). With this assumption, the remarkably high strength of the Nikkato alumina joint (BK33) suggests a glassy phase is not integral to formation of strong joints. The niobium/alumina interface is certainly expected to contain excess copper; and such an additive does not appear to degrade joint strength as in the case of silver [79]. Rühle [133] has briefly indicated that adding niobium to a copper/sapphire interface increases the fracture energy to values exceeding any of those reported in Chapter 2 (Table 2.2). The lack of copper and the faintness of the niobium grain boundaries in Figure 4.40 (the beam which failed during ultrasonic cleaning) seems to imply that very little copper was available in this part of the joint, *i.e.*, less liquid was available to preferentially dissolve grain boundaries, and the resulting interface may be similar to that obtained from solid-state diffusion bonding, thus producing a relatively weak joint.

Table 4.1: **Fracture Strength Results from Block 24 (Graphite Hot Press 1150°C)**

	Beam 1	**Beam 2**	**Beam 3**	**Beam 4**	**Beam 5**
Plate 1	This plate broke at the interface with light handling after first grinding and cleaning of thermal resin. IF				
Plate 2	This plate broke (likely in tension) at the interface while scraping thermal resin from the plate after second grinding. IF/ID				
Plate 3	* Multiple	83 MPa IF	88 MPa IF	50 MPa IF	36 MPa IF
Plate 4	266 MPa Anneal 1 I/C to IF	270 MPa Anneal 1 IF	143 MPa Anneal 1 IF	262 MPa Anneal 1 CFF	163 MPa Anneal 1 IF
Plate 5	This plate was dropped from about 4 to 5 feet above cement floor and it broke at the interface. IF/ID				
Plate 6	96 MPa IF	100 MPa IF	96 MPa IF	84 MPa IF	65 MPa IF

*This beam failed at the interface along with several other ceramic fractures as a result of lowering the crosshead too fast.

Anneal 1: (2/1/97) Plate 4 (as a single piece, *i.e.* not yet cut into beams) was annealed in the graphite hot press (≈1400°C for 6 h, heated and cooled as if a bonding cycle).

Table 4.2: **Fracture Strength Results from Block 29 (Molybdenum Hot Press 1150°C)**

	Beam 1	**Beam 2**	**Beam 3**	**Beam 4**
Plate 1	252 MPa CFF	275 MPa CFF	262 MPa CFF	254 MPa CFF
Plate 2	213 MPa CFC	216 MPa CFF	252 MPa CFF	120 MPa IF
Plate 3	164 MPa IF	* IF	176 MPa IF	173 MPa IF
Plate 4	180 MPa IF	155 MPa IF	142 MPa IF	239 MPa IF

*This beam failed as a result of lowering the displacement ram too fast; thus no strength could be measured.

Table 4.3: **Fracture Strength Results from Block 30 (Graphite Hot Press 1150°C)**

	Beam 1	**Beam 2**	**Beam 3**	**Beam 4**
Plate 1	* IF	69 MPa IF	154 MPa IF	243 MPa CFF
Plate 2	151 MPa IF	245 MPa CFF	247 MPa CFF	216 MPa CFF
Plate 3	91 MPa IF	250 MPa IF	131 MPa IF	140 MPa IF
Plate 4	83 MPa IF	89 MPa IF	203 MPa IF	290 MPa CFF

*This beam failed as a result of lowering the displacement ram too fast; thus no strength could be measured.

Table 4.4: **Fracture Strength Results from Block 23 (Graphite Hot Press 1400°C)**

	Beam 1	**Beam 2**	**Beam 3**	**Beam 4**	**Beam 5**
Plate 2†	258 MPa CF to C/I	247 MPa IF	265 MPa CFF	263 MPa IF	226 MPa IF
Plate 3	228 MPa CF to C/I	272 MPa CFF	241 MPa I/C to IF, ID	256 MPa CFF	231 MPa IF/ID
Plate 4	242 MPa CFF	225 MPa CFF	252 MPa CF to IF	231 MPa CFF	223 MPa IF/ID
Plate 5	231 MPa CFF	230 MPa CFF	248 MPa IF/CF*	241 MPa CFF	208 MPa IF*
Plate 6	190 MPa CF to IF	235 MPa CFF	263 MPa CFF	239 MPa CFF	235 MPa CFF

*BK23BM53 and BK23BM55 cannot be found for re-examination of fracture path. They were probably SEM samples that got placed somewhere else and have been shuffled around as a result of the move from Hearst Mining Building to Davis Hall. BK23BM53 will be treated as CF to IF, and BK23BM55 as IF for statistical purposes.

†The plates are numbered 2 to 6 because initial attempts to cut Plate 1 with a bent blade resulted in wasting part of the assembly which was equivalent in width to one plate; *i.e.*, if different strengths for edge beams are realized, only Beams 1 and 5 of Plate 2 should be treated as edge beams.

Table 4.5: Fracture Strength Results from Block 26 (Graphite Hot Press 1400°C)

	Beam 1	Beam 2	Beam 3	Beam 4	Beam 5
Plate 1	264 MPa IF	250 MPa CFF	250 MPa CFF	243 MPa I/C to IF	IF[‡]
Plate 2	146 MPa Anneal 12,13 IF	208 MPa Anneal 13-15 IF	253 MPa Anneal 12 IF	192 MPa Anneal 16 IF	231 MPa CFF
Plate 3	158 MPa Anneal 12 IF	237 MPa CFF	209 MPa Anneal 16 IF	258 MPa CFF	231 MPa Anneal 13-16 CFF*
Plate 4	249 MPa CFF	241 MPa CFF	266 MPa CFF	233 MPa IF	206 MPa IF
Plate 5	237 MPa Anneal 2 CF to IF	189 MPa Anneal 3 CFC	226 MPa Anneal 3 CFF	171 MPa Anneal 4 IF	261 MPa Anneal 4 CFC
Plate 6	160 MPa Anneal 12-15 IF	185 MPa Anneal 16 IF	244 MPa Anneal 12-16 IF	235 MPa Anneal 13 CFC	206 MPa Anneal 12 CFF[†]

[‡] This beam failed as a result of lowering the displacement ram too fast; thus no strength could be measured. An interfacial failure may have occurred due to the dynamic loading conditions.

*Two failures in the ceramic far from the interface on each side of the interlayer.

[†] This test may have actually been three point bend (3PB) since one of the contact points at the inner span of the testing jig may not have been in contact with the beam due to improper alignment. Failure was far from the interface, and using a 3PB stress state analysis (see Appendix III), yields a value of 280 MPa, somewhat more consistent with other ceramic failures. At the joining layer, the applied stress would have been ≈206 MPa. This data point will not be included in the analysis.

Anneal 2:	(9/8/97) Gettered-argon, 5 h at 1000°C. The titanium and zirconium chips have most likely been used for a while prior to this anneal.
Anneal 3:	(10/3/97) Gettered-argon, 50 h at 1000°C. The titanium and zirconium chips have most likely been used for a while (≈1 year) prior to this anneal.
Anneal 4:	(10/14/97) Gettered-argon, 50 h at 1000°C. The titanium and zirconium chips have most likely been used for a while (≈1 year) prior to this anneal.
Anneal 12:	(7/6/99) Gettered-argon, 50 h at 1200°C.
Anneal 13:	(7/19/99) Gettered-argon, 99 h at 1200°C. The furnace power was shut off after ≈99 h of annealing due to a power outage; the plan was to anneal for 100 h.
Anneal 14:	(8/5/99) Gettered-argon, 5-93.5 h at 1200°C. The furnace power was shut off somewhere between the stated time interval; this was likely due to a

fluctuation in the cooling water supply. This will be treated as a 49.25±44.25 h anneal.

Anneal 15: (8/10/99) Gettered-argon, 101 h at 1200°C. During this run, the tube which argon flows out became disconnected from the test tube containing mineral oil that the argon is bubbled through; this happened after ≈80 h of annealing, and again within the last 20 h. During the first disconnection, the tube was left like this for at most 3 h, while for the second one, this condition may have existed for up to ≈20 h. The disconnection of the tube warrants the possible contamination of the gettered-argon by back diffusion of air, due to the slow argon flow rate (of the order of a few mL/min).

Anneal 16: (8/20/99) Vacuum, 250 h at 1200°C.

Table 4.6: **Fracture Strength Results from Block 27 (Graphite Hot Press 1400°C)**

	Beam 1	**Beam 2**	**Beam 3**	**Beam 4**	**Beam 5**	**Beam 6 Edge**
Plate 1	CFF*	121 MPa Anneal 6 CF/IF*	232 MPa Anneal 6 CFF	222 MPa Anneal 6 CFF	237 MPa 800°C IF	140 MPa Anneal 6 IF
Plate 2	227 MPa 800°C CFF	190 MPa 900°C CFF	146 MPa 1000°C CFF	220 MPa CFF	50 MPa* Anneal 7 IF to I/C‡	
Plate 3	210 MPa 900°C CFF	220 MPa Anneal 7 IF to I/C	255 MPa CF to IF	206 MPa Anneal 7 IF	96 MPa 1000°C IF	
Plate 4	250 MPa CFF	186 MPa 900°C CFF	231 MPa Anneal 9/10 IF	233 MPa Anneal 8 IF	134 MPa 800°C IF	146 MPa IF*
Plate 5	140 MPa 1000°C CFF	86 MPa 1100°C CFF	225 MPa Anneal 8 CFF	214 MPa Anneals 9-10 IF†	158 MPa Anneal 9 IF	190 MPa CFF
Plate 6	274 MPa CFF	216 MPa Anneal 7 IF	228 MPa CFC	221 MPa Anneals 7-8 CFF	140 MPa Anneal 5 IF	122 MPa Anneal 5 IF

*In these beams a visible crack was present in the ceramic (in BK26BM46, on compression part of beam). These beams, as well as the edge beams (column 6) will not be included in statistical analysis or any plots of the data.

‡ILF.

†This beam contained a couple visible chips at the edge of the polished face of the ceramic.

Anneal 5: (1/12/99) Gettered-argon, 218 h at 1000°C. After ≈18 h, the furnace power shut off resulting in a quench of the sample from 1000°C. A 200 h program was run after this. The titanium and zirconium chips were changed just prior to this anneal.
Anneal 6: (3/12/99) Vacuum, 200 h at 1000°C. Beams were cooled at 30°C/h to 740°C, and then furnace power was shut off.
Anneal 7: (3/27/99) Gettered-argon, 200 h at 1000°C. The titanium and zirconium chips had a fair amount of use on them for this anneal.
Anneal 8: (4/9/99) Vacuum, 200 h at 1000°C.
Anneal 9: (5/18/99) Gettered-argon, 200 h at 1000°C. The titanium and zirconium were changed just prior to this anneal.
Anneal 10: (5/28/99) Vacuum, 200 h at 1000°C.

Table 4.7: **Fracture Strength Results from Block 31 (Graphite Hot Press 1400°C)**

Beam	Strength [MPa]	Failure	Notes
1	114	IF	
2	154	IF	
3	150*	IF	Anneal 11
4	233	IF	Anneal 11
5	177	IF	
6	258†	IF	Anneal 11
7	173	IF	Anneal 11
8	110	IF	Anneal 11
9	122	IF	
10		IF	failed during ultrasonic cleaning in acetone

*This beam was tested straight out of the furnace with no cleaning in ethanol, doesn't seem to make a difference anyways.

†The ceramic side of this beam was lost upon failure. It flew somewhere and could not be found.

Anneal 11: (7/10/99) Vacuum, 10 h at 1400°C.

Table 4.8: **Fracture Strength Results from Block 33 (Graphite Hot Press 1400°C)**

	Beam 1	Beam 2	Beam 3	Beam 4	Beam 5
Plate 1	220 MPa 1200°C IF	140 MPa 1300°C *	219 MPa 1200°C IF	226 MPa 1100°C CFF	335 MPa CFF
Plate 2	300 MPa 800°C CFF	366 MPa CFF	216 MPa 1000°C IF	265 MPa 1000°C CFF	347 MPa CFF
Plate 3	347 MPa CFF	211 MPa 1200°C IF	195 MPa 800°C CFF†	272 MPa 900°C	245 MPa 1100°C CFF
Plate 4	209 MPa 1200°C IF	237 MPa 1100°C CFF	242 MPa 1000°C I/C to IF	140 MPa 1300°C IF*	401 MPa CFF

*In these beams, the alumina underwent a substantial amount of creep. BK33BM12 never fractured.

†This data point will be discarded from the statistics as there was a visible flaw in the ceramic surface where failure occured.

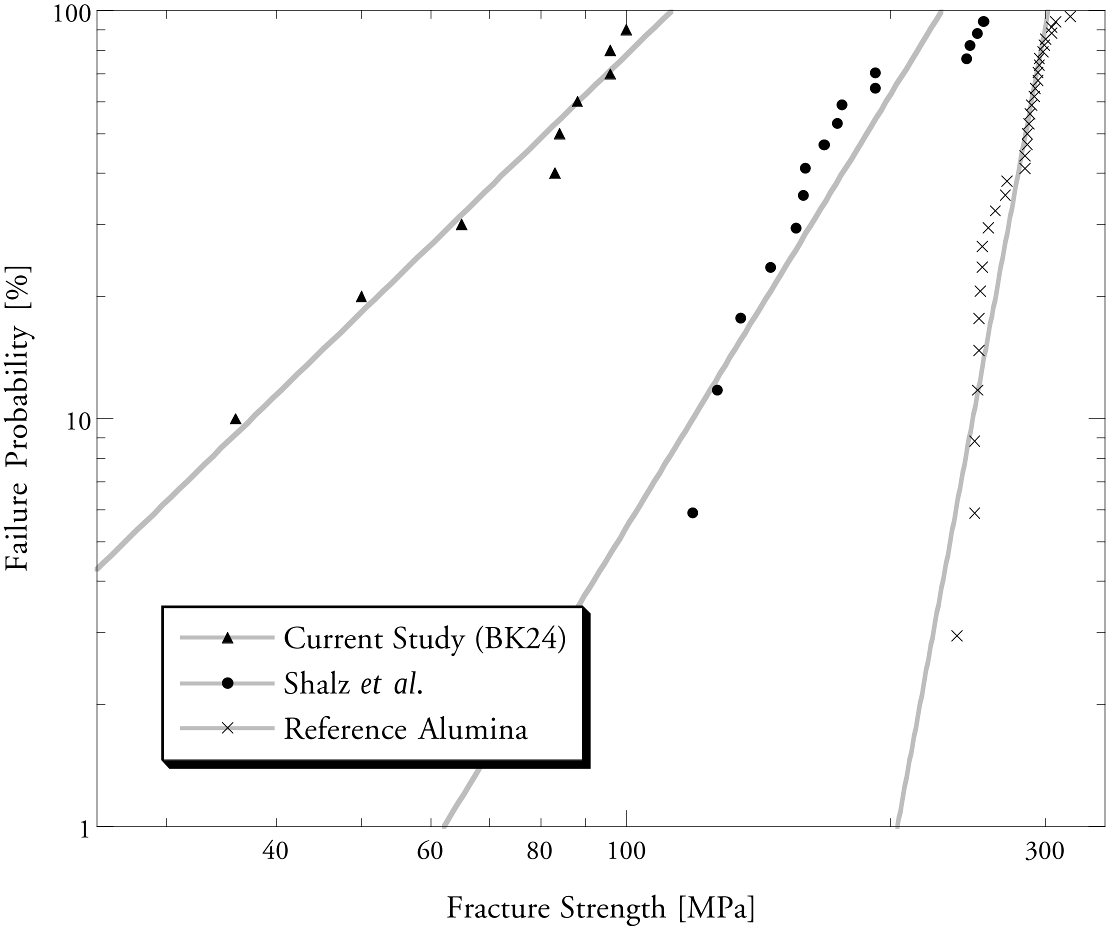

Figure 4.1: Failure probability plot for BK24 (graphite hot press, 1150°C, 2.2 MPa) in comparison to strength data from Shalz *et al.* [17] and from bulk Coors alumina measured by Sugar [127] and Dalgleish [128].

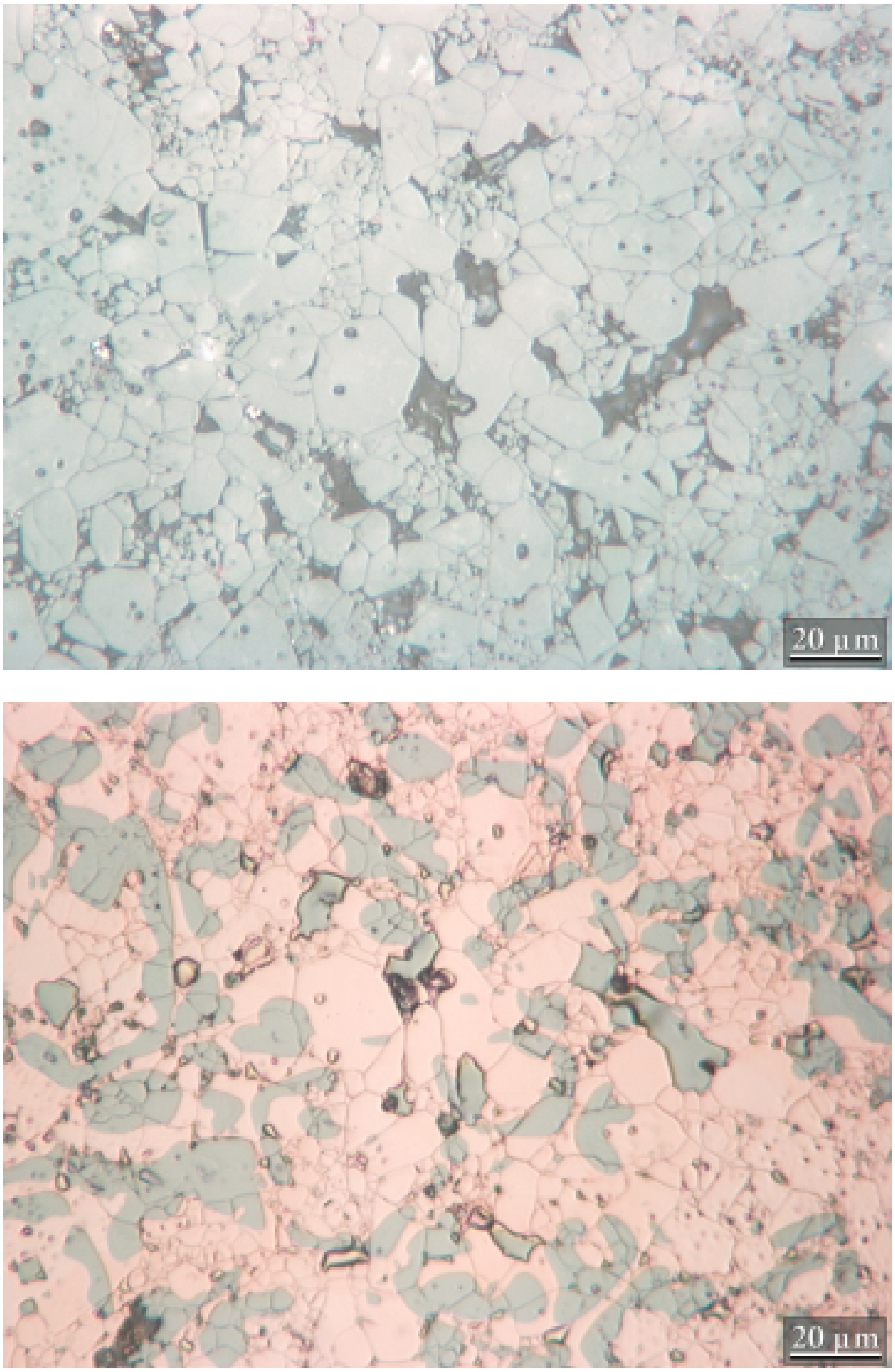

Figure 4.2: Optical micrographs of the ceramic (top) and metal (bottom) sides of the fracture surface in BK24BM65. This beam failed at 65 MPa.

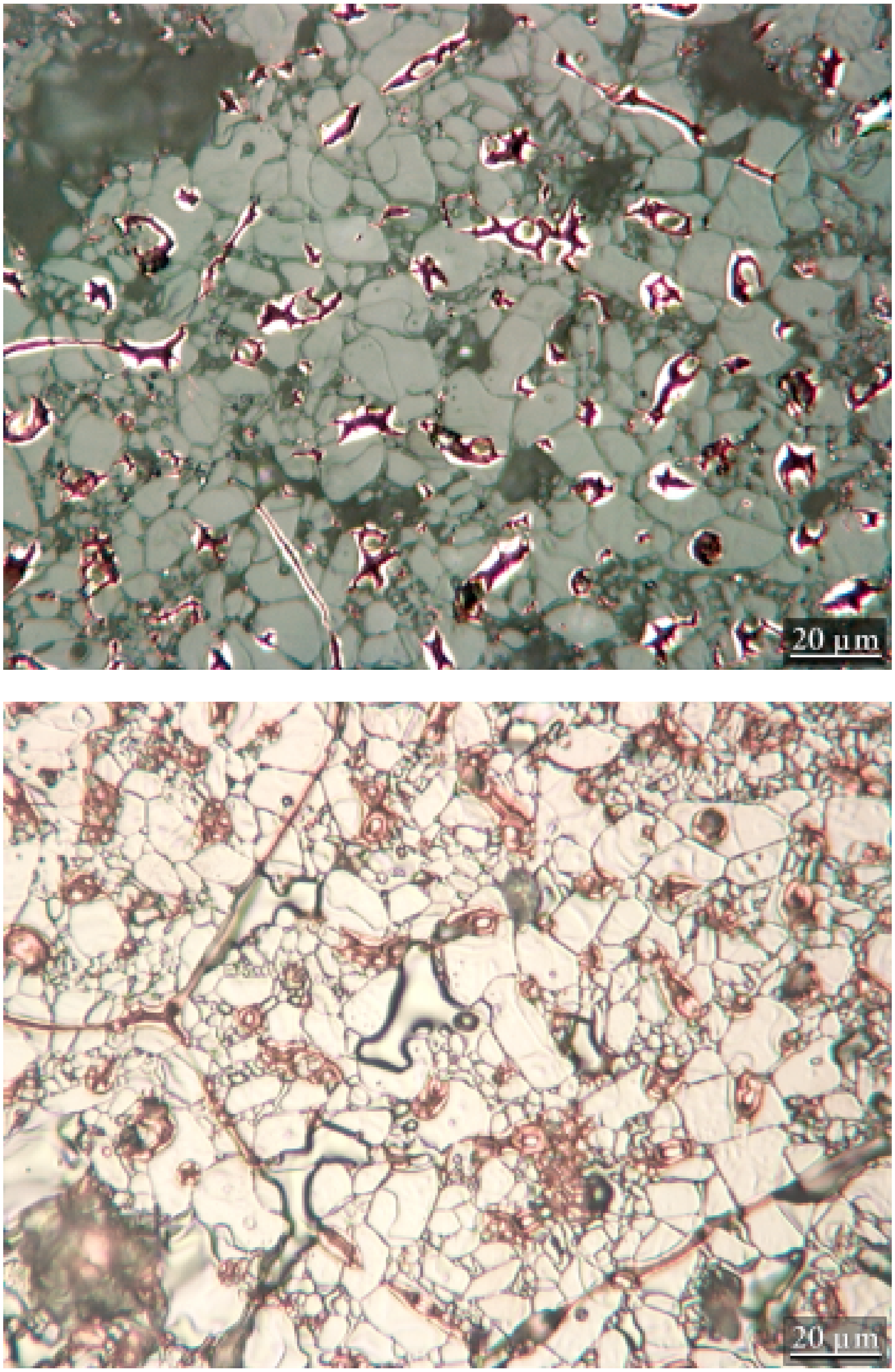

Figure 4.3: Optical micrographs of the ceramic (top) and metal (bottom) sides of the fracture surface in BK24BM42. This beam failed at 270 MPa.

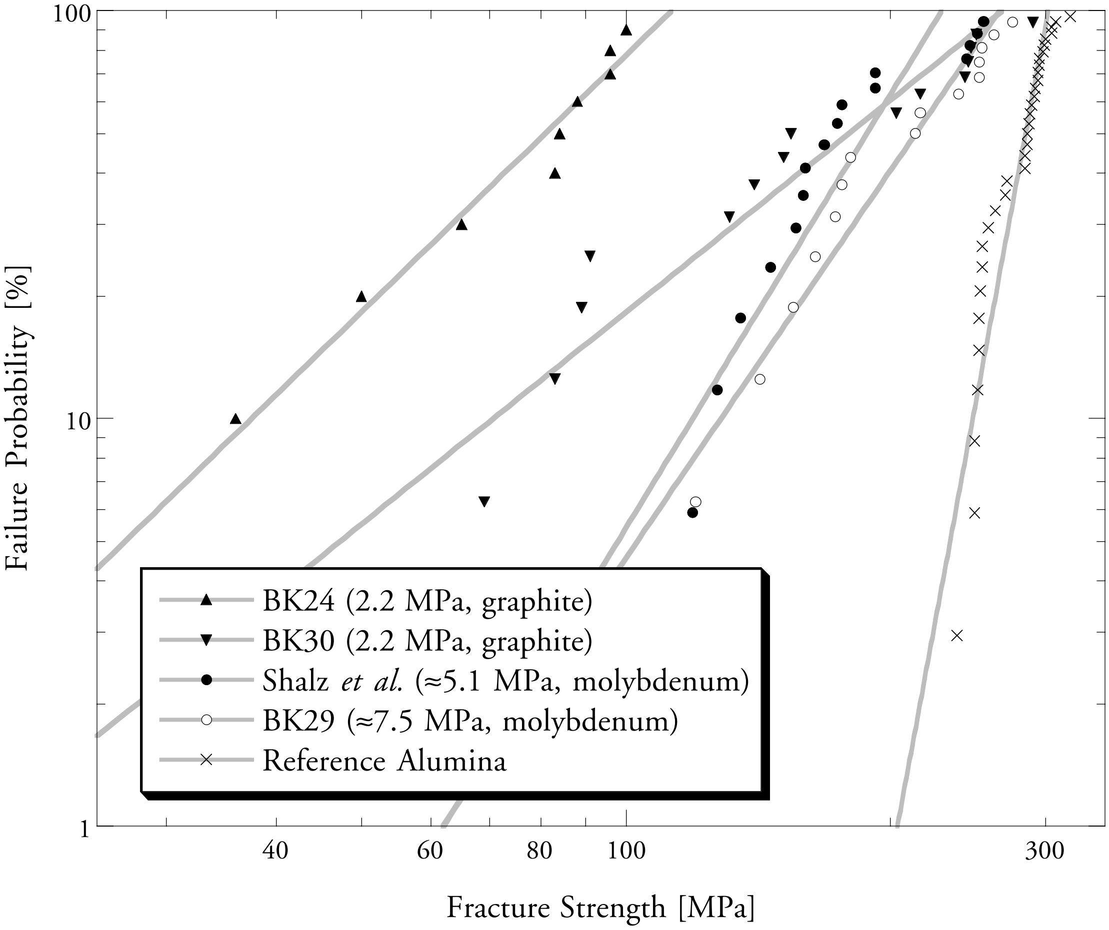

Figure 4.4: Failure probability plot containing the data for Blocks 24, 29, and 30, as well as the data from Shalz *et al.* [17] and the appropriate reference alumina strength [127,128].

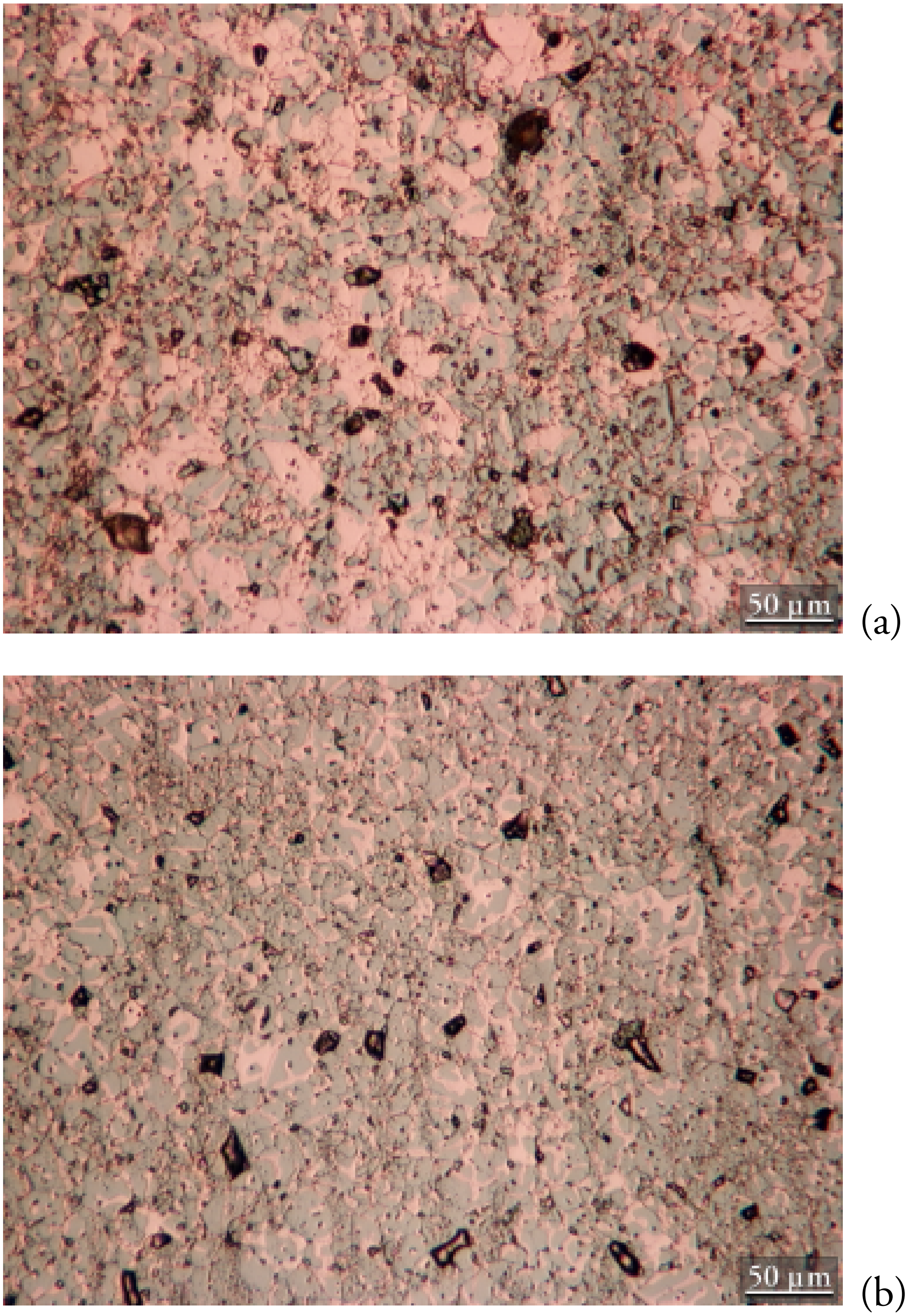

Figure 4.5: Series of optical micrographs of the metal side of fracture surfaces for progressively stronger beams from a joint processed in the molybdenum hot press at 1150°C and ≈7.5 MPa (BK29). The following labels correlate fracture strength with the appropriate image: (a) 120 MPa, (b) 155 MPa, (c) 180 MPa, and (d) 239 MPa.

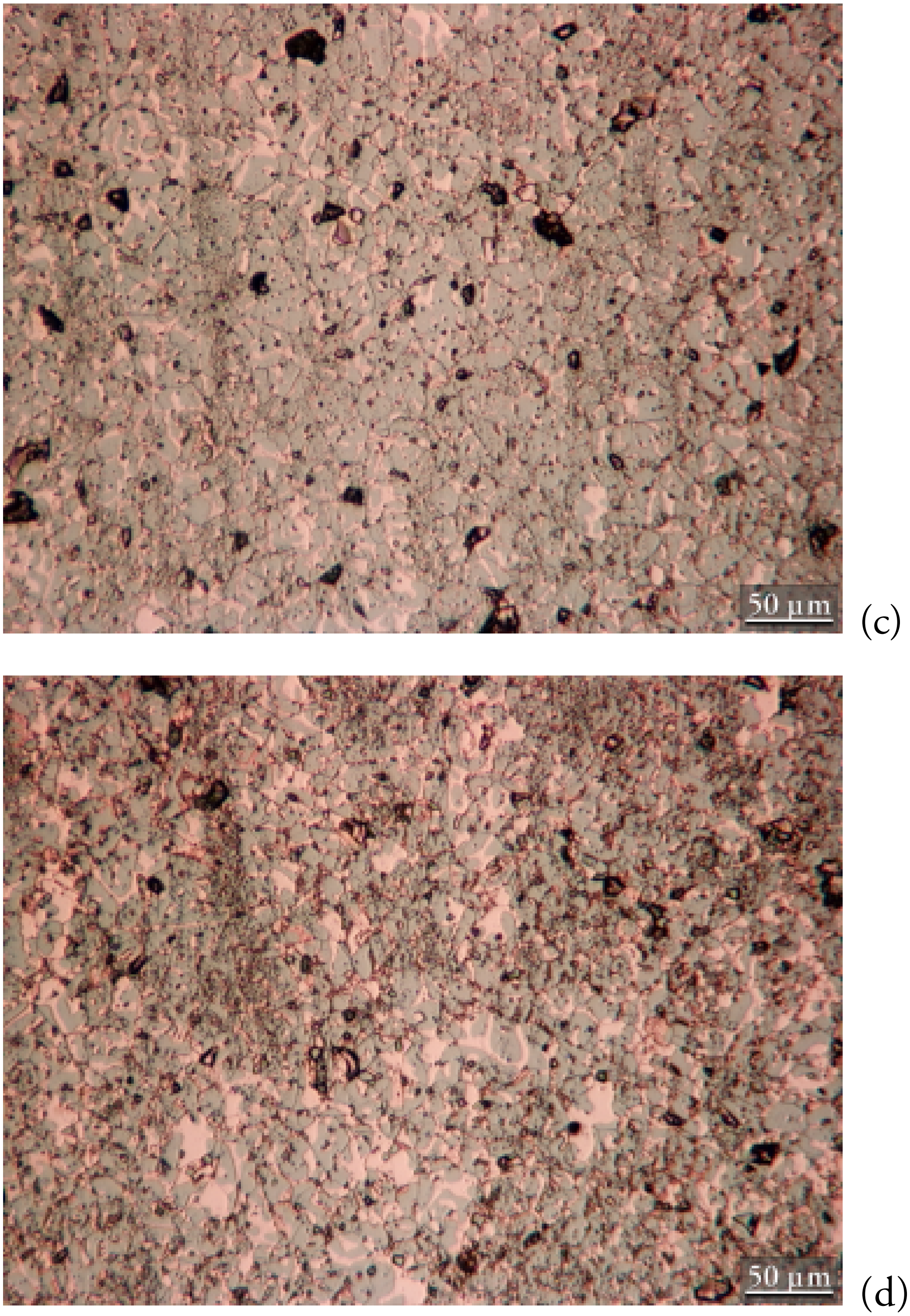

Figure 4.5: Series of optical micrographs of the metal side of fracture surfaces for progressively stronger beams from a joint processed in the molybdenum hot press at 1150°C and ≈7.5 MPa (BK29). The following labels correlate fracture strength with the appropriate image: (a) 120 MPa, (b) 155 MPa, (c) 180 MPa, and (d) 239 MPa.

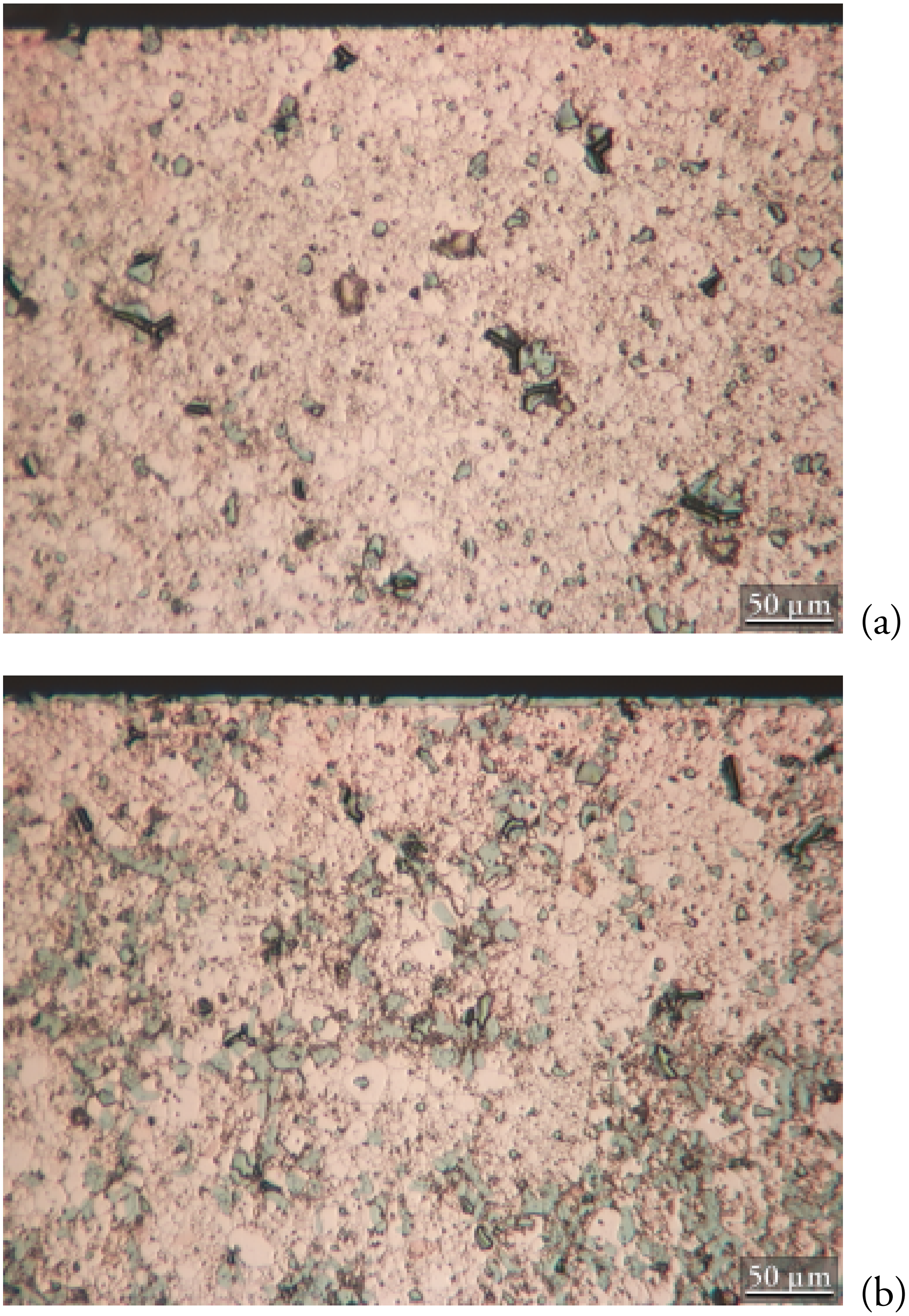

Figure 4.6: Series of optical micrographs of the metal side of fracture surfaces for progressively stronger beams from a joint processed in the graphite hot press at 1150°C and 2.2 MPa (BK30). The following correlate fracture strength with the appropriate image: (a) 83 MPa, (b) 151 MPa, and (c) 203 MPa.

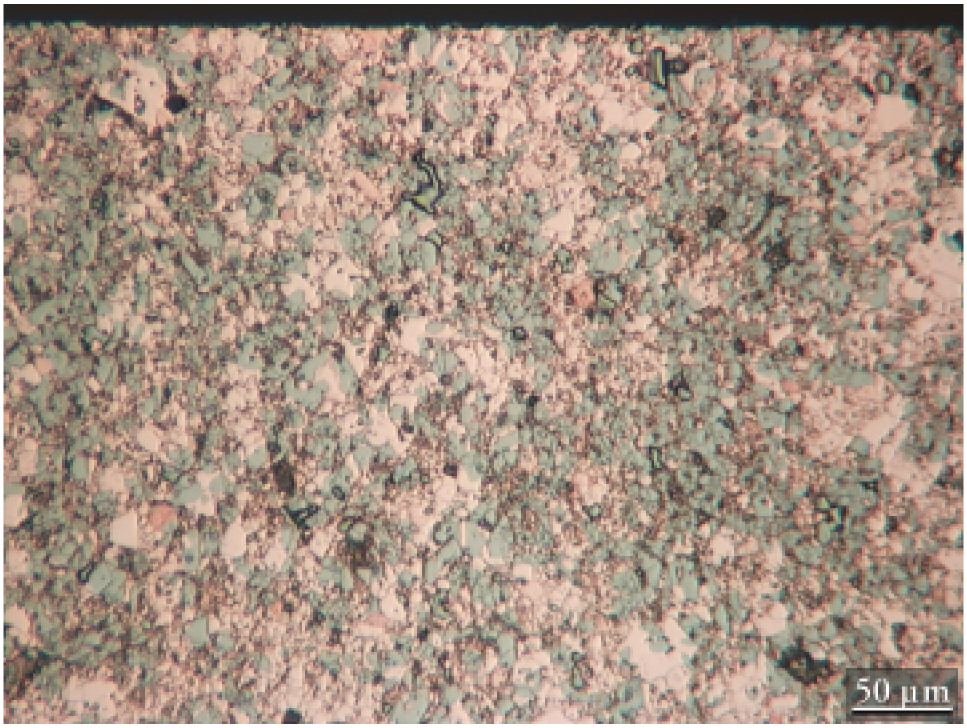

(c)

Figure 4.6: Series of optical micrographs of the metal side of fracture surfaces for progressively stronger beams from a joint processed in the graphite hot press at 1150°C and 2.2 MPa (BK30). The following correlate fracture strength with the appropriate image: (a) 83 MPa, (b) 151 MPa, and (c) 203 MPa.

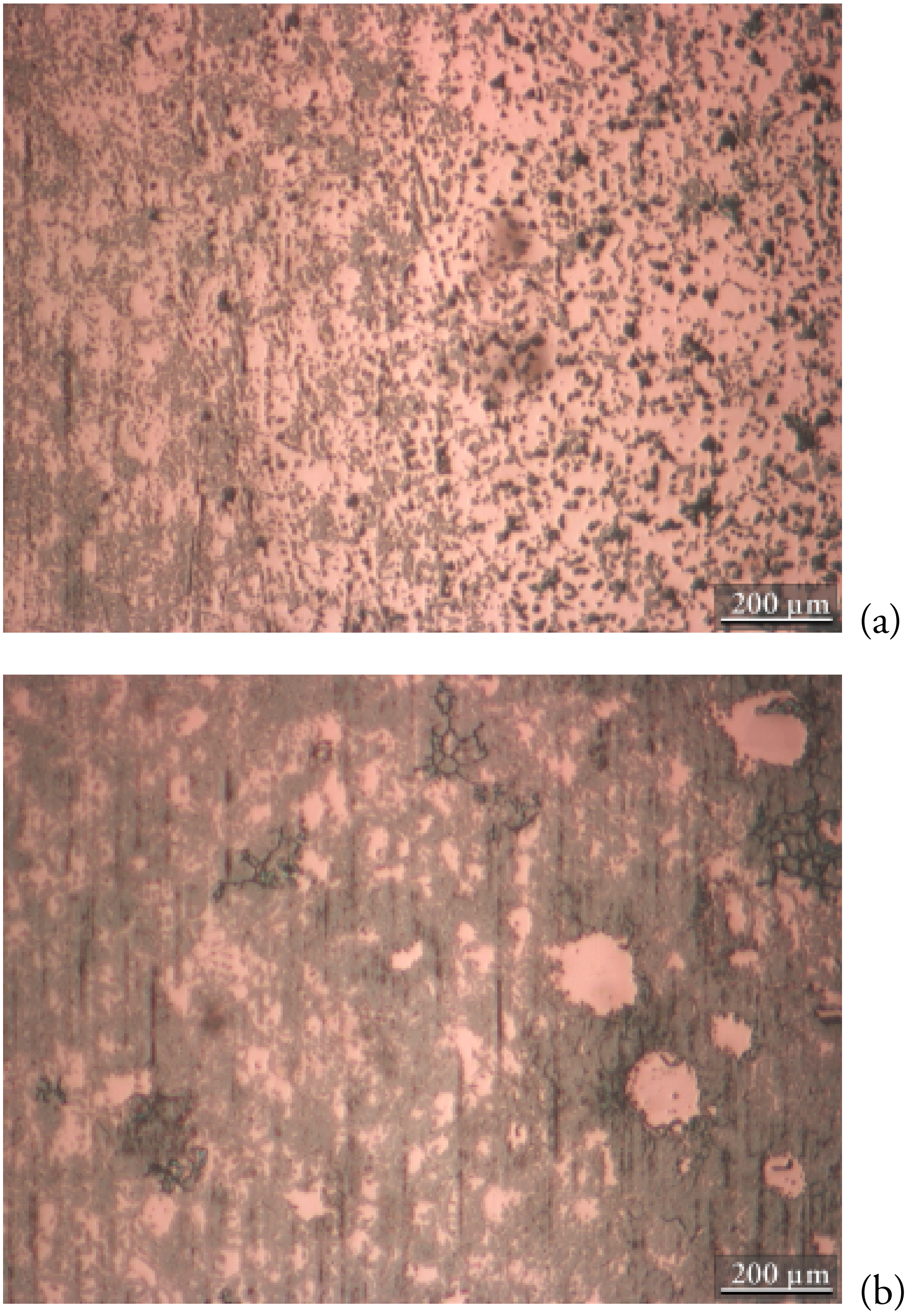

Figure 4.7: Optical micrographs illustrating the typical morphologies observed within the sapphire sample produced in the graphite hot press (1150°C, 5.0 MPa) exhibitting variable amounts of copper coverage.

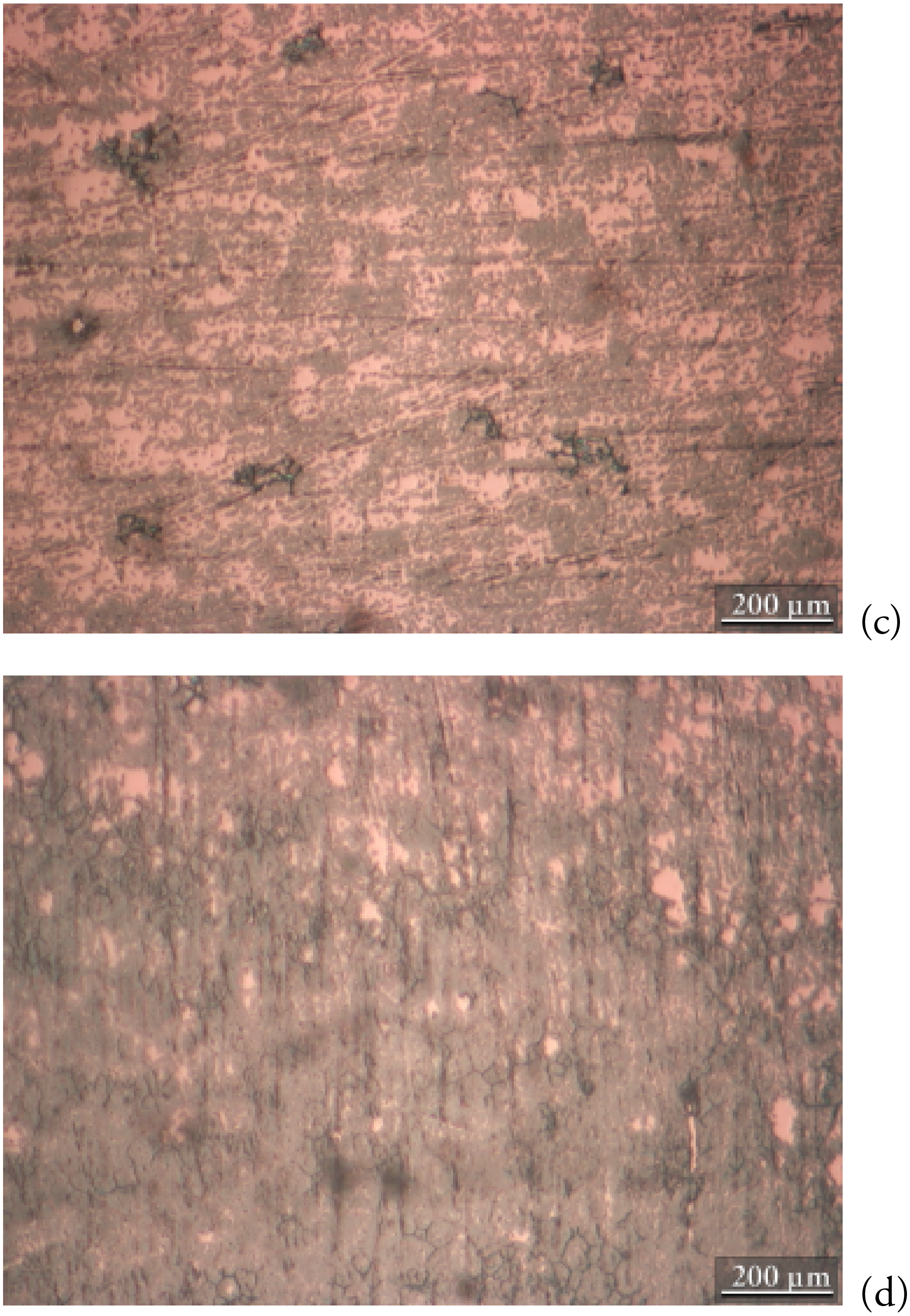

Figure 4.7: Optical micrographs illustrating the typical morphologies observed within the sapphire sample produced in the graphite hot press (1150°C, 5.0 MPa) exhibitting variable amounts of copper coverage.

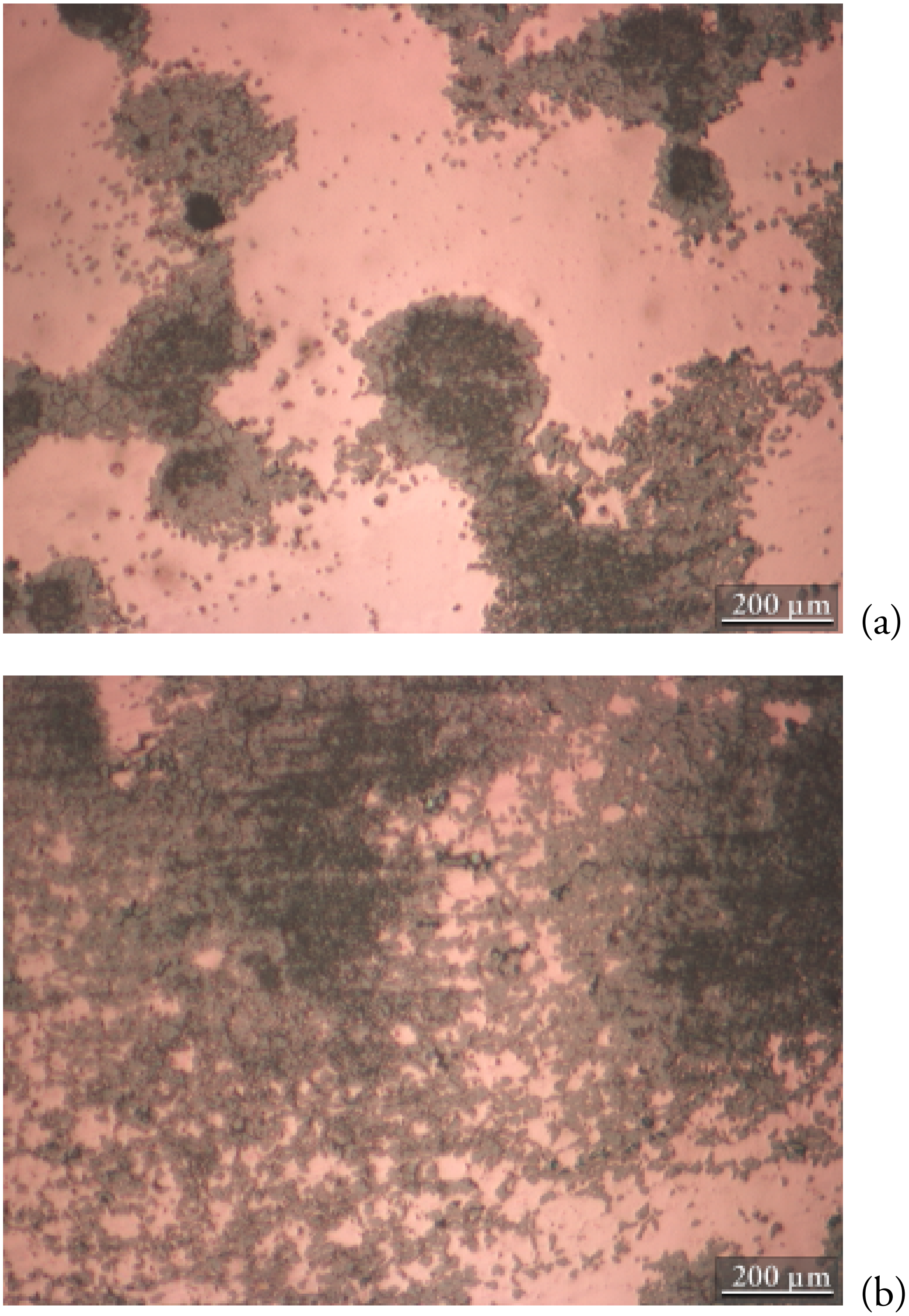

Figure 4.8: Optical micrographs illustrating the typical morphologies observed within the sapphire sample produced in the graphite hot press (1150°C, 1.6 MPa) exhibitting variable amounts of copper coverage.

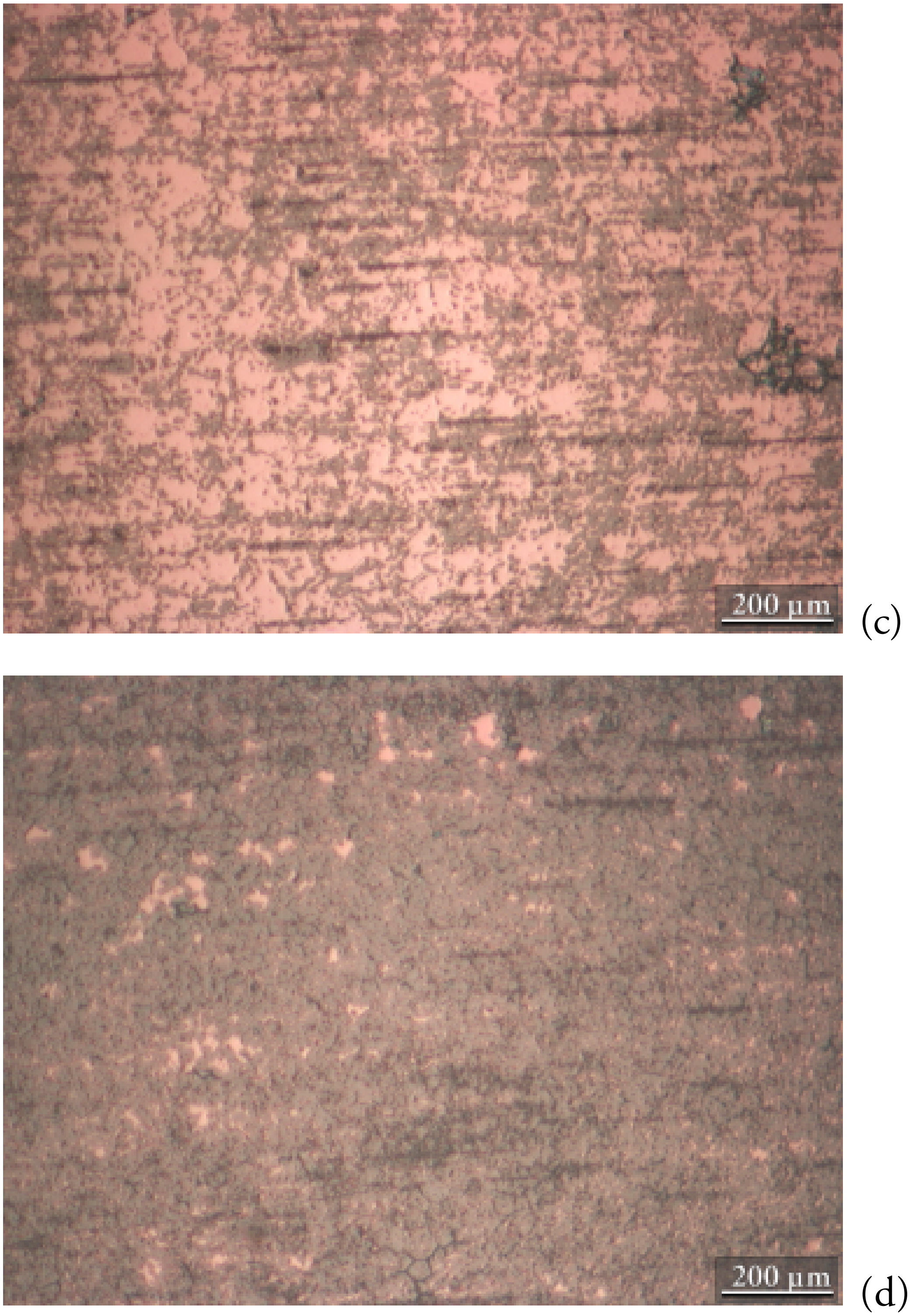

Figure 4.8: Optical micrographs illustrating the typical morphologies observed within the sapphire sample produced in the graphite hot press (1150°C, 1.6 MPa) exhibitting variable amounts of copper coverage.

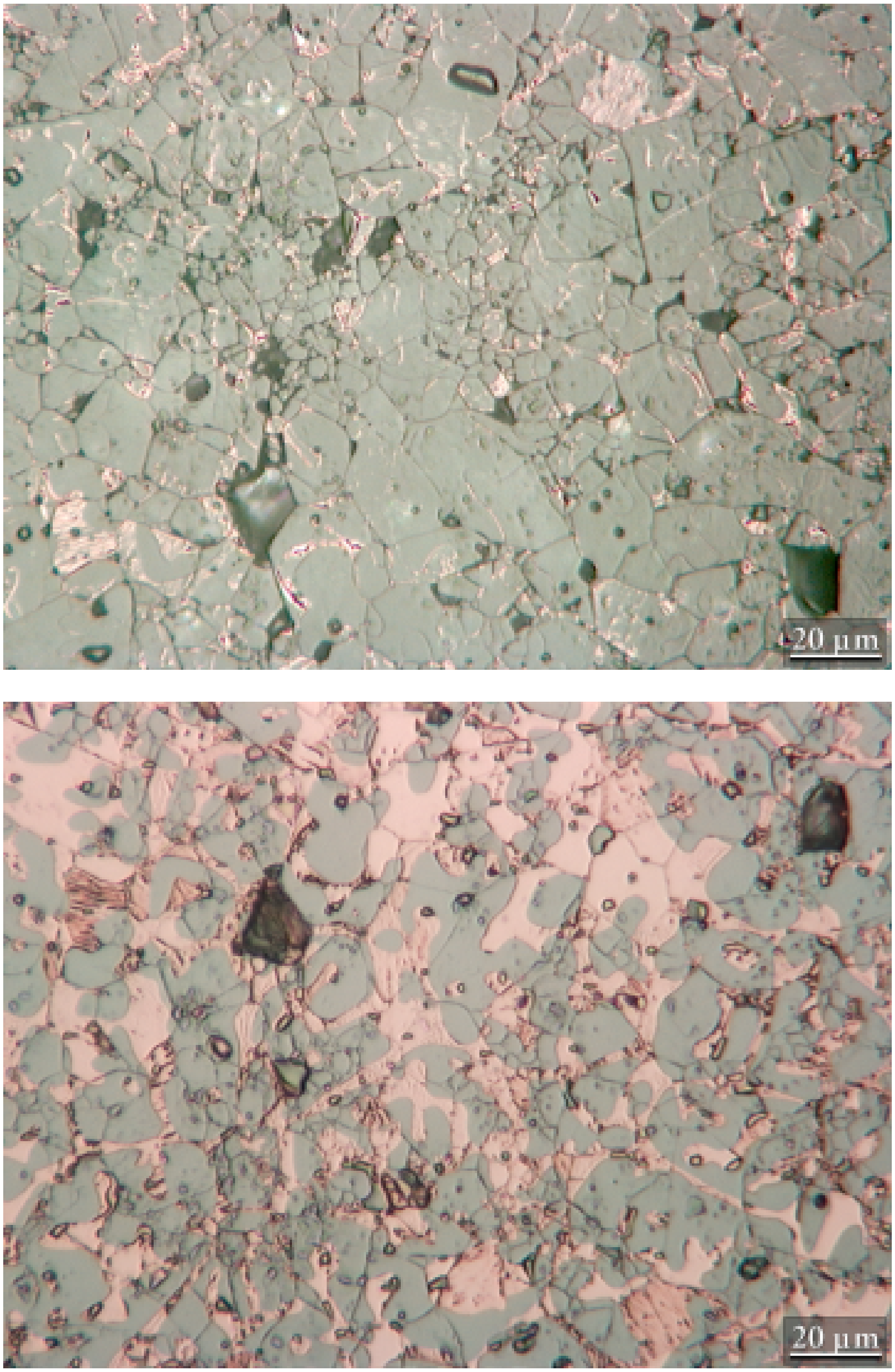

Figure 4.9: Optical micrographs of the ceramic (top) and metal (bottom) sides of the fracture surface of BK29BM24 which failed at 120 MPa. The beam is from a joint processed in the molybdenum hot press at 1150°C and ≈7.5 MPa.

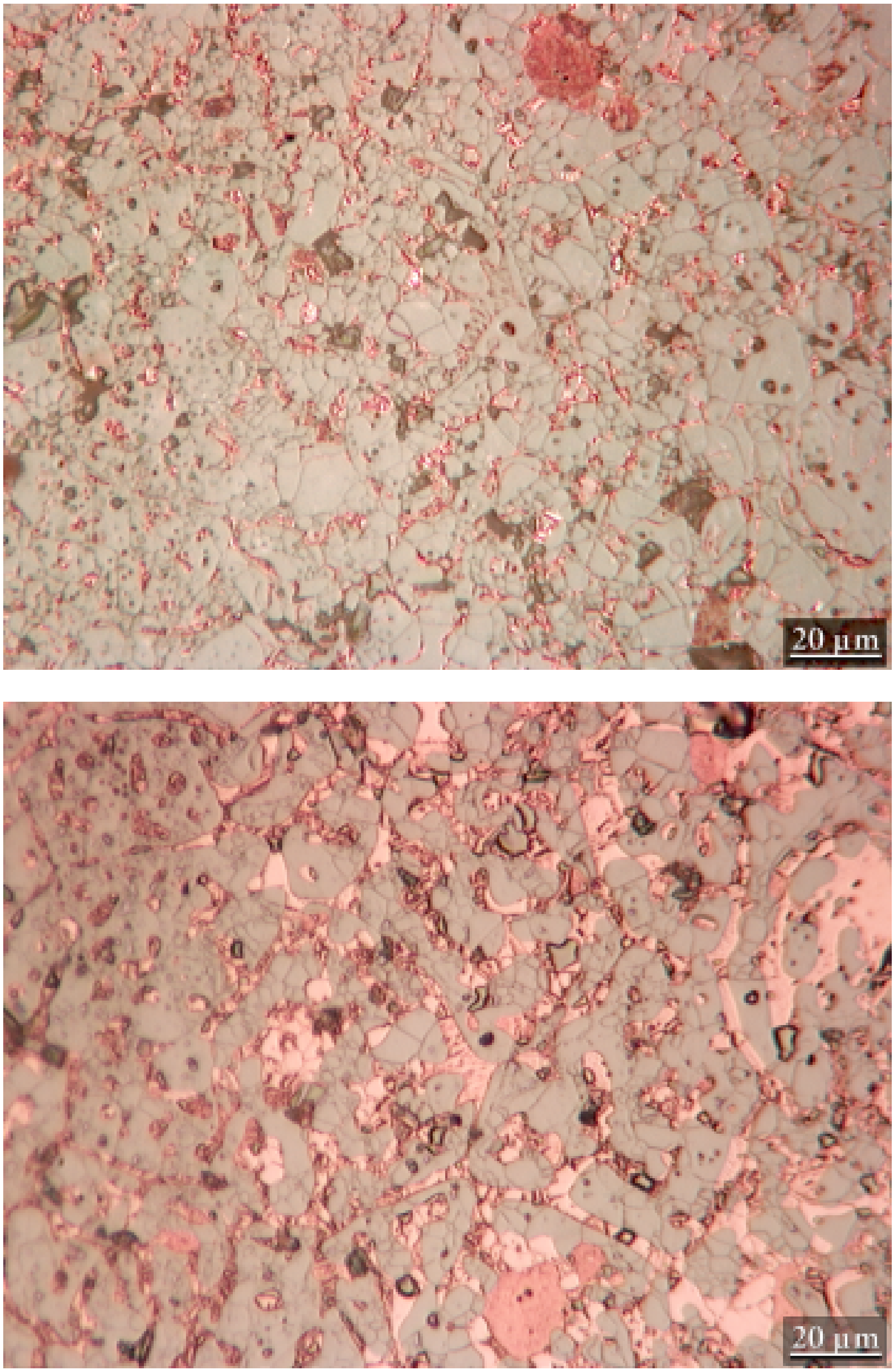

Figure 4.10: Optical micrographs of the ceramic (top) and metal (bottom) sides of the fracture surface of BK30BM34 which failed at 140 MPa. The beam is from a joint processed in the graphite hot press at 1150°C and 2.2 MPa.

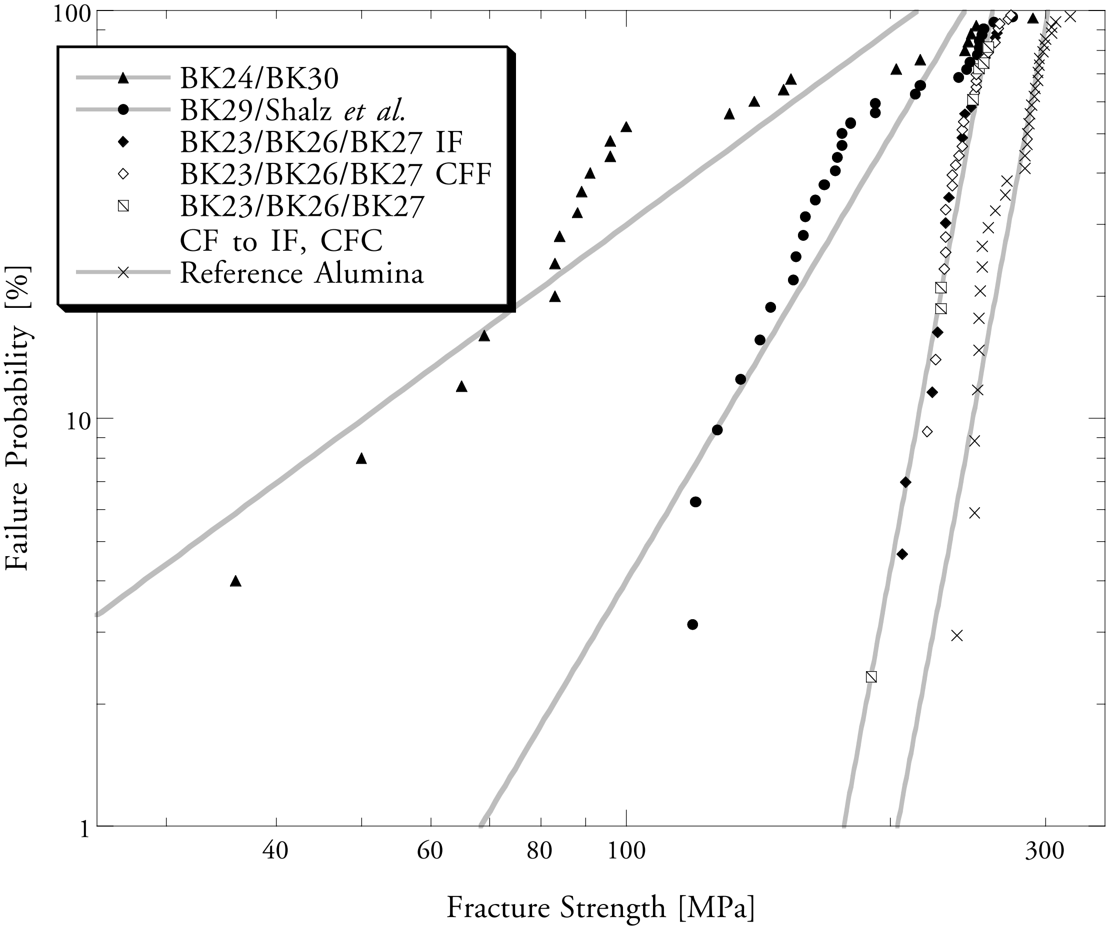

Figure 4.11: Failure probability for joints processed at 1400°C (BK23/BK26/BK27) in comparison to bulk Coors alumina [127,128] strength and joints processed at 1150°C.

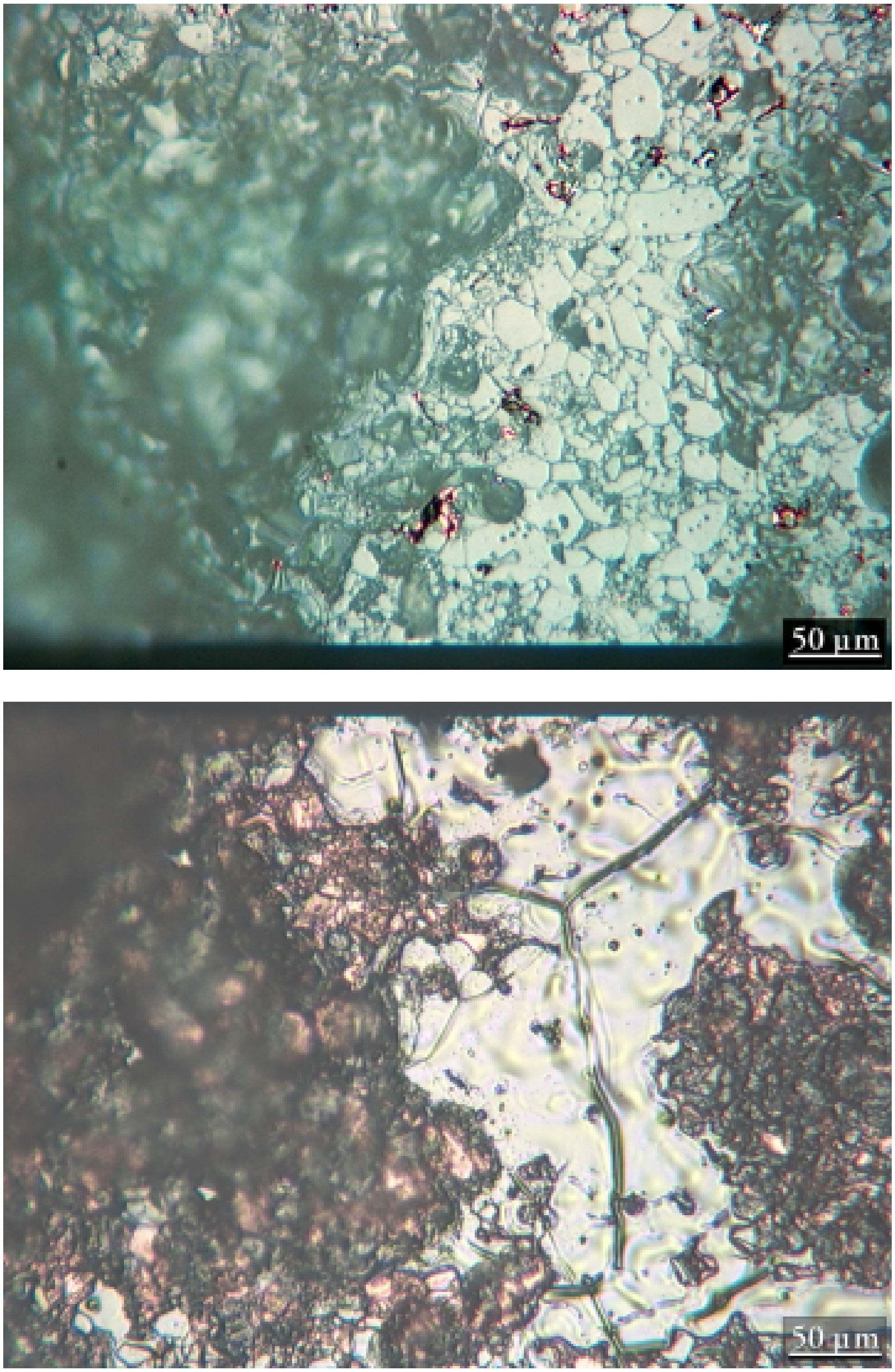

Figure 4.12: Optical micrographs of the ceramic (top) and metal (bottom) sides of the fracture surface of BK23BM25 which failed at 226 MPa. The beam is from a joint processed in the graphite hot press at 1400°C and 2.2 MPa.

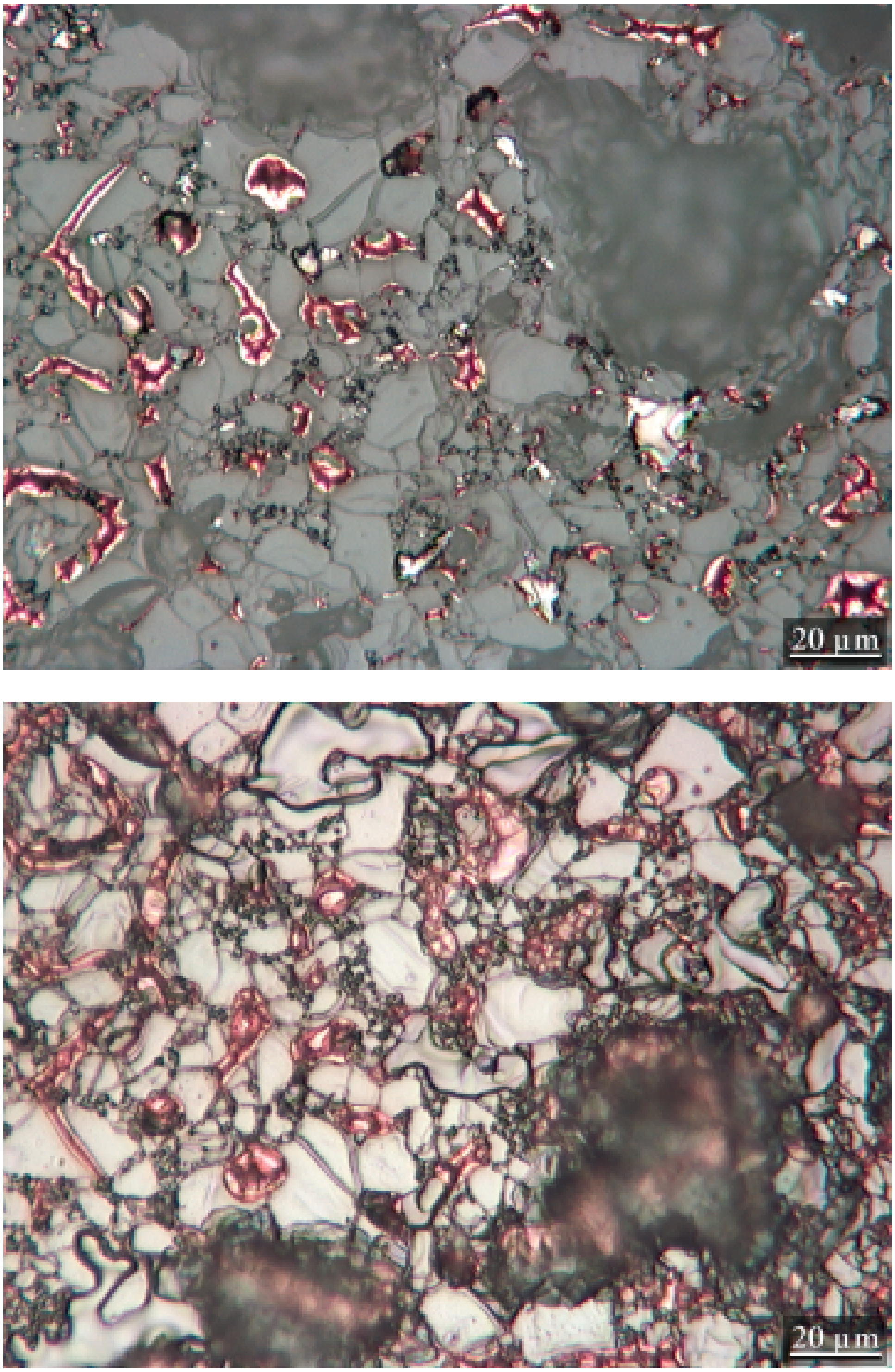

Figure 4.13: Optical micrographs of the ceramic (top) and metal (bottom) sides of the fracture surface of BK23BM24 which failed at 263 MPa. The beam is from a joint processed in the graphite hot press at 1400°C and 2.2 MPa.

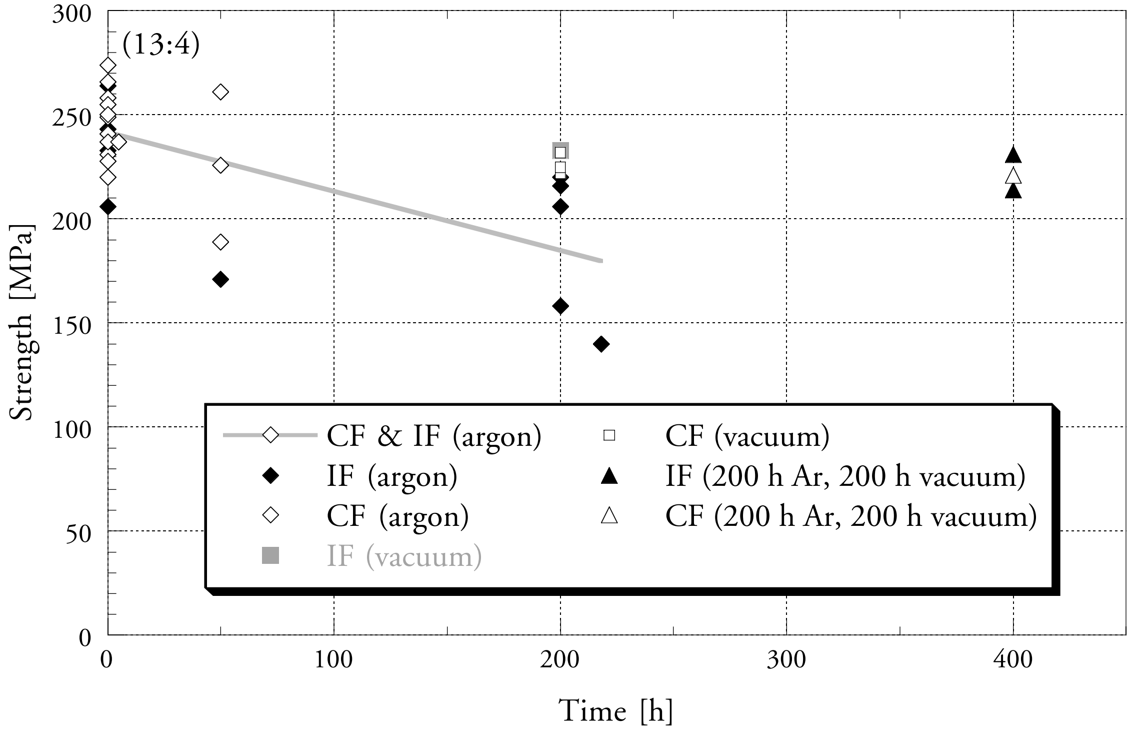

Figure 4.14: Plot of the failure strength of beams (from BK26 and BK27) against total annealing time in gettered argon and vacuum at 1000°C. The curve fit is for the strength data resulting from unannealed beams and those annealed in argon only. 13:4 indicates the CF:IF ratio for unannealed beams.

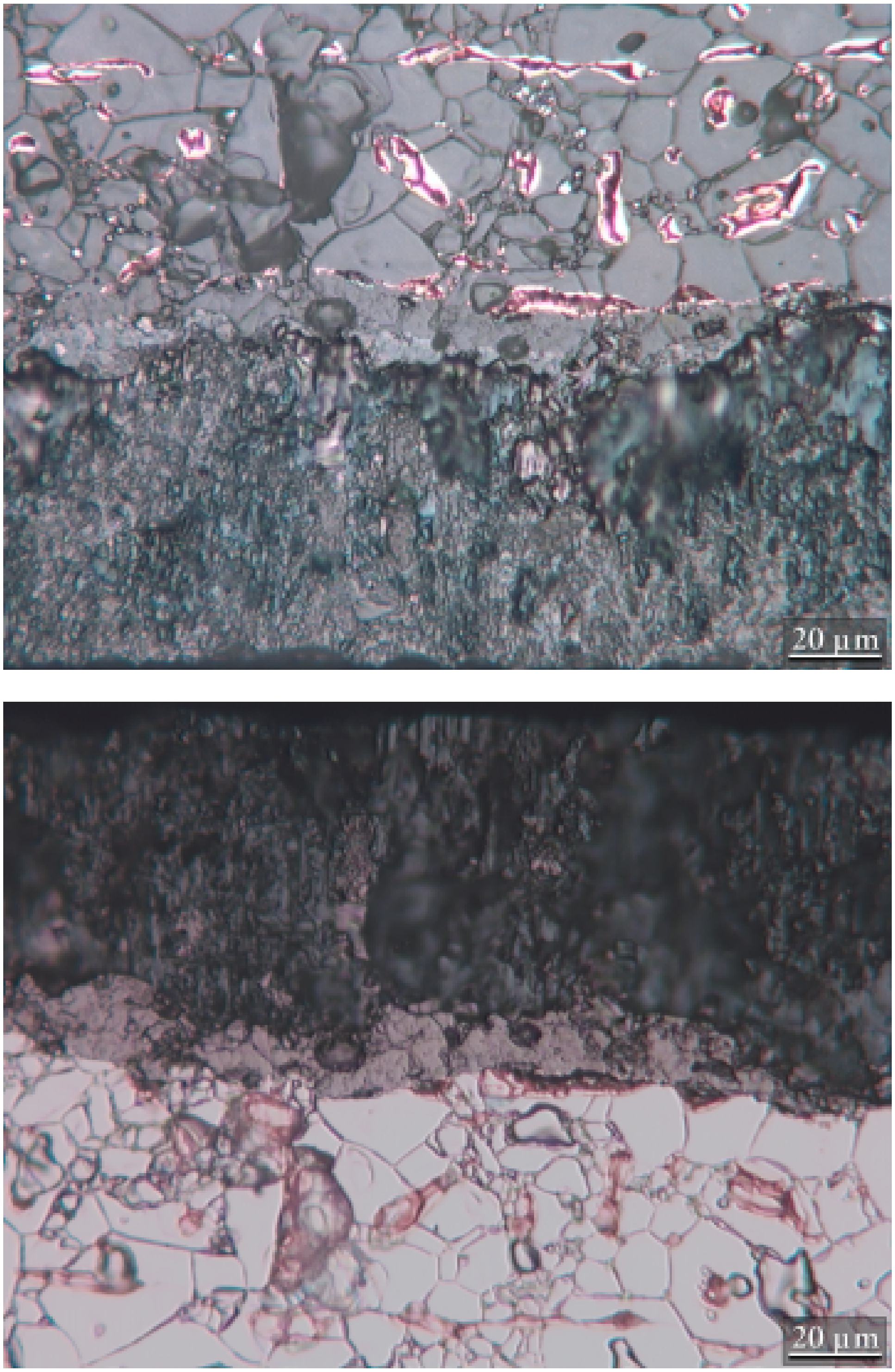

Figure 4.15: Optical micrographs of the ceramic (top) and metal (bottom) sides of a beam annealed (Anneal 5, see Table 4.6) in gettered-argon. The image is taken near the edge of the beam, where a reaction layer formed as a result of annealing. This beam failed at 140 MPa.

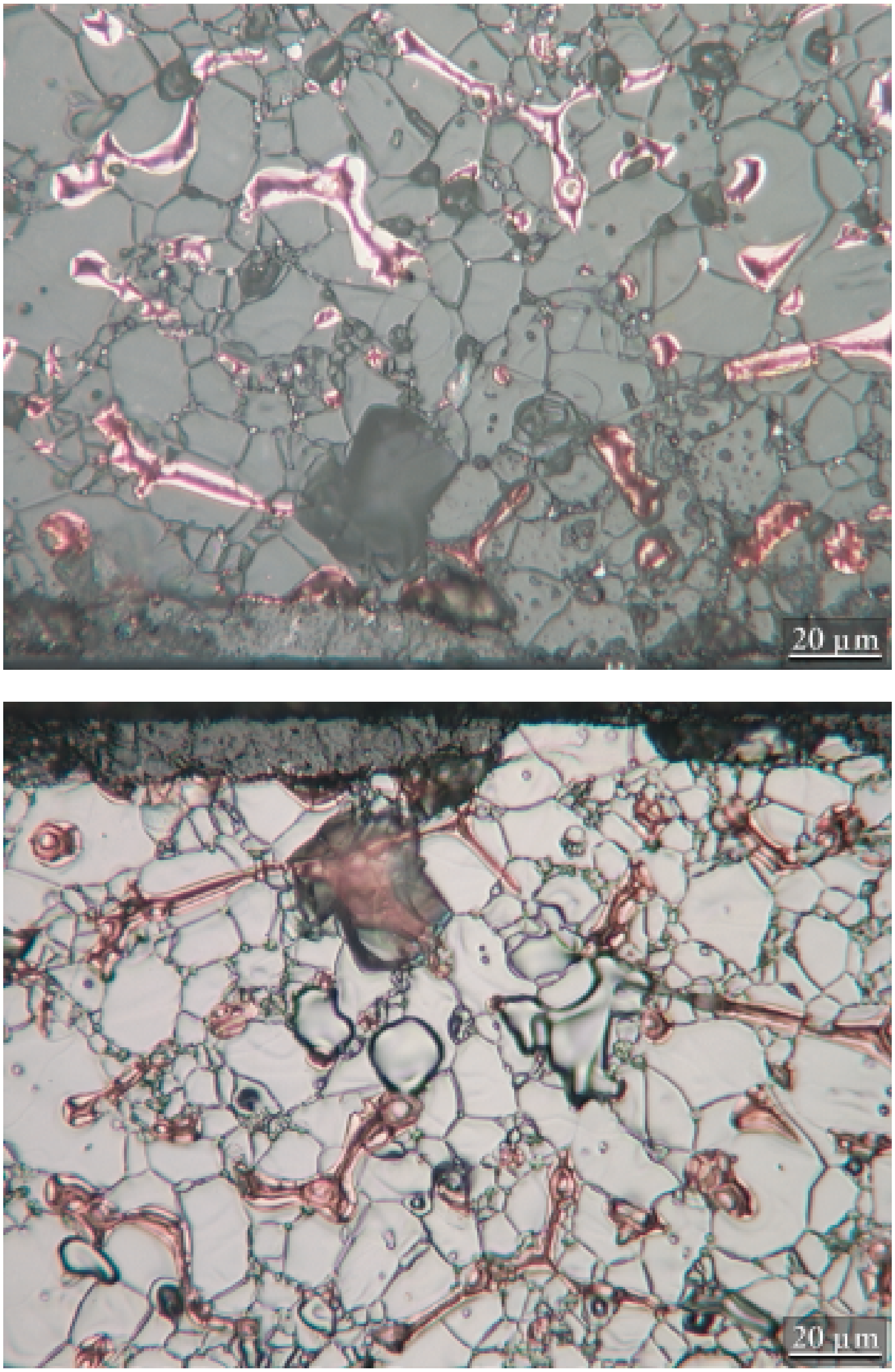

Figure 4.16: Optical micrographs of the ceramic (top) and metal (bottom) sides of a beam annealed (Anneal 7, see Table 4.6) in gettered-argon. The image is taken near the edge of the beam, where a reaction layer formed as a result of annealing. This beam failed at 216 MPa.

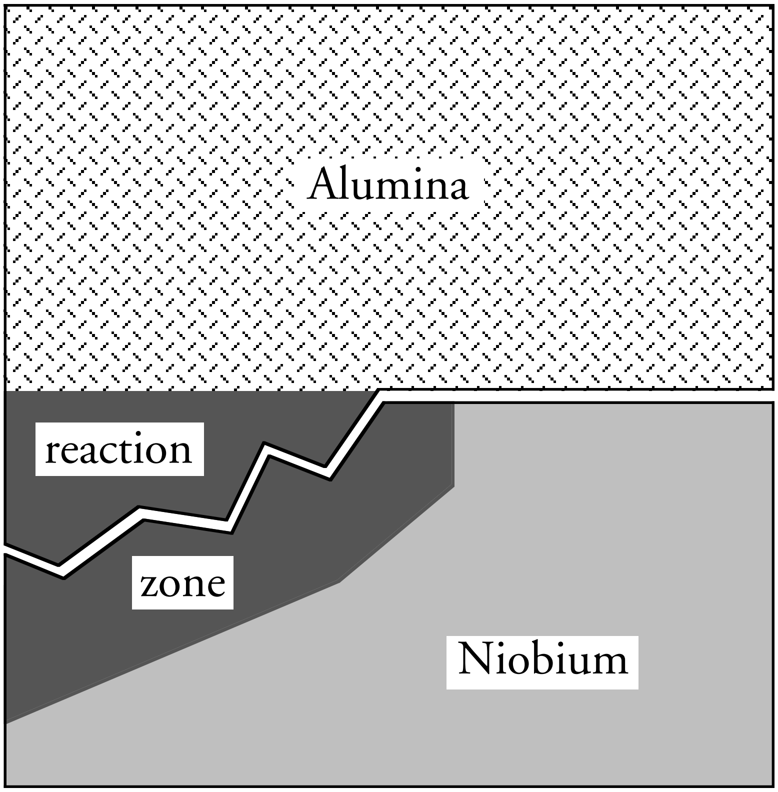

Figure 4.17: Schematic of crack propagation in niobium/alumina joint with brittle reaction layer. The crack may also initiate at the niobium/reaction layer interface; however, optical microscopy suggests it does not initiate at the alumina/reaction layer interface.

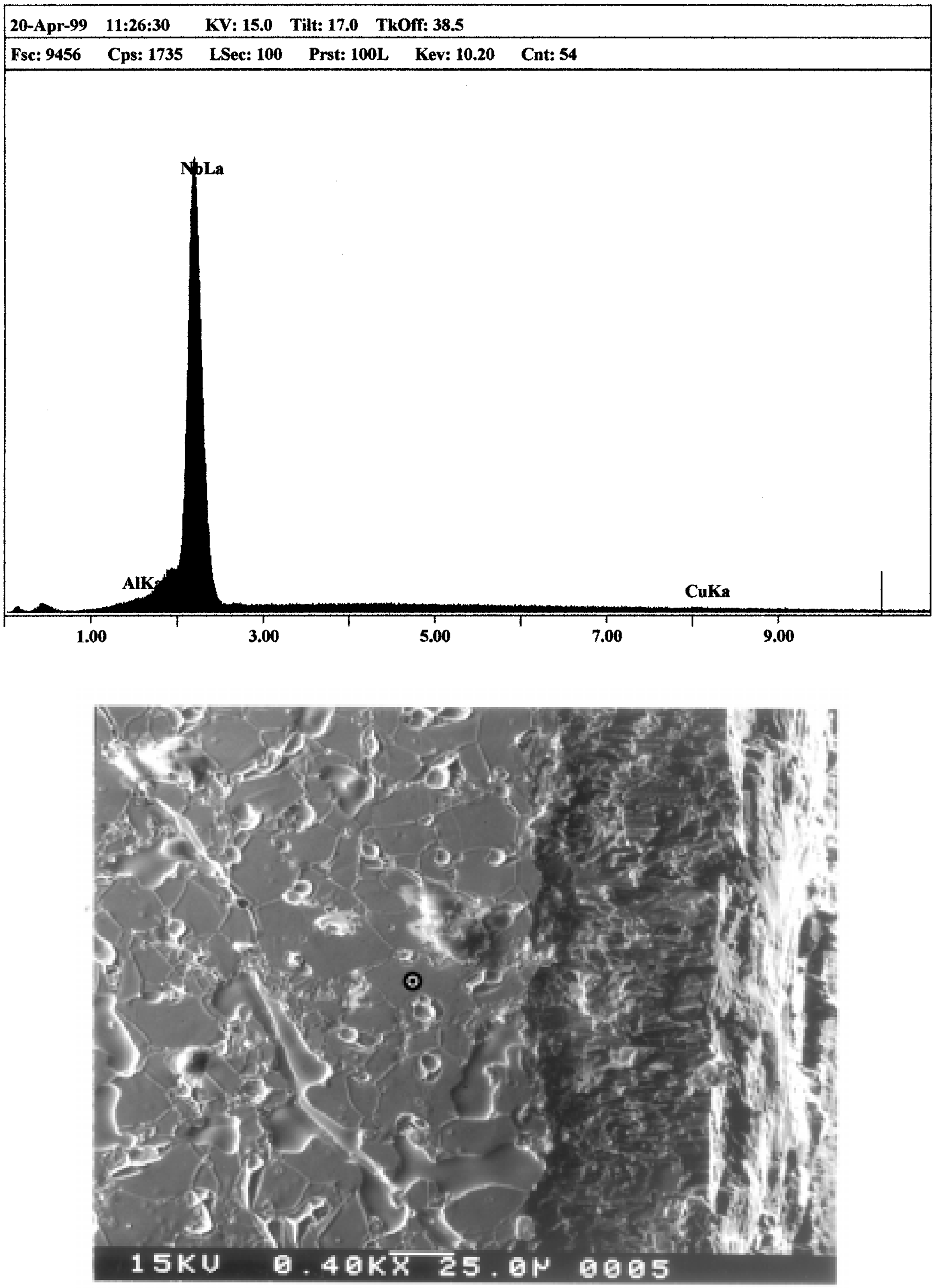

Figure 4.18a: EDS results from the metal side of a beam annealed in gettered-argon (Anneal 5) for 200 h at 1000°C. The target spot (◉) on the image indicates the portion of the sample from which the EDS data was collected, *i.e.*, outside the reaction layer region.

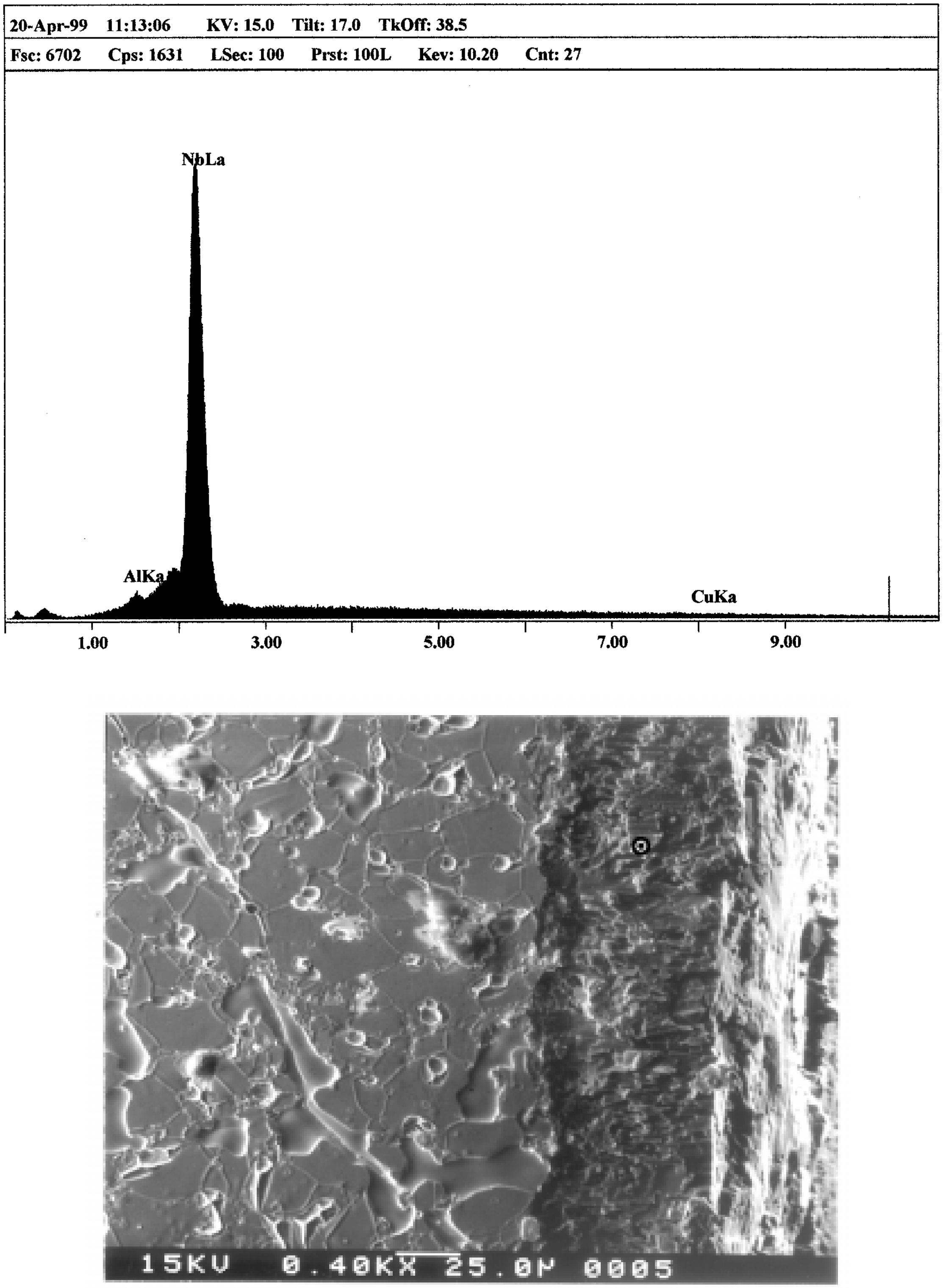

Figure 4.18b: EDS results from the metal side of a beam annealed in gettered-argon (Anneal 5) for 200 h at 1000°C. The target spot (◉) on the image indicates the portion of the sample from which the EDS data was collected, *i.e.*, within the reaction layer region.

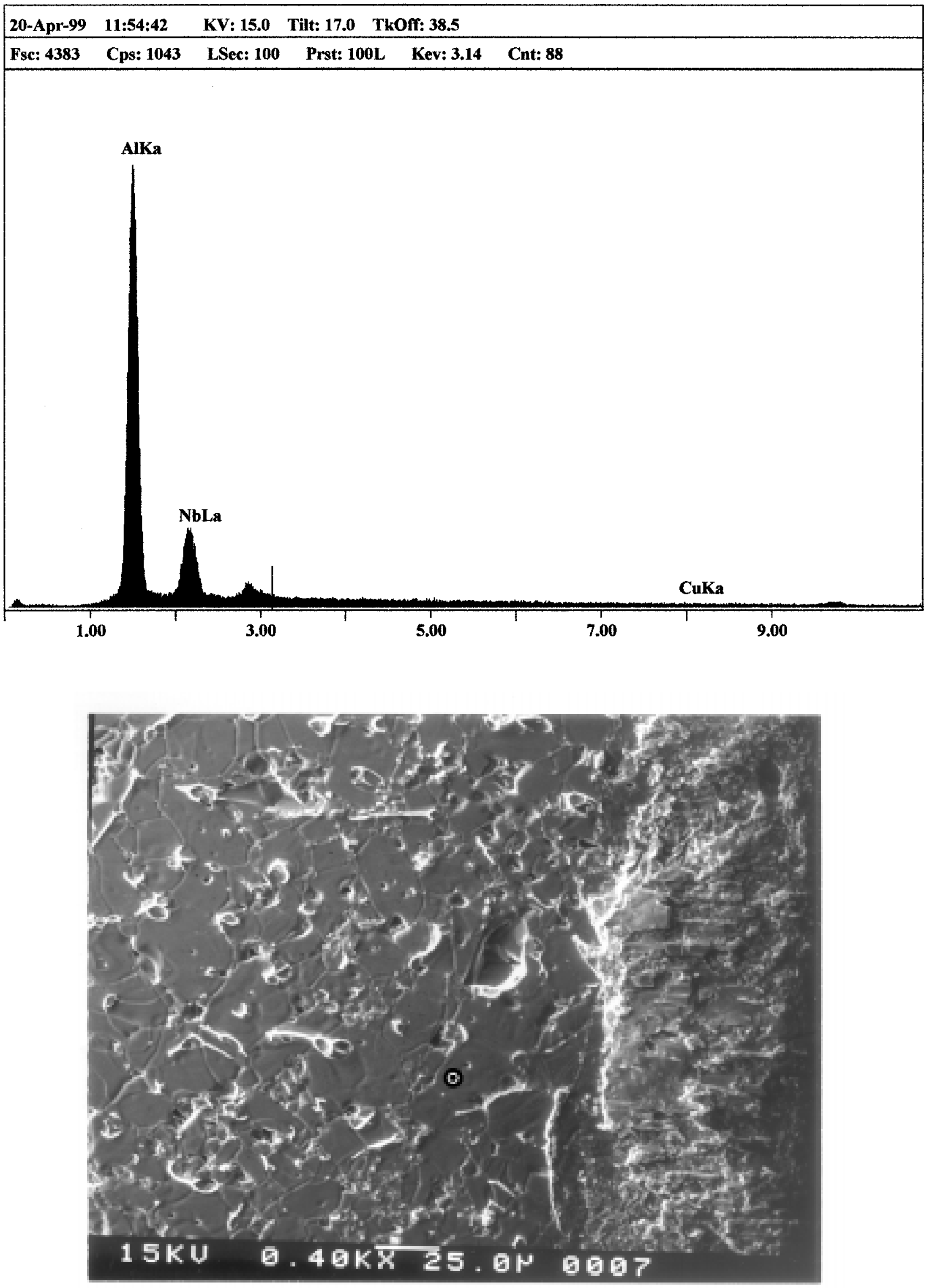

Figure 4.19a: EDS results from the ceramic side of a beam annealed in gettered-argon (Anneal 5) for 200 h at 1000°C. The target spot (◉) on the image indicates the portion of the sample from which the EDS data was collected, *i.e.*, outside the reaction layer region.

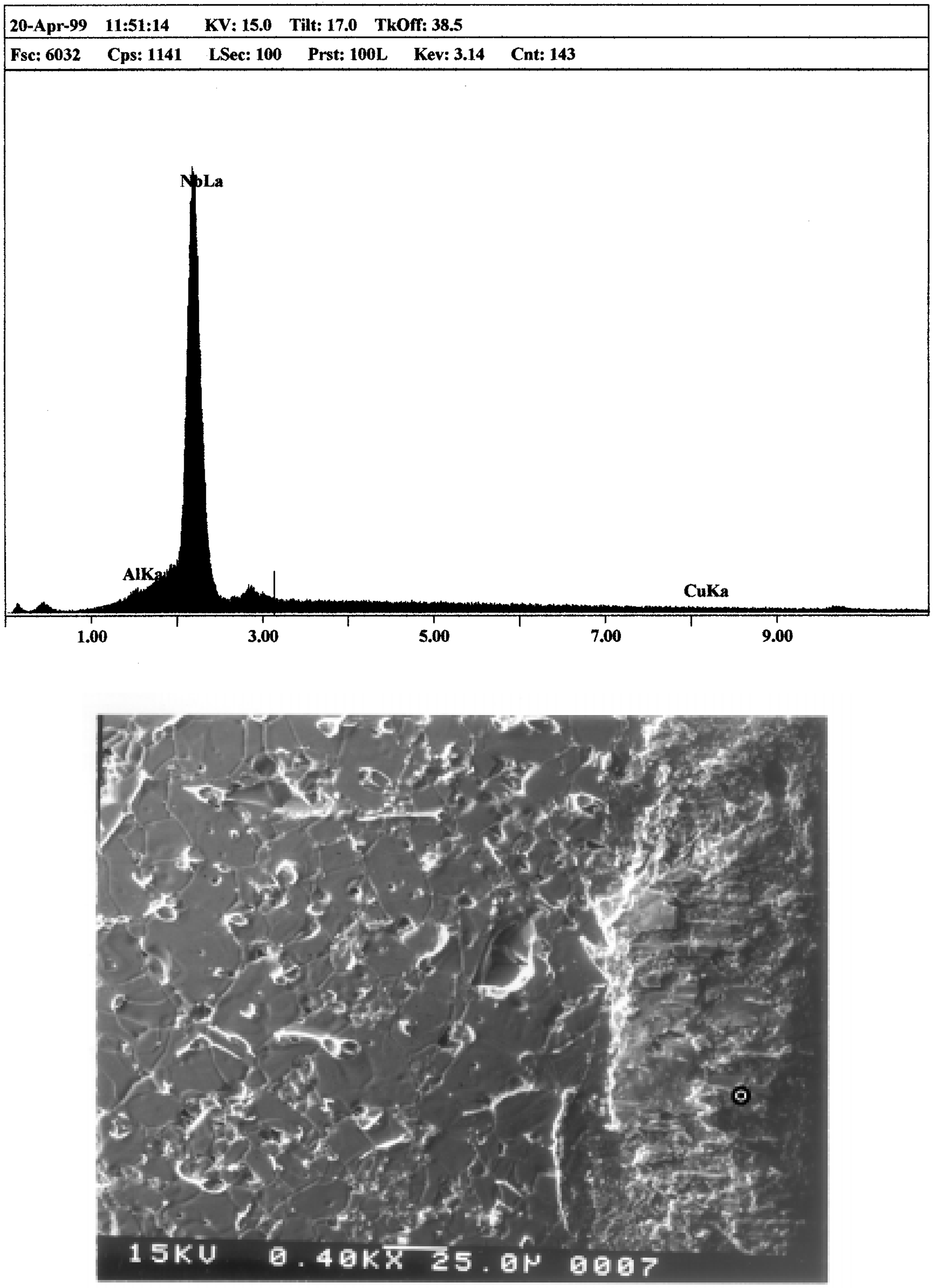

Figure 4.19b: EDS results from the ceramic side of a beam annealed in gettered-argon (Anneal 5) for 200 h at 1000°C. The target spot (◉) on the image indicates the portion of the sample from which the EDS data was collected, *i.e.*, within the reaction layer region.

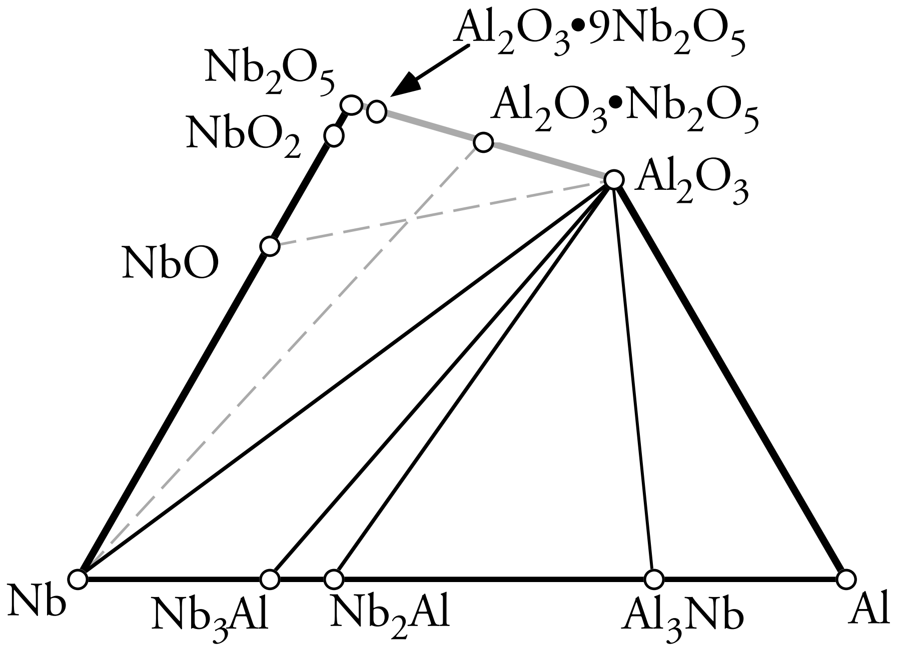

Figure 4.20: Schematic aluminum-niobium-oxygen ternary phase diagram. Other niobium aluminates (Al_2O_3•11Nb_2O_5, Al_2O_3•25Nb_2O_5, and Al_2O_3•49Nb_2O_5) are also reported in the Powder Diffraction File; however, little is reported about their stability. Al_2O_3•11Nb_2O_5 can be formed by firing a mixture of alumina and niobia (Nb_2O_5) powders at 1350°C. Al_2O_3•Nb_2O_5, Al_2O_3•9Nb_2O_5 and Al_2O_3•25Nb_2O_5 are found in an alumina-niobia phase diagram [134].

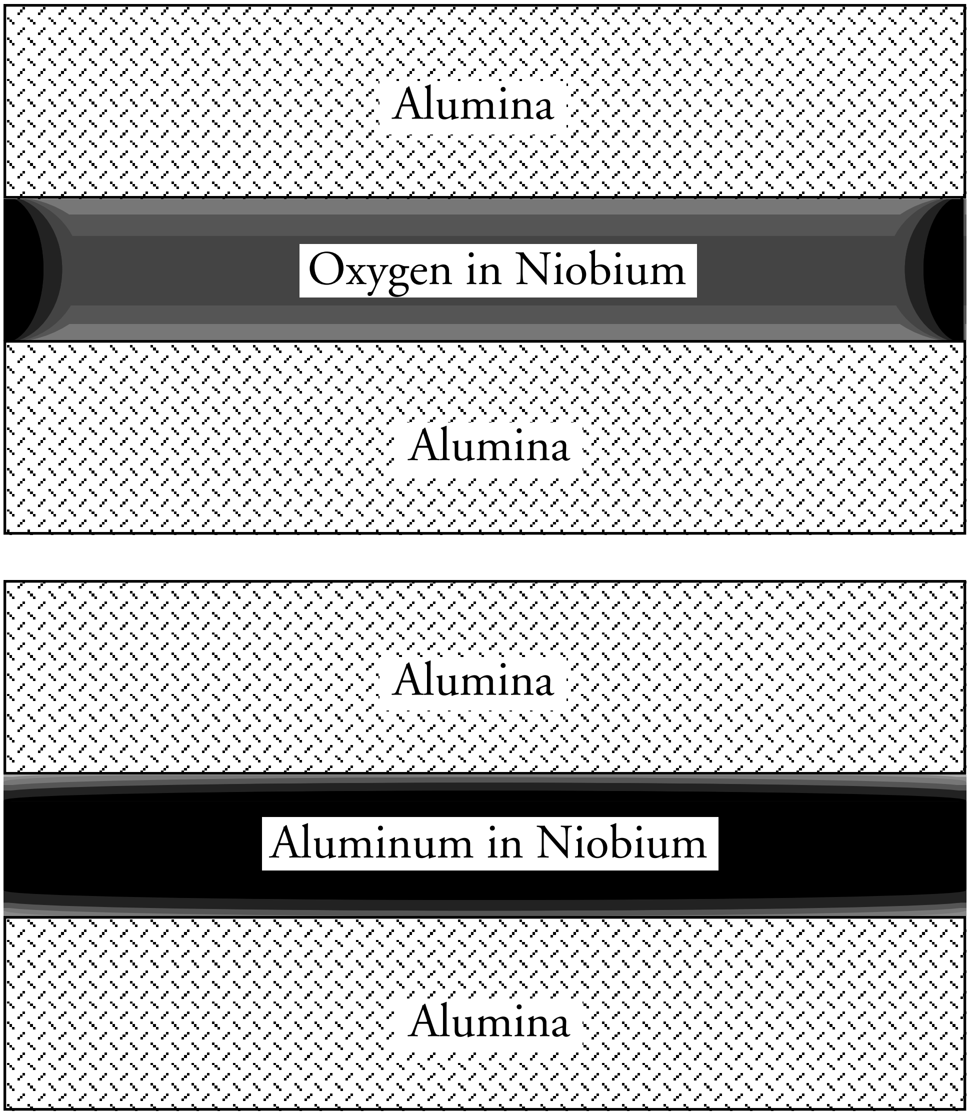

Figure 4.21: Schematic of oxygen (top) and aluminum (bottom) diffusion profile in niobium/alumina couple at low ambient p_{O_2}. An analogy to the oxygen diffusion profile would be to consider the temperature profile of a thin metal slab being heated from the large area surfaces and cooled from the small area edges; higher temperatures being analogous to higher oxygen content. As in other studies on alumina dissolution by niobium [19,20,80,83,131], this schematic assumes there is no coupling between these two diffusing species. Lighter regions represent more heavily concentrated regions of oxygen (top) and aluminum (bottom) respectively.

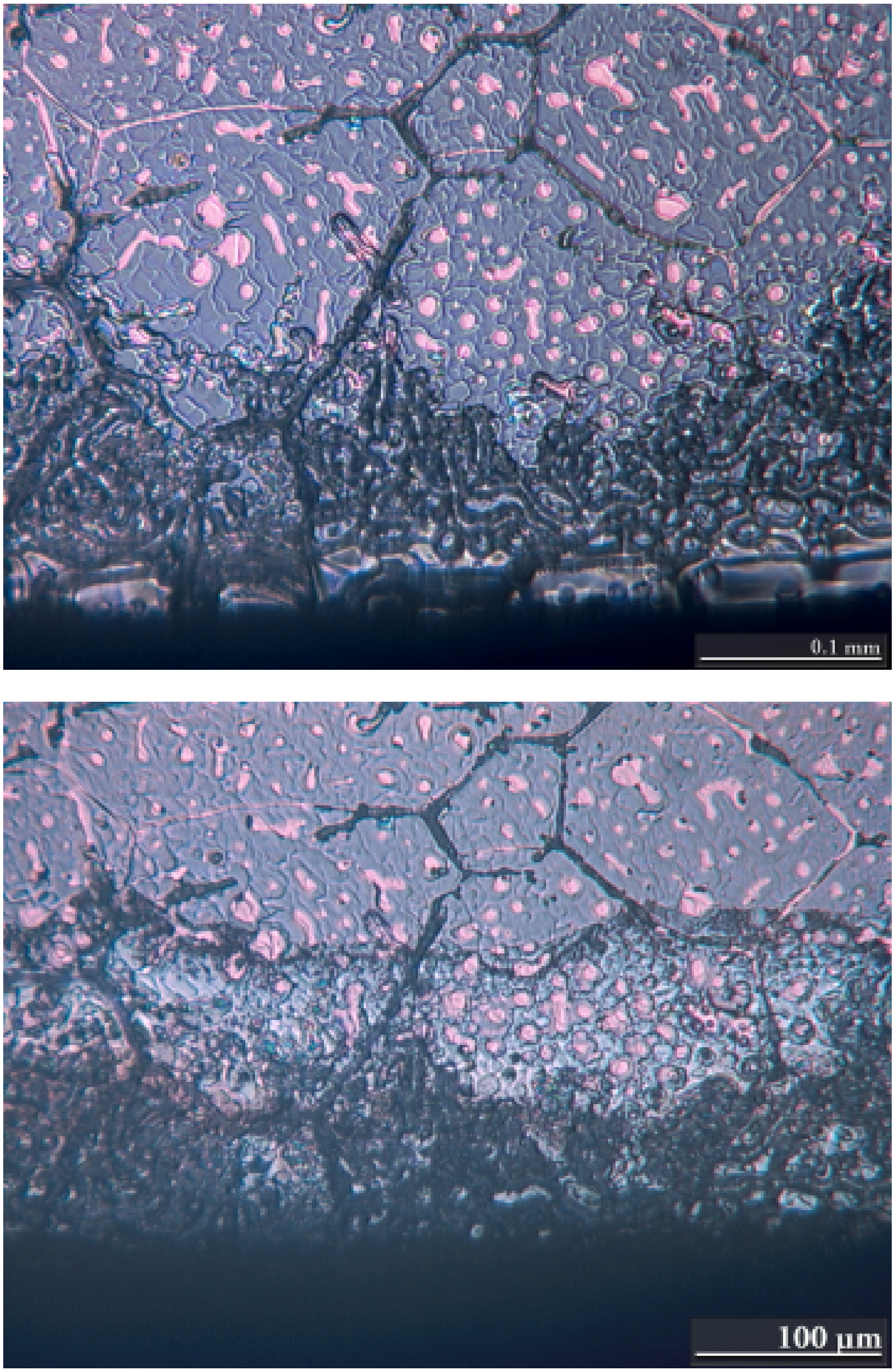

Figure 4.22: Optical micrographs of sapphire couple before (top) and after (bottom) annealing in gettered-argon for 218 h at 1000°C. The image is taken near the edge of the sample, illustrating the reaction layer which formed during Anneal 5.

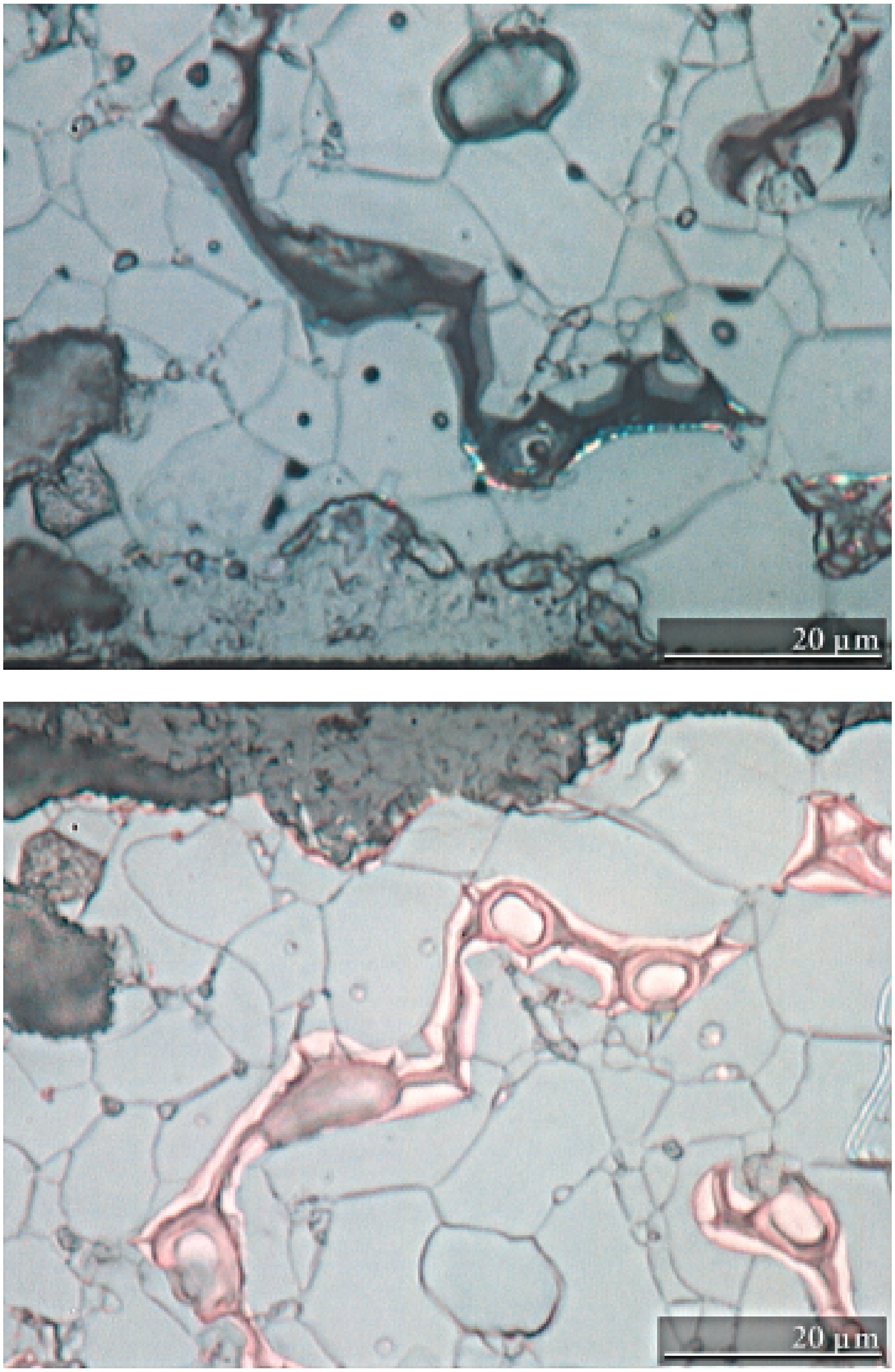

Figure 4.23: Optical micrographs of the ceramic (top) and metal (bottom) sides of a beam annealed (Anneal 7, see Table 4.6) in gettered-argon. The image is taken near the edge of the beam, where a reaction layer formed as a result of annealing. The dark brown appearance of the copper phase on the ceramic side is due to gold-palladium coating. This beam failed at 206 MPa.

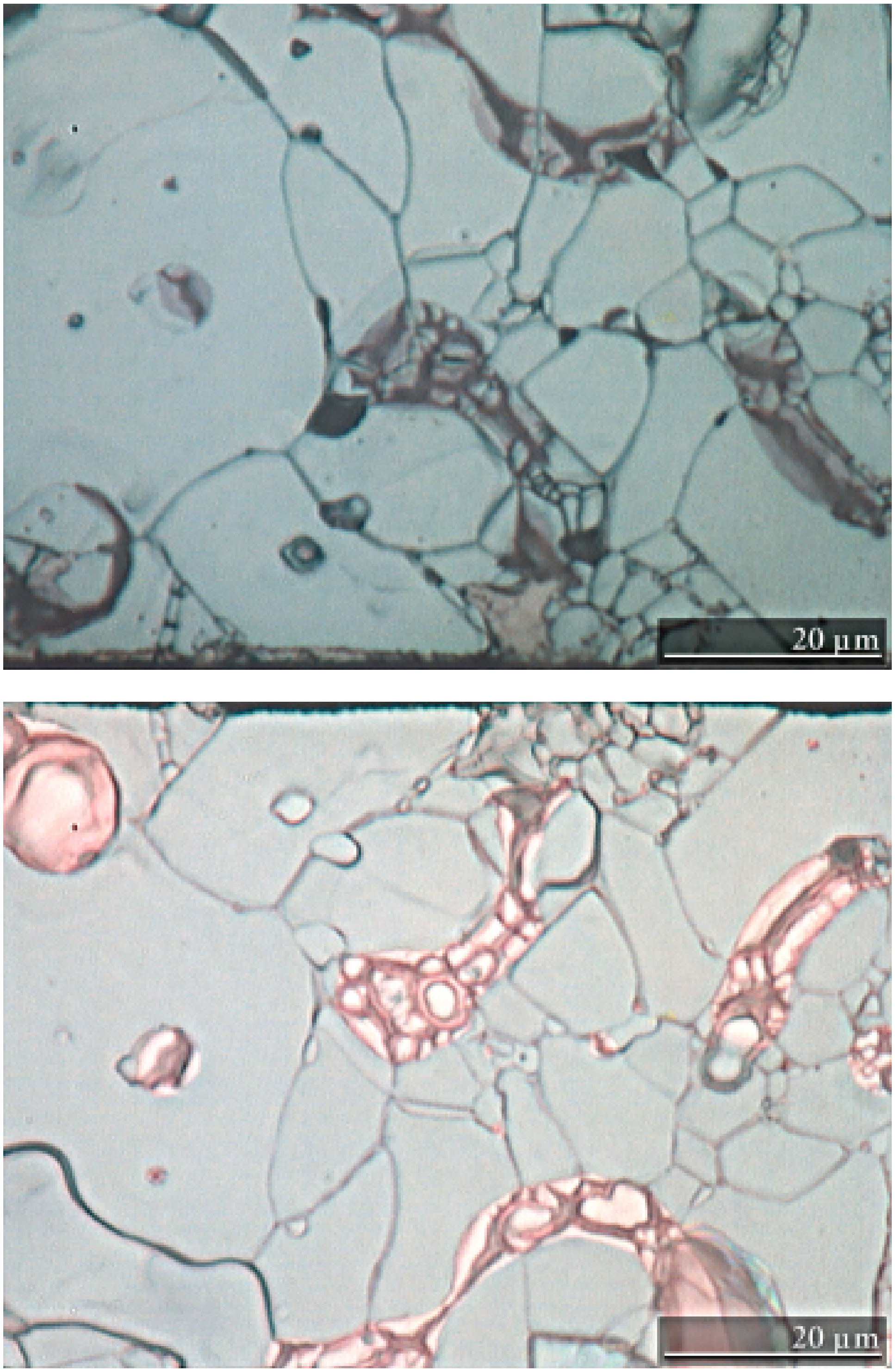

Figure 4.24: Optical micrographs of the ceramic (top) and metal (bottom) sides of a beam annealed (Anneal 8, see Table 4.6) in vacuum. The image is taken near the edge of the beam, no reaction layer is observed. The dark brown appearance of the copper phase on the ceramic side is due to gold-palladium coating. This beam failed at 233 MPa.

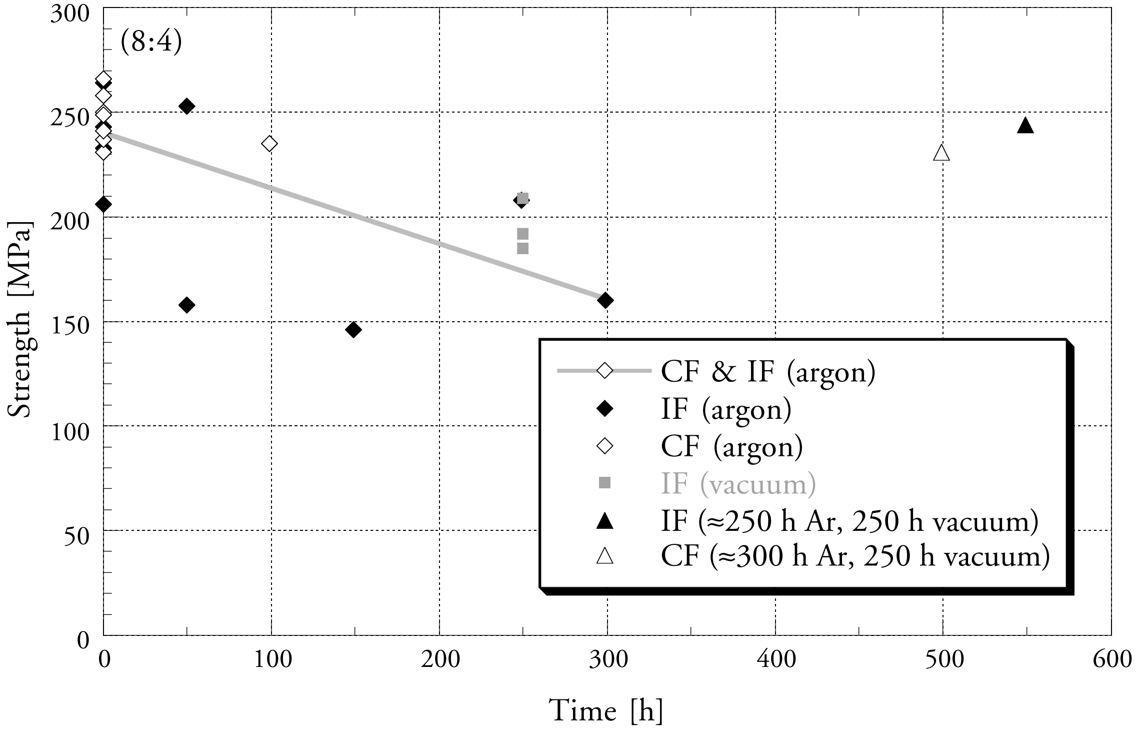

Figure 4.25: Plot of the failure strength of beams against total annealing time in gettered-argon and vacuum at 1200°C. The curve fit is for the strength data resulting from unannealed beams and those annealed in argon only. 8:4 indicates the CF:IF ratio for unannealed beams.

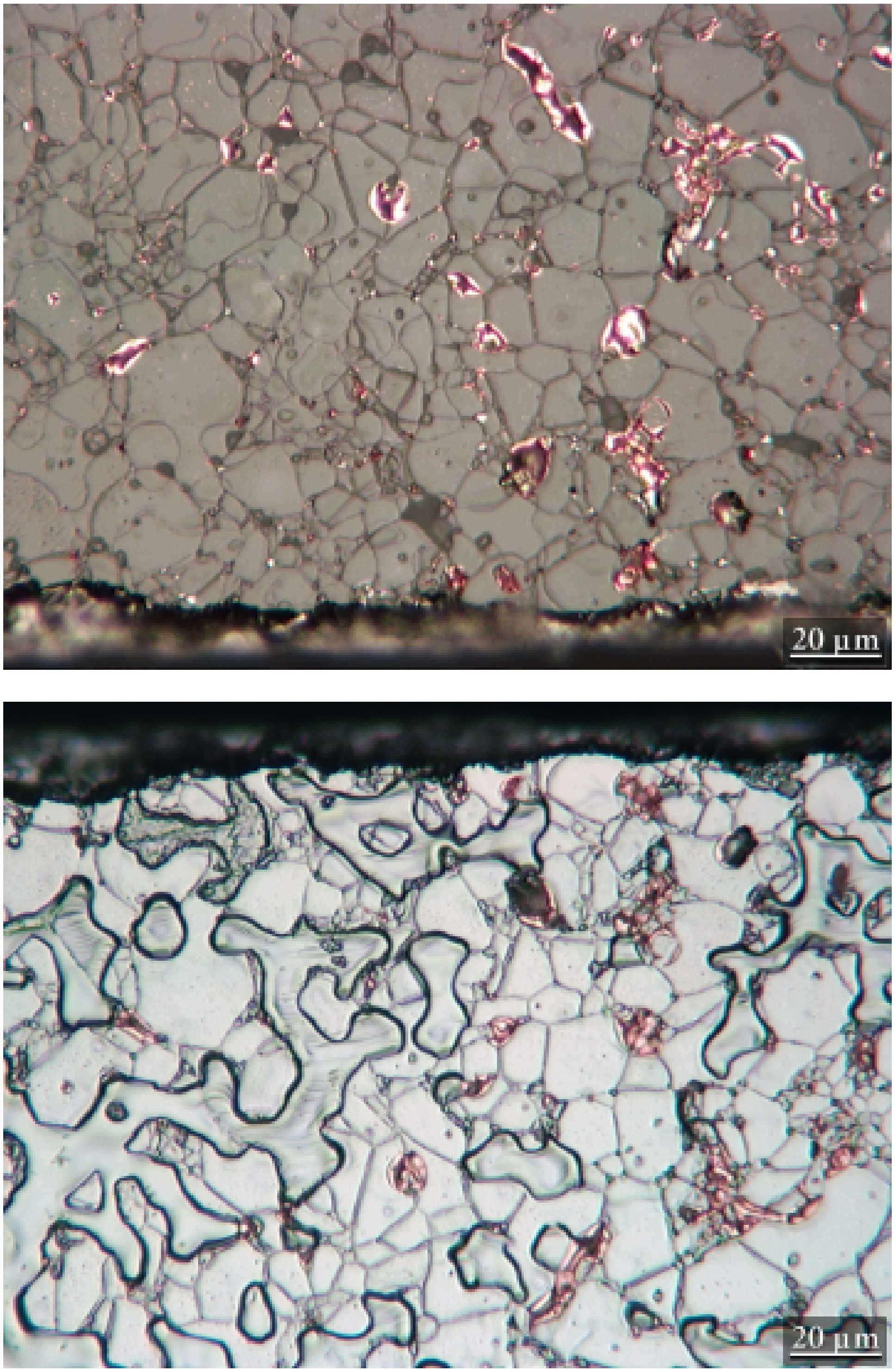

Figure 4.26: Optical micrographs of the ceramic (top) and metal (bottom) sides of a beam annealed in argon (≈150 h at 1200°C, see Table 4.5). This beam failed at 146 MPa.

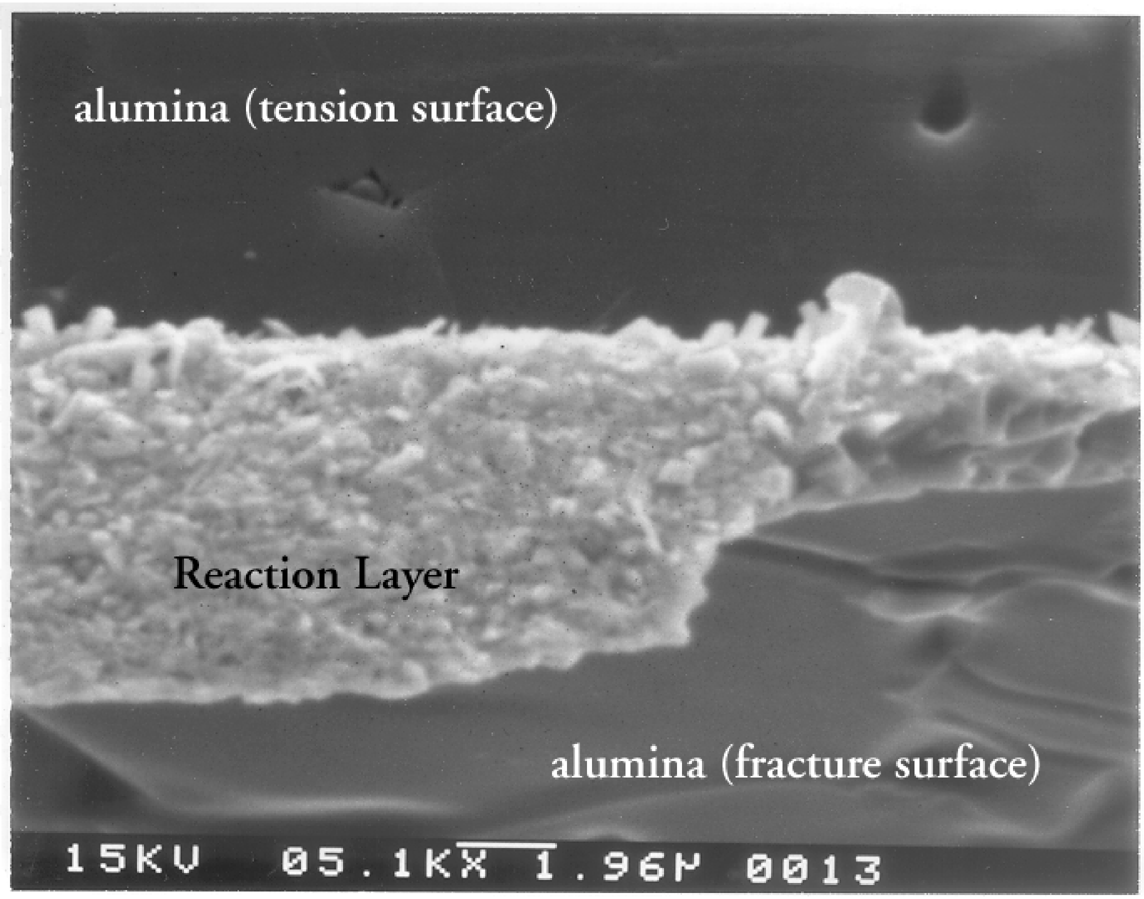

Figure 4.27: SEM micrograph of "reaction layer" observed after argon annealing at 1200°C. The image is taken in cross-section; however, since the sample somewhat tilted (≈20°), a portion of the ceramic side fracture surface can be seen.

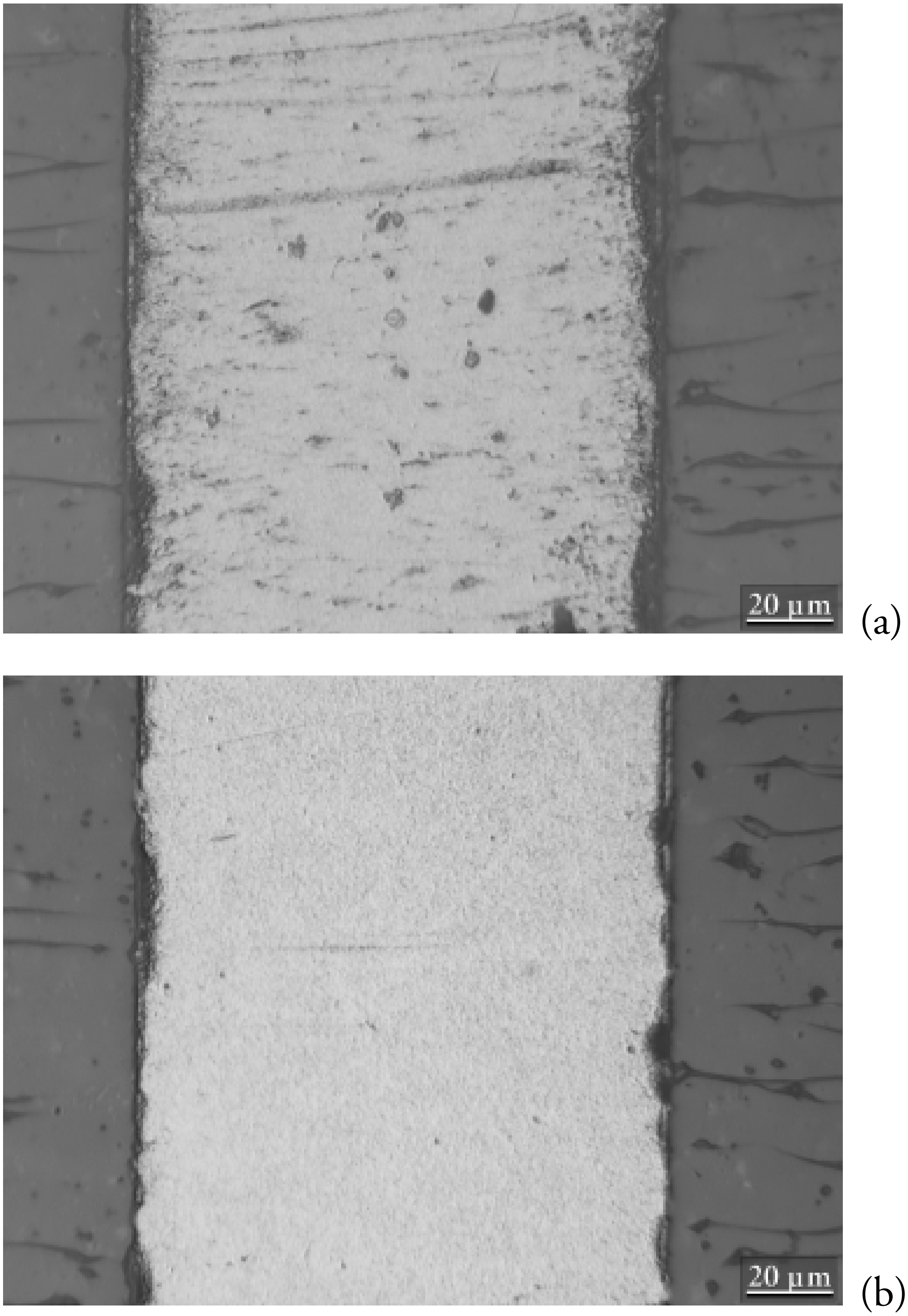

Figure 4.28: Optical micrographs of the interlayers (cross sections) of as processed joints and those annealing in vacuum at 1000°C and 1200°C. (a) as processed (BK27), (b) 200 h, vacuum, 1000°C (BK27), (c) as processed (BK26), (d) 250 h, vacuum, 1200°C (BK26).

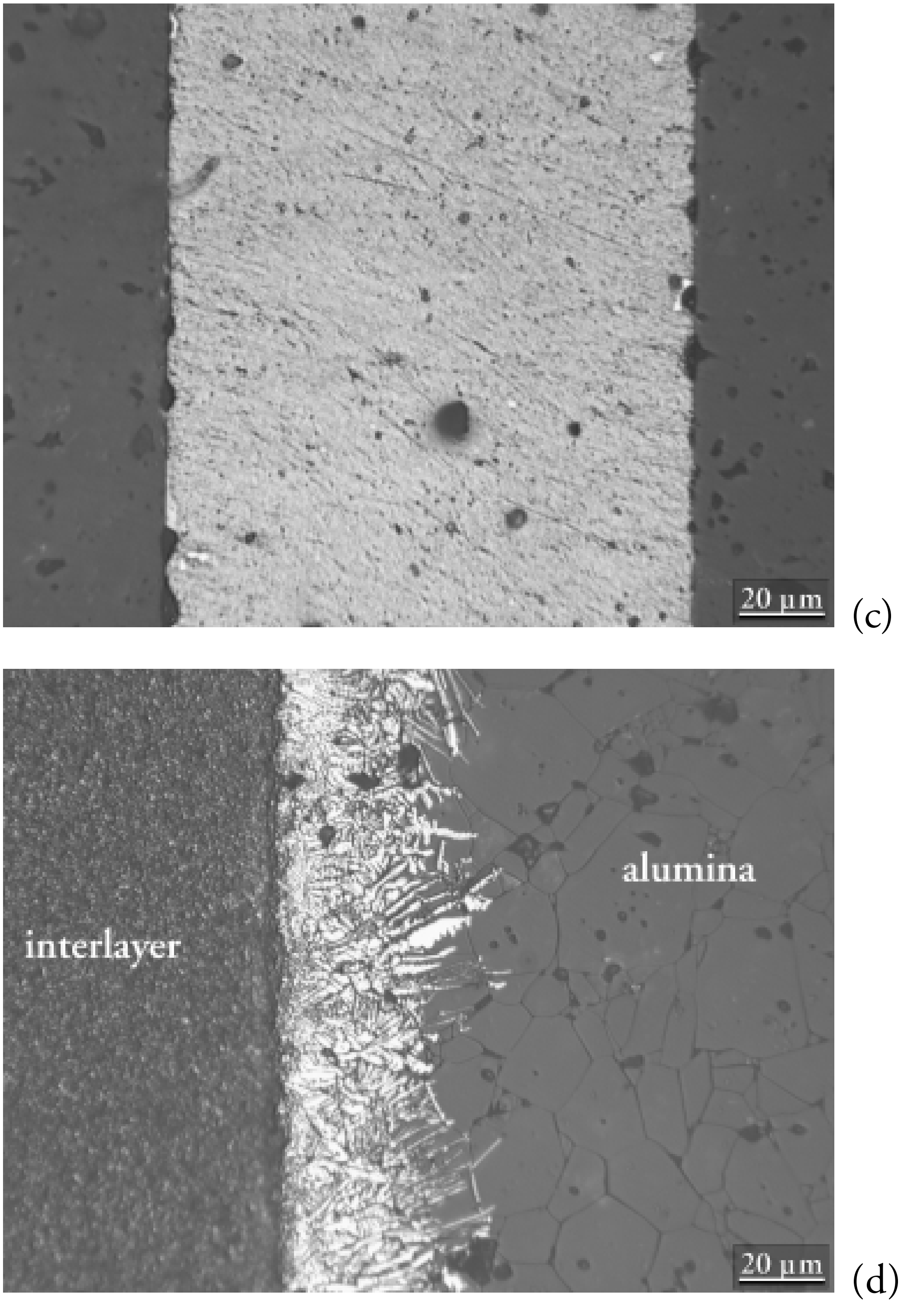

Figure 4.28: Optical micrographs of the interlayers (cross sections) of as processed joints and those annealing in vacuum at 1000°C and 1200°C. (a) as processed (BK27), (b) 200 h, vacuum, 1000°C (BK27), (c) as processed (BK26), (d) 250 h, vacuum, 1200°C (BK26).

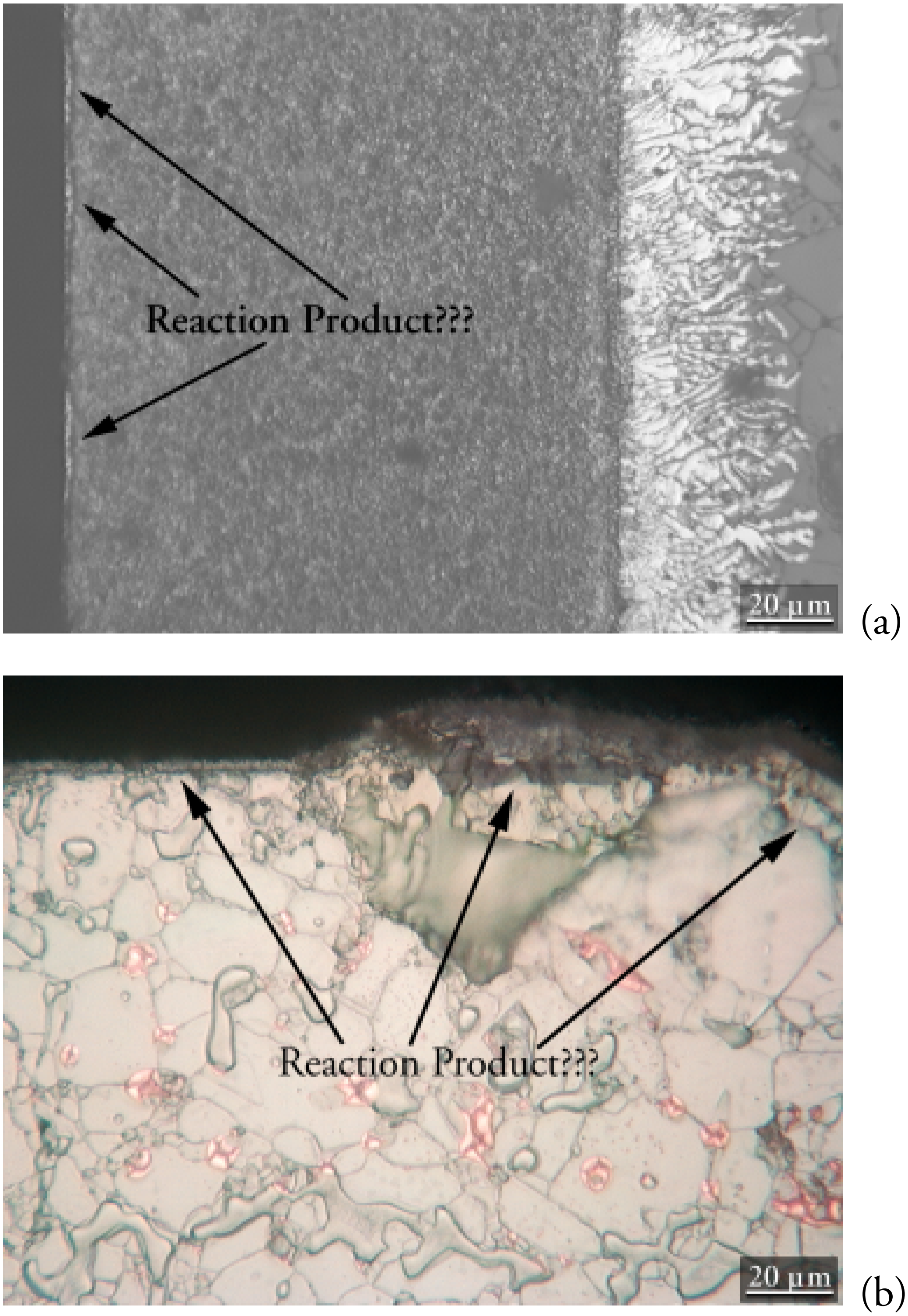

Figure 4.29: Optical micrographs of possible reaction products between tungsten and niobium, or tungsten and alumina. (a) interlayer cross section (b) metal side of fracture surface at tension edge

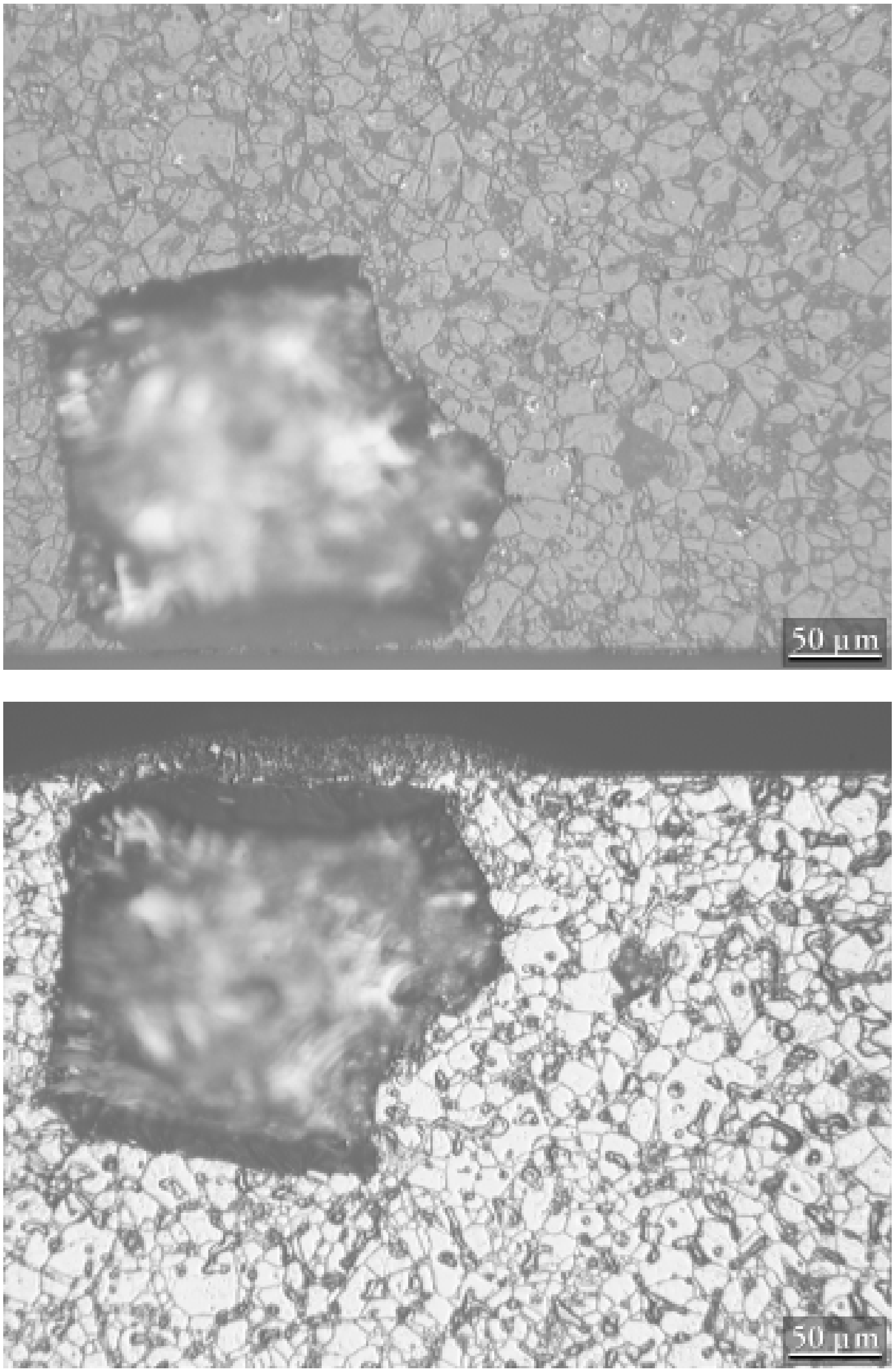

Figure 4.30: Optical micrographs of the ceramic (top) and metal (bottom) sides of the fracture surface from a beam annealed in vacuum for 250 h at 1200°C. This beam failed at 192 MPa.

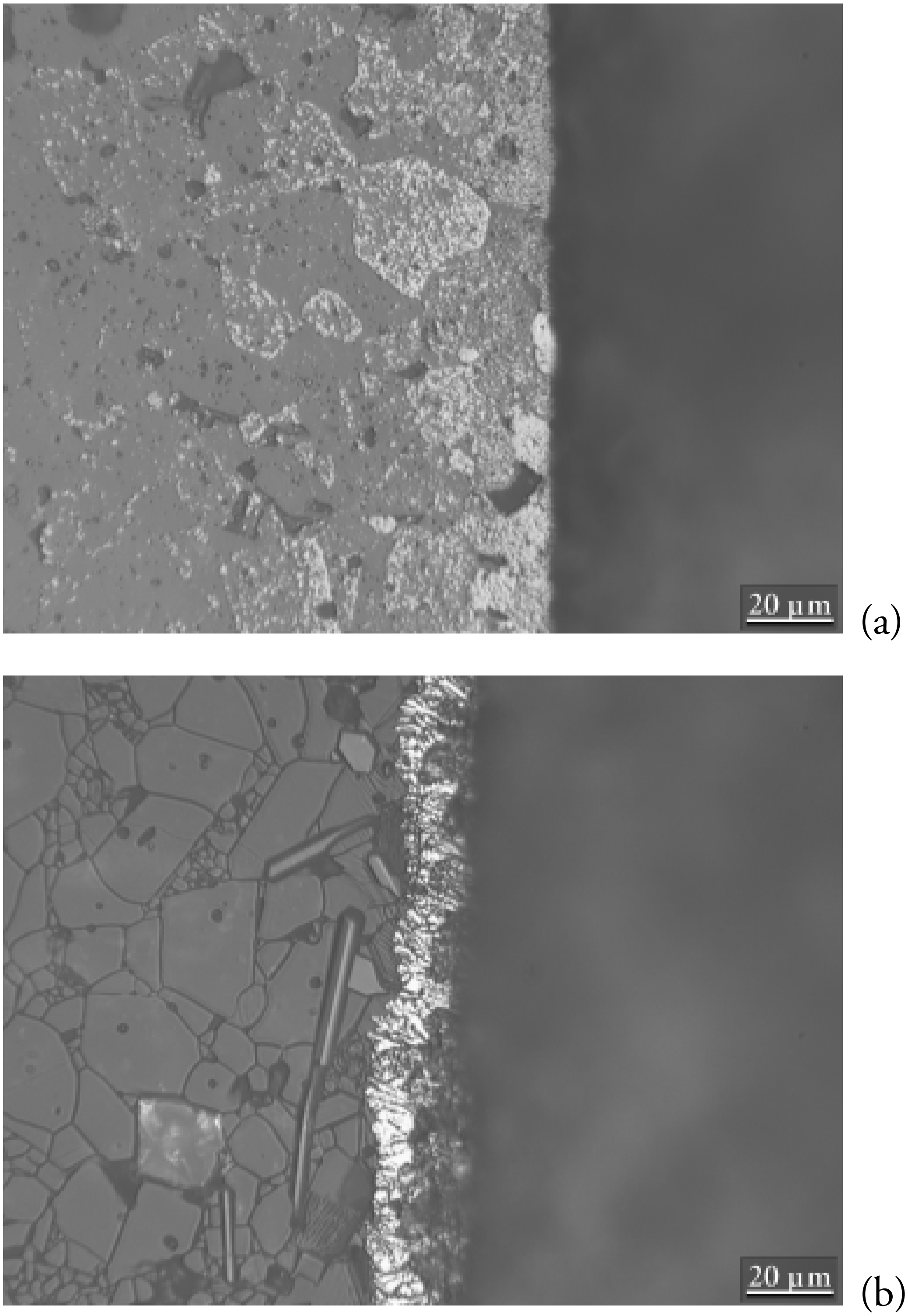

Figure 4.31: Optical micrographs of the interlayers (cross sections) of (a) a beam after argon annealing (1200°C) and (b) argon and vacuum annealing at 1200°C.

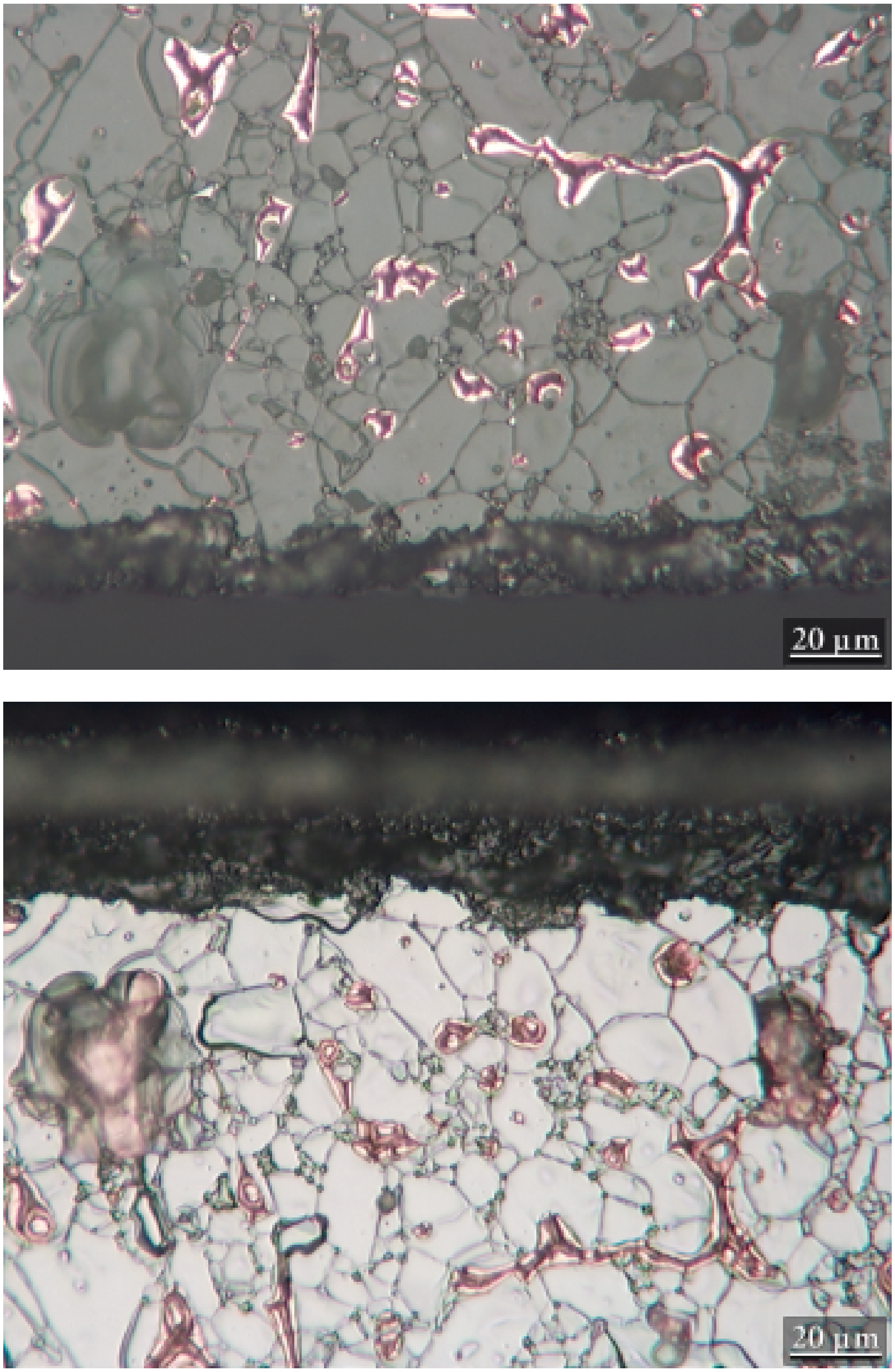

Figure 4.32: Optical micrographs of the ceramic (top) and metal (bottom) sides of the fracture surface from a beam annealed in argon and vacuum (200 h each) at 1000°C. This beam failed at 231 MPa.

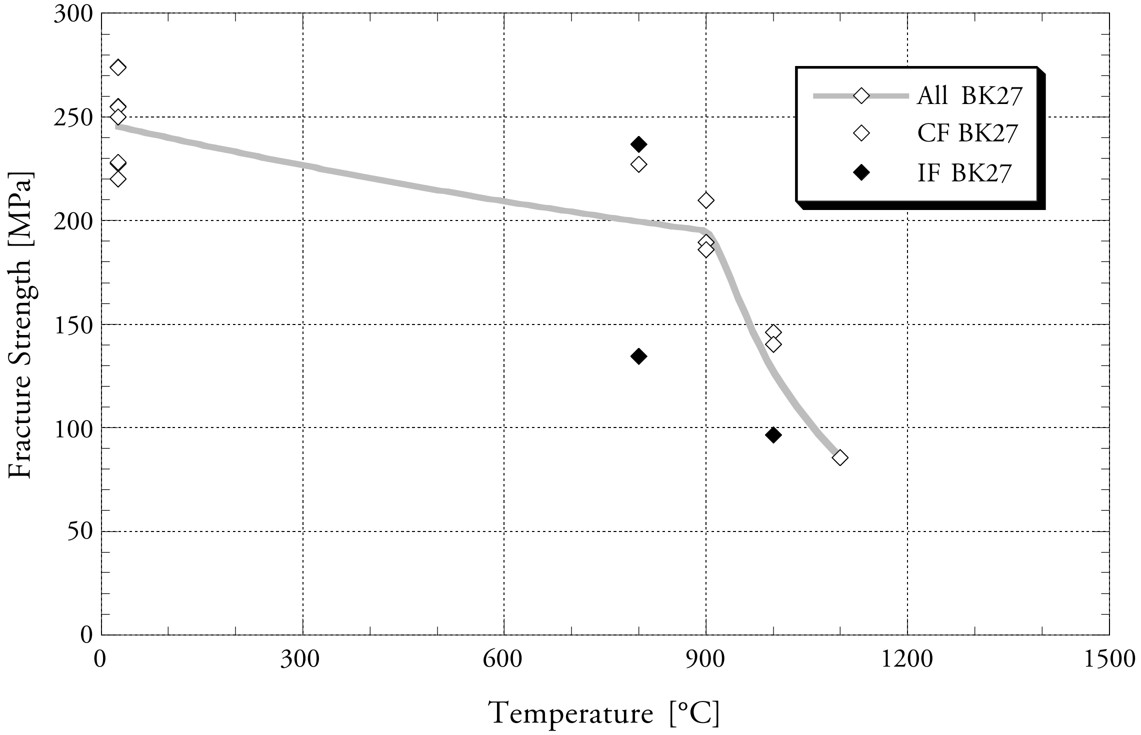

Figure 4.33: Temperature dependence of fracture strength for as processed beams from BK27 (graphite hot press, 1400°C, 2.2 MPa).

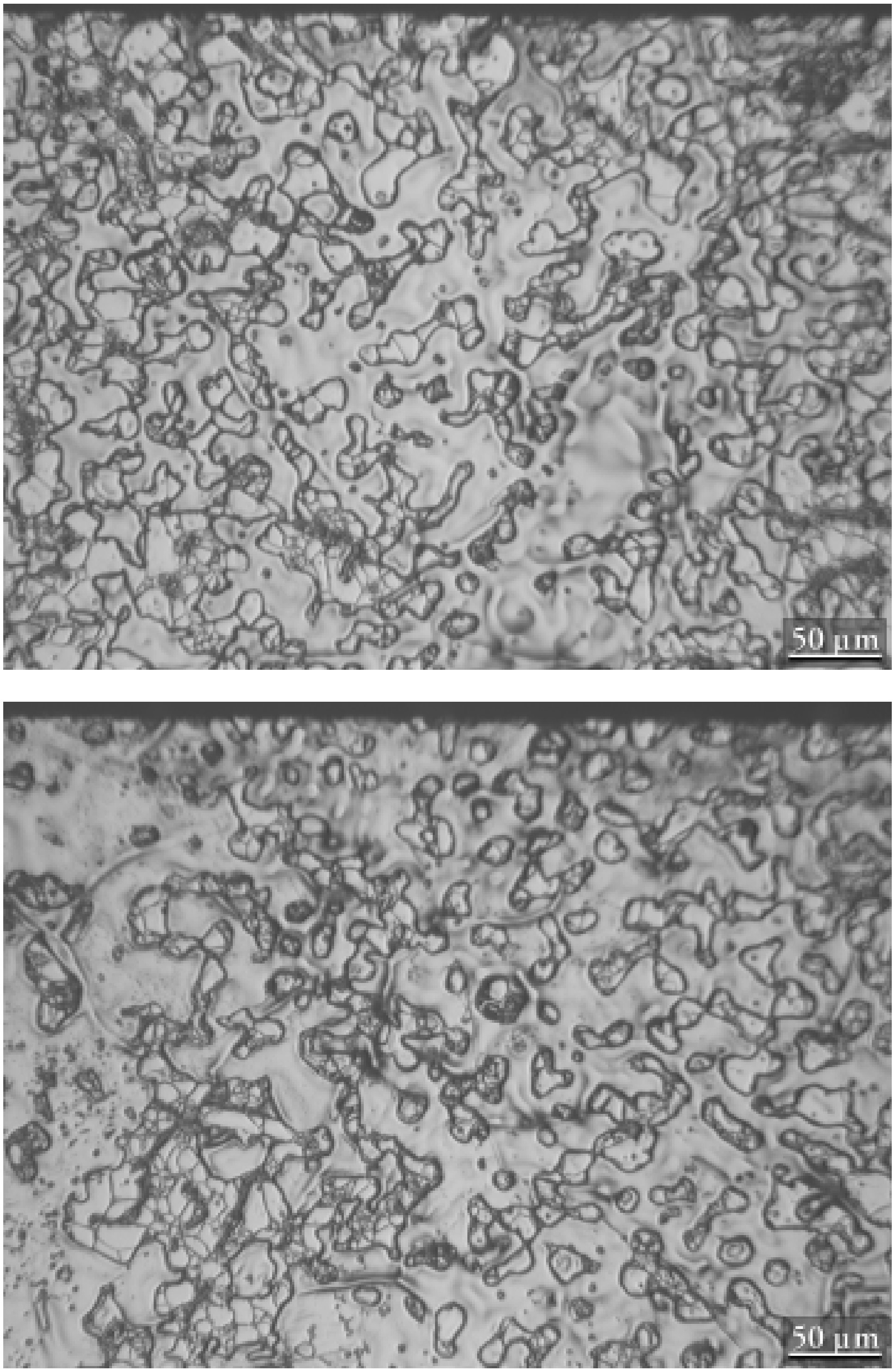

Figure 4.34: Optical micrographs of the metal side of fracture surfaces from beams tested at (a) 800°C ($\sigma_F = 134$ MPa) and (b) 1000°C ($\sigma_F = 96$ MPa). These two low strength interfacial failures appear to be associated with a large unbonded network at the interface.

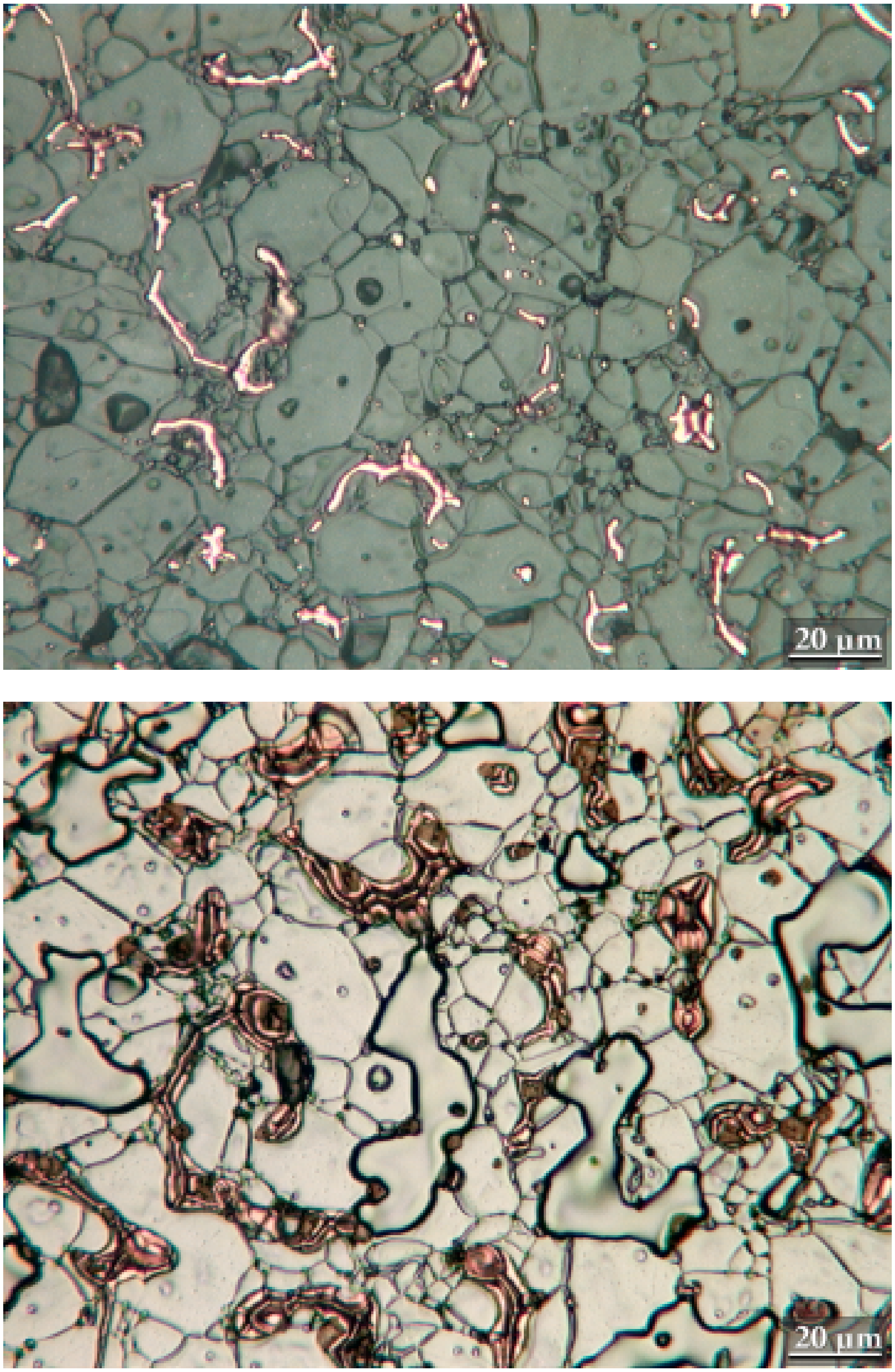

Figure 4.35: Optical micrographs of the ceramic (top) and metal (bottom) sides of a fracture surface from a joint tested at 800°C. The primary difference in interfacial fracture surfaces between fracture surfaces from high temperature and room temperature tests appears to be in the deformation the copper undergoes.

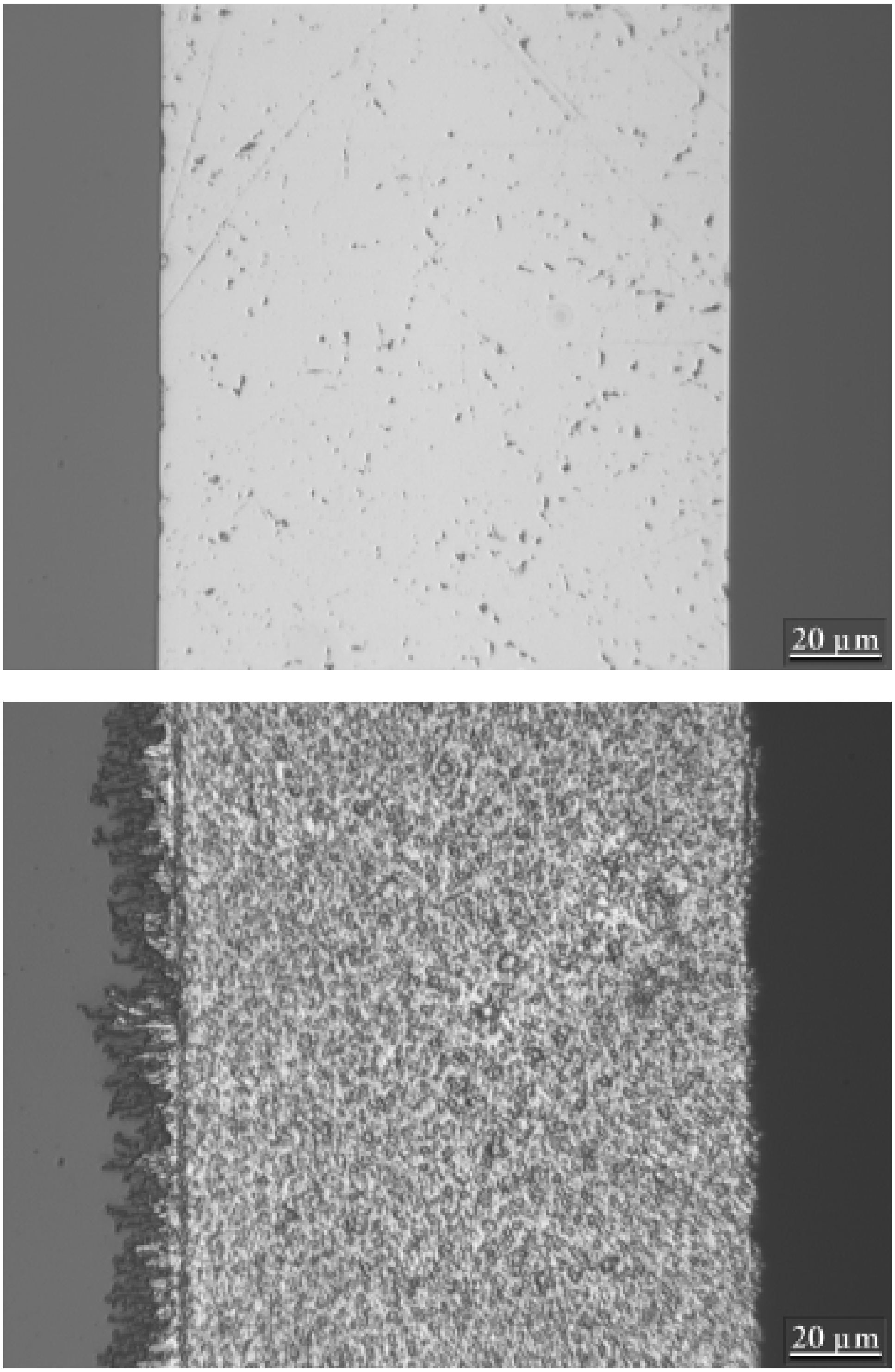

Figure 4.36: Optical micrographs comparing the interlayer cross section of an as processed beam (top), and one annealed at 1400°C for 10 h in vacuum (bottom).

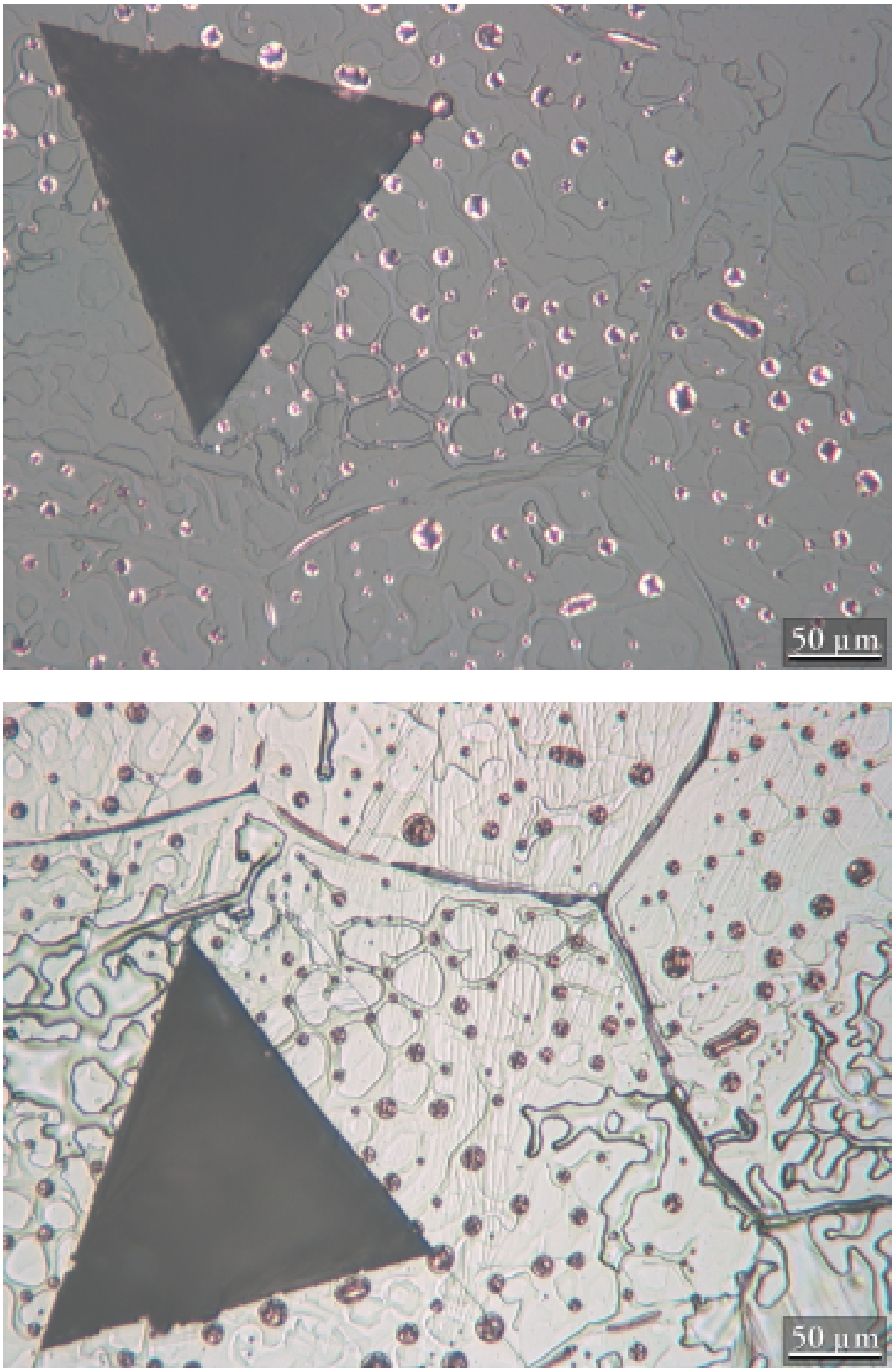

Figure 4.37: Optical micrographs of the ceramic (top) and metal (bottom) side of a fracture surface from the sapphire plug joint. The beam was annealed in vacuum for 10 h at 1400°C, and a large pulled out region of niobium (triangular) can be seen. The beam failed at 173 MPa.

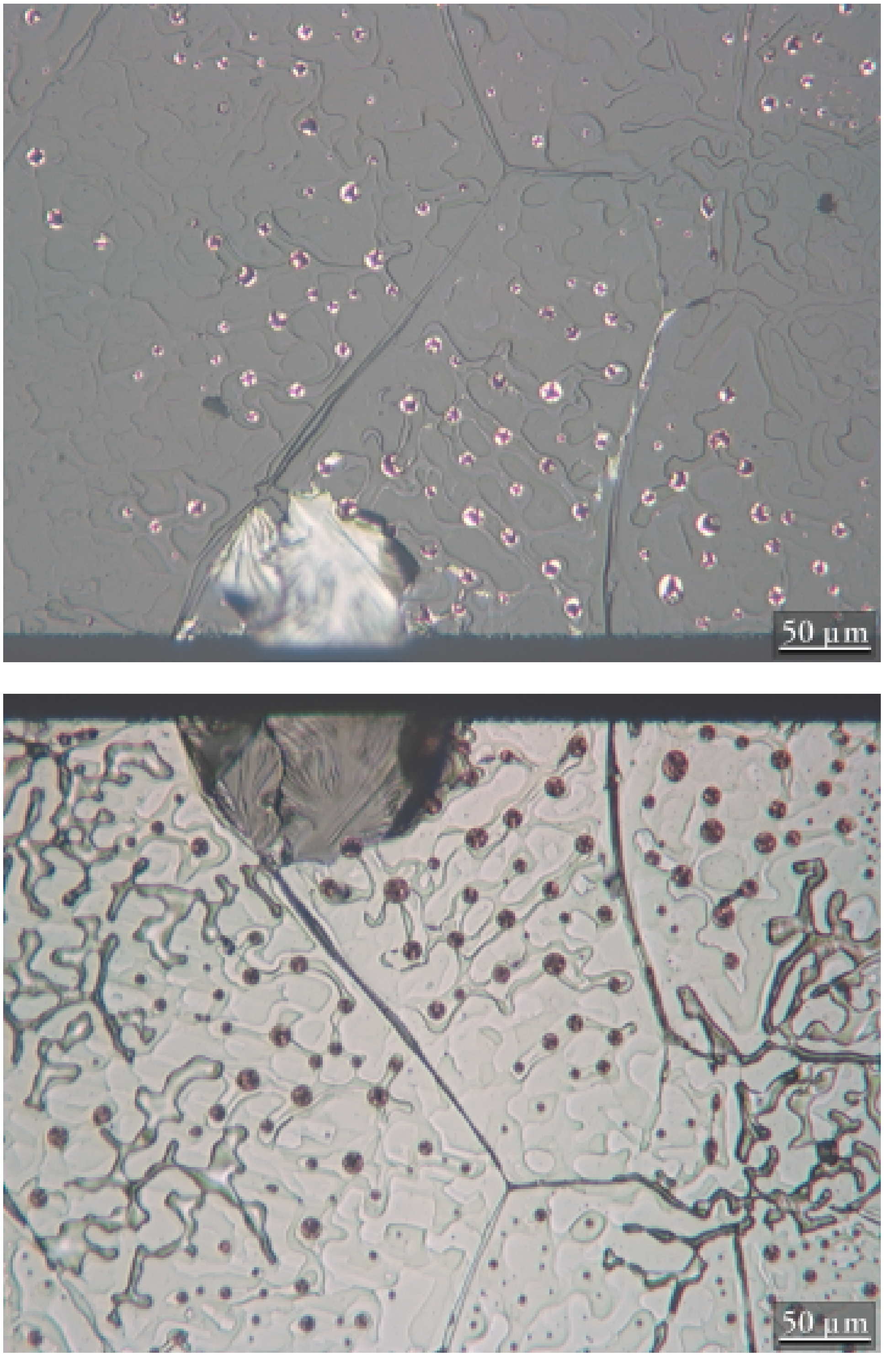

Figure 4.38: Optical micrographs of the ceramic (top) and metal (bottom) side of a fracture surface from the sapphire plug joint. The beam was annealed in vacuum for 10 h at 1400°C, and again, niobium which remained adhered to the sapphire is observed. The beam failed at 173 MPa.

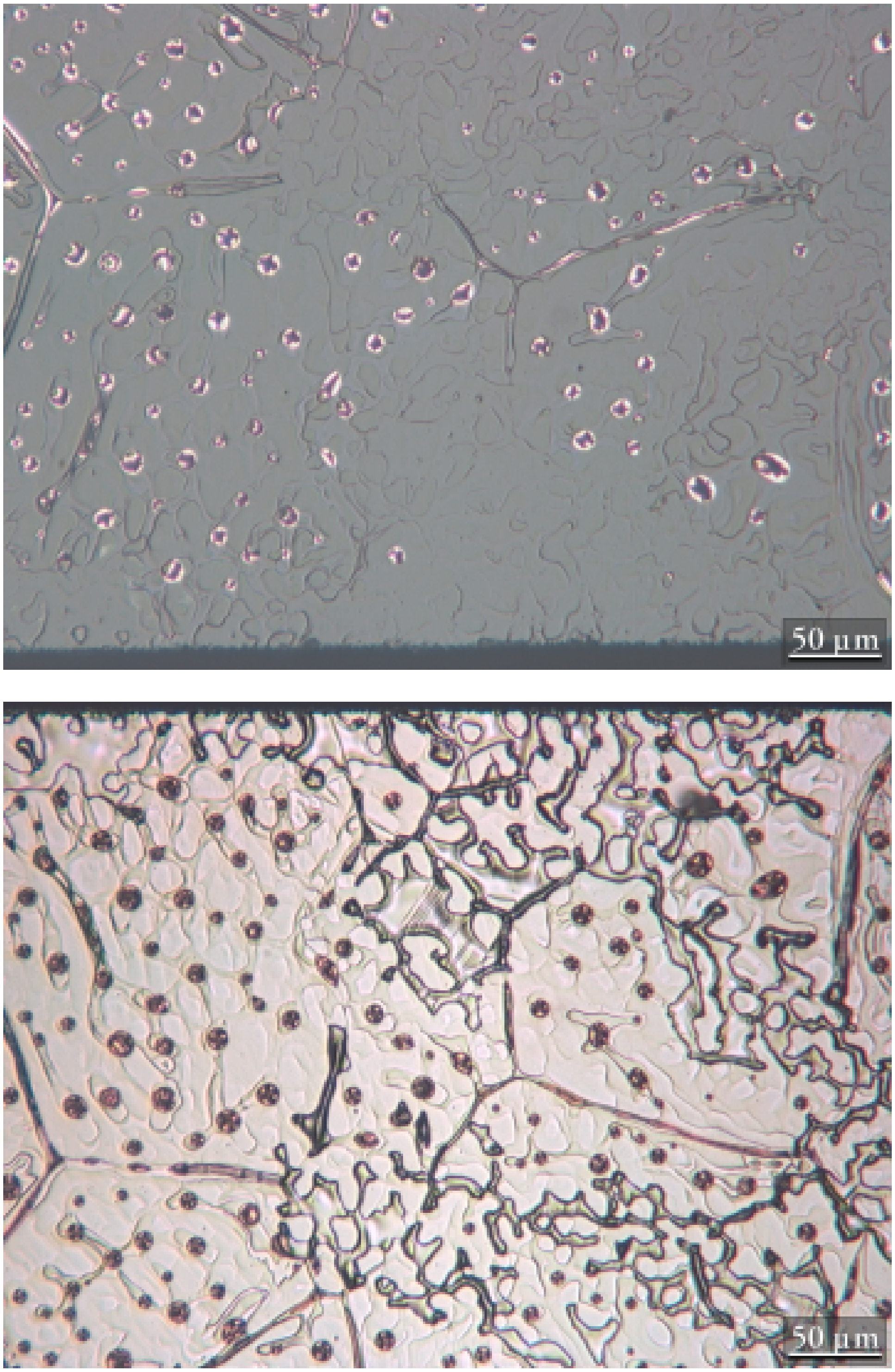

Figure 4.39: Optical micrographs of the ceramic (top) and metal (bottom) side of a fracture surface from the sapphire plug joint. The beam was annealed in vacuum for 10 h at 1400°C; note the imprint of unbonded areas on the sapphire side. The beam failed at 110 MPa.

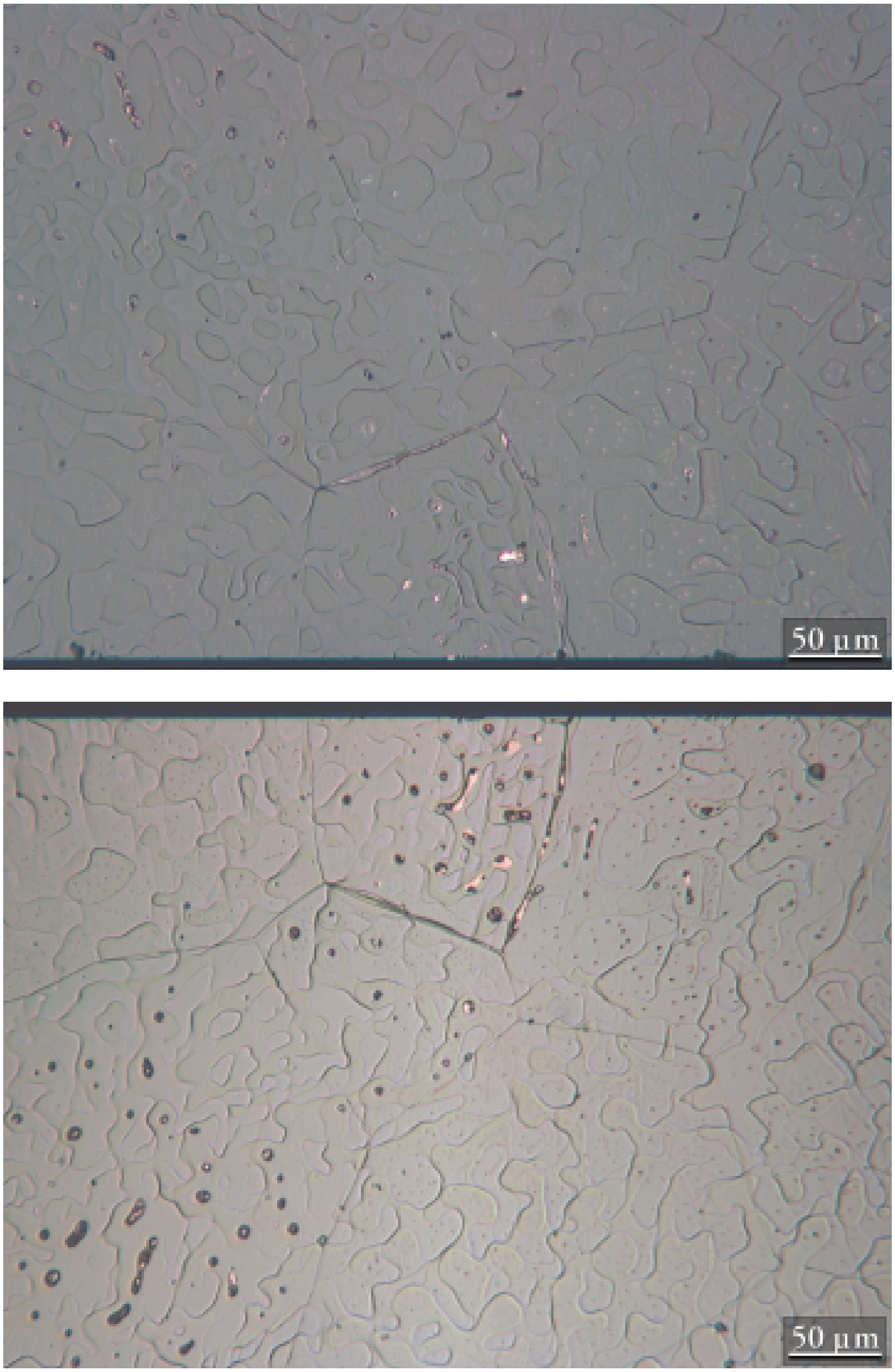

Figure 4.40: Optical micrographs of the ceramic (top) and metal (bottom) side of a fracture surface from the sapphire plug joint. Note the faintness of the niobium grain boundaries and lack of copper precipitates at the interface. The beam failed during ultrasonic cleaning in acetone.

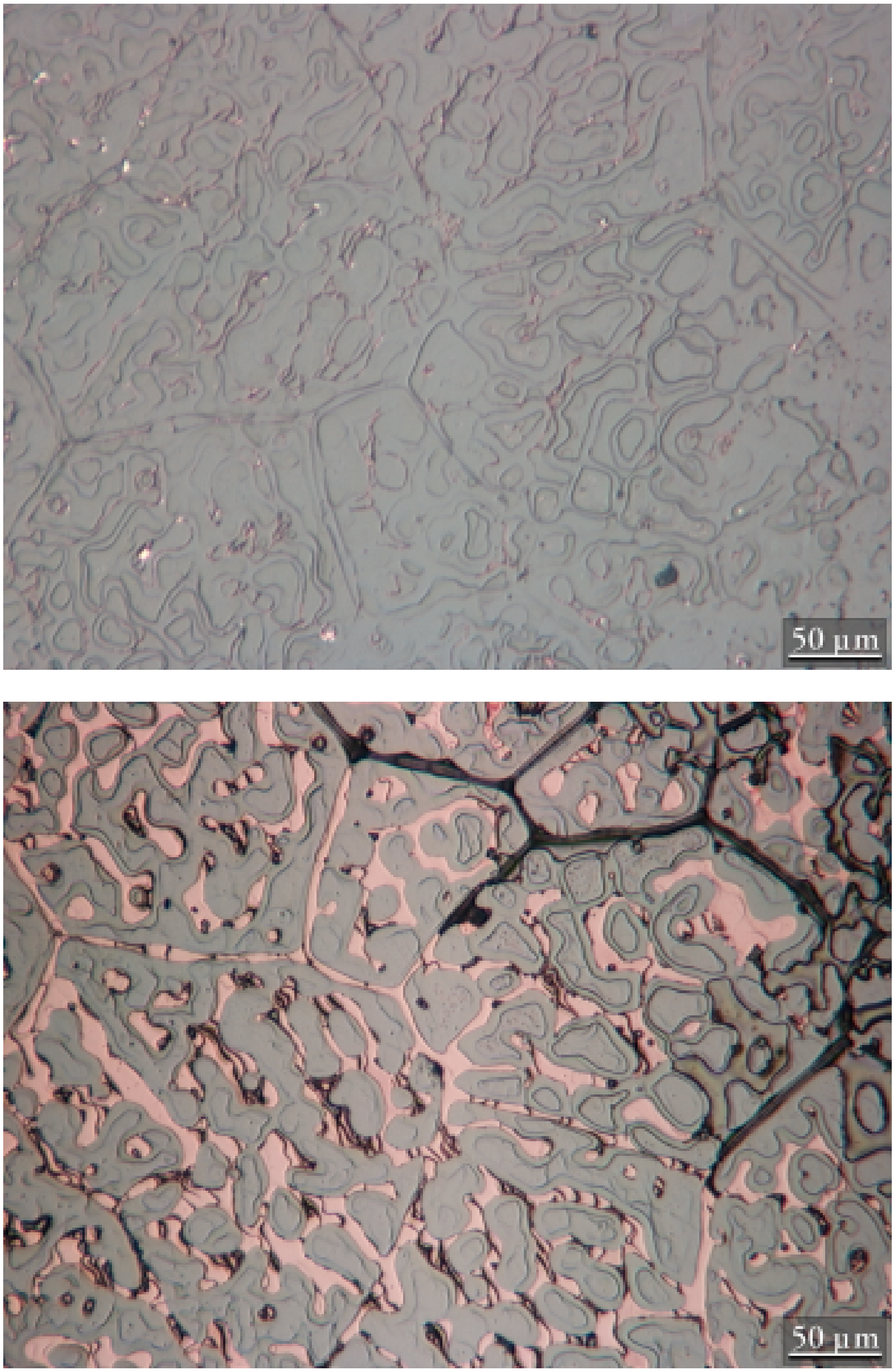

Figure 4.41: Optical micrographs of the ceramic (top) and metal (bottom) side of a fracture surface from the sapphire plug joint. Note the extent to which the copper phase remains connected. The beam failed at 114 MPa.

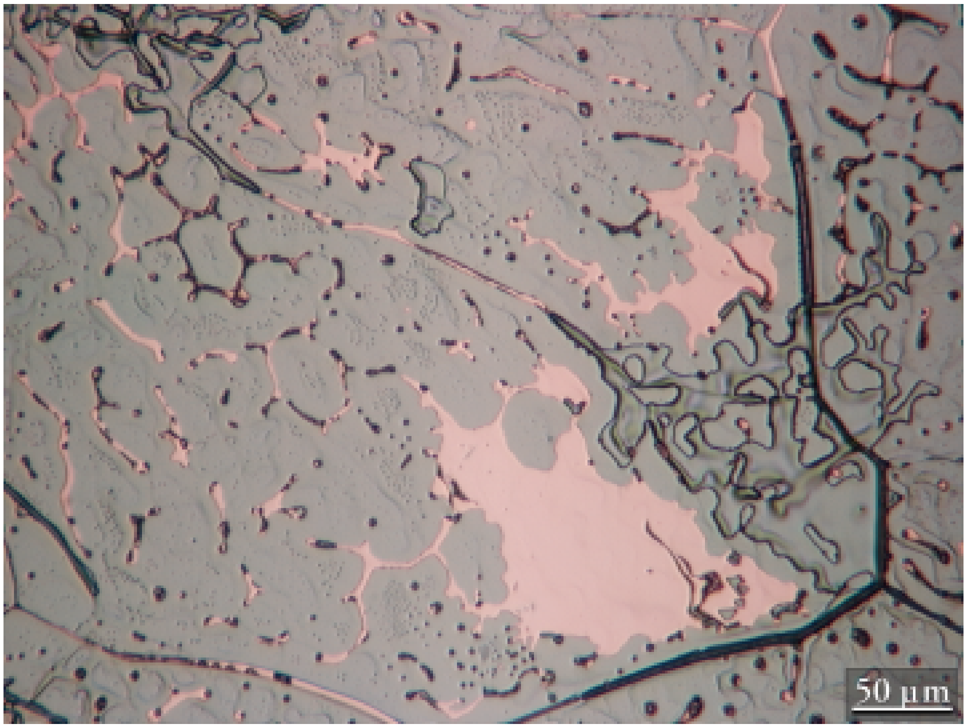

Figure 4.42: Optical micrograph metal side of a fracture surface from the sapphire plug joint. Some patches of a copper film remained at the interface of these beams which were not post bonding annealed in vacuum (1400°C, 10 h). The beam failed at 114 MPa.

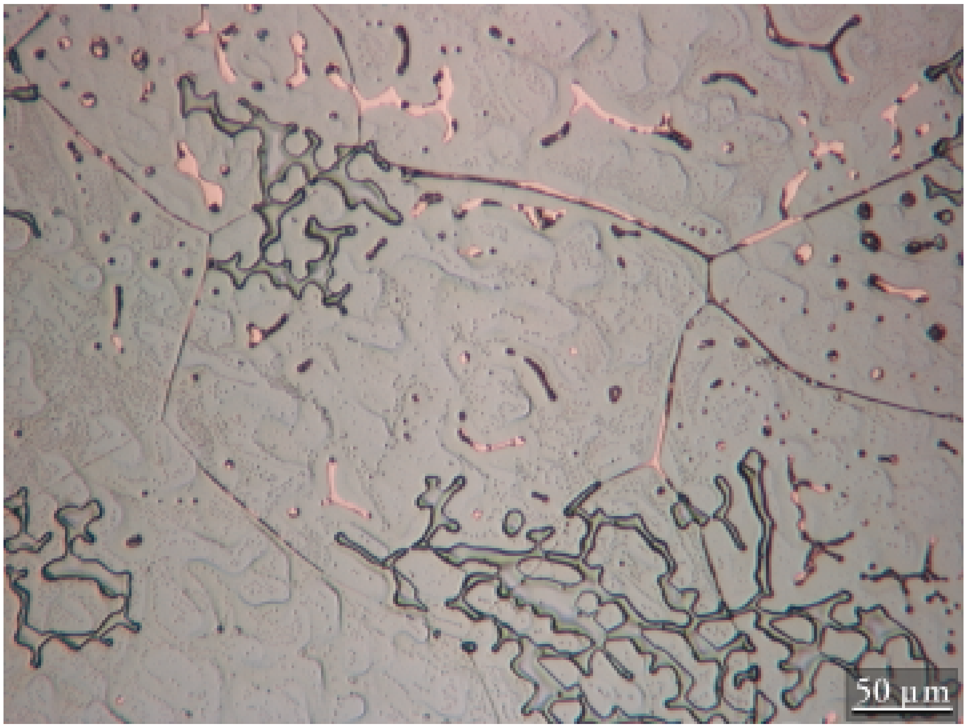

Figure 4.43: Optical micrograph of the metal side of a fracture surface in the sapphire plug joint. Portions of the copper phase still remain as narrow strips rather than broken into isolated particles in beams which were not post bonding annealed in vacuum (1400°C, 10 h). The beam failed at 122 MPa.

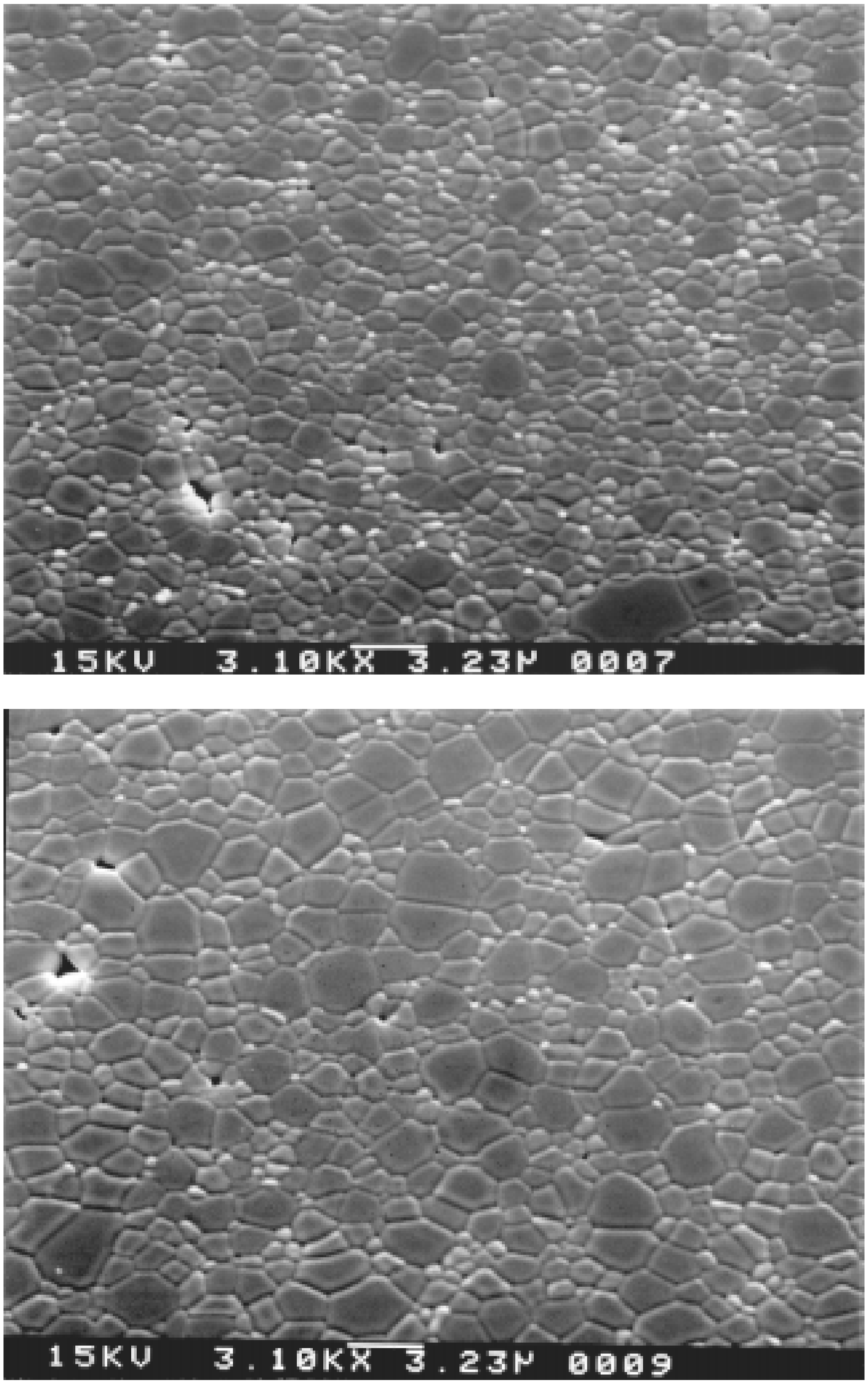

Figure 4.44: SEM micrograph of the microstructure of as received Nikkato alumina (top) and Nikkato alumina after processing joint at 1400°C (bottom). The grain boundaries are etched by thermal treatment for 45 min at 1350°C in vacuum.

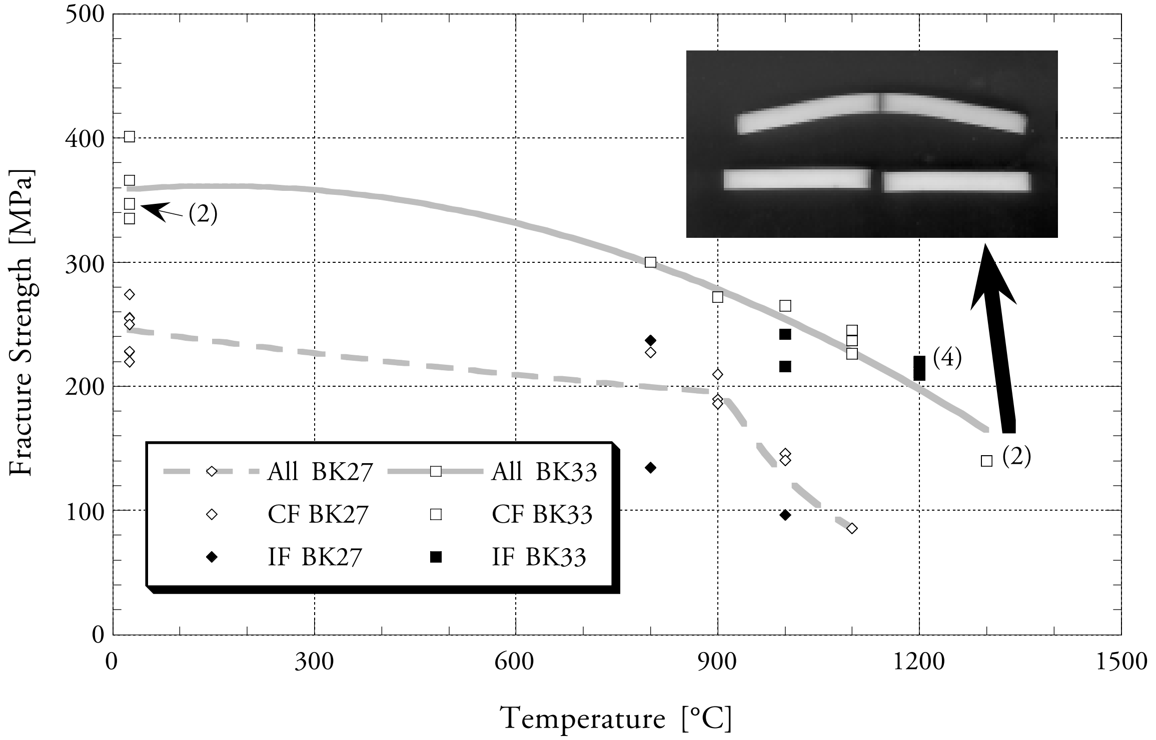

Figure 4.45: Temperature dependence of fracture strength for Nikkato alumina joint (BK33) compared to that of a Coors alumina joint (BK27). Both joints were processed in the graphite hot press at 1400°C for 6 h under ≈2 MPa applied load. The inserted image illustrates the deformation the ceramic underwent for the two beams tested at 1300°C. The numbers in parenthesis indicate the number of overlapping, or nearly overlapping data points.

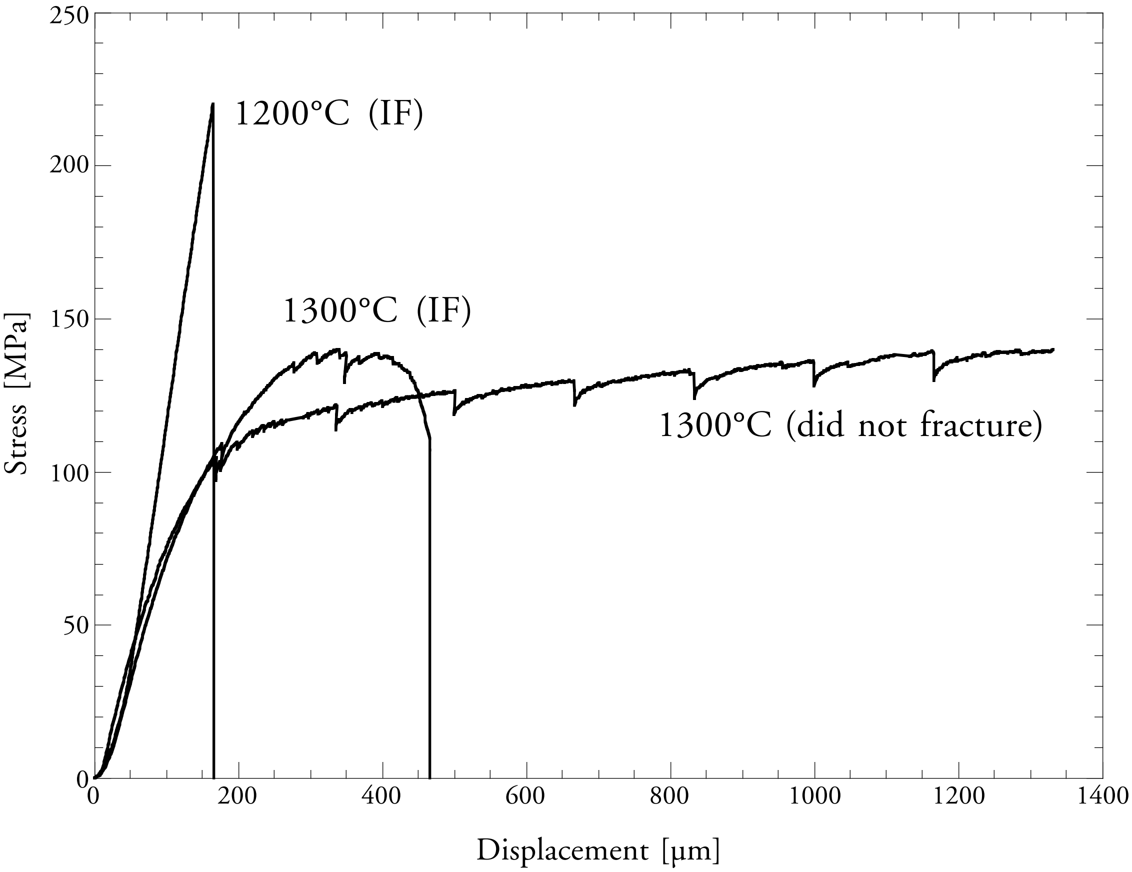

Figure 4.46: Stress versus displacement (time) curves for beams tested at 1300°C compared to that representative of lower temperature tests (≤1200°C).

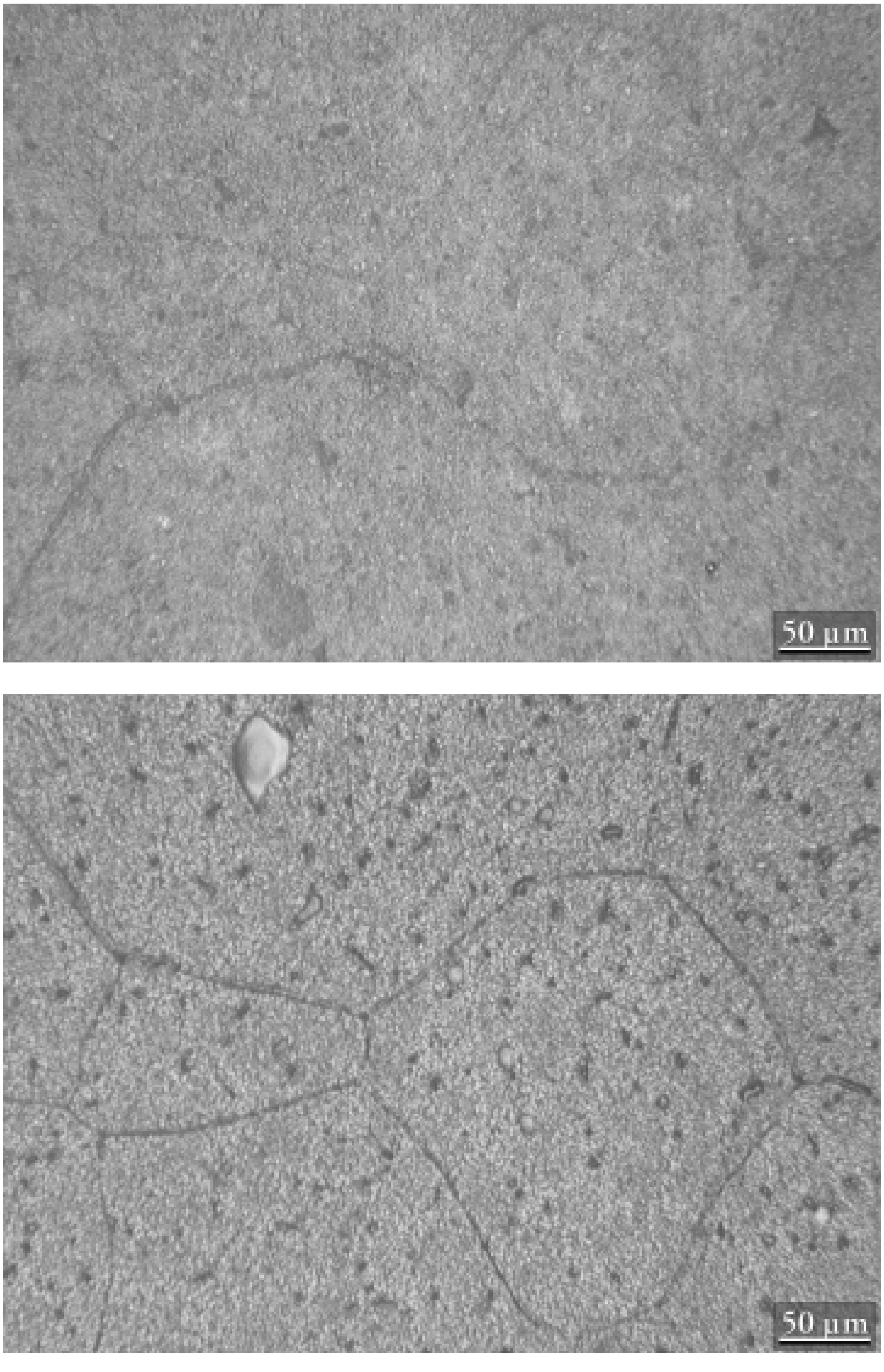

Figure 4.47: Representative optical micrographs of the ceramic side (top) and metal side (bottom) of the fractures surfaces in Nikkato Alumina joint. This particular beam (BK33BM41) failed at 209 MPa at 1200°C. Notice mirror image of niobium grain boundaries on . The speckled appearance is due the size scale of the alumina grains.

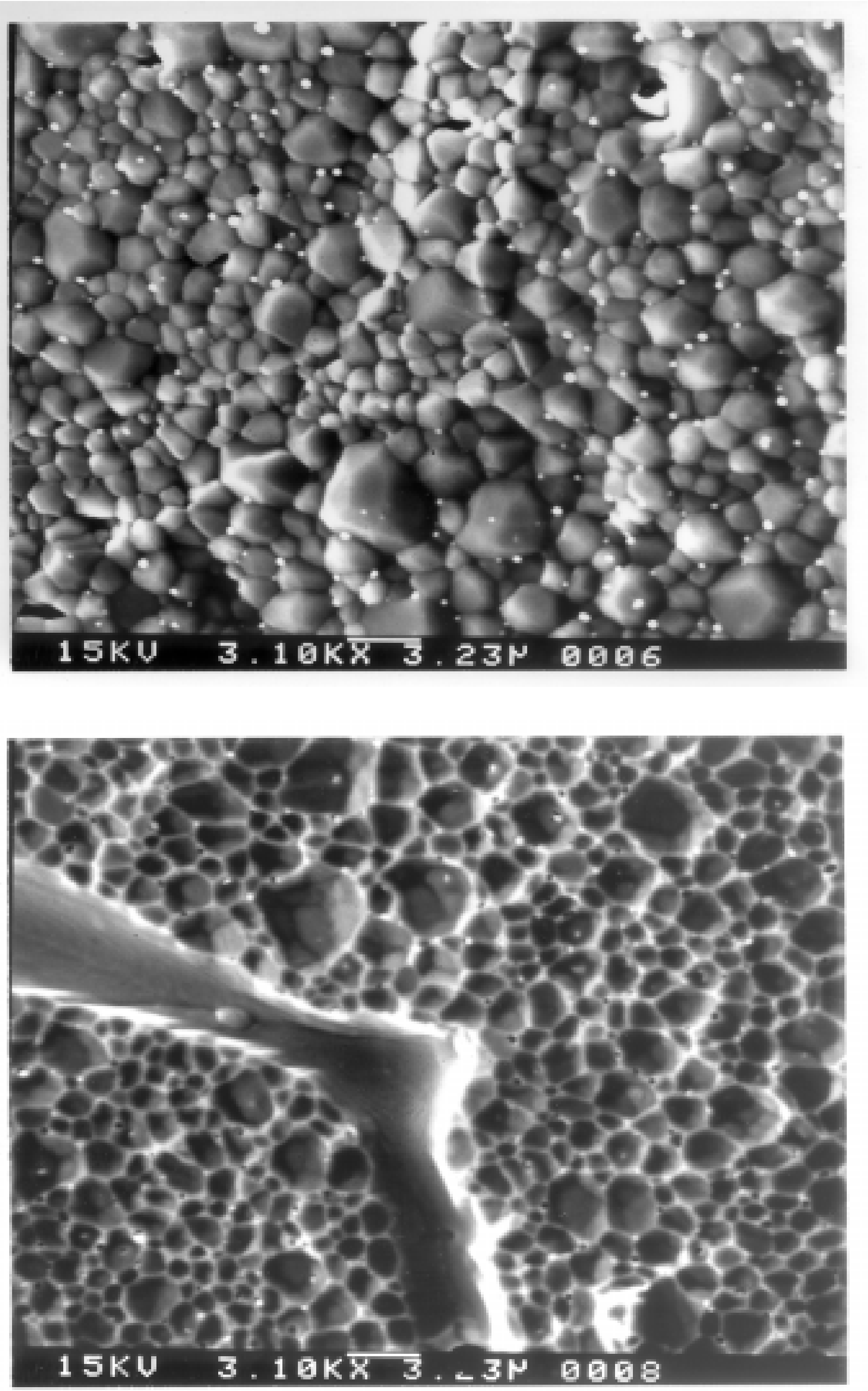

Figure 4.48: SEM micrographs of the ceramic (top) and metal (bottom) side of a fracture surface from BK33. As frequently observed, only two of the three intersecting niobium grain boundaries are grooved. The bright white spots (top) are small copper particles, and tend to not be present at in the grain boundary groove region.

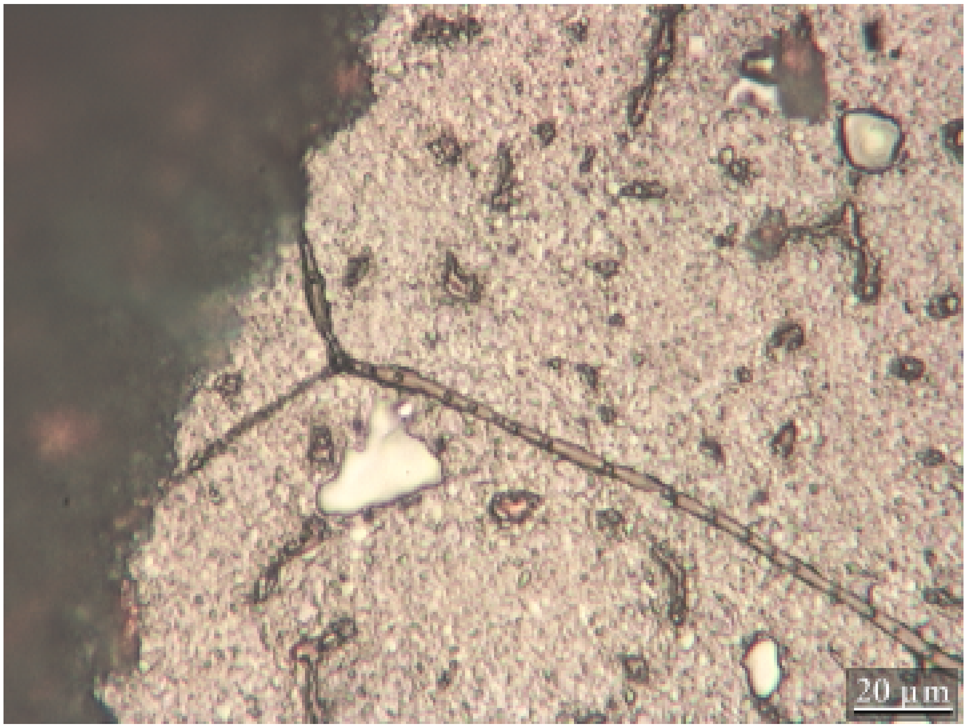

Figure 4.49: Optical micrograph of the metal side of a fracture surface from the Nikkato alumina joint. This beam failed at 242 MPa at 1000°C. Copper is observed below the region (blurry) where failure occurred in the ceramic

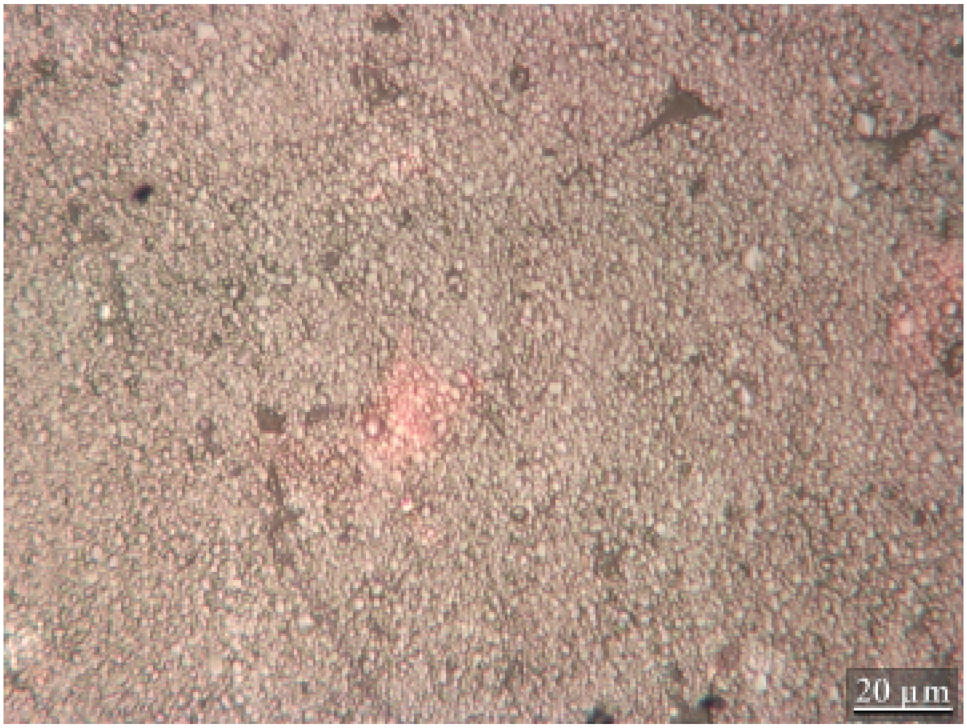

Figure 4.50: Optical micrograph of the ceramic side of a fracture surface in the Nikkato alumina joint. The beam failed at 216 MPa at 1000°C. The image illustrates one form (a faint trace) of copper found. Focusing below the surface reveals what appears to be small particles of bulk copper which may have diffused into the alumina.

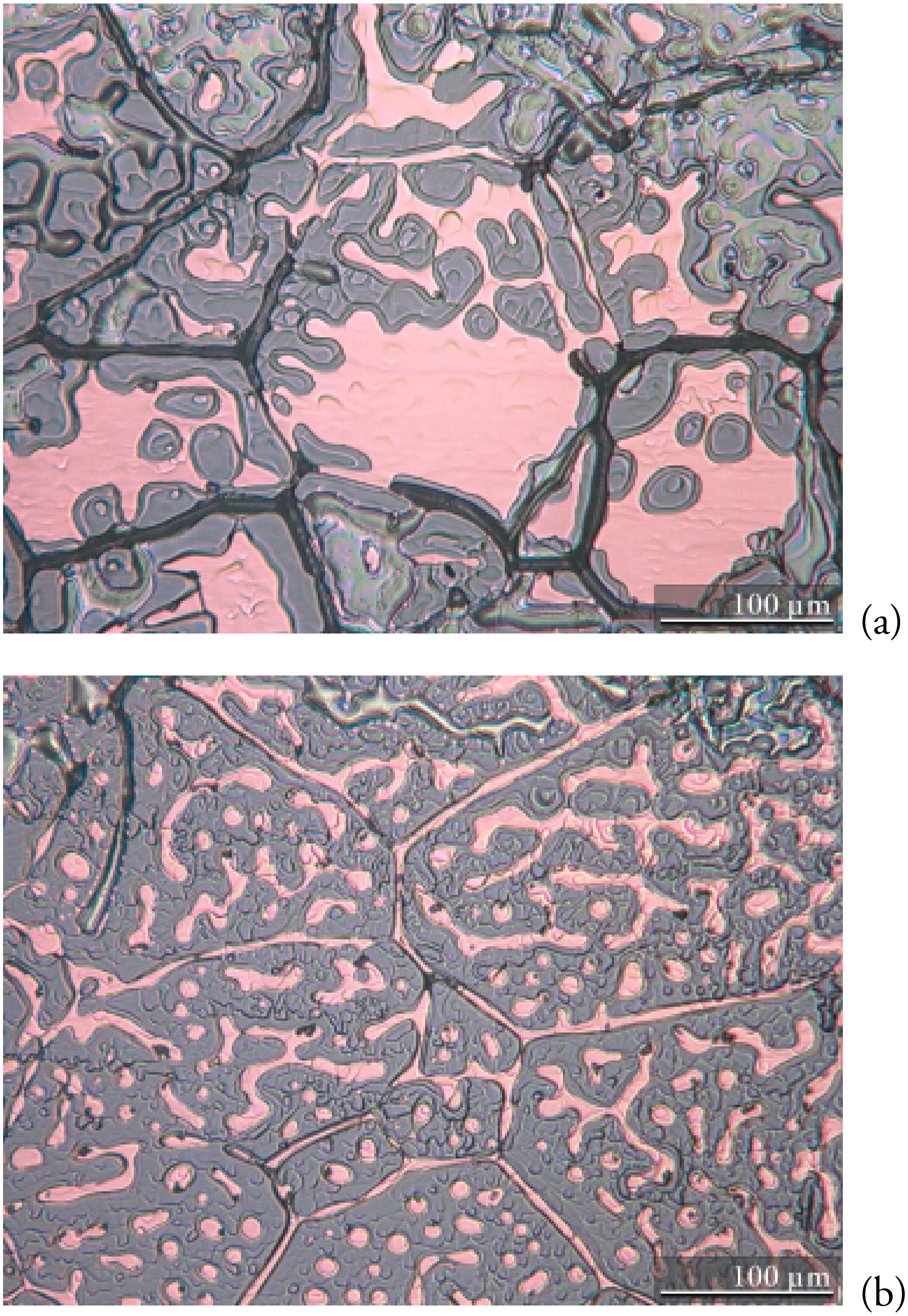

Figure 4.51: Optical micrographs of a sapphire window joint illustrating the proposed microstructural evolution in joints fabricated at 1400°C.

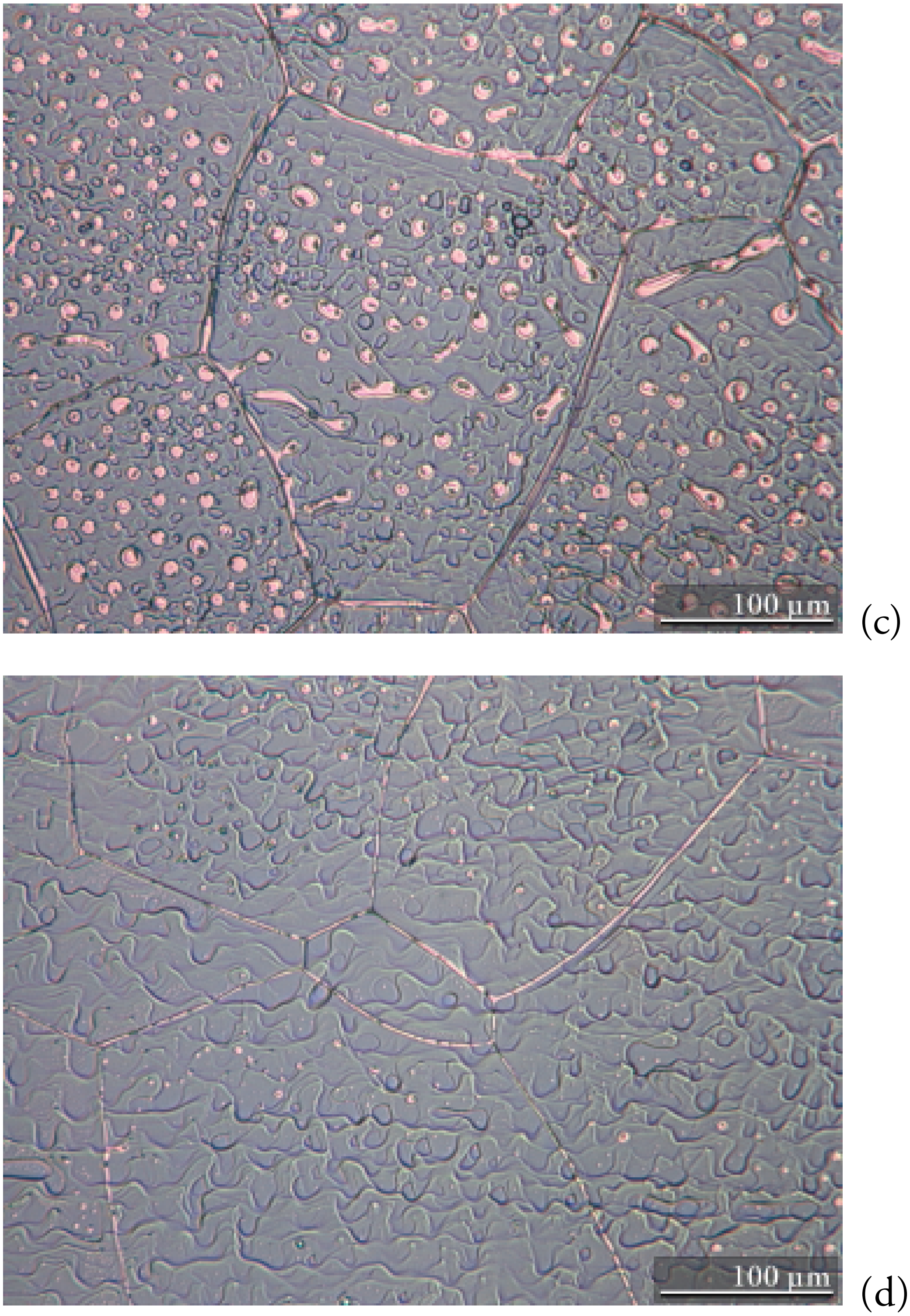

Figure 4.51: Optical micrographs of a sapphire window joint illustrating the proposed microstructural evolution in joints fabricated at 1400°C.

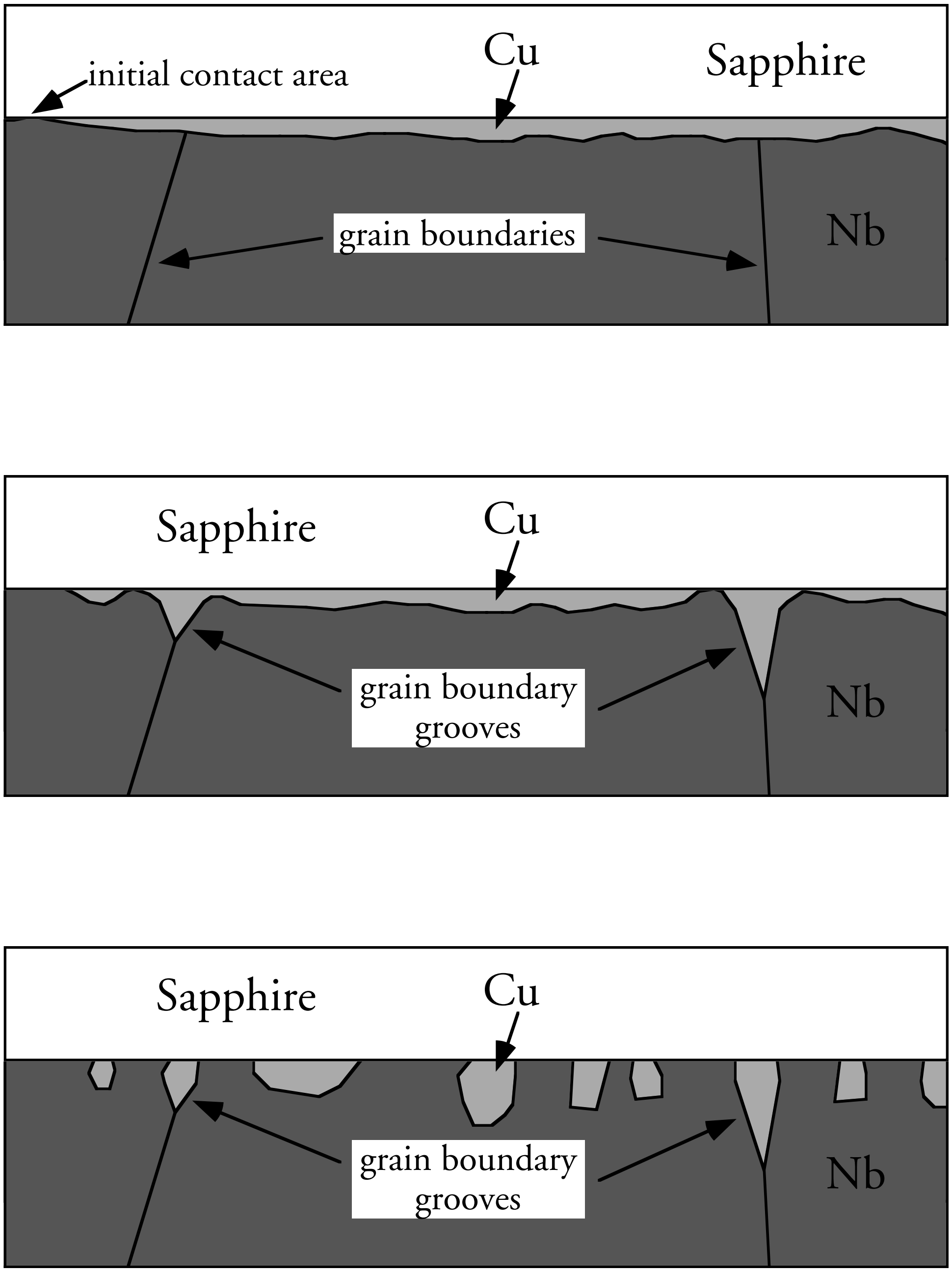

Figure 4.52: Schematic of the evolution sequence the copper film under goes.

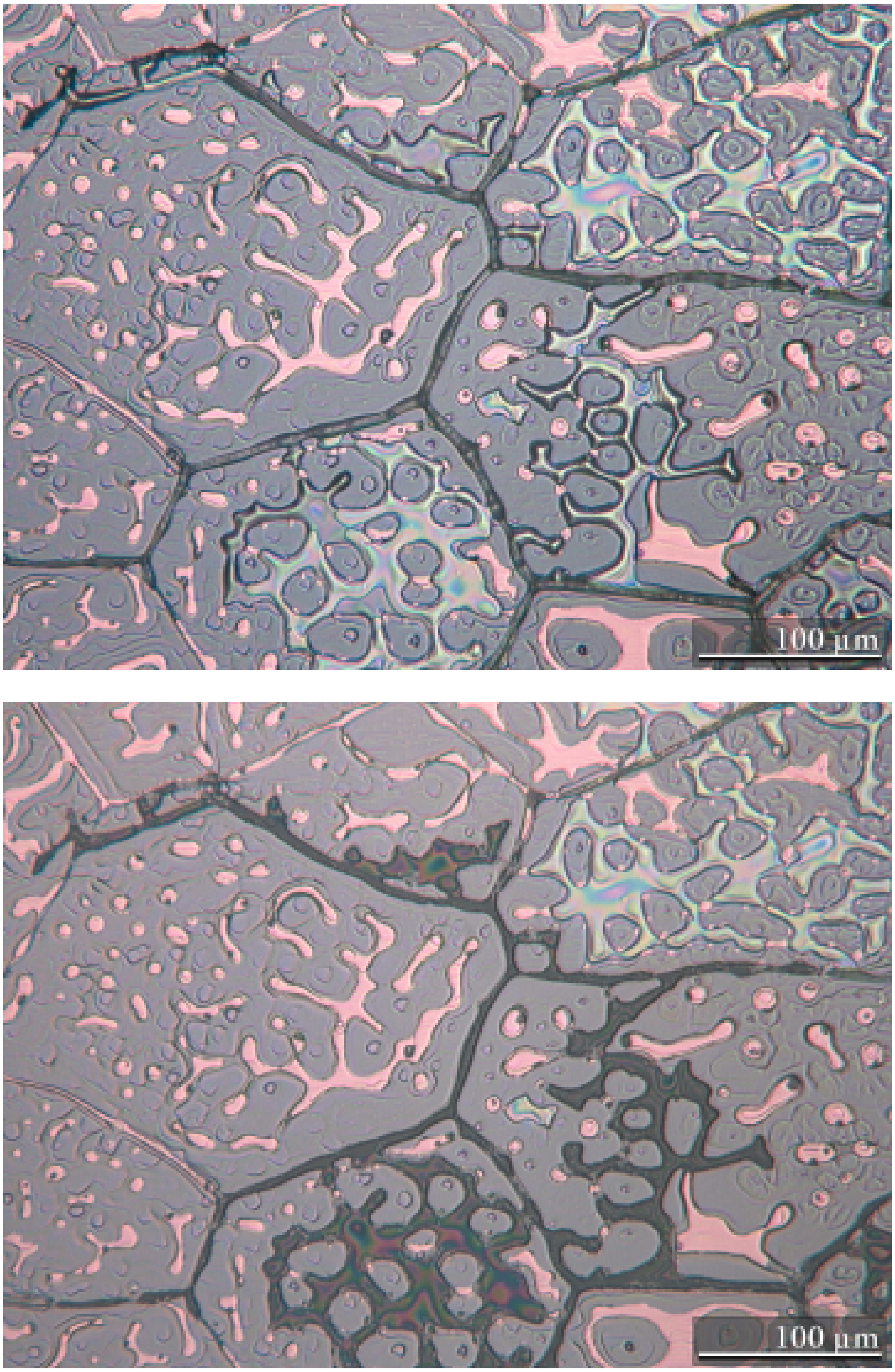

Figure 4.53: Optical micrographs of an as processed (top) sapphire window joint, and that observed after annealing in gettered argon for 200 h at 1000°C (bottom). Little change is observed in the morphology aside from a slight discoloration of some of the unbonded areas.

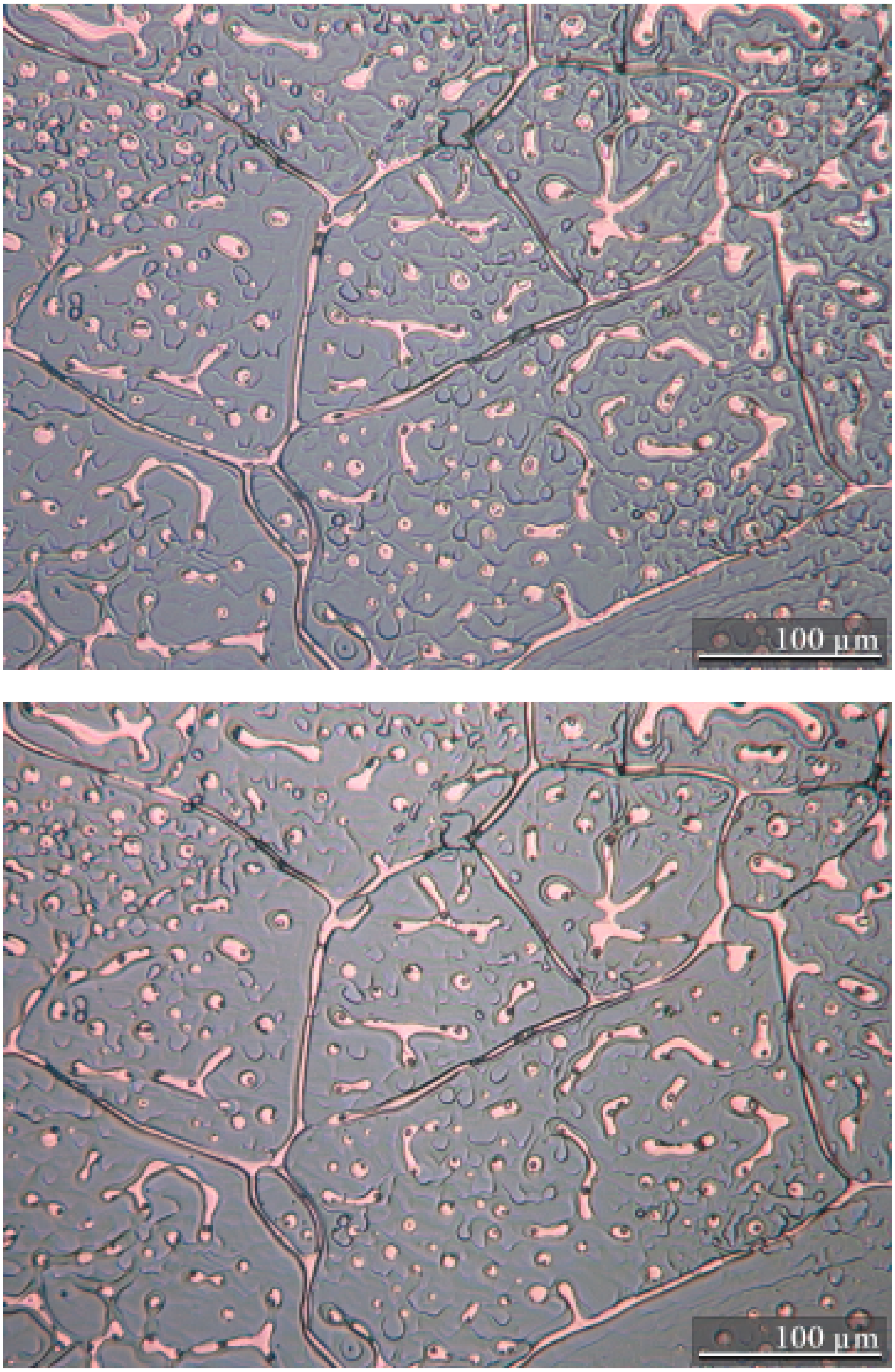

Figure 4.54: Optical micrographs of an as processed (top) sapphire window joint, and that observed after annealing in gettered argon for 200 h at 1000°C (bottom). Essentially no change is observed at this relatively low (copper is still solid) annealing temperature.

Chapter 5
Concluding Remarks

5.1 Conclusions

A liquid phase technique has been used to process a niobium-based joint for alumina. Strong joints can be made with copper/niobium/copper interlayers that retain substantial strength up to 1300°C. The strength of copper/niobium/copper joints depends strongly on processing conditions, but strong joints can be fabricated with small applied loads provided sufficiently high temperatures are used. The mechanical behavior of these joints is sensitive to long term exposure to various p_{O_2} environments. One might anticipate that the optimum p_{O_2} at which such joints would experience minimal degradation is the p_{O_2} in equilibrium with both niobium and the alumina phase(s) at various temperatures. The microstructure of the aluminum oxide (polycrystal versus single crystal) used may have pronounced effects on the strength. For polycrystalline joints, many ceramic failures were observed, indicating the interface is stronger than the aluminas used.

Generally, processing conditions that induce break-up of the copper film promote the best joints. The ability to obtain strong two-phase joints implies that systems exhibiting phase diagrams with high solubility of cladding material are not the only candidates for successful joints. A two-phase microstructure (even with a low melting point phase) is absolutely acceptable for refractory joints provided the low melting phase can undergo an instability similar to that observed in the current study. Perhaps, a similar approach can be used to join other refractory metals to alumina and/or other ceramics. Few metallic systems (binary or ternary) possess the desirable criteria for conventional PTLP joining, and the current study implies that there is potentially a much larger set of systems to consider for metal/ceramic joining. This joining method is certainly a type of PTLP bonding, but perhaps the name transient liquid phase assisted diffusion bonding (TLPADB) is more descriptive of the actual process.

5.2 Future Work

In order to assess the importance of ambient environment on joint strength, simultaneously processing two joints at 1150°C in both the molybdenum and graphite hot presses (same load ≈7.5 MPa) would provide insight. If interfacial microstructures and corresponding strengths similar to BK29 could be obtained by using a higher load in the graphite hot press, such a result would indicate the ambient environment (p_{O_2}) is not very important in determining joint quality. If the microstructure is similar to that of BK29, yet a strength improvement is observed, one would conclude that the ambient furnace environment will also influence joint strength. Sugar [127] is currently working on this experiment.

A detailed study of the wetting characteristics in the furnaces and at the temperatures used would serve as additional evidence supporting whether p_{O_2}, temperature, and/or applied load are responsible for the relative strengths observed under various processing conditions. Any additional thermodynamic information and fundamental studies on the aluminum-copper-niobium-oxygen system or a subset thereof would be beneficial and interesting.

The results from the gettered-argon and vacuum anneals justify a detailed study on the effects of ambient p_{O_2}. In the current study, the strength decrease as a result of annealing was subtle; however, it would be interesting to see if the strength of Nikkato alumina beams are reduced to the same level as in Coors alumina as a result of such annealing. Furthermore, this may give more insight into reaction layer formation (*i.e.*, whether or not impurities are influential). Machining away any of the observed reaction layers observed in the current study would enable one to determine whether these layers or the interfacial adhesion is responsible for changes in mechanical properties. Certainly, a system capable of monitoring p_{O_2} should be used in such experiments. Saiz [192] has suggested that the p_{O_2} in these furnaces can be determined by annealing various metals and observing which ones are oxidized.

A kinetic study of copper film break-up would provide further insight into the microstructural evolution of the interlayer. Model studies using other orientations of sapphire may identify parameters that impact the kinetics of copper film break-up. For example, the $(10\bar{1}0)$ sapphire/vapor interface is unstable and facets. If facetting occurs in the presence of the liquid phase, such facets may assist copper film break-up by inducing instabilities in the liquid phase, or fundamentally alter the interfacial microstructure. Sapphire surfaces of controlled surface roughness can be made *via* microlithographic techniques and used to investigate surface roughness effects on microstructural evolution. Provided a technique can be developed to produce sufficiently large sapphire bicrystals, these specimens could be used in copper/niobium/copper joints to monitor the effects of an alumina grain boundary on copper film evolution.

Other variables such as the effects of copper coating thickness should be explored. It is possible that regardless of the coating thickness, the liquid is thinned to the same level due to the applied load; however, some evidence from the current study suggests thicker coatings leave more copper at the interface. If such differences are substantial, these may also have pronounced effects on the kinetics of copper film break-up and resulting microstructure (*e.g.*, various isolated copper particle sizes) even after the film achieves an equilibrium morphology.

Fabricating a joint with alumina that is known not to contain a glassy phase would verify whether or not such a phase is instrumental in obtaining strong joints. Mammana and coworkers [3,135] have produced a sapphire bicrystal by growing two sapphire crystals through a thin slab of sintered alumina sandwiched between the sapphire crystals. No glassy phase could be detected by TEM at the bicrystal grain boundary, thus implying that sintering larger compacts of this powder would be useful for such an experiment.

Perhaps shorter processing times and lower temperatures (≈1250-1300°C range) are sufficient to produce a joint as strong as those processed at 1400°C. Titanium additions to the copper and/or niobium may improve the resulting interfacial adhesion [85], and produce even stronger joints. This would also assist in matching or improving the results obtained by processing at 1400°C with potentially lower processing temperatures.

Certainly other types of mechanical testing would be necessary to completely assess the mechanical reliability of these joints. This work is currently underway in collaboration with Ritchie and coworkers [24]. Generally extending this TLPADB technique to other systems, particularly those more compatible with oxidizing environments is worthwhile.

Appendix I
Estimation of Equilibrium Partial Oxygen Pressure

Calculations of the equilibrium p_{O_2} can be developed by considering the following general oxidation reaction of a species M (usually an elemental metal) to form an oxide $\mathrm{M}_x\mathrm{O}_y$.

$$\frac{2x}{y}\mathrm{M} + \mathrm{O}_2 \Leftrightarrow \frac{2}{y}\mathrm{M}_x\mathrm{O}_y \tag{I.1}$$

The equilibrium p_{O_2} is gotten by solving the following equation for the activity of oxygen, a_{O_2}, where the values of ΔG°_{rxn}, ΔS°_{rxn}, and ΔH°_{rxn} are those for which one mole of oxygen is consumed in the reaction, *i.e.*, a reaction like that in equation I.1.

$$K_{eq} = \exp\left(-\frac{\Delta G^\circ_{rxn}}{\mathrm{R}T}\right) = \frac{\left(a_{\mathrm{M}_x\mathrm{O}_y}\right)^{\frac{2}{y}}}{\left(a_{\mathrm{O}_2}\right)\left(a_{\mathrm{M}}\right)^{\frac{2x}{y}}} = \exp\left(\frac{\Delta S^\circ_{rxn}}{\mathrm{R}}\right)\exp\left(-\frac{\Delta H^\circ_{rxn}}{\mathrm{R}T}\right) \tag{I.2}$$

ΔG°_{rxn}, ΔS°_{rxn}, and ΔH°_{rxn} can be obtained from standard thermodynamic data tables [136-138]. If limited data on the temperature dependence of ΔS°_{rxn} and ΔH°_{rxn} is available, they may be treated as constants. In other words, one assumes that the sum of the heat capacities of the reactants is equal to the heat capacity of the oxide product (scaled by the appropriate reaction coefficients).

$$\tfrac{2}{y}C_{P,\mathrm{M}_x\mathrm{O}_y} = \tfrac{2x}{y}C_{P,\mathrm{M}} + C_{P,\mathrm{O}_2} \tag{I.3}$$

For the case in which a pure condensed reactant M forms a pure condensed product phase $\mathrm{M}_x\mathrm{O}_y$, the activities of these two phases will be unity. For ΔG°_{rxn} based on a standard state of 1 atm, the oxygen activity will just be the p_{O_2} in atmospheres. Consequently, for the case of a pure condensed reactant M and pure condensed oxide $\mathrm{M}_x\mathrm{O}_y$, equation I.2 can be written as an expression for the equilibrium p_{O_2} in atmospheres.

$$p_{\mathrm{O}_2} = \exp\left(\frac{\Delta G^\circ_{rxn}}{\mathrm{R}T}\right) = \exp\left(-\frac{\Delta S^\circ_{rxn}}{\mathrm{R}}\right)\exp\left(\frac{\Delta H^\circ_{rxn}}{\mathrm{R}T}\right) \tag{I.4}$$

This approach is equivalent to reading the equilibrium values of p_{O_2} for a metal/metal oxide reaction off an Ellingham or predominance diagram. ΔS°_{rxn} typically has a negative value since the reactants (a condensed phase and gaseous oxygen) react to form a condensed oxide product phase. Negative values of ΔS°_{rxn} imply that ΔH°_{rxn} must be negative in order for ΔG°_{rxn} to be less than zero and the equilibrium p_{O_2} to be less than 1 atm. This is in fact the case for most metals, and ΔH°_{rxn} values less than zero imply that the equilibrium p_{O_2} will increase with temperature. It is worth noting that oxidation reactions with $\Delta G^\circ_{rxn} > 0$ can be thermodynamically favorable if the p_{O_2} is sufficiently high (>1 atm), *e.g.*, the formation of gold oxides [23].

For the oxidation reactions in which the product is a gaseous species in addition to oxygen, a slightly more complicated approach is required (this is particularly of concern in the cases of graphite oxidizing to form gaseous carbon monoxide or carbon dioxide). The activity of the oxide becomes its partial pressure in atmospheres, and equation I.2 may be rewritten as follows.

$$p_{\mathrm{O}_2} = \left(p_{\mathrm{M}_x\mathrm{O}_y}\right)^{\frac{2}{y}} \exp\left(\frac{\Delta G^\circ_{rxn}}{\mathrm{R}T}\right) = \left(p_{\mathrm{M}_x\mathrm{O}_y}\right)^{\frac{2}{y}} \exp\left(-\frac{\Delta S^\circ_{rxn}}{\mathrm{R}}\right)\exp\left(\frac{\Delta H^\circ_{rxn}}{\mathrm{R}T}\right) \tag{I.5}$$

In considering these types of reactions, something more must be known about the system in order to evaluate the p_{O_2}, namely the $p_{\mathrm{M}_x\mathrm{O}_y}$. Equation I.5 implies that the greater the

$p_{\mathrm{M}_x\mathrm{O}_y}$, the greater the p_{O_2} will be. For estimating the p_{O_2} in such cases, it will be assumed that $\mathrm{M}_x\mathrm{O}_y$ is the dominating gaseous species in the vacuum chamber of the furnaces, and therefore, the total vacuum pressure can be used as a value for $p_{\mathrm{M}_x\mathrm{O}_y}$. This will provide an upper bound to the p_{O_2}.

Another consideration to make is that of reactants M which may form multiple oxides. For reactions in which the oxide product is a pure condensed phase, the oxidation reaction with the lowest (most negative) ΔG°_{rxn} is the one of interest; this will result in a lower value of p_{O_2} than for other reactions (see equation I.4). If the equilibrium p_{O_2} for other oxidation reactions were used, this would imply that two different oxide products would be in equilibrium together rather than an oxide in equilibrium with the furnace element material. Similarly, in determining the p_{O_2} in equilibrium with a higher order oxide (*e.g.*, NbO_2), a reaction between it and a neighboring oxide (in the binary system) must be considered (*e.g.*, NbO or Nb_2O_5). Considering the reaction with both neighboring oxides would provide the range of p_{O_2} over which the particular oxide is stable. Such ranges are apparent for NbO and NbO_2 for the p_{O_2} values given in Chapter 1 (the values assume equation I.3).

If multiple gaseous oxide products are potentially formed, such as in the case of a graphite furnace, a similar approach is used, *i.e.*, the reaction with the lowest ΔG°_{rxn} is applied to equation I.5. In the case of graphite and over the temperature range of interest, the reaction of interest is the formation of carbon monoxide. However, there will be an equilibrium amount of carbon dioxide that forms in the gaseous phase. In the temperature range of interest, and for the initial assumption that $p_{\mathrm{CO}} = P_{total}$, the resulting ratio $p_{\mathrm{CO}}\!:\!p_{\mathrm{CO}_2}$ is greater than 10^9, thus the amount of carbon dioxide present makes a negligible contribution to the total pressure and the initial assumption is reasonable for these purposes. Should the ratio $p_{\mathrm{CO}}\!:\!p_{\mathrm{CO}_2}$ be of the order of unity, it would be necessary to readjust the initial assumption $p_{\mathrm{CO}} = P_{total}$ accordingly and redo the calculation. If necessary, such a process can be done iteratively to produce a more precise result; even the contribution of oxygen to the total pressure could be accounted for.

Appendix II
Liquid Spreading Conditions in PTLP Bonding

Consider the same configurations illustrated in Figure 2.4. Any evolution of the liquid phase requires that:

$$\gamma_{lc}\mathrm{d}A_{lc} + \gamma_{cv}\mathrm{d}A_{cv} + \gamma_{lm}\mathrm{d}A_{lm} + \gamma_{mv}\mathrm{d}A_{mv} + \gamma_{lv}\mathrm{d}A_{lv} < 0 \qquad \text{(II.1)}$$

Additionally, it is required that $\mathrm{d}A_{cv} = -\mathrm{d}A_{lc}$ and $\mathrm{d}A_{mv} = -\mathrm{d}A_{lm}$. Applying these relations and the Young equation to equation II.1 yields:

$$\left(\gamma_{lc} - \gamma_{cv}\right)\mathrm{d}A_{lc} + \left(\gamma_{lm} - \gamma_{mv}\right)\mathrm{d}A_{lm} + \gamma_{lv}\mathrm{d}A_{lv} < 0 \qquad \text{(II.2)}$$

$$-\gamma_{lv}\left(\cos\theta_{lc}\right)\mathrm{d}A_{lc} - \gamma_{lv}\left(\cos\theta_{lm}\right)\mathrm{d}A_{lm} + \gamma_{lv}\mathrm{d}A_{lv} < 0 \qquad \text{(II.3)}$$

For spreading, $\mathrm{d}A_{lv} < 0$, thus the spreading conditions is:

$$\left(\cos\theta_{lc}\right)\frac{\mathrm{d}A_{lc}}{\mathrm{d}A_{lv}} + \left(\cos\theta_{lm}\right)\frac{\mathrm{d}A_{lm}}{\mathrm{d}A_{lv}} - 1 < 0 \qquad \text{(II.4)}$$

The derivatives ${}^{\mathrm{d}A_{lc}}\!/_{\mathrm{d}A_{lv}}$ and ${}^{\mathrm{d}A_{lm}}\!/_{\mathrm{d}A_{lv}}$ cannot be evaluated without detailed information on the geometry of system; however, they will be generally large and negative (compared to unity), thus spreading will be favored for contact angles below 90°. It can be further assumed that the core layer and ceramic surfaces are parallel and have no flaws, thus $\mathrm{d}A_{lc} = \mathrm{d}A_{lm}$, and the spreading condition may also be expressed as:

$$\cos\theta_{lc} + \cos\theta_{lm} - \frac{\mathrm{d}A_{lv}}{\mathrm{d}A_{lc}} > 0 \qquad \text{(II.5)}$$

The derivative will generally be small, and the spreading condition may be approximated as given by equations 2.4 and 2.5.

Now, to consider the filling of flaws, the following figure illustrates a liquid front approaching regions of the core and ceramic which deviate from the ideal parallel surfaces.

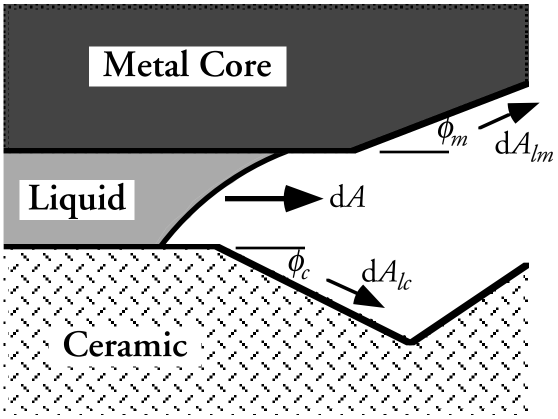

Ignoring the contribution of the liquid/vapor interface, equation II.3 may be rewritten as:

$$-\gamma_{lv}\left(\cos\theta_{lc}\right)\mathrm{d}A_{lc}-\gamma_{lv}\left(\cos\theta_{lm}\right)\mathrm{d}A_{lm}<0 \tag{II.6}$$

From the figure, $\mathrm{d}A_{lc}$ and $\mathrm{d}A_{lm}$, may be related to the normal area change, $\mathrm{d}A$, for parallel surfaces.

$$-\gamma_{lv}\left(\cos\theta_{lc}\right)\frac{\mathrm{d}A}{\cos\phi_c}-\gamma_{lv}\left(\cos\theta_{lm}\right)\frac{\mathrm{d}A}{\cos\phi_m}<0 \tag{II.7}$$

For spreading, $\mathrm{d}A>0$, and the condition may be simplified as:

$$\frac{\cos\theta_{lc}}{\cos\phi_c}+\frac{\cos\theta_{lm}}{\cos\phi_m}>0 \tag{II.8}$$

Clearly, for parallel surfaces, equation 2.4 is retained. The magnitude of the expression may be thought of as a driving force for liquid spreading. Clearly if both contact angles are <90°, flaws will be filled, and flaws having a steeper angle with respect to the average surface will more easily be filled than ideal parallel spreading; *i.e.*, more surface area is replaced with liquid/solid interface.

Considering a case in which the ceramic is not wetted, flaws with sufficiently small angle, ϕ_c, may still be filled; the negative contribution of the ceramic term will still be small compared to the positive metal term (see h in Figure 2.5). For flaws of larger ϕ_c, the liquid may be pinned at the ceramic flaw corner. The liquid may continue to cover the metal core (provided the increase in liquid/vapor surface area is not too large), and may cause the ceramic flaw to be bridged (b and g in Figure 2.5). Two liquid fronts may run into each other, causing flaws like a in Figure 2.5 to develop. Finally, steep angled flaws in the metal adjacent to ceramic flaws may assist filling of the ceramic flaw by increasing the liquid spreading driving force (equation II.8). Predicting the exact flaw geometry resulting from PTLP bonding will required extensive information on the joining surfaces, and other factors such as liquid availability influence the resulting structure; however, the general discussion given in Chapter 2 illustrates the primary concerns and provides a method for insuring optimum contact between liquid, core, and ceramic.

Appendix III
Derivation of Bend Stress for Static Loading Conditions

The following figure illustrates a beam under a load $P\ (= mg)$, in four-point bend, along with the associated moment, M_x, in the beam. The load P is distributed about the two upper inner span contact points by the fraction *f*, and the resulting loads on the lower outer span points can be evaluated from the conditions that the sum of all four forces (loads) be zero and that zero net torque be applied to the beam.

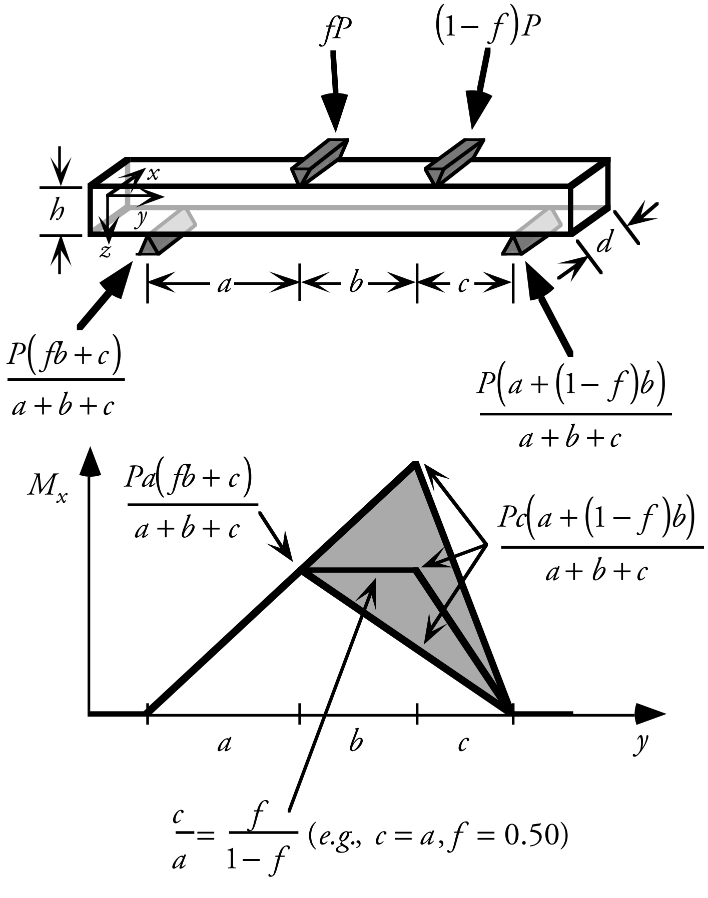

The moment at any position in the beam is also given by:

$$\mathrm{M}_x(y) = \int_{\frac{-d}{2}}^{\frac{d}{2}} \int_{\frac{-h}{2}}^{\frac{h}{2}} z\sigma_{yy}(x,y,z)\,\mathrm{d}z\mathrm{d}x \tag{III.1}$$

A simple stress state as depicted below may be assumed.

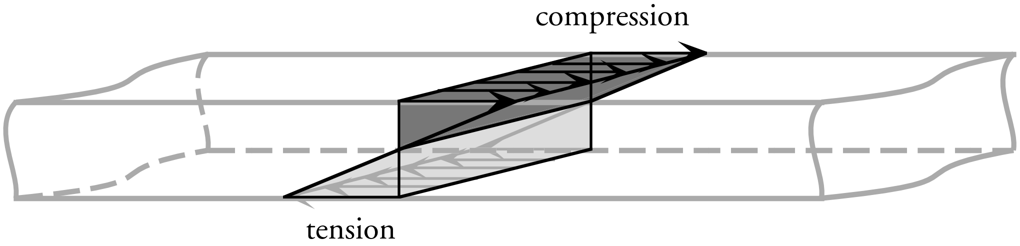

The assumptions are that the neutral axis is at the center of the beam (*i.e.*, the plane $z = 0$), and the stress σ_{yy} only depends on *y* and *z*, and may be described as follows

$$\sigma_{yy}(x,y,z) = \sigma_{yy}(y,z) = \frac{2z}{h}\sigma_{yy}^{\max}(y) \tag{III.2}$$

where $\sigma_{yy}^{\max}(y)$ is the maximum tensile stress in the beam at the particular position *y*. Applying equation III.2 to equation III.1 and integrating yields:

$$\mathrm{M}_x(y) = \int_{\frac{-d}{2}}^{\frac{d}{2}} \int_{\frac{-h}{2}}^{\frac{h}{2}} z\frac{2z}{h}\sigma_{yy}^{\max}(y)\,\mathrm{d}z\mathrm{d}x = d\,\frac{2\sigma_{yy}^{\max}(y)}{h}\left[\frac{z^3}{3}\right]_{\frac{-h}{2}}^{\frac{h}{2}} = \frac{dh^2\sigma_{yy}^{\max}(y)}{6} \tag{III.3}$$

Solving for $\sigma_{yy}^{\max}(y)$ gives the stress distribution in the beam.

$$\sigma_{yy}^{\max}(y) = \frac{6\mathrm{M}_x(y)}{dh^2} \tag{III.4}$$

The four-point bend jigs used in the current study are designed such that $a = c$, and the load applied to the inner span points should be equal (*i.e.*, $f = 0.50$). This information may be used to obtain the fracture stress, since fracture occurs exclusively in region *b* of the beam, which corresponds with the maximum moment.

$$\sigma_{\mathrm{F}}^{\mathrm{4PB}} = \frac{6}{dh^2}\left(\frac{Pa\left(0.5b + a\right)}{2a + b}\right) = \frac{3aP}{dh^2} \tag{III.5}$$

If one of the load points were to not contact the beam in a four-point bend test, an effective three-point bend test would be executed. The fracture stress for such a test may be found by applying the condition $f = 0$ (or $f = 1$), finding the maximum moment in the figure, and applying to equation III.4.

$$\sigma_{\mathrm{F}}^{\mathrm{3PB}} = \frac{6}{dh^2}\left(\frac{Pa\left(a + b\right)}{2a + b}\right) = \frac{6}{dh^2}\left(\frac{2.125Pa^2}{3.125a}\right) = \frac{4.08aP}{dh^2} \tag{III.6}$$

It is worth noting that failure may occur at a point outside the region (in four-point bend) or point (in three-point bend) of maximum applied stress if a flaw of sufficient stress intensity is present. Interior ceramic (*i.e.*, not at the tension surface) failures may also initiate for similar reasons. In the case of BK26BM65 (see Table 4.5), if the jig was in fact misaligned, and the joining layer was centered with respect to the inner span, the stress at the beam joint would be ≈0.75 times the value given by equation III.6.

Furthermore, the shear load within the beam is given by the gradient in the moment in the beam. Thus, there are no shear loads within the inner span of the four-point bend test. Since all failures occur within the inner span, this implies all failures are mode I. By comparing the maximum shear loads for both the three-point bend and four-point bend tests described, the maximum shear stress (σ_{yz}) in the beams is at least an order of magnitude lower than the tensile stress for the beam thicknesses used. Beams would have to be ≈50 mm in height, *h*, for the shear and tensile stresses to be comparable.

Appendix IV
Post-Bonding Anneals at 1200°C

Although the results from argon annealing at both 1000°C and 1200°C are similar, when joints are annealed in vacuum at 1200°C for 250 h interfacial failures are observed. The three beams tested had strengths of 185 MPa, 192 MPa, and 209 MPa; these points are also plotted in Figure 4.25. Figure 4.28 illustrates the interlayer cross section of as-processed joints in comparison to those annealed at 1000°C and 1200°C in vacuum. Some material has deposited on the ceramic adjacent to the niobium/alumina interface that was not observed in joints annealed in vacuum at 1000°C. EDS analysis revealed several characteristic peaks for tungsten from this region, likely due to deposition from the furnace elements. Since the layer is only observed adjacent to the metal/ceramic interface, the interlayer is instrumental in its formation. At 1000°C, the vapor pressure of tungsten will be substantially lower, and such deposition will be highly retarded.

Several possible interactions of the tungsten with the alumina and/or niobium may impose strength-limiting features. The tungsten may simply serve as a brittle layer from which a crack initiates and propagates along the interface. Since the thermal expansion coefficient of tungsten is about half that of both niobium and alumina (see Figure 2.8), the tungsten will be in compression and the nearby joint in tension as beams are cooled. This would be of particular concern if the tungsten filled in flaws on the beam surfaces. Dissolution of tungsten in niobium (the niobium-tungsten system has a simple lens phase diagram [23]) may reduce the interfacial adhesion or embrittle the niobium. Since the oxygen activity is estimated to be that at which tungsten oxide forms, tungsten aluminate ($2Al_2O_3 \cdot 5WO_3$) and/or any of the several tungsten niobates can form [139]. There certainly is evidence for discoloration and thin reacted zones near beam edges in addition to the deposited tungsten (see Figure 4.29); however, further work would be necessary for their exact identification. These results indicate a potential sensitivity of joints to different chemical environments at elevated temperature; however, the intended goal of these anneals was to investigate the effects of p_{O_2}.

In the vacuum furnace, the oxygen activity is expected to be sufficient to completely oxidize niobium (*i.e.*, form Nb_2O_5). The speckled appearance (surface roughening) of the interlayer in Figure 4.28d suggests some chemical attack has indeed occurred on the interlayer, possibly vaporization of volatile oxide molecules. At lower temperatures (*i.e.*, 1000°C) the kinetics of such attack will be substantially lower due to a lower p_{O_2}. Figure 4.29 illustrates the fracture surface of one of these vacuum-annealed joints. Note the large piece of niobium (the roughly square blurry region in Figure 4.30) that was pulled out from the interlayer. These niobium pullouts appear to occur around the perimeter of the beam and cause the interlayer to bulge out from the straight tension edge (see Figures 4.29b and the metal side of Figure 4.30). Since the fracture path does not deviate into the niobium for unannealed beams, this suggests embrittlement of the interlayer occurred.

In comparing Figure 4.28d to Figure 4.31b, the tungsten layer formed on joints annealed in vacuum (1200°C) only is considerably more extensive than those annealed in argon (1200°C) prior to vacuum annealing (1200°C). The interlayer region is blurry because its surface lies above the focus plane. This is most likely associated with molybdenum that plates out on the metal interlayer, although molybdenum is not detected *via* EDS (its primary peak lies very close to that of niobium). (This plating out is so apparent due to the low argon flow rate of ≈10 mL/min.) Prior annealing in argon, or the plating out on the interlayer may have chemical effects serving to inhibit the tungsten deposition rate.

The presence of the tungsten layer after re-annealing beams in vacuum and the increased strength seem to suggests that interfacial adhesion is lower for higher oxygen activities in niobium. The initial annealing of the joint in a low p_{O_2} environment should reduce the oxygen activity in niobium to the value dictated by alumina dissolution. Re-annealing in vacuum would require that the interlayer be resaturated with additional oxygen for oxygen embrittlement to occur. Furthermore, any material which deposits on top of the interlayer may shield the niobium from the atmosphere, thus inhibiting the kinetics of embrittling reactions or the vaporization of volatile species.

References

1. A.M. GLAESER, course instructor, “MSE 122 - Lecture 1”, Department of Materials Science and Mineral Engineering, University of California at Berkeley, (Spring Semester 1997).
2. A.M. GLAESER, course instructor, “MSE 122 - Lecture 18”, Department of Materials Science and Mineral Engineering, University of California at Berkeley, (Spring Semester 1997).
3. A.M. GLAESER, Lawrence Berkeley National Laboratory, private communication (1999).
4. S.M. JOHNSON and D.J. ROWCLIFFE, “Mechanical Properties of Joined Silicon Nitride”, *J. Am. Cer. Soc.*, **68**, [9], 468-72 (1985).
5. A.G. EVANS, M. RÜHLE, and M. TURWITT, “On the Mechanics of Failure in Ceramic/Metal Bonded Systems”, *Journal de Physique*, **46**, C4–613-26 (1985).
6. B.J. DALGLEISH, M.C. LU, and A.G. EVANS, “The Strength of Ceramics Bonded with Metals”, *Acta Metall.*, **36**, [8], 2029-35 (1988).
7. A.G. EVANS, B.J. DALGLEISH, M. HE, and J.W. HUTCHINSON, “On Crack Path Selection and the Interface Fracture Energy in Bimaterial Systems”, *Acta Metall.*, **37**, [12], 3249-54 (1989).
8. G. SOYEZ, G. ELSSNER, M. RÜHLE, and R. RAJ, “Constrained Yielding in Niobium Single Crystals Bonded to Sapphire”, *Acta Mater.*, **46**, [10], 3571-81 (1998).
9. JU. V. NAIDICH, “The Wettability of Solids by Liquid Metals”, in *Progress in Surface and Membrane Science*, edited by D.A. CADENHEAD and J.F. DANIELLI, (Academic Press, London, 1981) pp. 353-484.
10. G.R. VAN HOUTEN, “A Survey of Ceramic-to-Metal Bonding”, *Ceramic Bulletin*, **38**, [6], 301-7 (1959).

11. A.J. MOORHEAD, "Direct Brazing of Alumina Ceramics", A*dvanced Ceramic Materials*, **2**, [2], 159-66 (1987).

12. B. DERBY and E.R. WALLACH, "Theoretical Model for Diffusion Bonding", *Metal Science*, **16**, 49-56 (1982).

13. B. DERBY and E.R. WALLACH, "Diffusion Bonding: Development of Theoretical Model", *Metal Science*, **18**, 427-31 (1984).

14. I.E. REIMANIS, "Pore Removal During Diffusion Bonding of Nb-Al_2O_3 Interfaces", *Acta Metall. Mater.*, **40**, S67-74 (1992).

15. M.R. LOCATELLI, "Partial Transient Liquid Phase Brazing of Alumina via Microdesigned Ni-Based Interlayers", M.S. Thesis, Department of Materials Science and Mineral Engineering, University of California at Berkeley, (May 1997).

16. R.V. ALLEN and W.E. BORBIDGE, "Solid State Metal-Ceramic Bonding of Platinum to Alumina", *Journal of Materials Science*, **18**, 2835-43 (1983).

17. M.L. SHALZ, B.J. DALGLEISH, A.P. TOMSIA, R.M. CANNON, and A.M. GLAESER, "Ceramic Joining III: Bonding of Alumina via Cu/Nb/Cu Interlayers", *Journal of Materials Science*, **29**, 3678-90 (1994).

18. R.E. LOEHMAN and A.P. TOMSIA, "Joining of Ceramics", *Ceramic Bulletin*, **67**, [2], 375-80 (1988).

19. K. BURGER and M. RÜHLE, "Material Transport Mechanisms During the Diffusion Bonding of Niobium to Al_2O_3", *Ceram. Eng. Sci. Proc.*, **10,** [11-12], 1549-66 (1989).

20. K. BURGER and M. RÜHLE, "Material Transport Mechanisms During the Diffusion Bonding of Niobium to Al_2O_3", *Ultramicroscopy*, **29,** 88-97 (1989).

21. G. ELßNER and G. PETZOW, "Verträglichkeit zwischen Materialkomponenten in Metall-Keramik-Verbundwerkstoffen", *Z. Metallkde.*, **64**, [4], 280-6 (1973), in German.

22. E. FROMM and H. JEHN, “Thermodynamics and Phase Relations in Refractory Metal Solid Solutions Containing Carbon, Nitrogen, and Oxygen”, *Metallurgical Transactions*, **3**, 1685-92 (1972).

23. T.B. MASSALSKI, ed., *Binary Alloy Phase Diagrams,* 2nd Edition, Vol. 1-3 (ASM International, Metals Park, OH, 1990).

24. R.M. CANNON, A.M. GLAESER, J. KRUZIC, R.A. MARKS, J.M. MCNANEY, and R.O. RITCHIE, Lawrence Berkeley National Laboratory, unpublished research (1999).

25. L. BERNSTEIN and H. BARTHOLOMEW, “Applications of Solid-Liquid Interdiffusion (SLID) Bonding in Integrated-Circuit Fabrication”, *Transactions of the Metallurgical Society of AIME*, **236**, 405-12 (1966).

26. Y. IINO, “Partial Transient Liquid-Phase Metals Layer Technique of Ceramic-Metal Bonding”, *Journal of Materials Science Letters*, **10**, 104-6 (1990).

27. M.L. SHALZ, B.J. DALGLEISH, A.P. TOMSIA, and A.M. GLAESER, “Ceramic Joining Part I: Partial Transient Liquid-Phase Bonding of Alumina via Cu/Pt Interlayers”, *Journal of Materials Science*, **28**, 1673-84 (1993).

28. M.L. SHALZ, B.J. DALGLEISH, A.P. TOMSIA, and A.M. GLAESER, “Ceramic Joining II: Partial Transient Liquid-Phase Bonding of Alumina via Cu/Ni/Cu Multilayer Interlayers”, *Journal of Materials Science*, **29**, 3200-8 (1994).

29. M. PAULASTO, G. CECCONE, and S.D. PETEVES, “Joining of Silicon Nitride via a Transient Liquid”, *Scripta Materialia*, **36**, [10], 1167-73 (1997).

30. D.S. DUVALL, W.A. OWCZARSKI, and D.F. PAULONIS, “TLP™ Bonding: A New Method for Joining Heat Resistant Alloys”, *Welding Journal*, **53**, 203-14 (1974).

31. T. ISEKI, K. YAMASHITA, and H. SUZUKI, “Joining of Self-Bonded Silicon Carbide by Germanium Metal”, *Journal of the American Ceramic Society*, **64**, C–13-4 (1981).

32. T. ISEKI, K. YAMASHITA, and H. SUZUKI, “Joining of Self-Bonded SiC by Ge Metal”, *Proc. Brit. Ceram. Soc.*, **31**, 1-8 (1981).

33. R.E. LOEHMAN, “Transient Liquid Phase Bonding of Silicon Nitride Ceramics”, in *Surfaces and Interfaces in Ceramic and Ceramic-Metal Systems*, edited by J.A. PASK and A.G. EVANS, (Plenum, New York, 1981) pp. 701-11.

34. R.D. BRITTAIN, S.M. JOHNSON, R.H. LAMOREAUX, and D.J. ROWCLIFFE, “High-Temperature Chemical Phenomena Affecting Silicon Nitride Joints”, *Journal of the American Ceramic Society*, **67**, [8], 522-6 (1984).

35. M.L. MECARTNEY, R. SINCLAIR, and R.E. LOEHMAN, “Silicon Nitride Joining”, *J. Am. Cer. Soc.*, **68**, [9], 472-8 (1985).

36. S.J. GLASS, F.M. MAHONEY, B. QUILLAN, J.P. POLLINGER, and R.E. LOEHMAN, “Refractory Oxynitride Joints in Silicon Nitride”, *Acta Mater.*, **46**, [7], 2393-9 (1998).

37. M. GOPAL, L.C. DE JONGHE, and G. THOMAS, “Silicon Nitride Joining Using Rare-Earth Reaction Sintering”, *Scripta Materialia*, **36**, [4], 455-60 (1997).

38. M. GOPAL, L.C. DE JONGHE, and G. THOMAS, “Silicon Nitride: From Sintering to Joining”, *Acta Mater.*, **46**, [7], 2401-5 (1998).

39. P.A. WALLS and M. UEKI, “Joining SiAlON Ceramics Using Composite β-SiAlON-Glass Adhesives”, *J. Am. Ceram. Soc.*, 75, [9], 2491-7 (1992).

40. P.A. WALLS and M. UEKI, “Mechanical Properties of β-SiAlON Ceramics Joined Using β-SiAlON-Glass Adhesives”, *J. Am. Ceram. Soc.*, 78, [4], 999-1005 (1995).

41. Y. IINO and N. TAGUCHI, “Interdiffusing Metals Layer Technique of Ceramic-Metal Bonding”, *Journal of Materials Science Letters*, 7, 981-2 (1988).

42. M.R. LOCATELLI, Lawrence Berkeley National Laboratory, unpublished research (1995).

43. K. NOGI, K. OISHI, and K. OGINO, “Wettability of Solid Oxides by Liquid Pure Metals”, *Materials Transactions, JIM*, **30**, [2], 137-45 (1989).

44. J.G. LI, “Wetting and Interfacial Bonding of Metals with Ionocovalent Oxides”, *J. Am. Ceram. Soc.*, 75, [11], 3118-26 (1992).

45. J.E. McDonald and J.G. Eberhart, “Adhesion in Aluminum Oxide-Metal Systems”, *Transactions of the Metallurgical Society of AIME*, **233**, 512-7 (1965).

46. M.R. Locatelli, A.P. Tomsia, K. Nakashima, B.J. Dalgleish, and A.M. Glaeser, “New Strategies for Joining Ceramics for High-Temperature Applications”, *Key Engineering Materials*, **111-112**, 157-90 (1995).

47. H. Matsumoto, M.R. Locatelli, K. Nakashima, A.M. Glaeser, and K. Mori, “Wettability of Al_2O_3 by Liquid Cu as Influenced by Additives and Partial Transient Liquid-Phase Bonding of Al_2O_3”, *Materials Transactions, JIM*, **36**, [4], 555-64 (1995).

48. O.F. de Lima, M. Krehl, and K. Schulze, “Wetting Characteristics of Copper on Niobium”, *Journal of Materials Science*, **20**, 2464-70 (1985).

49. E.N. Hodkin, M.G. Nicholas, and D.M. Poole, “The Surface Energies of Solid Molybdenum, Niobium, Tantalum, and Tungsten”, *Journal of Less-Common Metals*, **20**, 93-103 (1970).

50. R.O. Ritchie, R.M. Cannon, B.J. Dalgleish, R.H. Dauskardt, and J.M. McNaney, “Mechanics and Mechanisms of Crack Growth at or Near Ceramic-Metal Interfaces: Interface Engineering Strategies for Promoting Toughness”, *Materials Science and Engineering*, **A166**, 221-35 (1993).

51. H.C. Cao, M.D. Thouless, and A.G. Evans, “Residual Stresses and Cracking in Brittle Solids Bonded with a Thin Ductile Layer”, *Acta Metall.*, **36**, [8], 2037-46 (1988).

52. A.G. Evans, M.C. Lu, S. Schmauder, and M. Rühle, “Some Aspects of the Mechanical Strength of Ceramic/Metal Bonded Systems”, *Acta Metall.*, **34**, [8], 1643-55 (1986).

53. M.L. Locatelli, “Crack Propagation Near Interfaces in Metal/Ceramic Systems”, MSE 212 Term Paper, Department of Materials Science and Mineral Engineering, University of California at Berkeley, (Spring 1995).

54. K. NAKASHIMA, Nikkato Corporation, Osaka Japan, unpublished research (1996).

55. P. KRITSALIS, J.G. LI, L. COUDURIER, and N. EUSTATHOPOULOS, "Role of Clusters on the Wettability and Work of Adhesion of the Cu-Cr/Al_2O_3 System", *Journal of Materials Science Letters*, **9**, 1332-5 (1990).

56. P. KRITSALIS, L. COUDURIER, and N. EUSTATHOPOULOS, "Contribution to the Study of Reactive Wetting in the CuTi/Al_2O_3 System", *Journal of Materials Science*, **26**, 3400-8 (1991).

57. P. KRITSALIS, V. MERLIN, L. COUDURIER, and N. EUSTATHOPOULOS, "Effect of Cr on Interfacial Interaction and Wetting Mechanisms in Ni Alloy/Alumina Systems", *Acta Metall. Mater.*, **40**, [6], 1167-75 (1992).

58. YU. V. NAIDICH and V.S. ZHURAVLEV, "Adhesion, Wettability, and Reaction of Titanium-Containing Melts with High-Melting Oxides", *Refractories (USSR)*, **15**, 55-60 (1974).

59. V. GHETTA, J. FOULETIER, and D. CHATAIN, "Oxygen Adsorption Isotherms at the Surfaces of Liquid Cu and Au-Cu Alloys and Their Interfaces with Al_2O_3 Detected by Wetting Experiments", *Acta Mater.*, **44**, [5], 1927-36 (1996).

60. E. SAIZ, A.P. TOMSIA, and R.M. CANNON, "Wetting and Work of Adhesion in Oxide/Metal Systems", submitted for *Ceramic Microstructures '96*, edited by A.P. TOMSIA and A.M. GLAESER, (Plenum, New York).

61. A.P. TOMSIA, E. SAIZ, S. FOPPIANO, and R.M. CANNON, "Reactive Wetting: Ridging, Adsorption, and Compound Formation", in *Proc. Int. Conf. High Temperature Capillarity*, edited by N. EUSTATHOPOULOS and N. SOBCZAK, (June 29 to July 2, Cracow, Poland, 1997), pp. 59-80.

62. T.E. O'BRIEN and A.C.D. CHAKLADER, "Effect of Oxygen on the Reaction Between Copper and Sapphire", *Journal of the American Ceramic Society*, **57**, [8], 329-32 (1974).

63. S.P. MEHROTRA and A.C.D. CHAKLADER, "Interfacial Phenomena Between Molten Metals and Sapphire Substrate", *Metallurgical Transactions B*, **16B**, 567-75 (1985).

64. C. BERAUD, M. COURBIERE, C. ESNOUF, D. JUVE, and D. TREHEUX, "Study of Copper-Alumina Bonding", *Journal of Materials Science*, **24**, 4545-54 (1989).

65. M. KITAYAMA, "The Wulff Shape of Doped and Undoped Alumina", Ph.D. Thesis, Department of Materials Science and Mineral Engineering, University of California at Berkeley, (December 1996).

66. J.J. BRENNAN and J.A. PASK, "Effect of Nature of Surfaces on Wetting of Sapphire by Liquid Aluminum", *Journal of the American Ceramic Society*, **51**, [10], 569-73 (1968).

67. W. CHEN, M.R. LOCATELLI, and A.M. GLAESER, Lawrence Berkeley National Laboratory, unpublished research (1996).

68. A.M. BROWN and M.F. ASHBY, "Correlations for Diffusion Constants", *Acta Metallurgica*, **28**, 1085 (1980).

69. R.P. ELLIOT, Constitution of Binary Alloys, First Supplement, (McGraw-Hill Book Company, New York, NY 1965) pp. 253-4.

70. E. SAIZ, Lawrence Berkeley National Laboratory, unpublished research (1995).

71. P. NIKOLOPOULOS, S. AGATHOPOULOS, and A. TSOGA, "A Method for the Calculation of Interfacial Energies in Al_2O_3 and ZrO_2/Liquid-Metal and Liquid-Alloy Systems", *Journal of Materials Science*, **29**, 4393-98 (1994).

72. M. NICHOLAS, R.R.D. FORGAN, and D.M. POOLE, "The Adhesion of Metal/Alumina Interfaces", *Journal of Materials Science*, **3**, 9-14 (1968).

73. G. ELßNER and R. PABST, "Bruchmechanische Untersuchung der Haftung bei Metall-Keramik-Verbundwerkstoffen", *High Temperatures-High Pressures*, **6**, 321-7 (1974), in German.

74. K. BURGER, W. MADER, and M. RÜHLE, "Structure, Chemistry, and Diffusion Bonding of Metal/Ceramic Interfaces", *Ultramicroscopy*, **22**, 1-14 (1987).

75. B. GIBBESCH, G. ELSSNER, W. MADER, and H. FISCHMEISTER, “Ultrahigh Vacuum Diffusion Bonding of Metals to Ceramics”, *Ceram. Eng. Sci. Proc.*, **10**, [11-12], 1503-14 (1989).

76. G. ELSSNER, S. RIEDEL, and R. PABST, “Fractography and Fracture Paths in Ceramic-Metal Composites”, *Practical Metallography*, **12**, 234-43 (1975).

77. S. MOROZUMI, M. KIKUCHI, and T. NISHINO, “Bonding Mechanism Between Alumina and Niobium”, *Journal of Materials Science*, **16**, 2137-44 (1981).

78. W. MADER and M. RÜHLE, “Electron Microscopy Studies of Defects at Diffusion-Bonded Nb/Al_2O_3 Interfaces”, *Acta Metall.*, **37**, [3], 853-66 (1989).

79. D. KORN, G. ELSSNER, H.F. FISCHMEISTER, and M. RÜHLE, “Influence of Interface Impurities on the Fracture Energy of UHV Bonded Niobium-Sapphire Bicrystals”, *Acta Metall. Mater.*, **40**, S355-60 (1992).

80. D. KNAUSS and W. MADER, “Chemical Composition and Lattice Relaxations at Diffusion-Bonded Nb/Al_2O_3 Interfaces”, *Ultramicroscopy*, **37**, 247-62 (1991).

81. B. GIBBESCH, G. ELSSNER, W. MADER, and H.F. FISCHMEISTER, “Ultrahigh Vacuum Diffusion Bonding of Nb and Cu Single Crystals to Sapphire”, in *Joining of Ceramics, Glass, and Metals*, edited by W. KRAFT, (DGM, Oberursel, 1989) pp. 65-72.

82. M. TURWITT, G. ELSSNER, and G. PETZOW, “Manufacturing and Mechanical Properties of Interfaces Between Sapphire and Niobium”, *Journal de Physique*, **46**, C4–123-7 (1985).

83. M. RÜHLE, M. BACKHAUS-RICOULT, K. BURGER, and W. MADER, “Diffusion Bonding of Metal/Ceramic Interfaces - A Model Study at the Nb/Al_2O_3 Interfaces”, in *Ceramic Microstructures ‘86*, edited by J.A. PASK and A.G. EVANS, (Plenum, New York, 1987) pp. 295-305.

84. M. RÜHLE, K. BURGER, and W. MADER, “Structure and Chemistry of Grain Boundaries in Ceramics and of Metal/Ceramic Interfaces”, *J. Microsc. Spectrosc. Electron.*, **11**, 163-77 (1986).

85. G. ELSSNER, D. KORN, and M. RÜHLE, “The Influence of Interface Impurities on Fracture Energy of UHV Diffusion Bonded Metal-Ceramic Bicrystals”, *Scripta Metallurgica et Materialia*, **31**, [8], 1037-42 (1994).

86. H.F. FISCHMEISTER, W. MADER, B. GIBBESCH, and G. ELSSNER, “ Preparation, Properties, and Structure of Metal/Oxide Interfaces”, *Mat. Res. Soc. Symp. Proc.*, **122**, 529-40 (1988).

87. G. ELSSNER and U. KROHN, “Probleme der Haftung bei Schichtverbindungen aus Keramik und Metall”, *Z. Metallkde.*, **70**, [2], 71-9 (1979), in German.

88. J.T. KLOMP, “Ceramic-Metal Reactions and Their Effect on the Interface Microstructure”, in *Ceramic Microstructures ‘86*, edited by J.A. PASK and A.G. EVANS, (Plenum, New York, 1987) pp. 307-17.

89. C.J. MCMAHON JR. and V. VITEK, “The Effects of Segregated Impurities on Intergranular Fracture Energy”, *Acta Metallurgica*, **27**, 507-13 (1979).

90. M.P. SEAH, “Adsorption-Induced Interface Decohesion”, *Acta Metallurgica,* **28**, 955-62 (1980).

91. M. FLORJANCIC, W. MADER, M. RÜHLE, and M. TURWITT, “HREM and Diffraction Studies of an Al_2O_3/Nb Interface”, *Journal de Physique*, **46**, C4–129-33 (1985).

92. M. KUWABARA, J.C.H. SPENCE, and M. RUHLE, “On the Atomic Structure of the Nb/Al_2O_3 Interface and the Growth Al_2O_3 Particles”, *J. Mater. Res.*, **4**, [4], 972-7 (1989).

93. J. MAYER, C.P. FLYNN, and M. RÜHLE, “High-Resolution Electron Microscopy Studies of Nb/Al_2O_3 Interfaces”, *Ultramicroscopy*, **33**, 51-61 (1990).

94. J .MAYER, J.A. DURA, C.P. FLYNN, and M. RÜHLE, “Electron Microscopy Studies of Nb-Al2O3 Interfaces Formed by Molecular Beam Epitaxy”, *Surface and Coatings Technology*, **43/44**, 199-212 (1990).

95. Y. ISHIDA, H. ICHINOSE, J. WANG, and T. SUGA, “HREM of Carbon/Metal and Ceramic/Metal Interfaces in Composite Materials”, in Proceedings of the 46th Annual Meeting of the Electron Microscopy Society of America, edited by G.W. BAILEY, (San Francisco Press, San Francisco, 1988) pp. 728-9.

96. W. MADER, “Structure and Chemistry of Interfaces Between Oxide Precipitates and a Metal Matrix”, *Z. Metallkde.*, **80**, [3], 139-51 (1989).

97. G. ELßNER, H. JEHN, and E. FROMM, “Influence of Gas Impurities on the Solid-State Bonding of Nb/Al_2O_3 Composites Above 1200°C”, *High Temperatures-High Pressures*, **10**, 487-92 (1978).

98. J. CADOZ, J. CASTAING, D.S. PHILLIPS, A.H. HEUER, and T.E. MITCHELL, “Work Hardening and Recovery in Sapphire (α-Al_2O_3) Undergoing Prism Plane Deformation”, *Acta Metall.*, **30**, 2205-18 (1982).

99. K.M. KNOWLES, L.B. ALEXANDER, R.E. SOMEKH, and W.M. STOBBS, “Electron Microscope Characterization of a Niobium-Sapphire Epitaxial Interface”, *Inst. Phys. Conf. Ser.*, **90**, 245-8 (1987).

100. F.S. OHUCHI, “Surface Science Studies of Nb-(0001) Al_2O_3 Interfacial Reactions”, *Journal of Materials Science Letters*, **8**, 1427-9 (1989).

101. F.S. OHUCHI and M. KOHYAMA, “Electronic Structure and Chemical Reactions at Metal-Alumina and Metal-Aluminum Nitride Interfaces”, *J. Am. Cer. Soc.*, **74**, [6], 1163-87 (1991).

102. J.R. HEFFELFINGER, M.W. BENCH, and C.B. CARTER, “On the Faceting of Ceramic Surfaces”, *Surface Science*, **343**, L1161-6 (1995).

103. J.R. HEFFELFINGER and C.B. CARTER, “Mechanisms of Surface Faceting and Coarsening”, *Surface Science*, **389**, 188-200 (1997).

104. R.A. MARKS, University of California at Berkeley, unpublished research (1999).

105. J.T. KLOMP, "Solid-State Bonding of Metals to Ceramics", *Science of Ceramics*, **5**, 501-22 (1970).

106. R.M. CRISPIN and M.G. NICHOLAS, "Alumina-Copper Diffusion Bonding", *Ceram. Eng. Sci. Proc.*, **10**, [11-12], 1575-81 (1989).

107. L. ESPOSITO, A. BELLOSI, S. GUICCIARDI, G. DE PORTU, "Solid State Bonding of Al_2O_3 with Cu, Ni, and Fe: Characteristics and Properties", *Journal of Materials Science*, **33**, 1827-36 (1998).

108. M. WITTMER, C.R. BOER, P. GUDMUNDSON, and J. CARLSSON, "Mechanical Properties of Liquid-Phase-Bonded Copper-Ceramic Substrates", J*ournal of the American Ceramic Society*, **65**, [3], 149-53 (1982).

109. C.A.M. MULDER and J.T. KLOMP, "On the Internal Structure of Cu- and Pt-Sapphire Interfaces", *Journal de Physique*, **46**, C4–111-6 (1985).

110. M. RÜHLE, A. LIEDTKE, U. ALBER, R. SCHWEINFEST, and G. ELßNER, "Structure, Composition, and Thermal Stability of the Cu/Al_2O_3 Interface", in *Interfacial Science in Ceramic Joining*, edited by A. BELLOSI *et al.*, (Kluwer Academic Publishers, Netherlands, 1998), pp. 3-14.

111. F. ERNST, P. PIROUZ, and A.H. HEUER, "HRTEM Study of a Cu/Al_2O_3 Interface", *Philosophical Magazine A*, **63**, [2], 259-77 (1991).

112. F.S. OHUCHI, R.H. FRENCH, and R.V. KASOWSKI, "Cu Deposition on Al2O3 and AlN Surfaces: Electronic Structure and Bonding", *J. Appl. Phys.*, **62**, [6], 2286-9 (1987).

113. D. BENJAMIN, ed., *Metals Handbook,* 9th Edition, Vol. 3 (American Society for Metals, Metals Park, OH, 1980) p. 333.

114. Y. YOSHINO, "Role of Oxygen in Bonding Copper to Alumina", J. *Am. Ceram. Soc.*, **72**, [8], 1322-7 (1989).

115. S.T. KIM and C.H. KIM, "Interfacial Reaction Product and its Effect on the Strength of Copper to Alumina Eutectic Bonding", *Journal of Materials Science*, **27**, 2061-6 (1992).

116. K. WANG and R.R. REEBER, "The Role of Defects on Thermophysical Properties: Thermal Expansion of V, Nb, Ta, Mo, and W", *Materials Science and Engineering,* **R23**, 101-37 (1998).

117. R.L. COBLE and W.D. KINGERY, "Effect of Porosity on Physical Properties of Sintered Alumina", *Journal of the American Ceramic Society*, **39**, [11], 377-85 (1956).

118. J.B. WACHTMAN JR., T.G. SCUDERI, and G.W. CLEEK, "Linear Thermal Expansion of Aluminum Oxide and Thorium Oxide from 100° to 1100°K", *Journal of the American Ceramic Society*, **45**, [7], 319-23 (1962).

119. T.H. NIELSEN and M.H. LEIPOLD, "Thermal Expansion in Air of Ceramic Oxides to 2200°C", *Journal of the American Ceramic Society*, **46**, [8], 381-7 (1963).

120. W.D. CALLISTER JR., *Materials Science and Engineering an Introduction*, 2nd Edition, (John Wiley and Sons, New York, NY 1991) pp. 662-4.

121. T.C. WILDER, "Direct Measurement of the Oxygen Content in Liquid Copper; the Activity of Oxygen in Dilute Liquid Cu-O Alloys", *Transactions of the Metallurgical Society of AIME*, **236**, 1035-40 (1966).

122. R. KIRCHHEIM, "Metals as Sinks and Barriers for Interstitial Diffusion with Examples for Oxygen Diffusion in Copper, Niobium, and Tantalum", *Acta Metallurgica*, **27**, 869-78 (1979).

123. M.M.A. EL-NAGGAR and N.A.D. PARLEE, "Diffusion Studies of Oxygen in Liquid Copper and Copper Alloys by a Solid Electrolytic Cell Technique", *High Temperature Science*, **3**, 138-54 (1971).

124. R.A. PERKINS and R.A. PADGETT JR., "Oxygen Diffusion in Niobium and Nb-Zr Alloys", *Acta Metallurgica*, **25**, 1221-30 (1977).

125. G.I. NIKOLAEV and N.V. BODROV, "Study by Atomic Absorption of the Evaporation of Aluminum Impurities from Tantalum and Niobium", *Russian Journal of Physical Chemistry*, **52**, [6], 821-3 (1978).

126. E. SAIZ, Lawrence Berkeley National Laboratory, private communication (1999).

127. J.D. SUGAR, Lawrence Berkeley National Laboratory, unpublished research (1999).

128. B.J. DALGLEISH, Lawrence Berkeley National Laboratory, unpublished research (1992).

129. L. ESPOSITO, Lawrence Berkeley National Laboratory, private communication (1999).

130. J.D. SUGAR and R.A. MARKS, unpublished research (1999).

131. M. BACKHAUS-RICOULT, "Diffusion Processes and Interphase Boundary Morphology in Ternary Metal-Ceramic Systems", *Ber. Bunsenges. Phys. Chem.*, **90**, 684-90 (1986).

132. F.F. LANGE and D.R. CLARKE, "Morphological Changes of an Intergranular Thin Film in a Polycrystalline Spinel", *Journal of the American Ceramic Society*, **65**, [10], 502-6 (1982).

133. M. RÜHLE, presentation, HREM of Heterophase Interfaces, Lawrence Berkeley National Laboratory, 1999.

134. G.K. LAYDEN, "The System Al_2O_3-Nb_2O_5", *Journal of the American Ceramic Society*, **46**, [10], 506 (1963).

135. A.M. GLAESER, R. GRONSKY, E. MAMMANA, and T. RADETIC, Lawrence Berkeley National Laboratory, unpublished research (1999).

136. D.R. GASKELL, *Introduction to Metallurgical Thermodynamics,* 2nd Edition, (Hemisphere Publishing Corporation, New York, NY 1981) pp. 585-6.

137. D.R. LIDE, ed., *CRC Handbook of Chemistry and Physics,* 71st Edition, (CRC Press, Boca Raton, 1990) pp. **5**-16 to **5**-67.

138. R.C. WEAST, ed. and S.M. SELBY, ed., *CRC Handbook of Chemistry and Physics,* 47st Edition, (The Chemical Rubber Company, Clevland 1966) pp. D-22 to D-27.

139. E.M. LEVIN, C.R. ROBBINS, and H.F. MCMURDIE, *Phase Diagrams for Ceramists*, Vol. II (The American Ceramic Society, Columbus, OH, 1969) pp. 97,113.